Development and Characterization of Radiation Resistant Nanocomposite Polymeric Membranes

By

Amita Bedar

ENGG01201504008

BHABHA ATOMIC RESEARCH CENTRE, MUMBAI

A thesis submitted to the
Board of Studies in Engineering Sciences

In partial fulfillment of requirements
for the Degree of

DOCTOR OF PHILOSOPHY

of

HOMI BHABHA NATIONAL INSTITUTE

23^{rd} March, 2021

Homi Bhabha National Institute

Recommendations of the Viva Voce Committee

As members of the Viva Voce Committee, we certify that we have read the dissertation prepared by **Amita Bedar** entitled **Development and Characterization of Radiation Resistant Nanocomposite Polymeric Membranes** and recommend that it may be accepted as fulfilling the thesis requirement for the award of Degree of Doctor of Philosophy.

Designation	Name	Signature	Date
Chairman	Prof. Srikumar Banerjee	Srikumar Banerjee	23.3.2021
Guide & Convener	Prof. R. C. Bindal		23.03.2021
Co-guide	Prof. P. K. Tewari		23.03.2021
Examiner	Prof. Sirshendu De	Sirshendu De	27.3.21
Member	Prof. N. K. Maheshwari	Naresh Kr Maheshwari	23.03.2021
Member	Prof. G. Sugilal	G Sugilal	23.03.2021
Member	Prof. R. Kapoor	Rajeev Kapoor	23/3/2021
Technology Advisor	Dr. Soumitra Kar	Soumitra Kar	23/03/2021

Final approval and acceptance of this thesis is contingent upon the candidates submission of the final copies of the thesis to HBNI.

I/We hereby certify that I/we have read this thesis prepared under my/our direction and recommend that it may be accepted as fulfilling the thesis requirement.

Date:

Place:

Signature
Co-guide

Signature
Guide

Homi Bhabha National Institute

Recommendations of the Viva Voce Committee

As members of the Viva Voce Committee, we certify that we have read the dissertation prepared by **Amita Bedar** entitled **Development and Characterization of Radiation Resistant Nanocomposite Polymeric Membranes** and recommend that it may be accepted as fulfilling the thesis requirement for the award of Degree of Doctor of Philosophy.

Designation	Name	Signature	Date
Chairman	Prof. Srikumar Banerjee	Srikumar Banerjee	23.3.2021
Guide & Convener	Prof. R. C. Bindal		23.03.2021
Co-guide	Prof. P. K. Tewari		23.03.2021
Examiner	Prof. Sirshendu De	Sirshendu De	27.3.21
Member	Prof. N. K. Maheshwari	Naresh Kr Mahesh	23.03.2021
Member	Prof. G. Sugilal		23.03.2021
Member	Prof. R. Kapoor	Rajeew Kapoor	23/3/2021
Technology Advisor	Dr. Soumitra Kar	Soumitra Kar	23/03/2021

Final approval and acceptance of this thesis is contingent upon the candidates submission of the final copies of the thesis to HBNI.

I/We hereby certify that I/we have read this thesis prepared under my/our direction and recommend that it may be accepted as fulfilling the thesis requirement.

Date:

Place:

Signature
Co-guide

Signature
Guide

Statement by Author

This dissertation has been submitted in partial fulfillment of requirements for an advanced degree at Homi Bhabha National Institute (HBNI) and is deposited in the Library to be made available to borrowers under rules of the HBNI.

Brief quotations from this dissertation are allowable without special permission, provided that accurate acknowledgement of source is made. Requests for permission for extended quotation from or reproduction of this manuscript in whole or in part may be granted by the Competent Authority of HBNI when in his or her judgment the proposed use of the material is in the interests of scholarship. In all other instances, however, permission must be obtained from the author.

Amita Bedar

Declaration

I, hereby declare that the investigation presented in the thesis has been carried out by me. The work is original and has not been submitted earlier as a whole or in part for a degree/ diploma at this or any other Institution/ University.

Amita Bedar

List of Publications arising from the thesis

Journals

1. **“Polysulfone-Ceria Mixed-Matrix Membrane with Enhanced Radiation Resistance Behavior”**, Amita Bedar, R. K. Lenka, N. Goswami, V. Kumar, A. K. Debnath, D. Sen, S. Kumar, S. Ghodke, P. K. Tewari, R. C. Bindal, and S. Kar, *ACS Applied Polymer Materials*, **2019** *1*, 1854-1865.

2. **“Enhancing γ-radiation resistant property of polysulfone membranes with carboxylated nanodiamond: Impact and effect of surface tunability”**, Amita Bedar, P. K. Tewari, R. C. Bindal, and S. Kar, *Applied Surface Science*, **2020** *507*, 144897.

3. **“Nanodiamonds as a state-of-the-art material for enhancing the gamma radiation resistance properties of polymeric membranes”**, Amita Bedar, N. Goswami, A. K. Singha, V. Kumar, A. K. Debnath, D. Sen, V. K. Aswal, S. Kumar, D. Dutta, B. Keshavkumar, S. Ghodke, R. Jain, B. G. Singh, P. K. Tewari, R. C. Bindal, and S. Kar, *Nanoscale Advances*, **2020** *2*, 1214-1227.

4. **“Effect of nanodiamond size on γ-radiation resistance property of polysulfone-nanodiamond mixed-matrix me-mbranes”**, Amita Bedar, V. Kumar, A. K. Debnath, N. N. Kumar, R. Jain, P. K. Tewari, R. C. Bindal, and S. Kar, *Diamond and Related Materials*, **2020** *108*, 107963.

5. **“Enhancement of γ-radiation stability of polysulfone membrane matrix by reinforcement of hybrid nanomaterials of nanodiamond and ceria”**, Amita Bedar, R. K. Lenka, N. K. Goel, S. Kumar, R. Jain, B. G. Singh, P. K. Tewari, R. C. Bindal, and S. Kar, *Materials Advances*, **2020** *1*, 1220-1231.

6. **“Kinetics Studies on Free Radical Scavenging Property of Ceria in Polysulfone-Ceria Radiation Resistant Mixed-matrix Membrane”**, Amita Bedar, B. G. Singh, P. K. Tewari, R. C. Bindal, and S. Kar, *International Journal of Chemical Reactor Engineering*, (Accepted).

Conferences

1. **"Synthesis and characterization of polysulfone-nanodia-mond composite membrane"**, Amita Bedar, P. K. Tewari, R. C. Bindal, and S. Kar, *India International Science Festival Young Scientists Conclave, Delhi, India*, **2016**.
2. **"Enhancing gamma radiation resistant property of polysulfone membrane with carboxylated nanodiamond"**, Amita Bedar, P. K. Tewari, R. C. Bindal, and S. Kar, *3rd International Conference on Applied Surface Science, Pisa, Italy*, **2019**.
3. **"Gamma radiation resistant behaviour of polysulfone-nanodiamond mixed matrix membrane: The effect of nanoparticle size and loading"**, Amita Bedar, P. K. Tewari, R. C. Bindal, and S. Kar, *4th International Conference on Materials Science & Engineering, Paris, France*, **2019**.
4. **"Development of polysulfone-nanodiamond composite membranes with enhanced γ-radiation stability"**, Amita Bedar, B. G. Singh, P. K. Tewari, R. C. Bindal, and S. Kar, *15th DAE-BRNS Biennial Trombay Symposium on Radiation & Photochemistry, Mumbai, India*, **2020**.
5. **"Kinetics studies on free radical scavenging property of ceria in polysulfone-ceria radiation resistant mixed-matrix membrane"**, Amita Bedar, B. G. Singh, P. K. Tewari, R. C. Bindal, and S. Kar, *International Conference on Advances in Chemical Engineering, Dehradun, India* , **2020**.

Amita Bedar

Dedicated to My Family

Acknowledgements

I would take this opportunity to thank all the people who had been along with me, guided me all through my wonderful journey of Ph.D.

First and foremost I would like to express my sincere gratitude to my Guide Prof. Ramesh C. Bindal for their unwavering support and belief in me. He has provided me all the facilities along with freedom of work, which gave me a lot of confidence and faith on myself as an independent researcher.

I would also like to thank my Co-guide Prof. Pradip K. Tewari to encourage me throughout this journey. My gratitude extends to my technology advisor Dr. Soumitra Kar to make himself always available to discuss ideas and provided me all the facility I required during my PhD. His friendly nature, motivation and excitement towards work always inspired me to be exited for implementing new ideas into work.

I am deeply grateful to my doctoral committee chairman Prof. Srikumar Benerjee for their insightful comments, suggestions and encouragement. Moreover, his curiosity and excitement towards each and every minute details inspired me to be curious for learning and researching different aspects of the things. I would like to extend my sincere thanks to all my doctoral committee members, Prof. G. K. Day, Prof. S. B. Roy, Prof. N. K. Maheshwari, Prof. G. Sugilal, and Prof. R. Kapoor for their critical reviews and valuable suggestions which incented me to widen my research from various perspectives.

I express my deep gratitude to Dr. (Mrs.) Payel Sarkar for helping me carry out the modelling of mixed matrix membrane. My sincere thanks to the people of my department for helping me out in every possible manner; Dr. Hemant S. Sodaye for introducing me to several instruments; Mr. Amit K. Singha for designing the table top membrane casting machine and helping me to provide the customised apparatus and equipments, Mr. Nitesh Goswami for helping me to refining my manuscripts, and Dr. Bitan Ghosh for helping me to solve the several problems of instruments. I would also like to thank Mr. R. B. Bramhane, Mr. P. P. Surve, Mr. U. R. More, and Mrs. Abhilasha Singha for their continuous support in the lab for carrying out the entire research work. I am grateful to the contract staff Mr. Ganesh and Mr. Husain to helping me during the laboratory work.

I am immensely thankful to Dr. Virendra kumar, Dr. Narender K. Goel, and Dr. Nilanjal Misra for providing me the facilities to carry out my research work like gamma chamber for irradiating my membranes, Drop shape analyser and Fourier-transform infrared spectroscopy (FTIR) to analyse my membranes. I was able to work smoothly due to the friendly and positive support I received from people of ISOMED.

I owe my deep sense of gratitude to Dr Beena G. Singh, for helping me out with all the free radical scavenging study of nanomaterials and membranes. Her energy and enthusiasm towards research makes my work with her more interesting.

I would like to thank the Dr. Raja Kishora Lenka for helping me in the synthesis of ceria nanoparticles. I am thankful to Dr. Dheeraj Jain and Mr. Jitendra Nuwal for providing me different size of nanodiamond particles. I am grateful to Prof. Raghvendra Tiwari, Dr. Naveen N. Kumar, and Mr. Sanjay Kumar for providing me FESEM and TEM facilities. My gratitude extend to all the people from various department for providing me the facilities and helping me in the analysis during my PhD; Dr. Debasis Sen and Dr. V. K. Aswal for SAXS study; Dr. A. K. Debnath for XPS analysis; Dr. A. K. Dubey and Mr. Sunill Shejwal for helping in gamma irradiation of membranes; Prof. R. D. Jain and Dr. Sharwari for GPC study; Dr. Dhanadeep Dutta for PALS analysis; Dr. Biju Keshavkumar for Monte-Carlo Simulation study; Dr. Chhavi Agarwal for porosimetry analysis.

A big shout-out to my friends who rally helped me remain sane during this journey of PhD. Thanks to my friends from my department Mamta, Bharat, Vaishnavi, Srija, Ritu, Samina, and Rutuja, with whom I remain energised during the work.

Our discussions and gossiping over tea breaks was the power breaks to get back to the work even more energetically. I am lucky to have friends like Tejaswi, Uma, Divya, Dhruvish, Jitendra, Prashant, Deepak, Nakul, Prateek, Milind, and Manish who kept me happy and spirited all the time. I can not Thank enough to Manish for his continuous support specially in writing work. I am grateful to my seniors Vineet, Eagle, Nitendra, Ruchi, Anita, Vishal, Nitin, and Eshita to guide me at every step. I want to thank my juniors Samyak and Harshit for always being there whenever I need. I am falling short of words to express how lucky I am to have Lakshya, Lokesh, Viswa, Taslim, Reny, Pavan, Swapnil, Sakshi, and Piyush as my batch mates who were continuous support and also the another family in Mumbai. I cannot even begin to adequately thank Piyush for motivating me and being there for me in my thin and thick. I would thank my cousin sister and my friend since birth Neha Gupta for helping me to stay energised.

Last, but never the least, I offer my immense gratitude and love to my wonderful family; My father Dr. Arvind Bedar is my inspiration to be fearless and supportive to the people; My mother Mrs. Rekha Bedar, from whom I learned to keep patience and be positive in every situation; My elder brother Mr. Amresh Bedar always nurtured and inspired me; My sister-in-low Mrs. Aakanksha Bedar is a treasure for me with full of energy, support, and positivity; My younger sister Anusha and brother Anudeep were always there to care and motivate me; Lots of love to my little bundle of Joy Aarshi, she gives me magical energy; Nothing in my life can ever be complete without you all.

Amita Bedar

Contents

List of Figures

List of Tables

Chapter 1

Introduction

1.1 Overview

A broad spectrum of radioactive waste is generated at various stages of nuclear fuel processing [1]. Hence, safe and effective management of radioactive waste is of utmost importance [2, 3]. Various methods have been established to treat and manage radioactive wastes. These processes typically include chemical treatment, adsorption, filtration, evaporation, ion exchange, extraction, etc. However, these processes have limitations in terms of their efficiency in eliminating all contaminants, high operating cost and/or production of secondary solid wastes [4].

Membrane technology has been demonstrated for successful removal of radioactive substances with significant advantages over the above-mentioned conventional processes [5]. As a unit operation, membranes can be used independently, or in combination with conventional technologies, for treatment of complex waste streams [6]. These hybrid technologies provide excellent capability for treating radioactive waste by improving the efficiency and effectiveness of conventional processes. Inorganic (ceramic) membranes have been found to have excellent stability against the radioactive environment [7], but their application is limited owing to the difficulty in their fabrication, inherent brittleness, and more importantly, limitation in fine-tuning pore sizes.

Polymeric membranes have gained attention due to their higher flexibility, processability, simple pore formation mechanism, tailorable properties, low cost and negligible secondary waste generation [8]. Also, properties of polymeric membranes can be altered for specific application by functionalization and/or modification in its internal structure (pores/porosity, internal network, etc.), with enhanced thermal, chemical, and mechanical stability [9]. However, application of polymeric membranes is limited in radioactive domain, owing to their low radiation stability [10]. Hence, there is an extensive interest in establishing new systems that are resistant to radiation and can enhance performance of membrane in γ-radiation environment.

Since nanomaterials have unique properties such as high surface area, tunability, low density, high porosity, etc. [11], they offer unprecedented opportunities to tailor-make membranes with desirable attributes keeping into account the targeted applications [12]. In polymer nanocomposites, larger surface-to-volume ratio of nanofillers results in a significant increase in the volume of interphase between nanomaterial and polymer, which makes the properties of the composite different from that of bulk polymer.

Nanocomposite membranes are established by incorporating nanomaterials into polymeric membrane matrix . Distinctive properties of nanomaterials helps improve membrane matrix in terms of their permeate flux, salt rejection, anti(bio)-fouling properties, and increasing mechanical, chemical, and thermal stability [13]. However, studies have not been focused on enhancement of radiation resistant properties of membranes to improve stability of polymeric membrane in radiation environment.

In this Chapter, radioactive effluent and requirement of their treatment, importance of membrane technology and their application in nuclear industries, polymeric membranes and effect of radiation on them, nanotechnology to overcome the drawbacks of polymeric membranes, and nanomaterials studied in this research work to enhance the radiation resistance of polymer are described in brief. The chapter ends with the motivation and objectives of this thesis.

1.2 Radioactive effluent

A broad spectrum of radioactive waste (low, intermediate, and high level) is generated at various stages of nuclear fuel processing (uranium ore mining and milling, fuel fabrication, reactor operation, and spent fuel reprocessing)[1].

Hazardous level of nuclear waste depends upon its radioactivity, which diminishes with time unlike other industrial wastes. Radionuclides containing alpha and beta emitters tend to have long half-lives, which makes their handling easier. However, more penetrating γ-rays emitters tend to have short half-lives. All radioactive nuclides decay into non-radioacive elements, while the highly radioactive isotope decays faster [14].

Radioactive waste management is determined by the radioactivity level of material. Radioactive wastes are classified into four broad categories, based on the radioactivity level as given below.

1.2.1 Exempt waste & very low level waste (VLLW)

Radioactive materials in exempt waste and very low level waste (VLLW) are not toxic to people or environment. This type of waste is generated through recovering or dismantling operations in nuclear industry or from industries like food processing, chemical, steel, etc. It mainly consists of dismantled materials, like concrete, plaster, bricks, metal, piping, etc. and disposed of with domestic refuse [15, 16].

1.2.2 Low-level waste (LLW)

Low-level waste (LLW) consists only 1% of the radioactivity of all radioactive waste and $\sim$ 90% of the volume. It is generated from nuclear industry, hospitals, and other industries [16, 17]. It contains small amounts of mostly short-lived radioactive mterials like, papers, rags, tools, clothing, filters, etc., which are compacted or incinerated before disposal.

1.2.3 Intermediate-level waste (ILW)

Intermediate-level waste (ILW) contains 4% of radioactivity of all radioactive waste and 7% of the volume. Sometimes, it requires shielding due to higher amounts of radioactivity (radioactive decay generates heat of less than about 2 kW/m^3), while non-solids may be solidified in concrete or bitumen for disposal. It generally consists of resins, chemical sludges, metal fuel cladding, and contaminated materials from reactor [16–18].

1.2.4 High-level waste (HLW)

High-level waste (HLW) is generated in nuclear reactor from burning of uranium fuel [19] and consists of fission products and transuranic elements. It is hot (thermal power above $\sim 2\ kW/m^3$) due to decay heat and hence requires cooling and shielding due to high radioactivity. HLW contains $> 95\%$ of total radioactivity generated in nuclear reactor; it is either a used fuel or seperated waste from reprocessing of a used fuel.

Management of radioactive waste is essential to protect human and environment. This implies that the rate or concentration of any radionuclides should be reduced by isolating or diluting the waste so that it become harmless. Hence, safe and effective management of radioactive waste is of utmost importance [2, 3].

1.3 Conventional methods to manage liquid radioactive waste

Various methods have been established to treat and manage radioactive wastes. These processes typically include chemical treatment [20], adsorption [21], filtration [22], evaporation, ion exchange [23], extraction [24], etc. However, these processes have limitations in terms of efficiency of eliminating all contaminants, high operating cost and/or production of secondary solid wastes [4].

Many nuclear power plants have generally used evaporation, conventional filtration, ion exchange, or a combination of these methods for treatment of low level liquid waste [25]. Limitation of these processes are: generation of significant quantities of radioactive solid waste; product effluent is not pure enough for environmental discharge or recycling; high operating cost with high energy consumption in case of evaporation; and conventional filtration and ion exchange techniques have not been able to seperate colloidal particles containing $^{58/60}Co$, ^{54}Mg, ^{55}Fe, and ^{125}Sb, etc. [26].

1.4 Membrane technology

Membrane is a selective barrier, which separates things by restricting transport of some things while allowing the others; these things can be molecules, ions, or other small particles [27]. A membrane can be homogenous or heterogeneous with symmetric or asymmetric structure in the form of solid or liquid, and can carry a charge of positive, negative, neutral, or bipolar. Transport phenomenon by a membrane can be through convection or diffusion of individual molecules, induced by one of the driving forces (e.g., electric field, concentration, pressure, and temperature gradient). A membrane technique separates inlet feed stream into two outlet streams known as permeate (passed through membrane) and concentrate (rejected by membrane).

Various types of membrane separation processes have been developed for specific industrial applications [28]. Some of the widely used processes are reverse osmosis (RO), nanofiltration (NF), ultrafiltration (UF), microfiltration (MF), electrodialysis (ED), membrane electrolysis, diffusion dialysis, gas seperation, vapour permeation, pervaporation, forward osmosis, membrane distilation, membrane contactors, and carrier mediated processes, etc. Selection of a membrane should be determined by the specific application objective like particulate or dissolved solids removal, hardness reduction or ultra pure water production, removal of specific gases/chemicals, etc. [29].

Several membrane technologies have been established for purification of water as well as waste liquors [30, 31]. Moreover, membrane technology has been demonstrated for successful removal of radioactive substances with many advantages over conventional processes [5, 32, 33], such as high removal capacity, flexibility of operation, cost effectiveness, less energy requirement, and easy synthesis of membrane materials. Hence, membrane technology has been accepted by nuclear industry as a feasible alternative for treatment of radioactive wastes [34]. Membrane technology can be practiced as an independent unit, or in combination with conventional technologies for complex waste treatments. These combined technologies provide excellent capability for treating radioactive wastes by improving efficiency and effectiveness of conventional processes.

Inorganic (ceramic) membranes have been found to have excellent stability against radioactive environment [7], but their application is limited due to difficulty in their fabrication, inherent brittleness, and more importantly limitation to fine-tune pore sizes. On the other hand, polymeric membranes have received extensive attention due to higher flexibility, processability, simple pore formation mechanism, tailorable properties, low cost, as well as low possibilities of secondary waste generation [35–37]. Also, polymeric membranes can be altered for specific application by functionalisation, uncomplicated modification in its internal structure (pores/porosity, internal network, etc.) and moderate stability (thermal, chemical, and/or mechanical stability), etc. [38–41]. However, due to low radiation stability of polymeric membranes, the application of such membranes in radioactive domain is limited [42–44].

1.4.1 Membrane technology in nuclear industry

The motivation behind using membrane technologies in nuclear industries are mainly as follows:

1. Radioactivity reduction for discharge to environment.
2. Solid waste removal from effluents.
3. Recovery of valuable products.

Application of membrane technology is distinctive due to specific local conditions, and different processing objectives, etc. and the choice of membrane systems is made based on their applications. Few applications of membrane technology in nuclear industries are mentioned below:

1.4.1.1 Reverse osmosis

Reverse osmosis is a well developed technology and applied for separation, product stream concentration, and wastewater treatment, as well as for removal of radionuclides from low level liquid wastes such as waste streams at nuclear power plants. Since reverse osmosis is capable of rejecting almost all contaminants from a solution (except dissolved gases and tritium), and hence the high purity permeate water can be recycled or discharged (generally the activity is low). Reverse osmosis systems are capable to replace or combine with existing evaporation and ion exchange technology. In nuclear industry, usually reverse osmosis is a part of liquid waste treatment system [33]. Atomic Energy of Canada Ltd's Chalk River Laboratories, Canada has tested cellulose acetate reverse osmosis membranes to recover boric acid from radioactive waste streams, which can be recycled to the plant [45].

1.4.1.2 Reverse osmosis with conventional pretreatment

A ‘zero-liquid’ discharge philosophy is adhered in nuclear power plant, which requires to recycle all liquid radioactive waste generated. The liquid radioactive waste has been divided into two major streams; one is clean waste with high purity from equipment, and other is floor drain waste with low purity from floor drains. Reverse osmosis technology reduces solid waste from effluent, reduces disposal costs, maximizes effluent storage capacity, reduces maintenance costs, and improves water chemistry [46]. In one of the nuclear power plant, reverse osmosis was combined with existing system to get processing of both clean and floor drain waste [46].

1.4.1.3 Reverse osmosis with ultrafiltration pretreatment

To acquire the most efficient, cost effective, reliable system in one of nuclear plant, a complete ZERO system was installed, which consisted of a tubular ultrafiltration unit, spiral reverse osmosis unit, followed by concentrates drum dryer unit and demineralizer system. This system was used to treat the floor drains, reactor outage wastes, spent resin sluice water, and other miscellaneous streams of plant wastes [46]. The Bruce nuclear power plant (Canada) established ultrafiltration and two stage reverse osmosis, for treatment of aqueous wastes arising from chemical cleaning of steam generators and heat exchangers [47].

1.4.1.4 Reverse osmosis with microfiltration pretreatment

Many soluble and sparingly soluble salts with predominant component as sodium nitrate generally contained in effluent, and reduction of concentrated waste volume are the goals of the effluent treatment facility. Major individual treatment steps in the overall process are: pH adjustment, microfiltration, mercury specific ion exchange, activated carbon for organic removal, reverse osmosis, polishing ion exchange, and evaporation [48].

1.4.1.5 Ultrafiltration

Ultrafiltration is utilized to remove colloids and other particulate foulants from streams. It is commonly used for alpha activity and actinide (generally in colloidal or pseudo-colloidal form) removal from radioactive waste stream. If metal ions are pretreated to form solid particles, hydroxo complexes or other less soluble chemical species, then ultrafiltration can be utilized to remove them from dilute aqueous solutions.

Ultrafiltration is used in treatment storage waters of fuel pond, solvent wash liquors, plutonium evaporator overheads, and aqueous effluents from plutonium fuel fabrication plants. To yield high decontamination factors for specific ions, ultrafiltration is combined with complexing agents [49]. Inorganic ultrafiltration membranes (zirconium, carbon, etc.) have shown potential in treatment of radioactive waste [50].

At Bhabha Atomic Research Centre, India, ultrafiltration enhanced by complexation with polyethylenimine was applied for radioactive cerium removal [51]. Polyethylenimine was employed to complex U(VI) and enhance removal of this isotope from contaminated environmental waters by ultrafiltration [52]. It was demonstrated that ultrafiltration without applying any additional processes and in combination with complexation, is effective for removal of uranium from contaminated water.

A combined system was proposed to treat laundary wastes, which contains ultrafiltration system whose objective is to recover the laundry solution in the permeate while removing the suspended particles followed by reverse osmosis system to remove the dissolve solids. This system is capable to recover the laundry solution and remove suspended particles, fibers, and biological matter [53].

1.4.1.6 Microfiltration

Microfiltration is used for particle separation in wastewaters generated by light water reactor (LWR) power plants. Precipitation processes can be merged with microfiltration, as long as the size of precipitated particles is suitably big for microfiltration process [6]. Depending on characteristics of the effluent, either organic or inorganic microfiltration membranes can be used. However, due to the material's radiation stability, inorganic microfilters have been used in nuclear industry for high activity wastewaters.

Radionuclides from soils and groundwaters can be removed by microfiltration. The AECL Chalk River Laboratory, Canada utilized a hollow fibre microfiltration system (pore size of 0.2 μm) for groundwater remediation [54]. Rocky Flats (USA) installed tubular microfiltration (pore size of 0.1 μm) system for processing groundwater and wastewater contaminated with isotopes of uranium, heavy metals, and organic toxic materials. This system was placed for pretreatment of effluent and reported removal of uranium isotopes was in excess of 99.9% [55].

1.5 Polysulfone-based membranes

Polymeric membranes have a wide range of applications including water and waste water treatment [56, 57], fuel cell application [58], gas separation [59], haemodialysis [60], sensors [61], industrial effluent treatment [62], etc. They have received extensive attention due to their reproducible properties, such as mechanical strength, flexibility, thermal stability, negligible secondary waste generation, as well as low cost availability [27].

In nuclear industry, during various stages of nuclear fuel cycle, high amount of radioactive effluent is generated and there is a need for safe and effective management of these effluents [63]. Materials used for such treatments should be stable in radioactive environments. Polysulfone (Psf) stands out to be a remarkable polymer, among other thermoplastic polymers, by virtue of its usability at high temperature and pressure, as well as chemical inertness [64]. Psf has reasonably high strength (tensile strength: 94.4 - 104 MPa) and high glass transition temperature (190 - 230 $^{\circ}C$) due its aromatic backbone [65], while being resistant towards radiation to some extent, as compare to other polymers [66]. Hence, it is the most preferred choice to work in the challenging radioactive environment [67].

1.5.1 Radiation effect on polysulfone

Polysulfone (Psf) is a commonly used polymer for membrane fabrication [68], but it undergos radiolysis in γ-radiation environment. Also, free radicals induced by γ-ray leads to chain scissioning and/or cross-linking, and hence leads to change in crosslink density of polymer matrix [42, 69]. This causes degradation in performance of the membranes [70]. Acidic effluent environment, in which the membranes are operated, is subject to radiolysis of water leading to transient reactive species like e^-_{aq}, $OH^\bullet$, $H^\bullet$, $HO_2^\bullet$, H_2O_2, H_3O^+, OH^-, H_2, and complex free radicals [71]. These free radicals cause further degradation of polymeric host matrix above and beyond the ones caused by direct γ-ray impingement.

Irradiation of Psf leads to generation of SO_2, as a main volatile product. Radiolysis consists of C-S main-chain scission followed by adjacent C-S bond scission, resulting in liberation of SO_2 from phenylene sulfonyl radical either directly or via phenylene sulfonic acid [72, 73]. Mechanism of C-S bond scissioning and libration of SO_2 is described by Equation (1.1) to (1.4).

$$-Ar-SO_2-Ar \longrightarrow -Ar-SO_2^\bullet + {}^\bullet Ar- \tag{1.1}$$

$$-Ar-SO_2^\bullet \longrightarrow -Ar^\bullet + SO_2 \tag{1.2}$$

$$-Ar-SO_2^\bullet + H^\bullet \longrightarrow -Ar-SO_2H \tag{1.3}$$

$$-Ar-SO_2H \longrightarrow -Ar-H + SO_2 \tag{1.4}$$

Scission and cross-linking in Psf leads to linkage of isopropylidene [74]. Possible reaction sequences are shown in Equation (1.5) to (1.9).

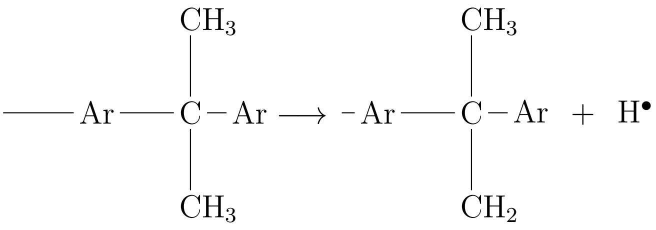

$$-\mathrm{Ar}-\overset{\mathrm{CH_3}}{\underset{\mathrm{CH_3}}{\mathrm{C}}}-\mathrm{Ar} \longrightarrow -\mathrm{Ar}-\overset{\mathrm{CH_3}}{\underset{\mathrm{CH_2}}{\mathrm{C}}}-\mathrm{Ar} + \mathrm{H}^\bullet \tag{1.5}$$

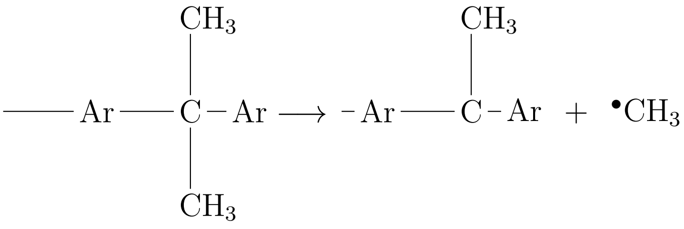

$$-\mathrm{Ar}-\overset{\mathrm{CH_3}}{\underset{\mathrm{CH_3}}{\mathrm{C}}}-\mathrm{Ar} \longrightarrow -\mathrm{Ar}-\overset{\mathrm{CH_3}}{\mathrm{C}}-\mathrm{Ar} + {}^\bullet\mathrm{CH_3} \tag{1.6}$$

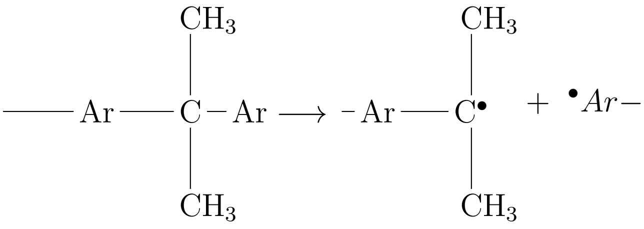

$$-\mathrm{Ar}-\overset{\mathrm{CH_3}}{\underset{\mathrm{CH_3}}{\mathrm{C}}}-\mathrm{Ar} \longrightarrow -\mathrm{Ar}-\overset{\mathrm{CH_3}}{\underset{\mathrm{CH_3}}{\mathrm{C}^\bullet}} + {}^\bullet Ar- \tag{1.7}$$

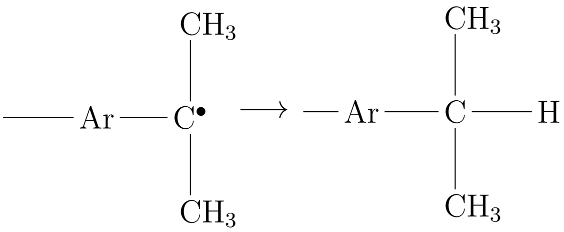

$$-Ar-\overset{\overset{CH_3}{|}}{\underset{\underset{CH_3}{|}}{C^\bullet}} \longrightarrow -Ar-\overset{\overset{CH_3}{|}}{\underset{\underset{CH_3}{|}}{C}}-H \tag{1.8}$$

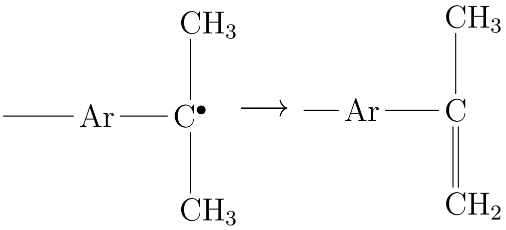

$$-Ar-\overset{\overset{CH_3}{|}}{\underset{\underset{CH_3}{|}}{C^\bullet}} \longrightarrow -Ar-\overset{\overset{CH_3}{|}}{\underset{\underset{CH_2}{\|}}{C}} \tag{1.9}$$

In main chain C-O scission in Psf, the expected phenomenon is given in Equation (1.10).

$$-Ar-O-Ar- \longrightarrow -Ar-O^\bullet + {}^\bullet Ar- \tag{1.10}$$

However, main-chain C-S scission is a primary reaction followed by scission of adjacent C-S bond and liberation of SO_2, given in Equation (1.11) and (1.12).

$$Ar-SO_2-Ar \longrightarrow Ar-SO_2^\bullet + {}^\bullet Ar \tag{1.11}$$

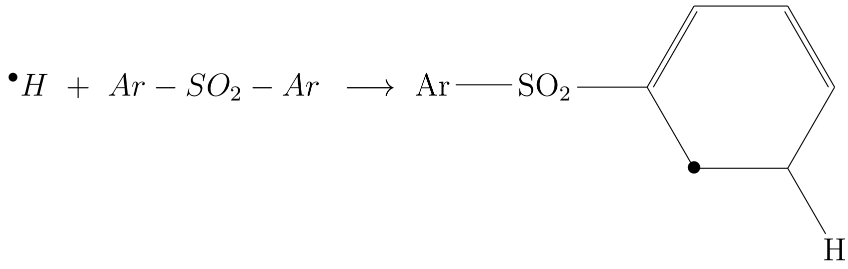

$${}^\bullet H + Ar-SO_2-Ar \longrightarrow \mathrm{Ar-SO_2-} \tag{1.12}$$

The source of H atom in Equation (1.12) might be from C-H scission in aromatic ring.

1.6 Nanomaterials

Nanomaterials can be zero, one, or two dimensional, having 0, 1, or 2 dimensions larger than nanoscale, respectively. Since nanomaterials have unique properties such as high surface area, tunability, low density, high porosity, etc. [11], they offer unprecedented opportunities to tailor-make the properties of material with desirable attributes keeping into account the targeted applications [12].

Studies show that the behaviour of small material is quite different from its bulk due to large number of surface atoms and less number of atoms inside the bulk [75]. Size of nanomaterial is one of the important parameters, as nature and extent of interaction of nanomatrial with host matrix depends on fraction of atoms at the surface of nanoparticle [76]. Also, number of particles dispersed in host matrix at a particular loading will vary with size of nanomaterial. Atoms inside particles are highly coordinated with other atoms through strong bonding between them and have higher coordination number. On the other hand, atoms at the surface of particles are least saturated, that provides affinity to form bonds and interact with host matrix [77]. Attribute to variation in fraction of saturated and unsaturated atoms, due of varying size of nanoparticles, helps in exploiting different properties of nanomaterial, like mechanical, physio-chemical, and thermal properties. However, dispersion of nanomaterial in composite system, which is the most important factor in realizing desired objectives, is influenced by size [76, 78]. As size of nanomaterial decreases, attraction forces between particles increase, which leads to aggregation of particles and loss of unique properties [79].

In polymer nanocomposites, larger surface to volume ratio of nano-fillers results in significant increase in the volume of interphase between nanomaterial and polymer, which makes the properties of the polymer nanocomposite different from that of bulk polymer [80].

Several nanoparticles with surface modification were utilized as additives in polymer matrix to enhance properties of membranes, like performance [81], mechanical properties [82], thermal properties [83], anti(bio)-fauling [84], antibacterial properties [85], etc. However, membrane matrix suffers from a major problem of agglomeration due to strong attraction forces between nanoparticles [86, 87]. This tendency of aggregation causes non-uniform distribution of nanoparticles in host membrane matrix and degrades its performance.

The idea of using nanomaterials in membrane matrix has been instrumental in synthesis of membranes with desired structure and unique properties [88–90]. Structure-property correlation and its effect on membrane host matrix depends solely upon interaction between the nanomaterial and the polymer [91–93]. These surface/bulk modified mixed-matrix membranes (MMMs) offer not only enhanced separation features but also novel material properties [94, 95].

1.7 Polymer nanocomposite membranes

Polymeric membranes assume significance owing to high removal capacity, flexibility of operation, ability to fictionalization, and cost effectiveness [8, 9]. However, it suffers from inorganic fouling, bio-fouling, low stability at high temperature, trade-off between flux and selectivity, and limited radiation stability [10]. Essential application of nanomaterials has been realized in membrane technology to improve the performance of membrane material and enhance membrane properties and life span. As a result, numerous nanocomposite membranes have emerged with improved hydrophilic, anti-fouling, self-cleaning, photocatalytic, and photo degradation properties [13, 57].

Polymer nanocomposite is a material consisting of a polymer matrix and filler nanomaterials, which have at least one dimension in nanoscale range (less than 100 nm) and can be organic or inorganic [80]. Polymer reinforcement has been one of the first and most obvious application to avail the properties of nanoparticles which emerged in early 1990s. Researchers have developed a number of polymer nanocomposite membranes including organic, inorganic as well as hybrid nanomaterials. Inorganic nanomaterials constitute TiO_2, SiO_2, Al_2O_3, Si, Ag, ZnO, ZrO_2, $Mg(OH)_2$, $CaCO_3$, $TiSiO_4$, etc. Organic nanomaterial consists graphene, graphene oxide (GO), carbon nanotubes, etc., while hybrid nanomaterials include $GO - SiO_2$, $GO - TiO_2$, $SiO_2 - TiO_2$, $Ag - SiO_2$, etc. Essentially metal, metal oxide, and carbonaceous nanomaterials are used to improve the performance of membrane in terms of improving permeate flux, increase salt rejection, and enhance mechanical, chemical, and thermal properties.

1.7.1 Metal and metal-oxide nanomaterials

Extensive research has been done for the application of TiO_2 nanoparticles due to their admirable photocatalytic effect in decomposing organic foulants and microbes, which has been described by Miyauchi et al. [96] as well as Madaeni and Ghaemi [97]. They observed two phenomena on illuminating TiO_2 nanoparticles with ultraviolet (UV) light: (1) electron-hole pairs are generated that react with oxygen producing super oxide radicals, which decompose foulants on membrane surface, and (2) empty sites of O_2-radical adsorbs OH-groups from water molecules, thereby inducing ultra-hydrophilicity.

Studies on self cleaning property of TiO_2 embedded polymer nanocomposite membrane have been done. Madaeni and Ghaemi [97] investigated the effect on thin-film nanocomposite membranes. On the other hand, Damodar et al. [12] observed the performance of mixed-matrix nanocomposite membranes. These studies showed that membrane surface remains hydrated due to affinity of metal oxide towards water through hydrogen bonding, concurrently removing contaminants. This is an excellent example of photo-catalysis on membrane surface in presence of UV light.

Yang and Wang [98] investigated the performance of UF membrane of polysulfone-TiO_2 metal oxide nanocomposite membrane synthesized by sol-gel technique. Addition of TiO_2 in polysulfone matrix leads to increase in hydrophilicity of the membrane, leading to decreased contact angle (hydrophilicity) and increased permeability. Furthermore, the porosity and thermal stability are enhanced by TiO_2 impregnation. Likewise, anti-fouling performance of emulsion poly(vinylchloride)-TiO_2 nanocomposite ultrafiltration membranes is reported by Rabiee et al.[99], which showed improvement in pure water flux and hydrophilicity of membrane.

Yu et al. [100] prepared SiO_2-poly(vinyl chloride) nanocomposite UF membrane and observed increased hydrophobicity of membrane surface, which repels protein foulants, BSA molecule, leading to enhanced anti-fouling ability and higher flux recovery in membrane. Liang et al. [101] analysed anti-fouling property of ZnO-blended polyvinylidene fluoride membrane. ZnO nanoparticles offered reduction in surface contact angle and showed the ability to reach around 100% flux recovery ratio. Miyauchi et al. [96] investigated and confirmed that ZnO nanoparticles hold antibacterial property and are quite cheaper than the SiO_2 nanoparticles, while hydrophilic and photocatalytic properties of ZnO nanoparticles are commensurable with SiO_2.

Daraei et al. [102] incorporated iron oxide (Fe_3O_4) nanoparticles in the polyethersulfone mixed-matrix membrane to improve the removal of Cu(II) from water by the adsorption separation mechanism. Likewise, polysulfone surface modified with Fe_3O_4 by Homayoonfal et al. [103]. In which, comparison study of three different processes of synthesis (iron oxide blending with the polymeric matrix, deposition by photopolymerization and deposition by interfacial polymerization) has been done. As the concentration of Fe_3O_4 increases, the contact angle decreases due to the hydrophilic nature of Fe_3O_4 nanoparticles.

Polymer-metal nanocomposite membranes are not that widely studied because metal oxides nanoparticles with special properties like photocatalysis, hydrophilicity, antibacterial, etc. [104] dominate over bare metal nanoparticles. However, one of the metal nanoparticles extensively investigated is silver nanoparticles, due to their excellent anti-bacterial property and hydrophilicity.

Silver nanoparticles immobilized on the surface of poly(vinylidene fluoride) by Li et al. [105] showed superior antifouling and biofouling properties as well as improvement in hydrophilicity. Basri et al. [106] described that silver ions helped to provide anti-organic fouling resistance and antibacterial performance of polyethersulfone-silver composite membrane. Cellulose acetate hollow fiber membrane was incorporated with silver ions by Chou et al. [107] and obtained superior antifouling performance.

Also, copper and selenium nanoparticles were utilized for their antimicrobial functionality. Dasari et al. [108] achived boicidal activity of polylactic acid (PLA) membrane containing functionalized sepiolite fibrillar particles by embedded silver and copper nanoparticles on the fiber surface. Kar et al. [109] improved the anti-biofuling properties of polysulfone membrane by impregnating silver and copper nanoparticles. Akar et al. [110] investigated the biofouling properties of polyethersulfone (PES) membrane by incoporating selenium (Se) and copper (Cu) nanoparticles into membrane matrix. Due to the antioxidant activity of Se and Cu, PES-Cu blend membrane improves protein rejection, while PES-Se blend membrane improves antifouling properties.

Combination of different techniques and different metal/metal oxide nanoparticles with different properties are continuously being researched for the common purpose of making anti-fouling or self-cleaning membrane.

1.7.2 Carbon-based nanomaterials

Among different nanofillers, carbonaceous nanoparticles such as gra-phene (2D), carbon nanotubes (1D), and nanodiamond (0D) are very promising due to their unique and highly tailorable combination of properties, such as mechanical strength, chemical stability, electrical conductivity, aspect ratio, etc. In this section, a brief discussion on carbon nanotube (CNT) and graphene impregnated composites is made, which the discussion on nanodiamond based system is discussed in latter section.

In polymer nanocomposites, larger surface-to-volume ratio of nano-fillers results in dramatic increase in volume of the interphase between nanomaerial and polymer, so that their properties are influenced by nanoparticle and are different from bulk polymer. When nanofillers are smaller than normal coil size or radius of gyration of the polymer, good dispersion is achievable even in cases when the particle and matrix might have been considered incompatible.

Exclusive properties of carbon-based nanomaterials acquire consideration in various applications with their different forms such as: single-walled carbon nanotube (SWNT) or multi-walled (MWNT); graphene altered in the form of graphene oxide, which is hydrophilic contrary to graphene (hydrophopic); other graphene-based nanomaterials comprising of nano platelets, nanoribbens, reduced form of graphene oxide (rGO), etc. [111, 112].

Graphene nanosheets depicts material consisting of thinnest cross-section achievable with excellent mechanical properties (extremely high in-plane tensile stiffness and highest tensile strength) [113]. Due to these distinct properties of graphene, it is impermeable to even smallest molecules. Therefore, to improve permeability and tune selectivity, nanopores of various diameters, geometry, edge quality and density must be realized in graphene nano-sheets [114, 115].

A number of studies have shown that graphene membranes with artificial nanopores have great promise for nano-filtration and reverse osmosis seawater desalination [116], gas separation [117] and selective ion passage [118]. However, several key technological issues still remain when creating nanopores for improved flux and selective filtering, including (i) ability to reliably create pores that have the appropriate attributes such as size, shape and density; (ii) ability to create pores with minimum plastic deformation around pores in order to preserve mechanical properties; and (iii) ability to create nanopores on large area nanosheets.

Graphene is highly hydrophobic in nature, graphene oxide (GO) overcomes this issue as GO itself is extremely hydrophilic. For example, despite triply charged nature of AsO_4^{3-}, the ion permeates across the membrane at the same rate of single charged Na^+ or Cl^-. On the other hand, Hu and Mi [119] indicate that permeation through GO nanosheets is greatly dependent on particle charge Debye lengths, or electrostatic repulsion between ions and membrane charge. Therefore, charges of ions contribute to separation mechanism of GO membranes [120]. This difference in salt rejection trends with respect to ion charge by these two studies requires further investigation [121]. Sun et al. [120] has demonstrated selective ion penetration and water purification properties of free standing GO membranes.

Sodium salts quickly permeate through GO membranes, whereas heavy-metal salts infiltrate much slower. $CuSO_4$ and organic molecules, such as rhodamineB, were blocked entirely because of their strong interactions with GO membranes. Several approaches have been used to incorporate GO into polymer casting solutions, either during membrane fabrication or post-coating of prefabricated membrane, in order to improve antimicrobial properties, increase permeability, and enhance mechanical strength [122–126].

Asymmetrically located oxygen functional groups in GO membranes maintain distance during dropcasting process, creating void spaces between nonoxidized regions which form a series of nano capillaries within the film, increasing water flux when potentially utilized in desalination processes [127].

A promising approach in applying graphenes in desalination membranes is by incorporating GO nanosheets in polymer matrix rather than surface coating. These hybrid materials present significant performance enhancements, not usually attained by typical nanocomposites or pristine polymers [128–130]. Hu and Mi [119] prepared a water filtration membrane with layered GO nanosheets on polydopamine coated polysulfone support with 1,3,5-benzene tricarbonyl trichloride as crosslinkers. They did not observe any decline of water flux with increasing GO layers. Ionic flux of sulfonated polyethersulfone membrane can be improved by 19% by incorporation of 10% GO as compared to unmodified membrane. Strong interfacial interactions due to reinforcement of GO nanofillers into sulfonated polyethersulfone matrix improve thermal and mechanical properties of nanocomposite membranes [131].

Considering strong affinity to aggregation of graphene platelets and carbon nanotubes, ultrafiltration membrane modification with these materials could be restricted [132, 133]. This results in deterioration of internal structure of the membrane as well as decline in mechanical properties due to weak interaction between graphene and polymer matrix [123, 134]. GO provides the reactive sites for covalent functionalization due to the presence of functional groups like epoxy, hydroxyl, and carboxyl [134]. Functionalization decreases van der Waals forces between GO and prevents it from aggregation, resulting in homogeneous dispersion and strong interaction with polymeric matrix [135].

Zhao et al. [136] studied the performance of membrane by adding GO and MWNTs to PVDF matrix and observed change in internal structure of membrane with addition of graphitic carbon material. This change in morphology of membrane is attributed to the surface properties of GO and MWNTs, that is surface charge, functional groups, and active site availability. Resultant membrane showed increase in the membrane roughness and porosity.

Likewise, mixed-matrix polyethersulfone membrane has been prepared by immersing GO nanoplatelets to revamp the performance and antifouling characteristics of membrane [137]. Higher dye rejection was obtained in mixed-matrix membrane in comparison to pure polyethersulfone owing to the presence of electrostatic repulsive forces on the surface of membrane. GO modified polyvinylidene fluoride ultrafiltration membrane received superlative flux recovery rate and antifouling performance with respect to pure polyvinylidene fluoride membranes on the ground that GO was well dispersed in membrane pore channel, which caused the attached contaminants to be easily washed away from pores [138]. Furthermore, Liu et al. [139] developed graphene-polypyrol and GO-polypyrol nanocomposite membranes, these served as cathode membranes along with high conductivity and antifouling properties for wastewater treatment.

Choi et al. [140] utilized surface modified MWNTs as a additive to prepare polysulfone-MWNTs blend membrane. The MWNT was found to be a good modifier for the formation of functional microporous and increasing hydrophilicity of polysulfone membranes. Liu et al. [141] reinforced CNTs in nafion composite membrane for developing H_2/O_2 fuel cell. These membranes showed the decrease in dimensional change and improved the mechanical strength. Zhijiang et al.[142] improved antifouling of nanofiltration membrane against oil and protein for the application in dye removal. Nanofiltration membranes were prepared by coating calcium alginate hydrogel on polyhydroxybutyrate-carbon nanotubes composite membrane. Verma et al. [143] blended carbon nanotubes into the polyethersulfone to prepare composite hollow fiber membranes with improved biocompatibility for bioartificial liver. Polyethersulfone-carbon nanotube composite membrane found to be promising, because they simultaneously provide tunable hydrophilicity along with selective permeability.

Indeed, graphene-based membranes showed very promising antifouling properties. Antimicrobial activity of graphene and GO was attributed to synergy of both chemical and physical effects. Most of the above findings are attributed to the antibacterial activity of GO and reduced GO to cellular membrane stress induced by sharp edges of graphene nanosheets, which may result in physical damage of cell membranes, and loss of bacterial membrane integrity. On the other hand, high hydrophilicity induced by functional groups at basal plane and terminals of GO sheets and CNTs should also have contributed to high water permeation and antifouling, owing to low interfacial energy between the membrane surface and water. Nevertheless, physicochemical properties of graphene-based materials, such as density of functional groups, size, and conductivity, can be tailored to increase their antimicrobial potentials.

1.8 Radiation resistant nanomaterials

It is rare to get nanomaterials with radiation resistant attributes. Two unique materials, namely nanodiamond and cerium oxide nano-particles were found in literature that have radiation resistant properties. A brief description of the same is given below.

1.8.1 Nanodiamond

Nanodiamond (ND) is a zero-dimensional carbon nanomaterial. Crystal structure of ND is a polyhedra consisting of sp^3 hybridized carbon in the core, which is partially coated by sp^2 hybridized carbons terminated with functional groups [144]. ND are synthesized by various techniques like detonation technique [145], laser ablation [146], high-energy ball milling of high-pressure and high-temperature diamond microcrystals [147], plasma-assisted chemical vapour deposition [148], autoclave synthesis from supercritical fluids [149], chlorination of carbides [150], ion irradiation of graphite [151], electron irradiation of carbon onions [152], ultrasound cavitation [153], etc.

Properties of ND can be modified through surface doping [154], interior doping [155], introduction of functional groups [156], etc. ND surface modification can be performed to a large extent and variety [156], i.e., hundreds of functional groups of the same or different types can be formed on the surface of ND particle without any detrimental effect on its structure, in a big contrast to CNTs and graphene, where excessive attachment of functional groups disrupts aromatic sp^2 carbon structure, resulting in degradation of properties. Due to rich chemistry of carbon and sp^2 hybridization, ND is superior in surface chemistry among all nanofillers in terms of variety of possible chemistries, as well as number of surface functional groups per particle.

These unique properties, structure, and stability of ND provide them utility in wide range of potential applications [144] such as electrolytic and electroless metal plating, chemical vapour deposition of diamond films, magnetic resonance imaging, chromatography, proteomics and mass spectrometry, tribology, drug delivery, bio imaging, tissue engineering, protein mimics, radiation detector and filler material for nanocomposites.

Major advantages of ND particles over their essential properties for nanocomposite materials are: (i) Superior Young's modulus, hardness, high thermal conductivity and electrical resistivity, low coefficient of friction, chemical stability, and biocompatibility indulged by diamond structure [157]. (ii) Quantum confinement and uniformity in size, provides compatibility for utilization, while eliminating the necessity of costly fractionation procedures [158]. (iii) Stable and approximately spherical shape of ND particles [159]. (iv) High external surface area, offer excessive interaction with polymer matrix [160]. (v) Superabundant and adjustable surface chemistry [161] contributes in wise application of nanocomposite. (vi) Radiation resistant attributes.

Confined size of ND (in all dimensions; zero-dimensional) is favorable in terms of larger loading of particles in the polymeric host matrix relative to other materials (which have at least one larger dimension; one-dimensional or two-dimensional). Hence, it provides greater interface volume in polymer-nanomaterial composite matrix. Furthermore, due to its spherical shape, ND particles do not stack together and do not create bundles (theoretically) [160]. ND provides better dispersion as compared to one-dimensional or two-dimensional nanomaterials [162]. ND has promises to deliver, owing to its prosperous surface chemistry, which offers diverse viable chemistries and varity of surface functional groups on it, and hence pronounced as a potential nano-filler material [163].

Several research studies confirm the thermodynamic compatibility of ND with different polymers [164], as well as Psf [165], in terms of strong mixed-matrix interaction through homogeneous dispersion. ND is an optimal candidate for reinforcing polymer matrices, where it can act through changing the properties of the interphase as well as forming a strong covalent interface with the matrix. ND can be thought of as a universal building block for polymer-nano composite design since its surface can be modified to virtually any extent in order to create desirable interfaces and influence the interphase with almost any polymer matrix without compromising the properties of the diamond core [166, 167]. Homogeneous dispersion and strong affinity of ND in Psf matrix was reported [168].

In studies, various polymers were embedded with ND to observe its effect on mechanical, thermal, tribiological, optical and rheological properties, as well as biocompatibility of polymers. These effects on properties were identified by influence of morphology, polymer/ND interface, functionality, and processing conditions. Ayatollahi et al., investigated mechanical and tribiological properties of Epoxy/ND composite [169]. Rheological characterstics of PDMS influenced by ND was reported by Gavrilov and Voznyakovskii [170]. Effect of ND on thermal properties of crosslinked high density poly-ethylene was stablished by Roumeli et al [171]. The wear performance of PTFE film was enhanced by incorporation of ND [172]. High refractive index materials were attained by incorporating ND into polymer matrices [173]. Biocompatibility of poly-L-lactide (PLLA)/ND-ODA composites was observed by Zhang et al. [174]. However, radiation resistant property of polymer-ND composite has not been explored in the literature.

Radiolysis of water, present in operating environment, results in production of highly reactive species, e.g., $e^{-}{}_{aq}$, $HO^{\bullet}$, $H^{\bullet}$, $HO_2^{\bullet}$, H_2O_2, H_3O^+, OH^-, and H_2 [71]. Along with the most stable structure in harsh environment and radiation resistant property, carboxyl and hydroxyl groups present on the surface of ND could interact with these free radicals and protect polymer membrane matrix from radiation-induced damages caused by radiolysed products of water. Possible mechanism of interaction of free radicals with carboxyl and hydroxyl group is given in Equation (1.13) to (1.16).

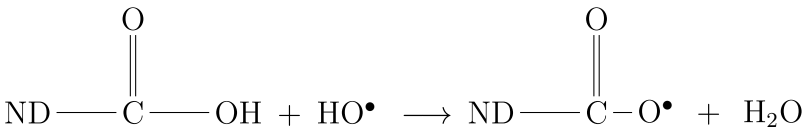

$$\mathrm{ND}-\overset{\mathrm{O}}{\overset{\|}{\mathrm{C}}}-\mathrm{OH} + \mathrm{HO}^{\bullet} \longrightarrow \mathrm{ND}-\overset{\mathrm{O}}{\overset{\|}{\mathrm{C}}}-\mathrm{O}^{\bullet} + \mathrm{H_2O} \tag{1.13}$$

$$\mathrm{ND}-\mathrm{OH} + \mathrm{HO}^{\bullet} \longrightarrow \mathrm{ND}-\mathrm{O}^{\bullet} + \mathrm{H_2O} \tag{1.14}$$

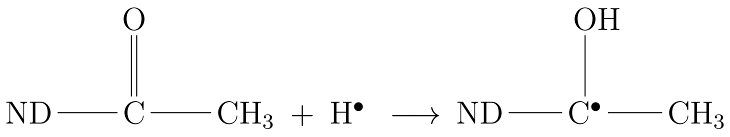

$$\mathrm{ND}-\overset{\mathrm{O}}{\overset{\|}{\mathrm{C}}}-\mathrm{CH_3} + \mathrm{H}^{\bullet} \longrightarrow \mathrm{ND}-\overset{\mathrm{OH}}{\overset{|}{\mathrm{C}^{\bullet}}}-\mathrm{CH_3} \tag{1.15}$$

$$\mathrm{ND}-\mathrm{OH} + \mathrm{H}^{\bullet} \longrightarrow \mathrm{ND}^{\bullet} + \mathrm{H_2O} \tag{1.16}$$

In this thesis, unique radiation-resistant property of ND has been exploited to develop Psf-ND mixed-matrix membranes (MMMs) with improved γ-radiation resistant behavior.

1.8.2 Cerium oxide (Ceria) nanoparticles

Rapid technological and industrial development has brought attention towards rare earth materials, also known as 'industrial vitamins' and a 'treasury' of new materials [175]. Rare earth elements have a different chemistry from other main group elements and transition metals due to the nature of their 4f orbitals. The 4f orbitals are shielded from the atom's environment by 4d and 5p electrons [175, 176] as they are enfolded inside the atom. Rare earth materials have unique catalytic, magnetic and electronic properties due to these 4f orbitals. These unique properties have been utilized to accomplish newer applications in various high-technology industries such as information and biotechnology [176], which were not feasible with the transition and main group metals.

Cerium (Ce), first element in the lanthanide group, has significant application potential in the areas of physics, chemistry, biology, and material science. Ce along with oxygen can develop nanoparticles in the form of cerium oxide (ceria), carrying a fluorite crystalline structure, which came out as a thought-provoking material to researchers [177].

Ceria possesses a fluorite crystalline structure, which has emerged as an outstanding material [177] having promising applications in several domains, such as high-temperature oxidation protection materials [178], catalytic materials [179], solid-oxide fuel cells [180], solar cells [181], potential pharmacological agents [182], gas sensor [183], and optical glass polishing [184]. The Ce atom acquires 4f shell for electron sharing and bonding, and hence, it can undergo conversion between Ce^{4+} and Ce^{3+} [185, 186]. In sync with Ce atom, an oxygen vacancy also gets created, transferred and eliminated [187]. This property can be exploited for absorption of reactive oxygen radicals [188, 189] as well as electron transfer [190]. Moreover, ceria can also act as radiation absorber [191, 192].

The lanthanide series elements generally exist in trivalent (+3) state. Interestingly, due to the presence of two partially occupied subshells of electron, Ce atoms exhibit either fully reduced (+3) state or fully oxidized (+4) state. Therefore, oxide of cerium (cerium oxide or ceria) play a dual character as reducing as well as oxidizing component. These phenomena occur due to feasible swapping between Ce^{4+} and Ce^{3+} [193–195]. Along with Ce atom, an oxygen vacancy also gets created, transferred, and eliminated [187]. This property improves adsorption of reactive oxygen radicals [188, 189, 196] and promotes electron transfer [190]. When Ce^{4+} is reduced to Ce^{3+}, oxygen vacancies are generated, represented by the following Kroger-Vinknotation [197] as given in Equation (1.17).

$$O_O^X + 2Ce_{Ce}^X \longrightarrow V_{\ddot{O}} + 2Ce_{Ce}^{'} + \frac{1}{2}O_2 \tag{1.17}$$

Where, O_O^X is a neutral oxygen and Ce_{Ce}^X is a neutral cerium on a neutral cerium site, $V_{\ddot{O}}$ is a +2 oxygen vacancy and $Ce_{Ce}^{'}$ is a Ce^{3+} atom in a Ce^{4+} site giving it a net negative charge of -1.

Ceria acts as oxygen buffer to either store or supply oxygen. This is due to a defect in its structure, which is dynamic in nature, as it may change in response to size and external parameters such as oxidizing or reducing environment. When the particle size is less than 15 nm [198], the fraction of oxygen vacancy and Ce^{3+} concentration increases. This phenomenon at nanoscale has been utilized in various areas of applications including biology [199], energy [200] and catalysis [201]. The antioxidant property of ceria nanoparticles provides protection against radiation induced damage [202].

The valence switching ability between Ce^{3+} and Ce^{4+} provides reactive oxygen species (ROS) scavenging capability as well as catalytic activity of ceria nanoparticles. Hydroxyl free radial ($OH^{\bullet}$) is a highly reactive one that could be scavenged by ceria nanoparticles through conversion from Ce^{3+} to Ce^{4+}, as shown in Equation (1.18) [138].

$$Ce_2O_3 + 2OH^{\bullet} \longleftrightarrow 2CeO_2 + H_2O \tag{1.18}$$

It can be regenerated as shown in Equation (1.19).

$$2CeO_2 \xrightarrow{H_{aq}^+} Ce_2O_3 + \frac{1}{2}O_2 \tag{1.19}$$

Peroxidase are capable to catalyze the reduction of peroxide in presence of certain co-factors, as shown in Equation (1.20) [203].

$$ROOR' + 2e_{aq}^- + 2H^+ \longrightarrow ROH + R'OH \tag{1.20}$$

Several nanomaterials are found to have peroxidase-like activity similar to the mechanism of Fenton reaction. Ce ion can also perform peroxidase-like activity, as shown in Equation (1.21) to (1.23).

$$Ce^{3+} + H_2O_2 + H^+ \longrightarrow Ce^{4+} + OH^\bullet + H_2O \tag{1.21}$$

$$OH^\bullet + H_2O_2 \longrightarrow HO_2^- + H_2O \tag{1.22}$$

$$Ce^{4+} + HO_2^- \longrightarrow O_2 + Ce^{3+} + H^+ \tag{1.23}$$

These distinctive properties of ceria nanoparticles are utilized to enhance radiation stability of polymeric membranes in the present study for application in treatment of radioactive effluent. Impregnation of ceria in Psf membrane matrix helps to protect the matrix by scavenging ROS ($OH^\bullet$, e_{aq}^-, H_2O_2, $^\bullet H$, H_2, H_3O^+) produced by water radiolysis under γ-radiation.

The ceria nanoparticles can be synthesized using different techniques including hydrothermal [204], precipitation [205], combustion [206], solvothermal [207], aqueous precipitation [208], reversed micelles [209], thermal decomposition [210] and flame spray [211] method. Though these techniques are efficient in fabricating pure ceria nanoparticles with narrow size distribution, achieving desired characteristics of nanoparticles is a critical step that depends on appropriate solution chemistry during fabrication process [212]. During the fabrication of ceria nanoparticles, it is essential that the sintering temperature is lower than the temperature at which oxidation state of cerium starts changing ($Ce^{4+} \rightarrow Ce^{3+}$) [213]. Among all available chemical routes, gel-combustion technique is capable of producing nanoparticles at higher reaction rate and lower calcination temperature with improved powder characteristics and at a lower cost [214].

Several studies have been published concerning the properties (mechanical, antifouling, thermal, electrical, etc.) of various polymers by using ceria nanoparticle as a filler material. Furthermore, ceria found to be stable and homogeneously dispersed in the polysulfone matrix [215, 216]. Ushakov et al., has stabilized cerium oxide nanoparticle in the matrix of linear density polyethylene, and suggested that homogeneous dispersion of nanoparticles exhibits dielectric properties [217]. Mithlas et al., improved durability and performance of membrane fuel cell by cerium oxide decorated polymer nanofibers [218]. Lakhotia et al., have discussed improvement on anti-fouling properties of thin film nanocomposite nanofiltration membrane using cerium oxide nanoparticles for water treatment [85]. Thermodynamics between polymer matrix and cerium oxide nanoparticles, through intrinsic and extrinsic interfacial regions, plays a vital role in ensuring homogeneous dispersion of cerium oxide nanoparticles in the host, and thus can lead to enhanced-performance composite with synergistic effects [219].

As part of this thesis, ceria nanoparticles were fabricated by gel combustion route using citric acid ($C_6H_8O_7.H_2O$) as a fuel and cerium nitrate ($Ce(NO_3)_3.6H_2O$) as an oxidizer. Participation of ceria nanoparticles were observed by incorporating in Psf membrane matrix.

1.9 Motivation and objectives of the work

The research work presented in this thesis attempts to enhance the radiation resistant property of polymeric membranes for their sustainable application in radioactive effluent treatment. To achieve the desired objectives, unique properties of ND and ceria nanoparticles were explored and utilized for protection of Psf membrane matrix from consequences of radiation damage and attack of free radicals. Mixed-matrix membranes with enhanced radiation resistance attributes were fabricated and characterized. Following investigations were carried out in this thesis.

1. Effect of reinforcement of ND particles on radiation resistant behaviour of Psf membrane and life-span analysis in radioactive environment.
2. Effect of carboxylated ND and comparison as to how it is superior than ND particles in offering enhanced radiation resistant feature to Psf membrane.
3. Effect of ND size on radiation resistant property of membrane, and finding an optimum size.
4. Effect of ceria nanoparticles on radiation resistant property of Psf membrane and assessment of life-span in radiation environment.
5. Combined effect of reinforcement of both ND and ceria nanoparticles on the radiation resistant property of membrane.

These objectives helped in understanding the role and influence of nanomaterials (ND and ceria) towards enhancing the life of polymeric membrane matrix in radiation environment.

1.10 Overview of Dissertation

Chapter 1 desribes the current scenerio of membrane technology and treatment of radiactive effluent. It offers the motivation and objectives of this research work.

Chapter 2 provides details of all experimental methods used in this work, along with a brief description of instrumental techniques used.

Chapter 3 presents development of Psf-ND mixed-matrix membrane (MMM) by incorporating ND into Psf membrane matrix. Effect of ND particles on structural, chemical, physical, and mechanical properties, as well as performance of MMM is discussed.

In **Chapter** 4, studies on effect of carboxyl functionalization of ND on properties on MMM is described.

The work presented in **Chapter** 5 describes the influence of ND particle size on internal structure, properties, and performance of Psf-ND MMM.

In **Chapter** 6, the role and influence of ceria nanoparticles is investigated, along with mechanistic evaluation of protection of Psf-ceria MMMs in radiation environment.

Chapter 7 describes the combined effect of ND and ceria nanoparticles on the stability of Psf-(ND+Ce) hybrid membranes in radiation environment.

At the end, **Chapter** 8 summarizes key contributions of this research in the field of polymer-nanocomposite membranes for application in treatment of radioactive effluent. Few recommendations for future work have also been made, based on the research carried out in this thesis.

Chapter 2

Experimental methodologies

2.1 Materials

2.1.1 Nanomaterials

1. Nanodiamond powder (ND$_{10}$, particle size: <10 nm, assay $\geq$ 97%, MW: 12.01 g/mol, density: 3.5 g/ml) was procured from Sigma-Aldrich.
2. Monodispersed carboxylated nanodiamond particles (CND, 5 nm, 10 $mg\ ml^{-1}$ in N-methyl-2-pyrrolidone, carboxylated) was procured from Sigma-Aldrich.
3. Nanodiamond powder (ND$_{250}$, Average particle size: 250 nm) were procured from Microdiamant.
4. Nanodiamond powder (ND$_{500}$, Average particle size: 500 nm) were procured from Microdiamant.

2.1.2 Materials for the synthesis of cerium oxide nanoparticle

1. Cerium nitrate ($Ce(NO_3)_3 \cdot 6H_2O$) AR-grade with purity > 99.9% was obtained from Indian Rare Earth Limited, India.
2. Citric acid ($C_6H_8O_7 \cdot H_2O$) of purity > 99% was procured from Merck, India.

2.1.3 Materials for membrane synthesis

1. Polysulfone (Psf, $M_W \sim 60$ kDa) was purchased from Solvay Specialties India Pvt. Ltd, India.
2. N-methyl-2-pyrrolidone (NMP) assay $\geq 99.5\%$) was purchased from SRL Pvt. Ltd, Mumbai, India.
3. Polyvinyl pyrrolidone (PVP) (K-30; molecular weight: 40 kDa) of AR grade was purchased from SRL Pvt. Ltd, Mumbai, India.

2.1.4 Materials for membrane characterization

1. Polyethylene oxide (PEO, molecular weight: 100 kDa) was purchased from Sigma-Aldrich.
2. Malachite green (MG) was procured from Sigma-Aldrich.
3. Ferrous sulfate ($FeSO_4.7H_2O$) was procured from Sigma-Aldrich.
4. Hydrogen peroxide solution (H_2O_2, 30% (w/w) in H_2O) was procured from Merck, India.
5. Tetrahydrofuran (THF, anhydrous, $\geq 99.9\%$) was purchased from S. D. Fine Chemicals Limited, India.
6. PTFE syringe filter (0.22 μm pore size and 25 mm diameter) was obtained from Axiva Sichem Biotech, India.
7. ‘Porefil’ solution ($\gamma = 16$ dyne/cm, vapour pressure: 3 mm Hg at 298 K) was supplied by Benelux Scientific, Belgium.

2.2 Synthesis of ceria nanoparticles

Gel-combustion method was employed to synthesize nano-ceria powder using cerium nitrate as oxidant and citric acid as fuel. Calculated amounts of $Ce(NO_3)_3.6H_2O$ and $C_6H_8O_7.H_2O$ were dissolved in deionized water to obtain a clear solution. The ratio of nitrate to citric acid was calculated based on propellant chemistry and the same is represented by Equation (2.1). Upon drying the solution on a hot plate at ~ 120 °C, the dehydration of solution leads to formation of a gel, termed as precursor. On further increasing the temperature to ~ 200 °C, auto ignition of the gel takes place with evolution of large amount of gaseous product. After combustion, a voluminous and fluffy mass is produced. The nature of ignition depends on fuel-to-oxidant ratio, pH of the solution and temperature. Fuel-deficient precursor was found to be more violent compared to fuel-rich composition. As the combustion process continues for a small duration (typically $\sim$ 5 s), residual carbonaceous products are expected. Fabricated powder was then calcined at 700 °C for 1 h to remove carbonaceous products and pure powder phase was formed. The reaction scheme of synthesis of ceria is given in Equation (2.1).

$$\begin{aligned} Ce(NO_3)_3.6H_2O \;+\; \frac{5}{6}C_6H_8O_7.H_2O \;+\; \frac{1}{4}O_2 \;&\longrightarrow \\ CeO_2 \;+\; \frac{3}{2}N_2 \;+\; 5CO_2 \;+\; \frac{61}{6}H_2O& \end{aligned} \tag{2.1}$$

2.3 Synthesis of membranes

Psf-nanomaterial MMMs were fabricated by non-solvent induced phase inversion technique as shown in Figure 2.1. To prepare the dope solution, different weight fractions of nanomaterial were taken as filler material and dispersed separately in 100 mL NMP solvent by ultra-sonication for 30 minutes. Control Psf membrane was prepared without addition of any nanomaterial. Each of these solutions was then mixed with 25 gm of Psf (base polymer) and 7.5 gm PVP (additive). The dope solutions were then kept for continuous stirring up to 24 hrs. Membranes with a thickness of 200 μm were prepared by phase inversion technique from these homogeneous dope solutions with the help of an automatic table-top membrane casting machine at ambient temperature, followed by instantaneous relocation into de-ionized water for gelling.

In Chapter 3, nanodiamond (ND) was taken as a filler material to synthesize Psf-ND MMMs. Different weight fractions of ND (0.1-ND, 0.5-ND, 1-ND, and 2-ND: wt% of Psf) was introduced in individual dope solutions.

In Chapter 4, carboxylated nanodiamond (CND) was taken as a filler material to synthesize Psf-CND MMMs. Different weight fractions of CND (0.1-CND, 0.5-CND, and 1-CND: wt% of Psf) was introduced in individual dope solutions.

In Chapter 5, nanodimonds with particle size of 10 (ND_{10}), 250 (ND_{250}), and 500 nm (ND_{500}) were taken as a filler material to synthesize Psf-ND MMMs. Different

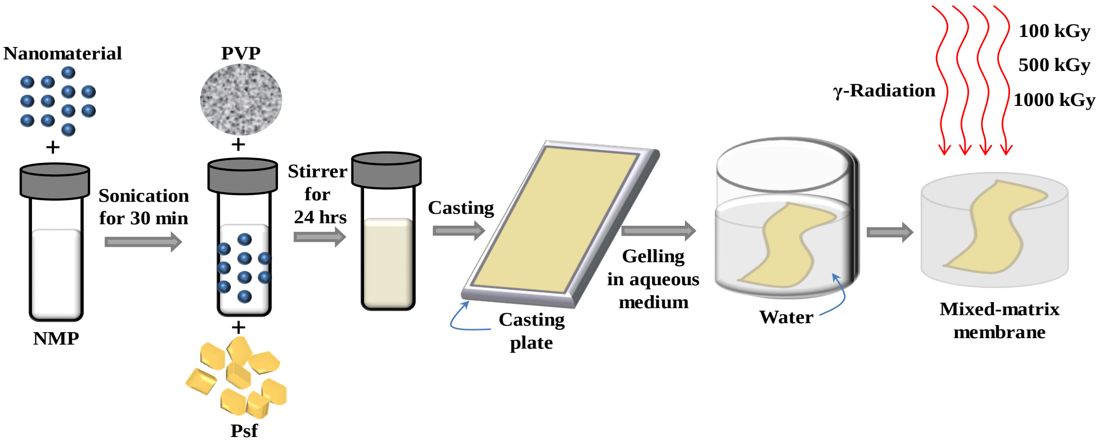

FIGURE 2.1: Schematic representation for synthesis of control Psf and mixed-matrix membranes by phase inversion technique.

weight fractions of each ND (0.1-ND, 0.5-ND, 1-ND, and 2-ND: wt% of Psf) was introduced in individual dope solutions.

In Chapter 6, cerium oxide (ceria) nanoparticles were taken as a filler material to synthesize Psf-ceria MMMs. Different weight fractions of ceria (0.1-Ce, 0.5-Ce, 1-Ce, and 2-Ce: wt% of Psf) was introduced in individual dope solutions.

In Chapter 7, combination of ND and ceria nanoparticles were taken as a filler material to synthesize Psf-(ND+Ce) hybrid MMMs. Composition and label of different membranes are given in Table 2.1.

TABLE 2.1: Compositions of dope solution for the membrane synthesis.

Type of membrane	**Membrane label**	**Psf (g)**	**NMP (ml)**	**PVP (g)**	**ND (%/Psf)**	**Ceria (%/Psf)**
Control Psf	Psf	25	100	7.5	0	0
Psf-(ND+Ce)	0.25ND-0.25Ce	25	100	7.5	0.25	0.25
	0.25ND-0.5Ce	25	100	7.5	0.25	0.5
	0.5ND-0.25Ce	25	100	7.5	0.5	0.25
	0.5ND-0.5Ce	25	100	7.5	0.5	0.5

2.4 Irradiation of membranes

Individual membranes immersed in de-mineralized water were sealed in the zip-lock polyethylene bags for irradiation. The ^{60}Co source gamma chamber GC-5000

(Board of Radiation & Isotope Technology, BRIT, India) was utilized for irradiation of membranes by keeping the prepared zip-lock bags containing membranes in gamma chamber with a dose rate of about 1 $kGy\ h^{-1}$ (Fricke dosimetry).

In Chapter 3, Psf and Psf-ND composite membranes were exposed to 100 (Psf-100, 0.1-ND-100, 0.5-ND-100, 1-ND-100, 2-ND-100), 500 (Psf-500, 0.1-ND-500, 0.5-ND-500, 1-ND-500, 2-ND-500), and 1000 kGy (Psf-1000, 0.1-ND-1000, 0.5-ND-1000, 1-ND-1000, 2-ND-1000) of radiation dose.

In Chapter 4, Psf and Psf-CND MMMs were exposed to different γ-radiation dose of 100 (Psf-100, 0.1-CND-100, 0.5-CND-100, and 1-CND-100), 500 (Psf-500, 0.1-CND-500, 0.5-CND-500, and 1-CND-500), and 1000 kGy (Psf-1000, 0.1-CND-1000, 0.5-CND-1000, and 1-CND-1000).

In Chapter 5, Psf and Psf-ND MMMs were exposed to the γ-radiation dose of 100 kGy (Psf-100, 0.1-ND_{10}-100, 0.5-ND_{10}-100, 1-ND_{10}-100, 2-ND_{10}-100, 0.1-ND_{250}-100, 0.5-ND_{250}-100, 1-ND_{250}-100, 2-ND_{250}-100, 0.1-ND_{500}-100, 0.5-ND_{500}-100, 1-ND_{500}-100, 2-ND_{500}-100), 500 kGy (Psf-500, 0.1-ND_{10}-500, 0.5-ND_{10}-500, 1-ND_{10}-500, 2-ND_{10}-500, 0.1-ND_{250}-500, 0.5-ND_{250}-500, 1-ND_{250}-500, 2-ND_{250}-500, 0.1-ND_{500}-500, 0.5-ND_{500}-500, 1-ND_{500}-500, 2-ND_{500}-500), and 1000 kGy (Psf-1000, 0.1-ND_{10}-1000, 0.5-ND_{10}-1000, 1-ND_{10}-1000, 2-ND_{10}-1000, 0.1-ND_{250}-1000, 0.5-ND_{250}-1000, 1-ND_{250}-1000, 2-ND_{250}-1000, 0.1-ND_{500}-1000, 0.5-ND_{500}-1000, 1-ND_{500}-1000, 2-ND_{500}-1000).

In Chapter 6, Psf and Psf-ceria MMMs were exposed to 100 (Psf-100, 0.1-Ce-100, 0.5-Ce-100, 1-Ce-100, and 2-Ce-100), 500 (Psf-500, 0.1-Ce-500, 0.5-Ce-500, 1-Ce-500, and 2-Ce-500), and 1000 kGy (Psf-1000, 0.1-Ce-1000, 0.5-Ce-1000, 1-Ce-1000, and 2-Ce-1000) of radiation dose.

In Chapter 7, Psf and Psf-(ND+Ce) hybrid membranes were exposed to 100 (0.25ND-0.25Ce-100, 0.25ND-0.5Ce-100, 0.5ND-0.25Ce-100, and 0.5ND-0.5Ce-100), 500 (0.25ND-0.25Ce-500, 0.25ND-0.5Ce-500, 0.5ND-0.25Ce-500, and 0.5ND-0.5Ce-500) and 1000 kGy (0.25ND-0.25Ce-1000, 0.25ND-0.5Ce-1000, 0.5ND-0.25Ce-1000, and 0.5ND-0.5Ce-1000) of radiation dose.

2.5 Viscosity measurement of membrane dope solution

Viscosity of dope solutions with different loading of nanomaterials were determined at room temperature using rotary rheometer (MCR 302, Anton Paar GmbH) by keeping 1 mm gap for the sample between parallel plate arrangement.

2.6 Morphological characterization by field emission scanning electron microscope (FESEM)

Surface and cross-sectional morphology of membranes were observed using FESEM (AURIGA 4553) at 20 and 5 kV operating voltages, respectively. To observe the cross-sectional morphology, membranes were freeze dried and cracked in the liquid nitrogen. For analysis, membrane pieces were made electrically conducting by a sputter coater with gold-palladium alloy target at a current of 15 mA for 100 s.

2.7 Elemental composition analysis using energy dispersive X-ray spectrometer (EDS)

Quantitative elemental analysis of selected membrane surfaces was carried out using an energy dispersive X-ray spectrometer (EDS, INCA, Oxford Instruments, UK), coupled with FESEM and a micro analysis system. In EDS analysis, acceleration voltage of 20 kV and magnification of 4000X were used. The spectra were acquired for elements of interest, i.e., Ce and O for ceria nanoparticles, while Ce, C, S, and O for Psf-ceria MMMs.

2.8 Structural morphology of nanomaterials by transmission electron microscope (TEM) and selected area electron diffraction (SAED)

Transmission electron microscopy (TEM) and selected area electron diffraction (SAED) analysis of nanomaterials (ND, CND, ND-250, ND-500, and ceria nanoparticles) were carried out using a JEOL 2000FX-200KV TEM. Prior to examination, sample was prepared by dispersing nanomaterials into methanol with the help of 5 min bath sonication. Individually dispersed nanomaterials were deposited on to the surface of 300 mesh size 3 mm copper TEM specimen grid having a carbon support film and dried in ambient condition.

2.9 Size distribution analysis of nanomaterials by dynamic light scattering (DLS) technique

Dynamic light scattering (DLS) analyses were carried out to obtain hydrodynamic diameter of the particles using autosizer 4800 (Malvern, 7132 digital correlator). For analysis, sample was prepared by adding nanomaterials or polyethylene oxide (PEO) into de-ionized water and sonicated using bath sonicator for 30 minutes to get dispersed solution.

2.10 Average pore size of the membrane using porometer

Average pore size of membranes was determined using porometer (Porolux 1000 model, Benelux Scientific, Belgium). Data acquisition and analysis was carried out using LabView software for 25 mm diameter of membrane sample. ‘Porefil’ solution was used as wetting liquid for capillary flow porometry, as it is a non-toxic, inert fluorocarbon wetting fluid having zero contact angle in membrane, i.e., Cos θ =1.

2.11 Topography analysis by atomic force microscope (AFM)

Topography of membrane surface was analyzed using atomic force microscope (AFM, Model: SOLVER next, NT-MDT, Russia). A small (1 cm^2) dry membrane piece was taken for AFM analysis and pasted onto metal substrate. AFM images were acquired in tapping mode with the aid of a silicon cantilever NSG 10 (NT-MDT, Russia) with spring constant of 11.8 N/m and resonating frequency of 240 kHz. Imaging was carried out at room temperature and ambient pressure, and root mean square (RMS) surface roughness of these membranes was obtained by NOVA-P9 software. The effect of nanomaterial loading and radiation dose on surface roughness of the membrane was examined within a scan range $3\mu m \times 3\mu m$.

2.12 Membrane surface water contact angle measurements by drop shape analyzer (DSA)

Water contact angle at membrane surface was measured through KRUSS Advance drop shape analyzer (DSA100, Germany) under ambient conditions. In order to measure contact angle, a small membrane piece was placed on glass slide and water drop was located onto the surface of the membrane using a syringe. The drop was illuminated from one side and a camera at the opposite side records an image of drop. The drop image was analyzed using KRUSS Advance software. Contact angles in three different regions on each membrane sample were measured and averaged.

2.13 Functional group characterization by attenuated total reflectance Fourier-transform infrared spectroscopy (ATR-FTIR)

Vibrational spectra of nanomaterials and membranes were observed through attenuated total reflectance Fourier-transform infrared spectroscopy (ATR-FTIR; IR Affinity-1 spectrometer, Shimadzu, Japan) at single reflectance ATR mode. Result was evaluated and substantiated by taking 50 scans with a 4 cm^{-1} spectral resolution. Nanomaterial or surface of membrane was kept in contact with

ATR crystal element and slight pressure was applied using a high pressure clamp (MIRacle) with torque-limited press. The infrared spectrum was recorded in absorbance mode in the range from 400 to 4000 cm^{-1} at room temperature with radiation penetration depth of 2 mm.

2.14 Elemental Composition determination by X-ray photoelectron spectroscopy (XPS)

X-ray photoelectron spectroscopy (XPS) measurements of nanomaterials and air-dried membranes were accomplished using Mg-K_α (1253.6 eV) source and DESA-150 electron analyzer (Staib Instruments, Germany). Calibration of binding-energy scale was carried out to Au-$4f_{7/2}$ line of 84.0 eV. The analyzer was operated at 40 eV pass energy. Pressure in the chamber during analysis was $\sim 7 \times 10^{-9}$ torr. Surface composition (C_i) and percentage of elements were calculated by binding energy value obtained from XPS spectrum, using Equation (2.2) [220, 221].

$$C_i = \frac{I_i/S_i}{\Sigma(I_j/S_j)} \tag{2.2}$$

Where, i and j are elements C, S, O and Ce. Here I_i is intensity of the C-1s, S-2p, O-1s, and Ce-3d peaks determined by total area under the core level peak (by least-squares fitting of Gaussian curve). S_i represents the atomic sensitivity factor with values 0.296, 0.666, 0.711 and 8.808 for C-1s, S-2p, O-1s, and Ce-3d peaks, respectively.

2.15 Phase analysis by X-ray diffraction (XRD)

X-ray diffraction (XRD) pattern of nanomaterials and membranes was analyzed through Cu-K_α radiation by Philips X-ray diffractometer (Model PW 1927) at 40 kV and 30 mA. Diffraction patterns were taken at the interval of 0.2° with 1 min scanning time per interval in the range from 20 to 90°.

2.16 UV-Vis spectra of nanomaterial

UV spectra of nanomaterial were recorded using UV-Vis spectrometer (JASCO V-630 spectrophotometer). Nanomaterial was dispersed in de-mineralised water and poured into a quartz cuvette (1 cm × 1 cm) for analysis.

2.17 Raman spectra of nanomaterial

Raman spectra of nanomaterials was recorded using a confocal Raman microscope (Alpha300R, WITec, Germany). Nanomaterial was kept on a glass substrate for analysis. A laser of wavelength 600 nm and beam spot-size of $\sim 3\ \mu$m during analysis.

2.18 Average molecular weight determination by gel permeation chromatography (GPC)

Average molecular weight of membrane samples were determined using gel permeation chromatography (GPC) system (Malvern 270 dual detector, UK) equipped with refractive index detector and light scattering detector (λ: 670 nm, consisting of two scattering angles: 7° and 90°) along with general mixed organic column T6000M (300×8 mm, Viscotek, Malvern, UK). The detector and column were kept at 22° C temperature. Mobile phase consisted of tetrahydrofuran at a flow rate of 0.5 mL/min. Samples were filtered through a PTFE syringe filter with 0.22 μm pore size and 25 mm diameter. Sample volume injected was 100 μL. Both detectors were calibrated with polystyrene standards having narrow molecular-weight distribution. Data was analyzed using Viscotek OmniSEC 5.12 software.

2.19 Free volume estimation by positron annihilation lifetime spectroscopy (PALS)

Positron annihilation lifetime (PAL) in membrane was determined at room temperature using two scintillation detectors (BaF_2) connected to fast-fast coincidence system. The ^{22}Na ($\sim 10\ \mu Ci$) wrapped in a thin Kapton foil ($\sim 8\ \mu$m thick) was used as positron source which was sandwiched between stacks of membrane. Source-sample assembly was kept between two BaF_2 detectors. Time resolution of spectrometer measured with a ^{60}Co prompt gamma source in ^{22}Na window setting was 250 ps. Time calibration was fixed at 25 ps per channel. Spectrum with approximately 5×10^6 counts was acquired for each measurement. The positron lifetime histogram is a multi-exponential decay curve as given in Equation (2.3).

$$F(t) = \sum_{i=1}^{k} \frac{I_i}{\tau_i} e^{-\frac{t}{\tau_i}} \tag{2.3}$$

Here, F(t) is the number of counts at time t, k represents the number of exponential decays, τ_i and I_i are the corresponding lifetime and intensity of the i^{th} component respectively. Lifetime spectra was fitted to four discrete components with minimum χ^2 using PALSfit analysis program [222].

Third lifetime component within the range of 1.8-1.9 ns corresponds to spin-triplet ortho-positronium (o-Ps) pick-off annihilation with an electron from the inner surface of free volume. Fourth component with lifetime in the range of 10 - 30 ns corresponds to o-Ps annihilation in intergranular region. Intensity of the third lifetime component is within the range of 14 - 17%, whereas intensity of the fourth component is very small ($< 0.6\%$). So we have not considered this fourth component in further discussion. Third lifetime component was converted into average radius (R) of spherical free volume using the following empirical relation from well-known Tao-Eldrup model (Equation (2.4)) [223, 224].

$$\tau_3 = \frac{1}{2}\left[1 - \frac{R}{R_0} + \frac{1}{2\pi}\sin\frac{2\pi R}{R_0}\right]^{-1} \tag{2.4}$$

Here, τ_3 is third lifetime component and R_0 = R + 0.166 nm. Relative fractional free volume (f) was calculated by Equation (2.5).

$$f = \frac{4}{3}\pi R^3 \times I_3 \tag{2.5}$$

Here, I_3 is relative intensity (in %) of third lifetime component (τ_3).

2.20 Membrane molecular structure interpretation by small angle X-ray scattering (SAXS)

Small angle X-ray scattering (SAXS) measurements were performed using a laboratory-based SAXS instrument with Cu-Kα (λ=1.54 Å) as probing radiation. Radial averaged scattering intensity (I(q)) was obtained within a wave vector transfer (q $= 4\pi sin(\theta)/\lambda$, where λ is the wavelength and 2θ is the scattering angle) range from $\sim$ 0.1 to 2.5 nm^{-1}. The sample to detector distance was nearly 1 m. It was found that three cumulative power law scattering contribution could explain fairly well the scattering profile of Psf membrane. Thus, for Psf membrane, the model shown in Equation (2.6) was used.

$$I_{Psf}(q) = C_1 q^{-k} + C_2 q^{-m} + C_3 q^{-n} + C_4 \tag{2.6}$$

Here C_1, C_2, C_3, and C_4 are q independent constant parameters, and were estimated by fitting this model to scattering data using non-linear least square method.

Scattering data from ND and ceria impregnated membranes were analyzed by adding an extra scattering term as shown in Equation (2.7) and (2.8).

$$I_{total}(q) = I_{Psf}(q) + I_{ND/ceria}(q) \tag{2.7}$$

$$I_{ND/ceria}(q) = C_n \int_0^{\infty} P(q,r) r^6 D(r) S(q,r) dr \tag{2.8}$$

Here, P(q,r) represents form factor of a spherical particle of radius r. D(r) is particle size distribution and S(q,r) represents the structure factor of particles. A fractal like structure factor [225] was considered for present data. D(r) was estimated from scattering profile of ND particles and ceria nanoparticles, for respective membranes. C_n is a q-independent constant and is proportional to the product of number density of the particle and respective scattering contrast. Particle size distribution of ND particles and ceria nanoparticles were calculated from virgin ND particles and synthesized ceria nanoparticles, respectively. Size distribution of ND and ceria obtained from SAXS was used during the fitting of SAXS curve for Psf-ND and Psf-ceria MMMs, respectively.

2.21 Membrane oxidative degradation analysis by differential scanning calorimetry (DSC)

Thermograms of membranes were recorded in differential scanning calorimeter (DSC 1 STARe system, Mettler-Toledo AG (MTANA), Switzerland) over temperature range of 40 to 600 $°C$ in flowing oxygen atmosphere (flow rate: 40 $mL\ min^{-1}$). For DSC measurements, a small piece of each membrane was sealed into 40 μL aluminium pan by covering lid with a small hole in it.

2.22 Mechanical properties evaluation by universal testing machine (UTM)

Universal testing machine (UTM, Hemetek Techno Instrument, model LRX Plus, India) was used to measure the mechanical properties of membranes at room temperature and 40-50% relative humidity. Dumbbell shaped specimens of membranes each of 5 cm length and 0.6 cm width were prepared for analysis. During the analysis, a constant deformation rate of 100 mm/min was applied. NEXYGEN plus software was used to calculate tensile strength and percentage elongation at maximum force for the membrane.

2.23 Permeability measurement of membrane

Pure water permeability measurements of membranes were carried out in an ultrafiltration test skid (membrane cross-section area A = 14.5 cm^2) at room temperature and 1 bar trans-membrane pressure. Steady state pure water permeability (PWP) was determined by measurement of permeate flow in terms of liters per square meter per hour (LMH). The PWP (LMH) through the membrane area A (m^2) was measured by volume V (L) collected during time period T (h) and illustrated by Equation (2.9).

$$PWP = \frac{V}{A \times T} \tag{2.9}$$

To achieve stabilized performance, membranes were initially placed for compaction for 1 h in water under standard ultrafiltration test conditions.

2.24 Solute rejection study of membrane

Membrane samples were placed in an ultrafiltration test skid for cross-flow permeation measurement, with an effective membrane cross-flow area of 14.5 cm^2. PEO of molecular weight: 100 kDa was used as a solute for rejection measurement. PEO solution (200 ppm) was prepared in distilled water by dissolving pre-weighed amounts of PEO. Solute rejection studies were carried out at room temperature and 1 bar transmembrane pressure. Concentration of PEO was determined by measuring total organic carbon (TOC) content of the samples (in both feed and permeate stream) using TOC analyzer (ANATOC, SGE analytical science, Australia). Percentage rejection of PEO ($\%R_{PEO}$) was calculated using Equation (2.10).

$$\%R_{PEO} = \frac{C_f - C_p}{C_f} \times 100 \tag{2.10}$$

Here, C_f is concentration in the feed and C_p is concentration in the permeate stream.

2.25 Pulse radiolysis studies for evaluation of e^-_{aq} scavenging capability

Pulse radiolysis experiments were carried out with high-energy electron pulses (7 MeV, 500 ns) obtained from a linear electron accelerator. Transient species formed by pulse radiolysis were detected by optical absorption method. Aerated aqueous solution of KSCN (1×10^{-2} M) was used for determining the dose delivered per pulse, monitoring the transient $(SCN)_2^{\bullet-}$ at 475 nm, using $G\epsilon$ (475 nm) $= 2.59 \times 10^{-4}\ m^2/J$. Here, G denotes radiation chemical yield in $mol\ J^{-1}$ and ϵ denotes molar extinction coefficient in $m^2 mol^{-1}$. The dose per pulse was close to 10-12 Gy/ pulse (1 Gy = 1 $J\ .kg^{-1}$). Radiolysis of N_2-saturated neutral aqueous solution leads to radiolysis of water as given in Equation (2.11)

$$H_2O \longrightarrow H^\bullet,\ OH^\bullet,\ e^-_{aq},\ H_2,\ H_2O_2,\ H_3O^+ \tag{2.11}$$

In studies, the ability of nanomaterial to scavenge e^-_{aq} was investigated using different concentration in de-mineralized water, and compared with de-mineralized water without adding any nanomaterial in it. The ability of MMMs to scavenge e^-_{aq}

was investigated using membrane coupons of $3 \times 1\ cm^2$ immersed in de-mineralized water, and compared with control Psf membrane. Among the radicals generated, yield of hydroxyl ($OH^\bullet$) and hydrated electron (e^-_{aq}) are relatively high at neutral pH. The $OH^\bullet$ radicals and e^-_{aq} are strongly oxidizing and reducing in nature, respectively. Therefore, in order to investigate the reaction of polymer composite with e^-_{aq} , 1 M tert-butanol was added to the aqueous solution to scavenge $OH^\bullet$ radicals, giving a total radiation chemical yield (G value) of 0.27 $\mu mol/J$ under N_2 saturated condition.

2.26 Hydroxyl radical scavenging studies

Scavenging activity of nanomaterials was evaluated by performing competition kinetics using MG as reference solute. Hydroxyl ($OH^\bullet$) radical was generated by Fenton reaction, where Fe^{2+} ion is oxidized by hydrogen peroxide as shown in Equation (2.12) [226].

$$Fe^{2+} + H_2O_2 \longrightarrow Fe^{3+} + OH^- + OH^\bullet \tag{2.12}$$

MG is a triphenyl methane dye which is intense green in colour having absorption peak at 615 nm. The $OH^\bullet$ radicals formed reacts instantly with MG and oxidizes it, as shown in Equation (2.13). This results in decolourization of the dye. Decay of absorbance at 615 nm was monitored in absence and presence of different concentrations of nanomaterials (ND or ceria) as an independent scavenger.

$$MG + OH^\bullet \longrightarrow MG_{OX} \tag{2.13}$$

Final composition of reaction mixture contains 12 μM MG, 0.15 mM $FeSO_4$ and varying concentration of nanomaterial (ND or ceria), as well as different loading of nanomaterial (ND or ceria) in MMMs (3 cm × 1 cm membrane area). The reaction was initiated by adding 1 M hydrogen peroxide. Absorbance-time plot in absence and presence of different scavengers was fitted with first order kinetics. These studies were performed using UV-Vis spectrometer (JASCO V-630 spectrophotometer) in a quartz cuvette (1 cm × 1 cm).

2.27 Peroxidase activity analysis

Peroxidase-like activity of nanomaterials (ND and ceria) and MMMs (Psf-ND and Psf-ceria) was investigated by using MG and hydrogen peroxide as substrates. Oxidation of MG by nanomaterial (ND or ceria) and hydrogen peroxide can be written as shown in Equation (2.14).

$$MG + H_2O_2 \longrightarrow MG_{OX} + 2H_2O + O_2 \tag{2.14}$$

Reaction mixture containing 12 μM MG, 1 M hydrogen peroxide, and varying concentration of nanomaterial (ND or ceria) was taken up for evaluation of activity. Variation in absorbance value of different concentration of nanoparticles (ND or ceria) was determined at the wavelength of 615 nm in UV-Vis spectrometer. Catalytic kinetics of the material was evaluated by employing Linweaver-Burk plot, using the relation shown in Equation (2.15) [138].

$$\frac{1}{V} = \frac{K_m}{V_{max}} \left[\frac{1}{C} + \frac{1}{K_m} \right] \tag{2.15}$$

Here, two different sets were used. In the first set, to evaluate affinity between nanoparticles (ND or ceria) and MG, reaction was monitored by following oxidation of MG in presence of fixed concentration of nanoparticles, H_2O_2 and varying the concentration of MG. Resulting linear portion of absorption-time plot at 615 nm was fitted and the slope was divided by extinction coefficient of MG ($1.4 \times 10^5 M^{-1} cm^{-1}$) to obtain initial velocity (V, M/s). Double reciprocal plot of initial velocity against concentration of MG was plotted and the linear fit gave the slope and intercept from where Michaelis-Menten constant (K_m) and maximum initial velocity (V_{max}) were calculated. Similarly, affinity of nanomaterials towards H_2O_2 was evaluated by performing oxidation of MG in presence of fixed concentration of MG, nanomaterial and varying the concentration of H_2O_2. Similarly, this set was evaluated for estimating the kinetic parameter, K_m and V_{max}. These parameters were not evaluated for MMMs due to the limitation of adsorption of MG on Psf membrane.

2.28 Monte Carlo simulation studies for life-span assessment of membrane in radioactive environment

Radiation dose absorbed by membrane in intermediate level radioactive waste environment was calculated using Monte Carlo simulations. Monte Carlo method involves actual mathematical simulation of transport of particles through the medium using random sampling techniques with the help of high speed computers. This method is considered to be the most accurate method of solving radiation transport problems, which takes care of complicated and heterogeneous geometries and source emission. Various information such as, energy imparted, fluence, and energy distribution of the radiation can be scored during the transport. A validated Fluka ((FLUKA2011.2x-3) [227, 228] code was used for this purpose. FLUKA code can simulate the propagation and interaction of photons of energies from 1 keV to thousands of TeV in very complex geometries, modeled using Combinatorial Geometry (CG) package.

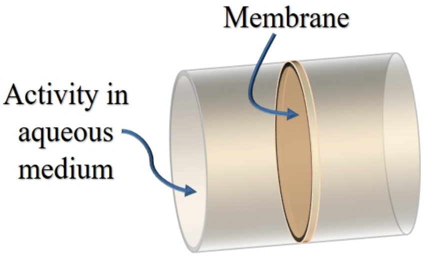

FIGURE 2.2: Monte Carlo simulated geometry for membrane performance in liquid radioactive waste environment.

A Psf membrane of cross sectional area 1 m^2 with thickness 150 μm and density 1.02 gm/cm^3 was dipped in a radioactive effluent cylindrical column. The modeled geometry is shown in Figure 2.2. As a close approximation to reality, it is assumed that radioactive effluent contains 50% of Cs-137 and Sr/Y-90 radionuclides each. Emission particulars of these radionuclides are shown in Table 2.2. Length of effluent column used for simulations is 100 cm and 2 cm for gamma and beta radiations, respectively. The beta spectrum used for calculations is taken from RAdiation Dose Assessment Resource (RADAR). Energy absorbed by the membrane was scored when radiation was emitting uniformly from the cylindrical volume of effluent isotropically. Dose absorbed by the membrane enclosed by liquid radioactive effluent is obtained using USRBIN region based scoring.

Table 2.2: The energy emission from radionuclides.

Radionuclide	**Emission**	**Energy (MeV)**	**Yield%**
Cs-137	Gamma	0.662	85.1
Sr/Y-90	Beta	0.546 (Max)	100
	Beta	2.284 (Max)	100

2.29 Mathematical modeling of solute transport across the membrane

Various models based on different approaches are reported to describe and predict the solute passage through the membrane [229–231]. Kedem-Katchalskys irreversible thermodynamics approach has been considered in the present work, as the mechanisms of molecular transport within the membrane are not fully understood. The basic equations for the solute flux and the solvent flux [232] are given in Equation (2.16) and (2.17), respectively.

$$J_v = L_p \left[\Delta p - \sigma \Delta \pi\right] \tag{2.16}$$

$$J_s = (C_s)_{ln}(1-\sigma)J_v + \omega\Delta\pi \tag{2.17}$$

$$(C_s)_{ln} = \frac{C_m - C_p}{ln\frac{C_m}{C_p}} \tag{2.18}$$

Here, J_v and J_s represent solvent and solute flux, respectively, L_p is the filtration coefficient, Δp is pressure drop across the membrane, σ is reflection coefficient, ω is the solute permeability and $\Delta\pi$ is the osmotic pressure difference between the fluid on membrane surface and product stream, $(C_s)_{ln}$ is logarithmic concentration, C_m is concentration of solute on membrane surface and C_p the concentration of solute in product stream.

In essence, σ indicates the solute rejection property of the membrane and ω indicates the solute permeability through the membrane. Since σ is dependent on membrane, there needs to have an appropriate correction factor for σ reflecting the membrane nature. Similarly, ω requires modification as it refers to the permeability of solute species having a size distribution.

2.29.1 Incorporation of pore theory in rejection model

Pappenheimer [232] and Verinory [233] incorporated pore theory for trans-capillary transport. According to this theory, the membrane structure can be estimated by the parameters σ and ω. Nakao-Kimura et.al. [234] has described the structural implications of the ultrafiltration membrane using the 'pore theory'. They have assumed that cylindrical membrane pore has a constant radius r_p and length ΔX and that the spherical solutes have a radius r_s. σ and ω can be written in terms of pore theory as in Equation (2.19) and (2.20).

$$\sigma = 1 - g(q)S_F \tag{2.19}$$

$$\omega = D.f(q)S_D \left[\frac{A_k}{\Delta X}\right] \tag{2.20}$$

D is diffusivity of solute. A_k is the ratio of total cross-sectional pore area to the effective membrane area. q is ratio of solute radius to pore radius (Equation (2.21)).

$$q = \frac{r_s}{r_p} \tag{2.21}$$

S_D and S_F are the steric hindrance factors for diffusion and filtration flow, respectively, and are defined as in Equation (2.22) and (2.23).

$$S_D = (1 - q)^2 \tag{2.22}$$

$$S_F = 2(1 - q)^2 - (1 - q)^4 \tag{2.23}$$

f(q) and g(q) are the correction factors for the effects of a cylinder wall and are calculated as shown in Equation (2.24) and (2.25).

$$f(q) = \frac{1 - 2.1q + 2.1q^3 - 1.7q^5 + 0.73q^6}{1 - 0.76q^5} \tag{2.24}$$

$$g(q) = \frac{1 - 0.6667q^2 - 0.2q^5}{1 - 0.76q^5} \tag{2.25}$$

Equation (2.17) can be rewritten as:

$$J_s = (C_s)_{ln}(1-\sigma)(L_p(\Delta p - \sigma\Delta\pi)) + \omega\Delta\pi \tag{2.26}$$

$$J_s = (C_s)_{ln}(g(q)S_F)(L_p(\Delta p - \sigma\Delta\pi)) + Df(q)S_D\frac{A_k}{\Delta X}\Delta\pi \tag{2.27}$$

$$J_w = L_p\Delta p = \left[\frac{r_p^2}{8\mu}\right]\left[\frac{A_k}{\Delta X}\right]\Delta p \tag{2.28}$$

$$\frac{A_k}{\Delta X} = \frac{L_p 8\mu}{r_p^2} \tag{2.29}$$

A_k is constant for a specific membrane and can be expressed in terms of pure water flux using Hagen Poiseuille equation and J_w is pure water permeability, μ is solvent viscosity. J_s is the solute flux. L_p, C_m and Δp were measured during the experiments. The r_p was estimated by the pore size distribution of the membranes using BET analysis. Solute flux was calculated using Equation (2.27). Δp was taken equal to the operating pressure as the pressure drop along the length of the membrane was negligible. As the experiments were conducted at very low concentrations, $\Delta\pi$ is not significant. Therefore, values could be estimated based on the molar concentration. D and μ were obtained from literature. r_s was obtained from the particle size distribution of solute (PEO, 100 kDa) using dynamic light scattering (DLS) analysis.

2.29.2 Experimental used for mathematical modeling

Mathematical model for transport phenomena of membranes was determined by utilizing the experimental values of membranes. Pure water permeability and solute rejection for PEO (100 kDa) were measured as mentioned in the earlier section. Particle size distribution of PEO solute was acquired using dynamic light scattering (DLS) analysis. Pore size distribution of membranes were determined with the help of nitrogen adsorption-desorption isotherm using BET technique (Soptomatic 1990 Instrument).

Chapter 3

Polysulfone-nanodiamond mixed-matrix membranes (Psf-ND MMMs)

3.1 Overview

The question this Chapter sets out to address is whether incorporation of nanodiamond (ND) in Psf membrane matrix would result in enhanced radiation resistant property of membrane. The major considerations in building such kind of system are: (a) interaction of ND particles with Psf matrix, (b) dispersion of ND particles in Psf membrane matrix, (c) role of ND during synthesis of Psf-ND MMMs, (d) effect of ND on membrane morphology and topography, (e) effect of ND on membrane hydrophilicity/hydrophobicity, (f) effect of ND on membrane mechanical properties, (g) effect of ND on membrane performance, (h) effect of γ-radiation on the performance of Psf-ND MMMs, and (i) Underlying mechanism of how ND would protect the Psf-ND MMMs against direct impingment of γ-ray energy, as well as radiolysed products of water.

In this Chapter, the unique radiation-resistant property of ND has been exploited to develop Psf-ND MMMs with improved γ-radiation resistant behavior. ND particles were characterized by TEM (to observe the morphology), XRD and Raman (to determine the structure), SAXS (to obtained the size of particle), XPS and ATR-FTIR (to observe the bonding and functional groups of ND), scavenging activity (to determine the capability of ND to scavenge free radicals generated by radiolysis of water), and peroxidase activity (to determine peroxidase-like activity of ND). Psf-ND MMMs were synthesized using phase inversion technique by incorporating ND particles in Psf matrix. Psf-ND MMMs were characterized using FESEM, to observe the effect of ND loading and γ-radiation dose on membrane morphology; AFM, to analyse surface topography of membrane at different loading of ND and at different γ-radiation dose; membrane surface water contact angle, to determine membrane surface hydrophilicity/hydrophobicity and the effect of ND loading and γ-radiation dose; ATR-FTIR and XPS, to obtain variation in chemical structure in presence of ND and radiation dose; GPC, to see the effect of γ-radiation on molecular weight of the membrane; PALS, to determine the alteration in free volume of Psf membrane matrix due to ND loading and γ-radiation dose; SAXS, to evaluate structural parameter in presence of ND and different radiation dose; UTM, to analyse the effect on mechanical properties of membrane by incorporating ND and γ-radiation dose; flux and solute rejection, to observe the performance of Psf-ND membranes in radiation environment; scavenging and peroxidase activity, to analyse the mechanism of protection of membrane in γ-radiation environment due to scavenging of highly reactive species by ND present in the membrane matrix; Monte Carlo simulation study, for life-span analysis of membrane.

3.2 Results and discussion

3.2.1 Characterization of nanodiamond particles

3.2.1.1 TEM images of nanodiamond particles

Figure 3.1 shows TEM image of crystalline ND. The strong attraction forces between particles, due to small size of ND particles, brings them together and are seen in an agglomarated form.

3.2.1.2 XRD pattern of nanodiamond particles

X-ray differection (XRD) pattern (Figure 3.2) of ND particles shows differaction peaks of 2θ at 43° and 75°, corresponding to (111) and (220) planes of the diamond, respectively [235], demonstrating the cubic structure of crystalline phase in ND particles.

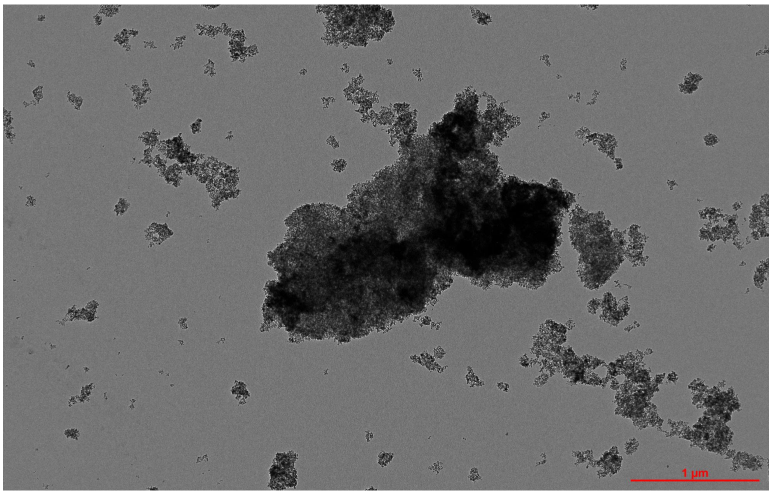

FIGURE 3.1: TEM image of ND particles.

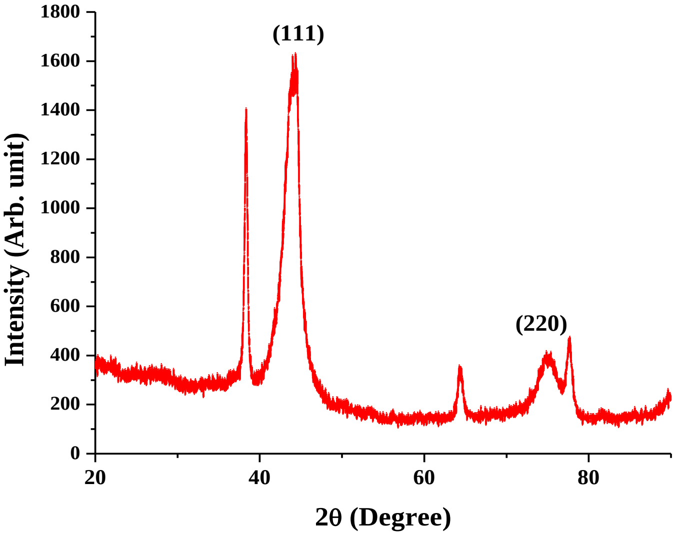

FIGURE 3.2: XRD pattern of ND particles.

3.2.1.3 Raman spectra of nanodiamond particles

Raman spectra of ND particles (Figure 3.3) shows signature peak of diamond at 1318 and 1594 cm^{-1}, attributed to diamond-like sp^3 bonded and polycrystalline graphite-like sp^2 bonded crystals, respectively [236].

3.2.1.4 Nanodiamond particle size distribution by SAXS

Figure 3.4 shows the particle size distribution of ND obtained from SAXS. Average diameter of ND particles acquired is $\sim$ 4.9 nm.

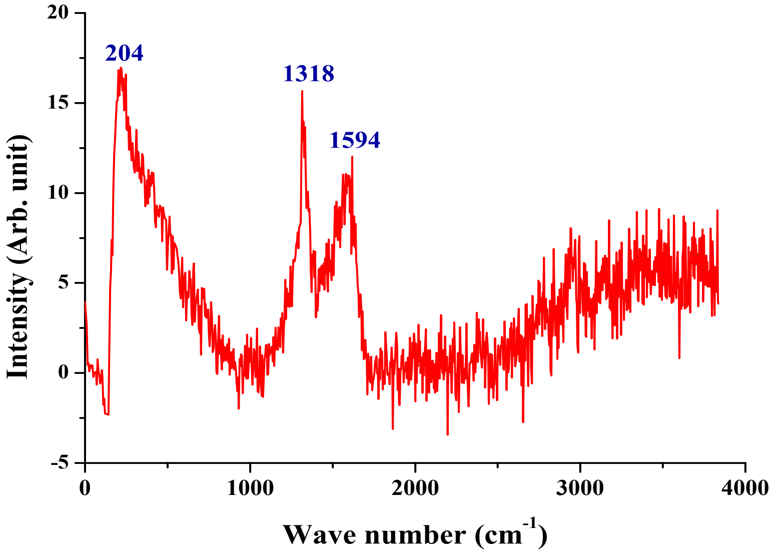

FIGURE 3.3: Raman spectra of ND particles.

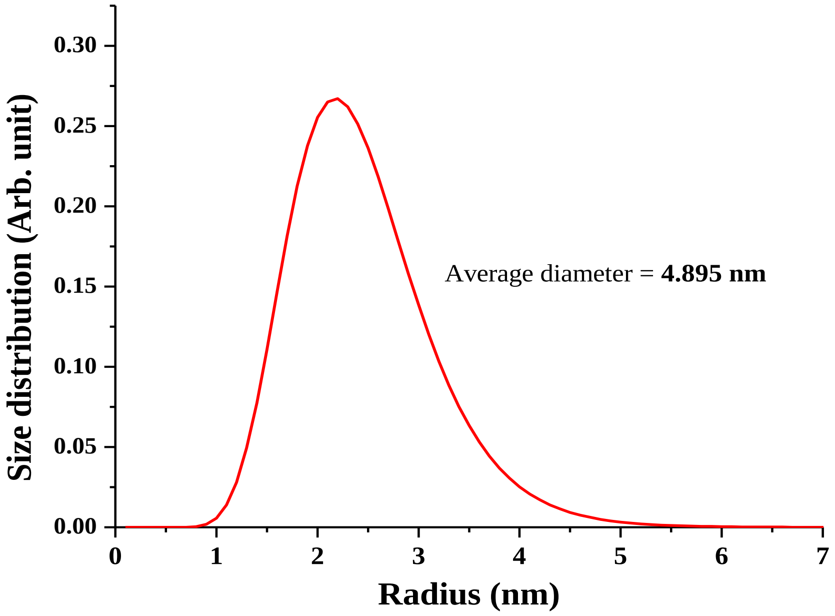

FIGURE 3.4: Size distribution of ND particles obtained by SAXS analysis.

3.2.1.5 XPS analysis of the nanodiamond particles

Figure 3.5(a) shows XPS spectra for C-1s peak of ND particles. XPS spectra exhibits binding energy peak for C-H bond at 283.8 eV, C-C bond at 285 eV, and C-O bond at 286.5 eV. Figure 3.5(b) shows XPS spectra for O-1s peak of ND particles. XPS spectra exhibits binding energy peak for oxide bond 530 eV, -COO- bond at 531.2 eV, and C-O bond at 532.3 eV. XPS spectra for C-1s and O-1s peak confirm the presence of carboxyl and hydroxyl functional groups on surface of ND particles [237].

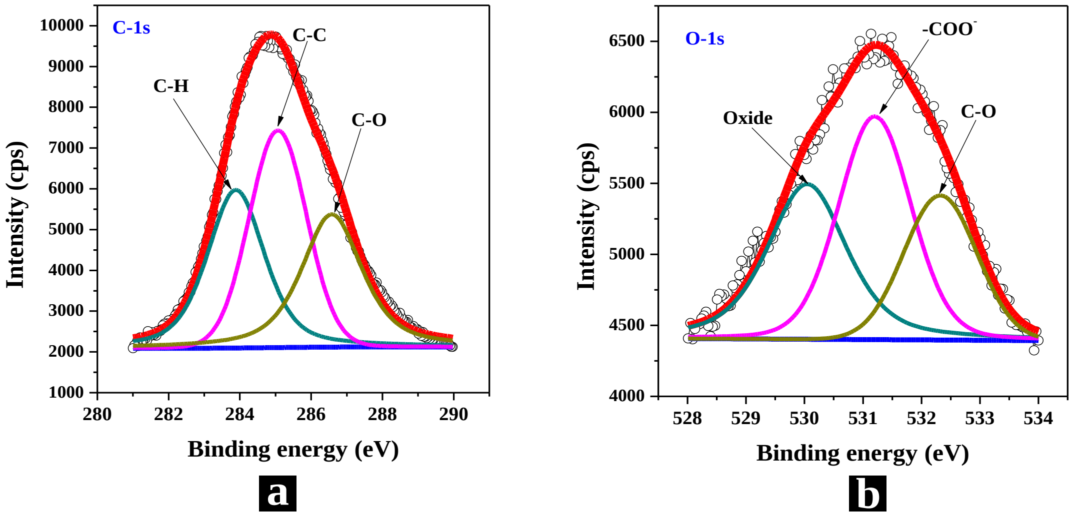

FIGURE 3.5: XPS spectra of ND particles: (a) C-1s peak and (b) O-1s peak.

3.2.1.6 ATR-FTIR spectra of the nanodiamond particles

The FTIR spectra of ND particles in Figure 3.6 shows major absorption bands at about 3410 cm^{-1} (OH stretching vibration), 1647 cm^{-1} (C=O stretching of carboxyl groups), and 1100 cm^{-1} (C-O stretching vibration of -COOH groups). This validates presence of carboxyl and hydroxyl functional groups on surface of ND particles [238].

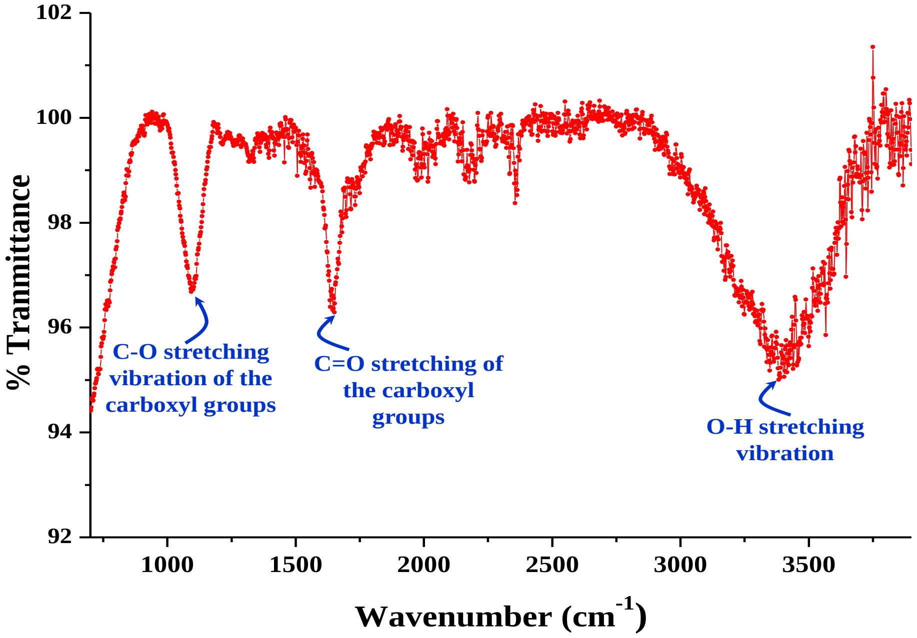

FIGURE 3.6: ATR-FTIR spectra of ND particles.

3.2.1.7 e^-_{aq} scavenging capability of nanodiamond particles

The characteristic absorption spectrum of e^-_{aq} has a broad, structureless band with a maximum around 700 nm in aqueous system. In general, reactivity of e^-_{aq} is investigated by monitoring time absorption plot at 700 nm in presence of different concentration of ND particles. Scavenging of e^-_{aq} radical by ND particles was confirmed by monitoring their reaction with varying concentration of ND particles (Figure 3.7). Results showed that increasing ND concentration leads to rapid decay of hydrated electron, which confirms that ND is responsible for scavenging the radiolysed product (e^-_{aq}) of water.

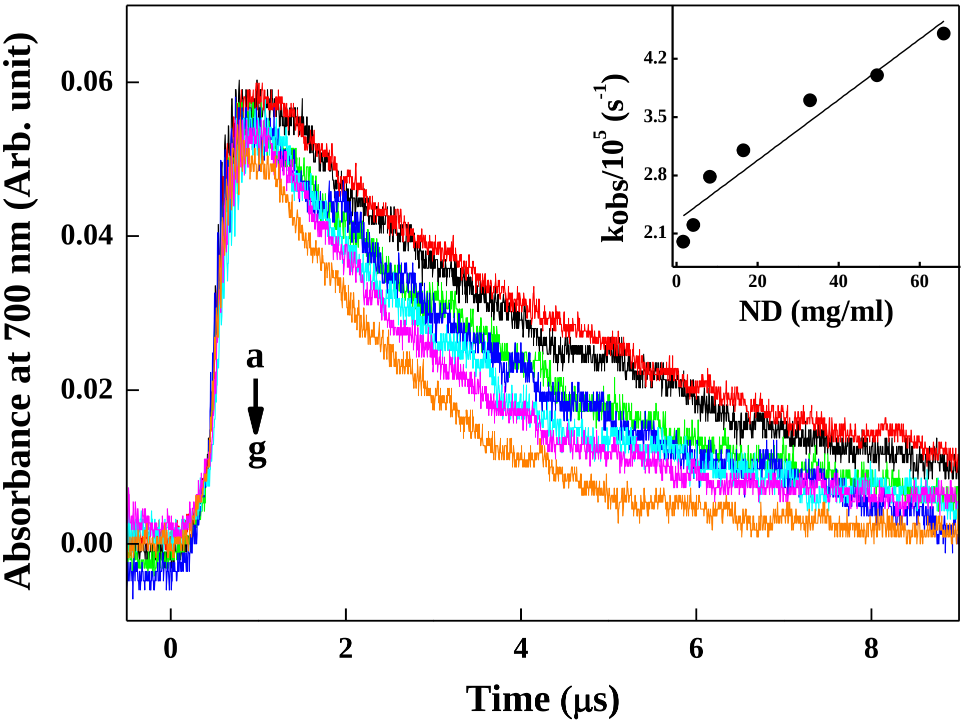

FIGURE 3.7: Absorption-time plot of hydrated electron of water at 700 nm in presence of varying concentration of ND particles suspended in aqueous solution containing 1 M t-butanol at pH 7 under N_2 saturated condition. Here plot corresponds ND concentration at (a) = 1.65 $\mu g/ml$, (b) = 4.12 $\mu g/ml$, (c) = 8.25 $\mu g/ml$, (d) = 16.5 $\mu g/ml$, (e) = 33 $\mu g/ml$, (f) = 49.5 $\mu g/ml$, (g) = 66 $\mu g/ml$. Inset shows the plot of observed rate of hydrated electron as a function of ND particles concentration at pH 7.

3.2.1.8 Hydroxyl radical scavenging capability of nanodiamond particles

Maximum absorption peak of MG is at 615 nm. To understand participation of ND particles in the reaction, oxidation of MG was performed by $OH^\bullet$ radical in presence of different concentration of ND particles. Figure 3.8 shows degradation of MG in presence of different concentration of ND. As shown in inset of Figure 3.8, with increase in the concentration of ND, degradation rate of MG decreases. This indicates scavenging of $OH^\bullet$ radical by ND particles. The $OH^\bullet$ radical scavenging phenomenon of ND particles can be expressed as in Equation (3.1).

$$ND + OH^\bullet + H^+ \longrightarrow ND_{OX} + H_2O \tag{3.1}$$

Decrease in degradation rate of MG (k_{obs}) with concentration of ND depicts increase in $OH^\bullet$ radical scavenging activity of ND.

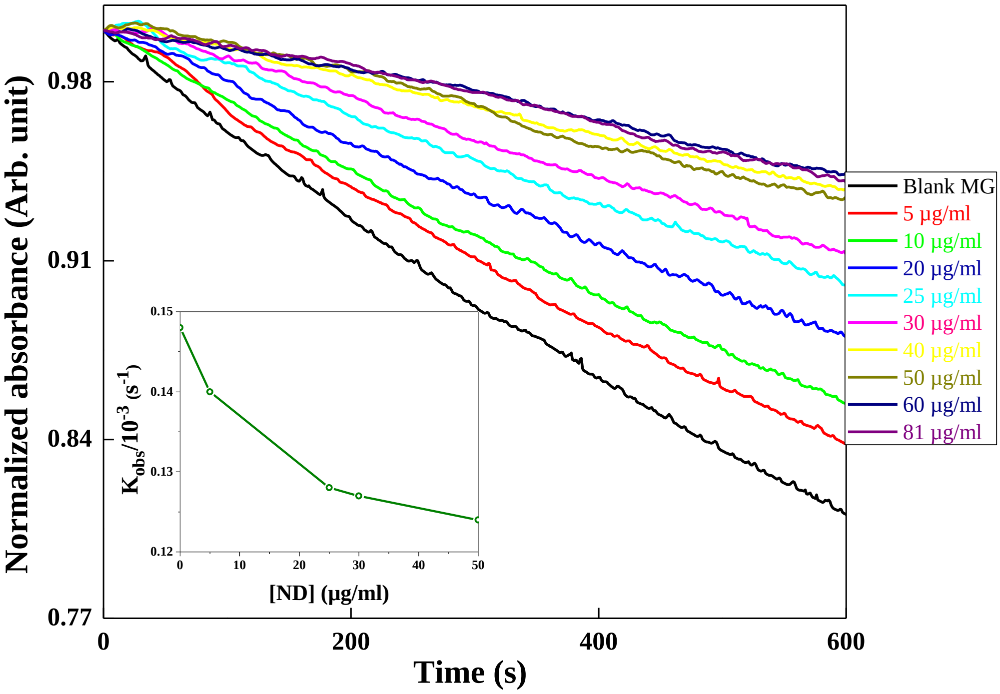

FIGURE 3.8: Hydroxyl radical scavenging by ND particles. Inset shows inhibition of absorbance of MG due to $OH^\bullet$ radical induced degradation in presence of different concentration of ND particles (5 - 81 $\mu g/ml$).

3.2.1.9 Peroxidase activity of nanodiamond particles

Peroxidase-like activity of ND particles was analyzed by using MG and hydrogen peroxide as substrate. Inset of Figure 3.9 shows time dependent peroxidase-like activity of ND particles. Peroxidase-like activity increases with increasing concentration of ND particles (Figure 3.9). To understand the affinity of MG with ND particles, steady state kinetics was studied by varying the concentration of MG with fixed concentration of ND particles and hydrogen peroxide, as shown in

Figure 3.10. The steady state kinetic parameters were found using Linewear-Burk method. The value of K_m was estimated $\sim$ 40.075 M and V_{max} $\sim$ 1.195 M/s.

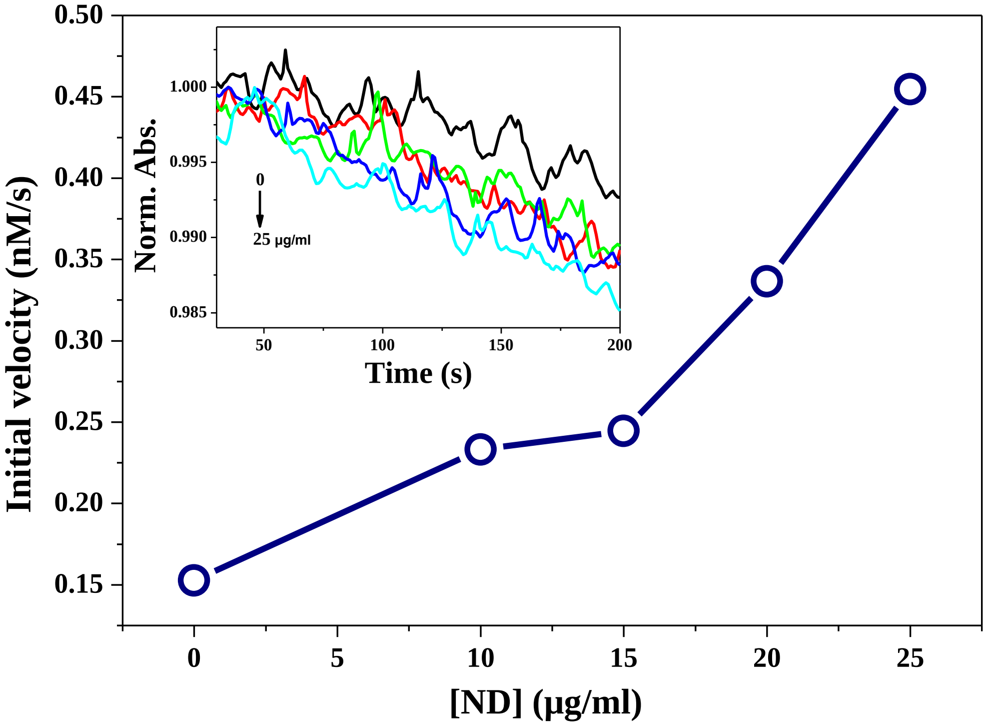

Figure 3.9: Peroxidase activity exhibited by different concentration of ND particles. Inset shows time dependent peroxidase-like activity for different concentration (0 → 25 $\mu g/ml$) of ND particles.

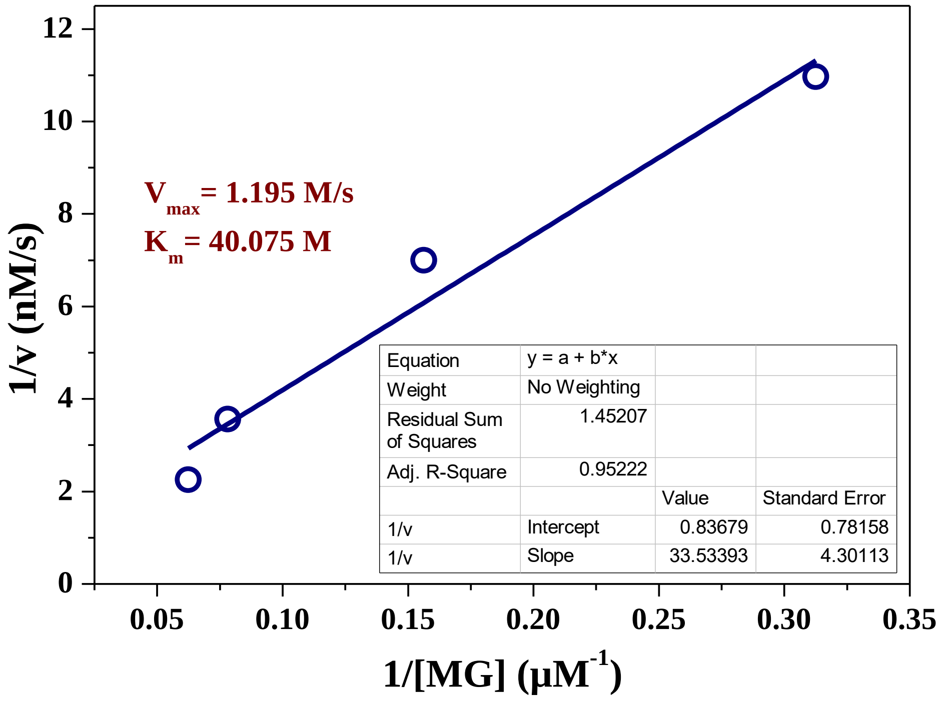

Equation	y = a + b*x		
Weight	No Weighting		
Residual Sum of Squares	1.45207		
Adj. R-Square	0.95222		
		Value	Standard Error
1/v	Intercept	0.83679	0.78158
1/v	Slope	33.53393	4.30113

Figure 3.10: Double reciprocal plot of initial velocity for decay of MG by H_2O_2 catalyzed by ND particles as a function of MG concentration.

3.2.2 Membrane morphology study using FESEM

Surface and cross-section morphology of membranes are shown in Figure 3.12 and 3.13, respectively, for different ND concentrations and irradiation doses. Top surface morphology of control Psf and Psf-ND MMMs is indistinguishable, except for the presence of ND in Psf matrix, as shown in Figure 3.12. ND particles are homogeneously distributed on the surface of MMMs. However, with increased loading of ND, the proportion of ND particles has increased on top surface of the membrane, leading to agglomeration at 1% ND loading (Figure 3.12(c), (f) and (i)). Fingering has been observed in all the membranes, as clearly seen in Figure 3.13, which is a characteristic of membranes synthesized by nonsolvent-induced phase inversion technique [239]. Cross-sectional images of MMMs show the presence of ND in bulk of the membrane matrix, offering mechanical strength to the membrane [57], as discussed later in the section of mechanical properties of the membranes. FESEM images (insets of Figure 3.13(a), (b) & (c)) reveal that an increase in ND loading results in decrease in pore density and increase in pore size. This can be explained by delay in exchange between solvent and water during phase inversion due to the increased viscosity of dope solution by added ND nanoparticles [95]. The viscosity of dope solution increases with the loading of ND, as shown in Figure 3.11.

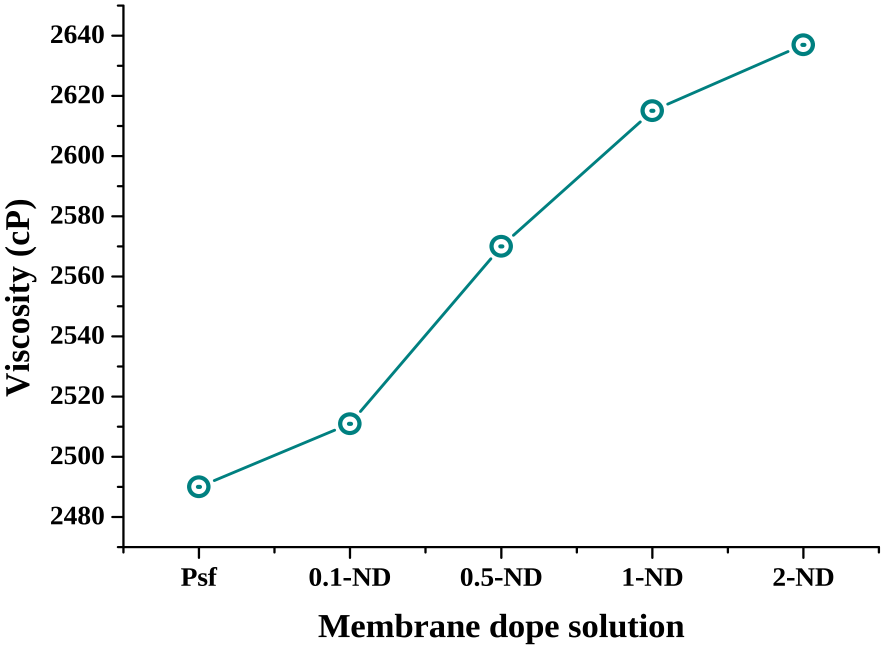

FIGURE 3.11: Viscosity of dope solution with different loading of ND in membrane.

With radiation exposure, different phenomena like pore closure, pore merger and pore splitting [240] are observed because of cross-linking and chain scissioning

[241], as seen in Figure 3.13. With increase in radiation dose, the Psf membranes showed significant pore closure, leading to reduction in pore density, as shown in Figure 3.13(a), (d), & (g). However, on exposure to radiation, for the MMMs, 0.5-ND and 1-ND, pore splitting and pore merger phenomena occur statistically, but simultaneously, leading to an overall reduction in pore density of membranes, as shown in Figure 3.13(e), (f), & (i). Similar finding has been observed in SAXS studies as shown in Figure 3.20. The reduced pore density of MMMs resulted in reduced permeability, as disscussed in later section (Figure 3.22). Interestingly, membrane 0.5-ND shows comparatively less changes with radiation in porosity. FESEM images study clearly indicate that presence of ND has got a profound and positive implication on the structure and morphology of MMMs, and the effects are more so pronounced in presence of γ-radiation.

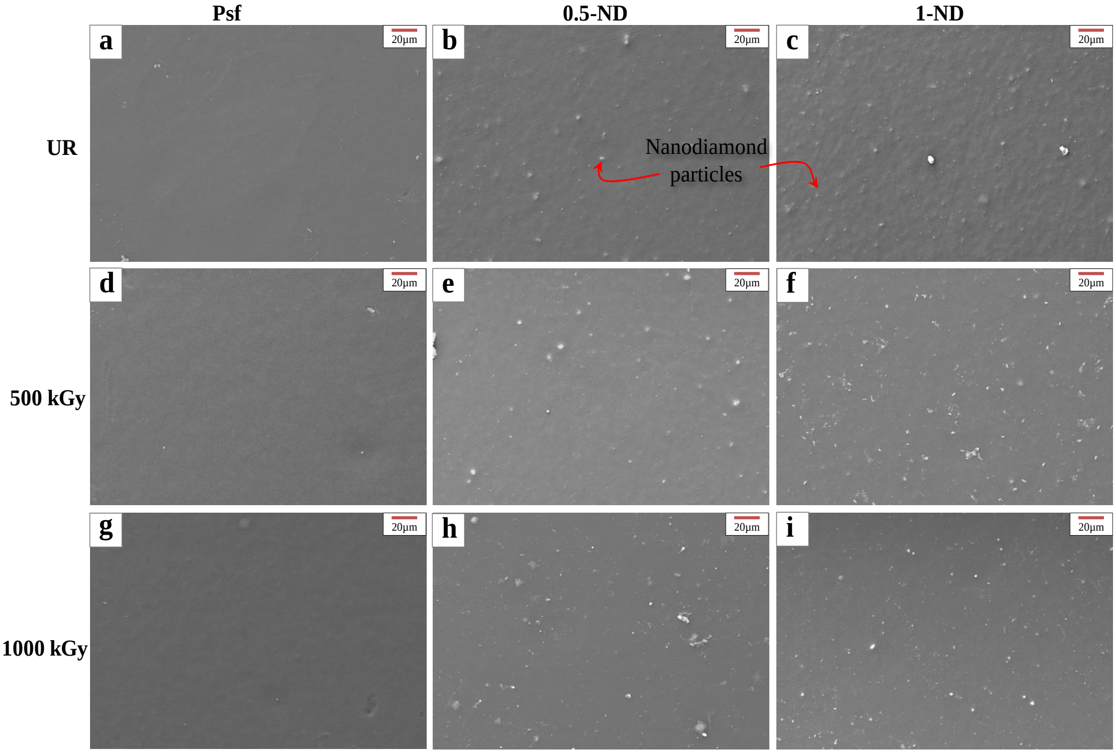

FIGURE 3.12: FESEM images of top surface of the membrane with and without ND: (a) to (c): Unirradiated (UR) membranes, (a) Psf, (b) 0.5-ND, and (c) 1-ND; (d) to (f): Exposure to 500 kGy radiation dose, (d) Psf-500, (e) 0.5-ND-500, and (f) 1-ND-500; (g) to (i): Exposure to 1000 kGy radiation dose, (g) Psf-1000, (h) 0.5-ND-1000, and (i) 1-ND-1000.

3.2.3 Membrane surface topography study using AFM

Root mean square (RMS) roughness of the membranes, obtained from AFM studies, is shown in Figure 3.14. The RMS roughness of control Psf membrane was

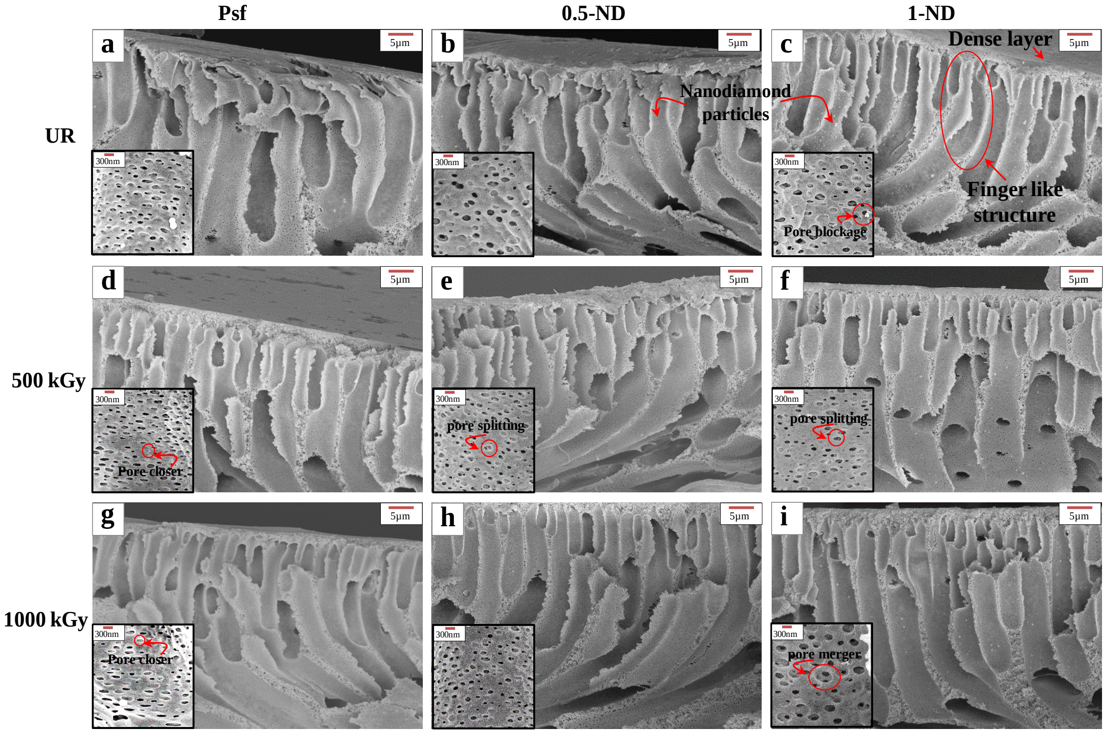

FIGURE 3.13: FESEM images of cross-section of membrane with and without ND: (a) to (c): Unirradiated (UR) membranes, (a) Psf, (b) 0.5-ND, and (c) 1-ND; (d) to (f): Exposure to 500 kGy radiation dose, (d) Psf-500, (e) 0.5-ND-500, and (f) 1-ND-500; (g) to (i): Exposure to 1000 kGy radiation dose, (g) Psf-1000, (h) 0.5-ND, and (i) 1-ND-1000. Inset in the images shows pores in respective membranes.

found to be 2.02 nm. Surface roughness is increasing with ND loading and RMS roughness value of 3.20 nm is obtained for 2% loading. This is due to interfacial defects created between ND and Psf matrix (as observed by PALS analysis shown in Figure 3.19). The surface roughness of membranes increases with radiation dose due to deterioration of membrane structure, which results in a rough topography. Psf membrane undergoes chain scissioning and cross-linking phenomena and increases the surface roughness even at 100 kGy radiation dose. For Psf-ND MMMs, change in roughness is not significant up to 100 kGy of radiation dose, while appreciable change was observed for radiation dose of 500 and 1000 kGy, which leads to increase in surface roughness up to 4.6 nm (2-ND-500) and 5.2 nm (2-ND-1000). Up to a radiation dose of 100 kGy, presence of ND prevents Psf membrane matrix from the effect of γ-radiation. On the other hand, beyond 500 kGy radiation dose, chain scissioning and cross-linking phenomenon deteriorate the Psf membrane matrix, which is evident from surface roughness values (maximum of 76.2% increase for 0.5-ND-1000). The findings indicate that least deterioration of membrane structure has occurred at 2% loading, with 60.3% increase in roughness value (2-ND-1000). AFM results demostrate that control Psf membrane surface starts deteriorating even at 100 kGy radiation dose, while Psf-ND MMMs showed significant changes in surface roughness only after 500 kGy radiation dose.

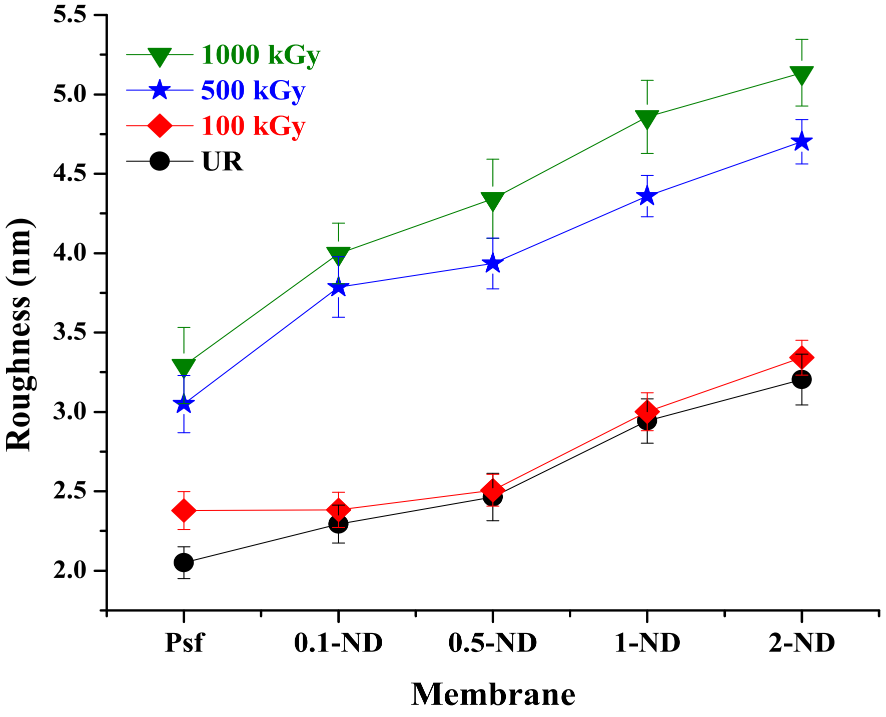

Figure 3.14: Variation of RMS roughness of membranes at different loadings of ND and radiation dose.

3.2.4 Membrane surface water contact angle studies using DSA

Water contact angle studies were carried out to determine hydrophilicity/hydrophobicity of membrane, as shown in Figure 3.15. The water contact angle of control Psf membrane was found to be 80°, which decreases with loading of ND (74.2° for 0.1-ND and 70.2° for 0.5-ND) because of the enhanced surface hydrophilicity in presence of hydrophilic (hydroxyl and carboxyl) groups of ND (observed in FTIR spectra Figure 7.7) [242]. However, beyond 0.5% loading, the contact angle increases (75.4° for 1-ND and 76.1° for 2-ND), which could be the result of less physical interaction of ND with Psf matrix due to aggregation. The contact angle values of membranes irradiated up to 1000 kGy remained almost similar, and in line with the trend observed for unirradiated membranes, with 2% loaded one being an exception. At 100 kGy radiation dose, significant change of contact angle has been observed only in the case of control Psf membrane due to enhancement of hydrophilicity because of increase in surface roughness (as reflected in surface roughness values Figure 3.14). At 500 kGy radiation dose, contact angle decreases, which is due to pore splitting, that increases pore density and thus increase in hydrophilicity. Almost similar values of contact angles, 72°, 71.2°, and 76.2° in case of 0.1-ND-1000, 0.5-ND-1000, and 1-ND-1000 membranes, respectively, with their unirradiated counter parts (70.2° and 75.4°), is one important observation to be made here. However, dip in contact angle value of irradiated membranes at 2% ND loading is due to agglomeration of ND at high concentration. Less interaction between ND and polymer at 2% loading could be responsible for having a similar trend in contact angle values of 2-ND membranes with that of control Psf membrane.

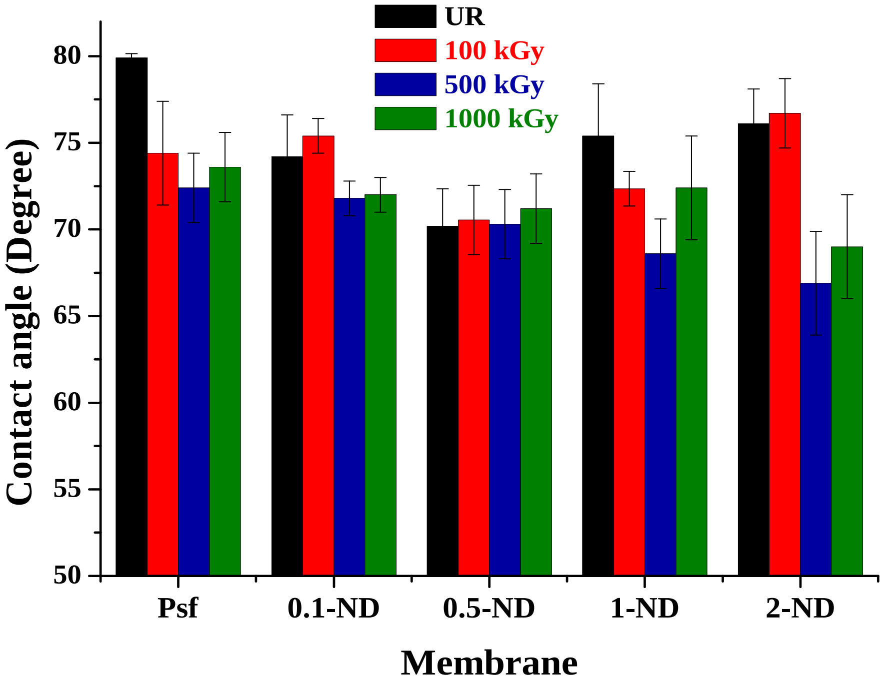

Figure 3.15: Variation of membrane surface water contact angle with loading of ND in membrane matrix, before and after irradiation.

3.2.5 Functional group studies of membrane surface using ATR-FTIR

FTIR spectra, as shown in Fig. 3.16, exhibits significant absorption band around 834 cm^{-1} (C-H stretching of aromatic ring of Psf), 1014 cm^{-1} (symmetric O=S=O stretching of sulfone group), 1080 and 1105 cm^{-1} (aromatic ring vibration), 1149 cm^{-1} (symmetric O=S=O stretching of sulfone group), 1168 cm^{-1} (asymmetric O=S=O stretching of sulfone group), 1238 cm^{-1} (asymmetric C-O-C stretching of aryl ether group), 1293 & 1322 cm^{-1} (asymmetric O=S=O stretching of sulfone group), 1364 cm^{-1} (symmetric C-H bending deformation of methyl group), 1411 cm^{-1} (asymmetric C-H bending deformation of methyl group), 1487 & 1586 cm^{-1} (aromatic C=C stretching), 2873 & 2968 cm^{-1} (asymmetric and symmetric C-H stretching vibration include complete methyl group), and 3440 cm^{-1} (O-H stretching vibration). FTIR spectra of pure ND powder shows major absorption bands around 3410 cm^{-1} (O-H stretching vibration), 2359 cm^{-1} (absorption vibration of the CO_2), 1647 cm^{-1} (C=O stretching of the carboxyl groups), and 1100 cm^{-1} (C-O stretching vibration of the -COOH groups). This validates presence of carboxyl and hydroxyl functional groups on the surface of ND. The hydroxyl and carboxyl groups present over ND are responsible for scavenging secondary free radicals generated during radiolysis of water, which in turn protects MMMs leading to an enhanced life-span in radioactive environment. This finding has also been corroborated with our in-house data on radiation stability of MMMs with carboxyl-functionalised ND [243]. No-shifting in characteristic absorption bands of Psf-ND MMMs indicates the fact that impregnation of ND in control Psf matrix does not affect internal molecular structure of membrane. Characteristic band of ND at 2359 cm^{-1} shows physical presence of ND, whose intensity increases with loading of ND, as seen in Figure 3.16.

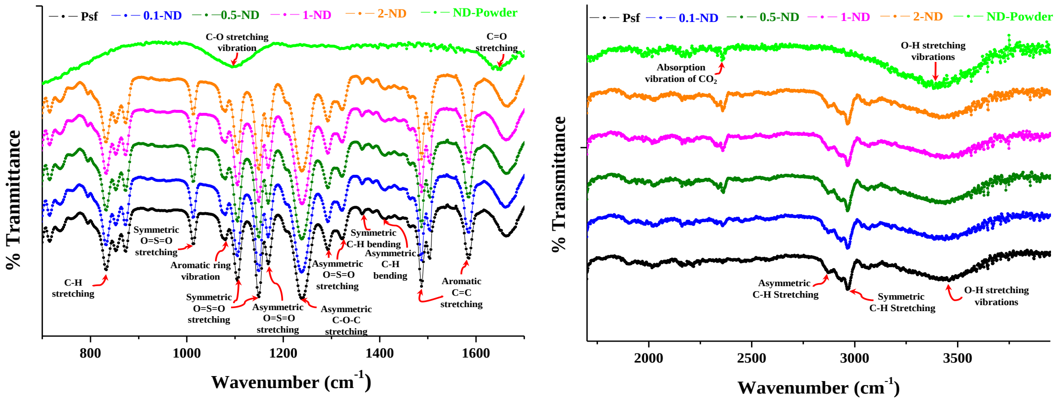

FIGURE 3.16: ATR-FTIR spectra of unirradiated control Psf and Psf-ND MMMs.

3.2.6 Studies on nature of bonding in membrane matrix using XPS

XPS spectra of C-1s peak of membranes, as shown in Figure 3.17, exhibits binding energy peak for C-C bond around 284.9 eV, C-OH bond around 286.3 eV, and C=O bond around 287.5 eV. XPS spectra of S-2p and O-1s peaks of membranes. No shift in XPS peaks of bonds confirms that there is no chemical interaction between ND and Psf, even at increased loading of ND, confirming only physical entrapment of ND in membrane matrix.

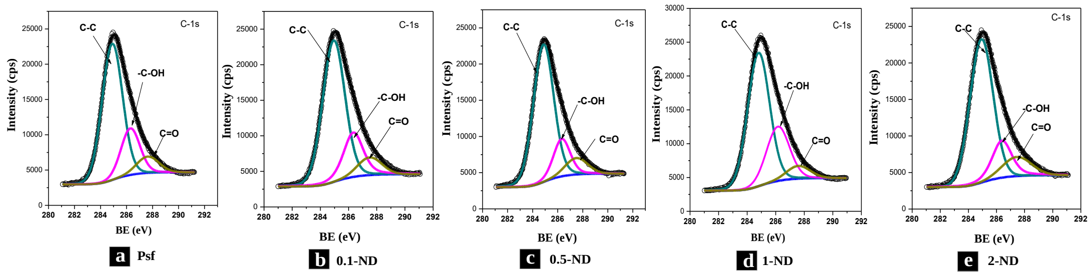

a Psf **b** 0.1-ND **c** 0.5-ND **d** 1-ND **e** 2-ND

FIGURE 3.17: XPS spectra of unirradiated membranes: (a) Psf, (b) 0.1-ND, (c) 0.5-ND, (d) 1-ND, and (e) 2-ND.

As seen in Table 3.1, the atom ratio of carbon to sulfur (C/S) was found to be increasing with loading of ND, owing to increase in concentration of carbon contributed from ND addition. Also, the ratio of C/S was found to be increasing with radiation dose for both control Psf and MMMs, which is mainly attributable to the elimination of sulfone group with irradiation due to chain scissioning [42, 239]. It is interesting to see that the increase in C/S ratio from 20.9 for 0.5-ND to 26.5 for 0.5-ND-1000 was minimal in case of membrane with 0.5% loading of ND, confirming this membrane to be the most radiation resistant amongst all MMMs. Results indicate that a better interaction of polymeric chain with ND exists at an optimum loading of ND, which is 0.5%. At loadings lower than 0.5%, concentration of ND in polymeric host matrix is not reasonable enough to bring about significant interfacial interactions, whereas, at loadings beyond 0.5% (that is for 1-ND & 2-ND membranes), the agglomeration of ND and interfacial defects lead to reduced interaction between the inter- and intra-polymeric chains.

TABLE 3.1: Carbon to sulfur atom ratio (C/S) obtained from XPS: for different concentration of ND in membrane at different doses of γ-radiation.

C/S ratio in membrane matrix					
Radiation dose	**Psf**	**0.1-ND**	**0.5-ND**	**1-ND**	**2-ND**
UR	20.6	20.7	20.9	22.7	25.3
100 kGy	21.1	21.4	21.2	28.7	30.9
500 kGy	29.1	23.4	21.4	35.5	43.2
1000 kGy	38.8	47.6	26.5	42.1	53.4

3.2.7 Weighted average molecular weight studies of the membrane using GPC

Weighted average molecular weight (M_w) of un(irradiated) Psf and Psf-ND MMMs are shown in Figure 3.18. At γ-radiation dose of 100 kGy, there is no significant change observed in terms of M_w, as compared to their unirradiated counter parts. At 500 kGy irradiation dose, M_w decreased by 25.6, 2.6 and 16.7% for Psf-500, 0.1-ND-500 and 2-ND-500 membranes, respectively, compared to their unirradiated counter parts. This is because chain-scissioning of Psf chain dominates, which leads to reduction in molecular weight [70, 244]. The 0.5-ND-500 and 1-ND-500 membranes show negligible rise (i.e., 1.4 and 8.1%, respectively) compared to their unirradiated counter parts, which might be due to dominant cross-linking of Psf chains. The extent of change in M_w of 0.1-ND, 0.5-ND, and 1-ND membranes is very less up to 500 kGy radiation dose, compared to their unirradiated counter parts. This reveals the least effect of chain scissioning in case of 0.5-ND and 1-ND membranes.

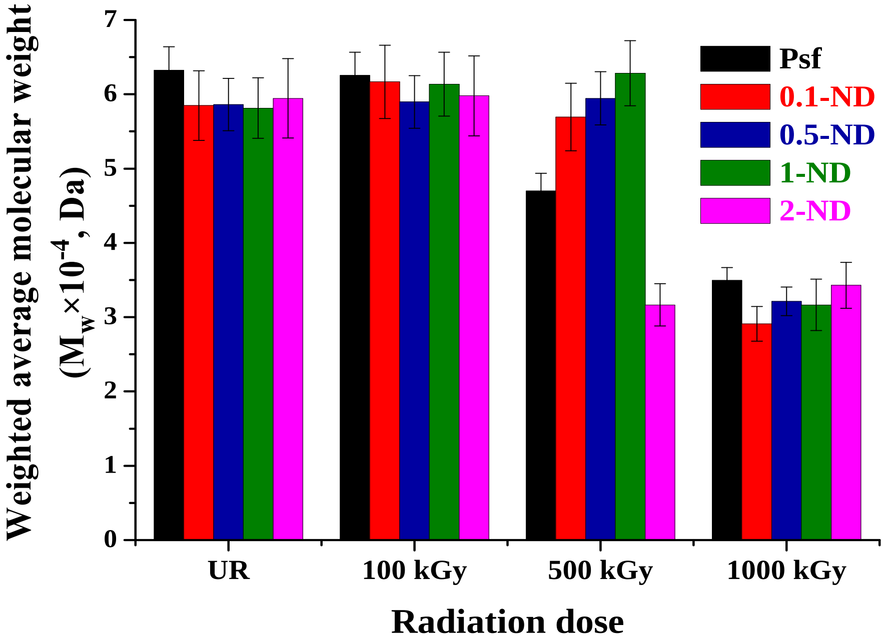

FIGURE 3.18: Weighted average molecular weight (M_w) obtained from gel permeation chromatography of membrane: with variation of ND loading and radiation dose.

3.2.8 Free volume determination in membrane matrix using PALS

Free volume in membrane matrix was investigated with the help of PALS [245] and results are shown in Figure 3.19. There is a rise from 960 (Psf) to 1270 (0.1-ND) in relative fractional free volume after impregnation of ND in the membrane matrix. This is due to formation of interfacial free volume at the interface of ND particles and polymer matrix in the MMMs [13]. Interfacial free volume initially increases with ND loading (up to 1373 for 0.5-ND membrane), due to increase in number density of particles. However, further increase in ND loading (beyond 0.5%) leads to agglomeration of ND particles resulting in reduction of overall interfacial free volume, and hence a reduction in relative fractional free volume (1254 and 1158 for 1-ND and 2-ND membranes, respectively). On exposure of radiation up to 1000 kGy, there is an increase in relative fractional free volume by 35.2, 8, 8.9, 8.2, and 9.3% for Psf-1000, 0.1-ND-1000, 0.5-ND-1000, 1-ND-1000, and 2-ND-1000 membranes, respectively, due to defects created in membrane matrix as a result of structural rearrangement of polymer chains. Extent of change in relative fractional free volume is less in case of ND impregnated membranes as compared to that of Psf membrane. Hence, Psf-ND MMMs are structurally more radiation resistant at all reported loadings.

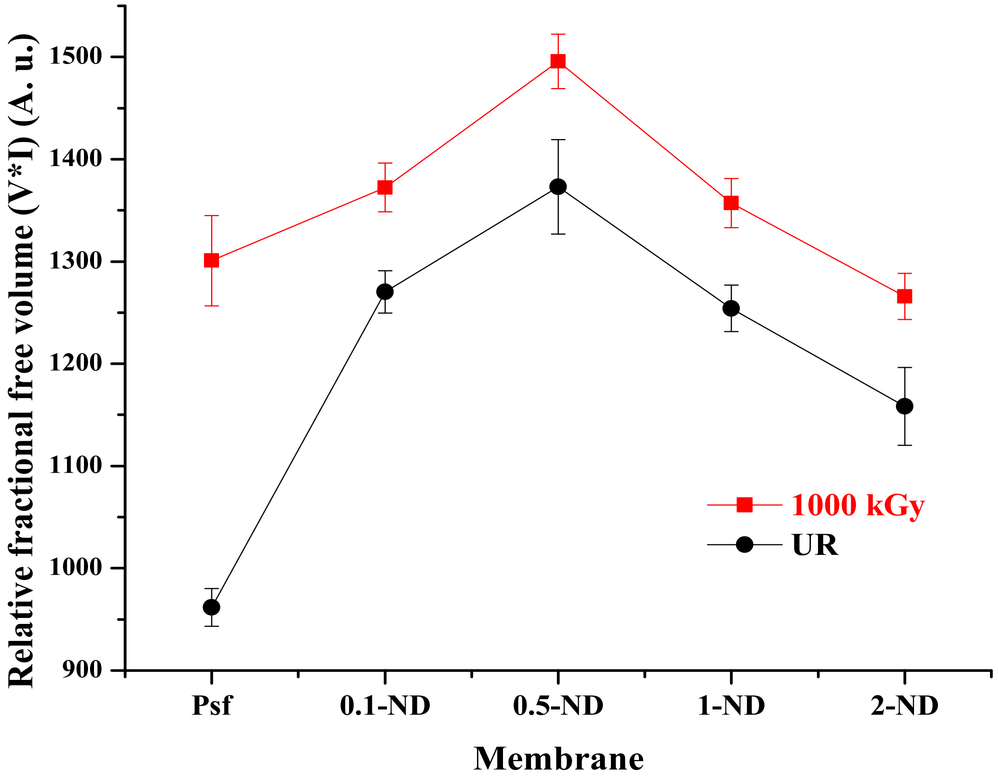

FIGURE 3.19: Variation of relative fractional free volume with loading of ND in membrane matrix and radiation dose, obtained from PALS.

3.2.9 Structure evaluation of membrane matrix using SAXS

Structural evolution, as probed by SAXS analysis, is shown in Figure 3.20. Increased relative number density with increase in ND loading confirms an even distribution of ND in membrane matrix. On the other hand, relative scattering contrast is found to be decreasing with radiation dose, which is due to reduction in pore density. This is because of pore-closure and pore merger phenomenon, as observed in FESEM images (inset of Figure 3.13). Value of relative 'number density × contrast' has been calculated by taking Psf membrane as a reference. After irradiation, variation in relative contrast is increasing with increasing ND loading with respect to Psf membrane. This indicates that after irradiation, reduction in pore density is more pronounced at higher loadings of ND.

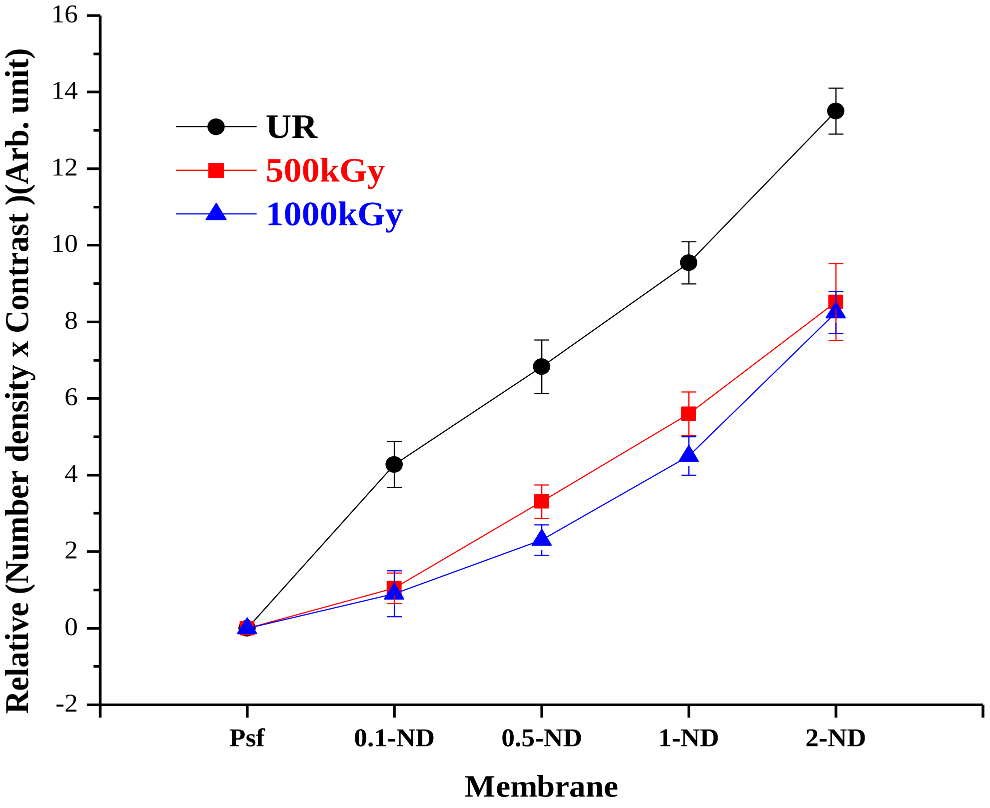

FIGURE 3.20: Variation of relative "number density × contrast"of membrane matrix, obtained from SAXS with loading of ND at different radiation dose.

3.2.10 Membrane mechanical properties evaluation using UTM

UTM analysis (Figure 3.21(a)) shows that tensile strength (TS) of Psf membrane is 3.07 MPa, which remained almost same (3.11 MPa) after impregnating 0.1% ND (0.1-ND). Further increase in ND loading up to 0.5% reduced TS to 2.88 MPa, as hard ND is expected to introduce rigidity between polymer chains. A further increase in concentration of ND in MMMs enhances its TS to 3.25 and 3.36 MPa for 1-ND and 2-ND membranes, respectively, which may be due to reduced physical interaction between the ND and polymeric chains at higher loadings [246]. The percentage elongation at maximum force (%E) of unirradiated membranes decreases from 14.2 (for Psf membrane) to 13, 9.1, and 12.7 for 0.1-ND, 0.5-ND, and 1-ND membranes, respectively (Figure 3.21(b)), owing to the impregnation of nanomaterials onto porous polymeric host matrix, which in turn reduces the ductility of membranes. No significant changes were observed in TS and %E up to 100 kGy radiation dose.

Further irradiation of membranes leads to degradation in terms of chain scissioning of polymer chains and hence reduction in TS. At 500 kGy irradiation, membranes show 17.5, 9, 1.4, 12.6, and 6.7% reduction in TS for Psf-500, 0.1-ND-500, 0.5-ND-500, 1-ND-500, & 2-ND-500 ND loaded membranes, compared to their unirradiated counter parts. Interestingly, a negligible change in TS (1.4%) confirm the stability of 0.5-ND membrane up to 500 kGy of radiation dose, which indicates that a 0.5% loading of ND is capable of protecting the Psf host matrix from extensive chain scissioning, while being responsible for scavenging of radiolysed products (free radicals) of water. This is also corroborated with GPC studies (Figure 3.18). Furthermore, at 1000 kGy irradiation, Psf membrane (Psf-1000) shows 16.6% reduction in TS as compared to unirradiated control Psf membrane. The membranes impregnated with ND shows 12.2, 0.7%, 20.9%, and 18.2% reduction in TS at 1000 kGy for 0.1-ND-1000, 0.5-ND-1000, 1-ND-1000 and 2-ND-1000 membranes, respectively, compared to their unirradiated counter parts. This shows that the membrane with 0.5% loading of ND is restoring its mechanical properties even after exposed up to 1000 kGy radiation.

The %E is decreasing with higher radiation dose [247], as chain scissioning of polymer reduces the ductility of the membranes. At 500 kGy irradiation, membrane shows reduction in %E by 62.8, 46.7, 23.6, and 34.3% for Psf-500, 0.1-ND-500, 1-ND-500, and 2-ND-500 membranes, respectively, compared to their unirradiated counter parts. While the membrane with 0.5% loading has not shown any significant change. This confirms that Psf-ND MMMs are stable up to 500 kGy of radiation dose, compared to Psf membrane, with 0.5-ND membrane being the most stable MMMs (similar trend has been observed for TS). Further irradiation up to 1000 kGy shows significant reduction in %E by 83%, 78%, 74%, 78.8%, and 86% for Psf-1000, 0.1-ND-1000, 0.5-ND-1000, 1-ND-1000, and 2-ND-1000 membrane, respectively, compared to their unirradiated counter parts. Thus, ductility of membranes is lost and they become brittle at irradiation dose of 1000 kGy, making the membranes unusable.

3.2.11 Membrane performance evaluation

Permeability offered by MMMs shows around 32, 38.5, 44.9 and 61.5% enhancement with 0.1, 0.5, 1, and 2% impregnation of ND, respectively, compared to

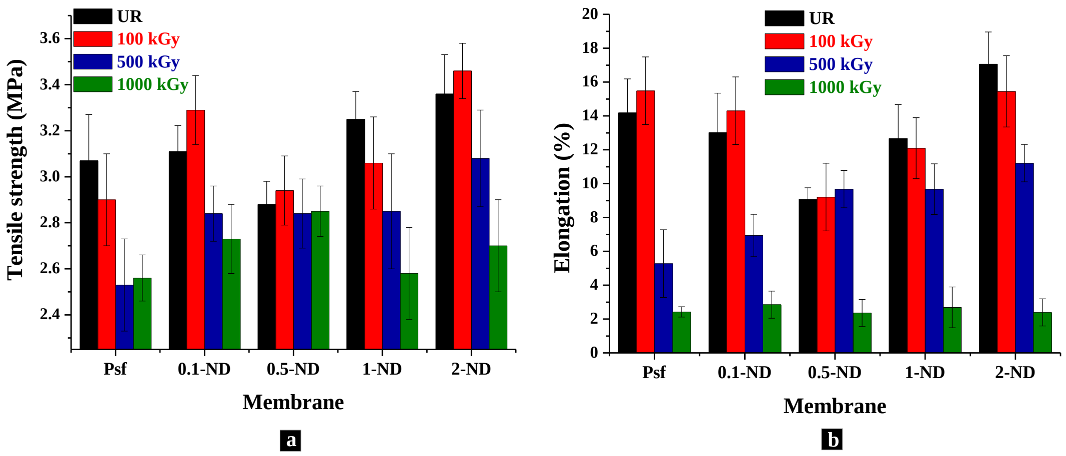

FIGURE 3.21: Mechanical properties of membrane with loading of ND in membrane matrix and γ-radiation dose:(a) Variation in tensile strength with loading of ND into membrane matrix and radiation dose; (b) Change in percentage elongation at maximum force of membrane with loading of ND and radiation dose.

control Psf membrane, as shown in Figure 3.22(a). Rise in permeability is attributed to increase in surface hyrophilicity due to the presence of hydroxyl and carboxyl functional groups of ND (as verified by water contact angle studies reported in Figure 3.15). As membranes were exposed to γ-radiation, simultaneous chain scissioning and cross-linking events take place in the polymer chains. As a result, internal structure of the membrane gets altered leading to pore closure, pore merger, pore splitting, creation of defects, etc. When membranes were exposed to 100 kGy of γ-radiation, Psf-ND MMMs did not show any observable changes in permeability, while slight reduction (9%) in permeability has been observed for control Psf membrane. This is attributed to reduction of free volume (pore closure, reduction in pore density) within the polymer matrix. At 500 kGy of radiation dose, further reduction in pore density and porosity decreases the permeabilty, as a result of radiation dose (as verified by SAXS results in Figure 3.20). Reduction in permeability of membranes exposed up to 1000 kGy radiation dose is due to excessive pore closure, as evident in FESEM images (Figure 3.13) and SAXS analysis (Figure 3.20). Permeability of control Psf membrane reduces by 23% on exposure to 1000 kGy of radiation dose (Psf-1000). At 1000 kGy, change in permeability of Psf-ND MMMs are 41.7, 31.4, 41.6, and 42.8% for 0.1-ND-1000, 0.5-ND-1000, 1-ND-1000 and 2-ND-1000 membranes, respectively, compared to their unirradiated counter parts. Trend of permeability with radiation dose indicates that 0.5-ND membrane is the most stable one in terms restoration of performance subsequent to radiation exposure.

Solute rejection attributes of Psf-ND MMMs remain unaffected with ND loading, with PEO (M_w=100 kDa) rejection in the range of 94.63% (for Psf membrane) to 99.11% (for 2% ND loaded membrane), as shown in Figure 3.22(b). This indicates an absence of defects in MMMs because of ND impregnation. Rejection rate increases from 94.63 to 96.5% with increasing loading of ND (from 0.1 to 1%). Further higher loading of ND (2-ND membrane) contributes to a higher rejection up to 99.11%, which is due to blockage of the pores. Membranes exposed to 100 kGy of radiation do not show much variation in terms of rejection rate which varies from 92 to 94%. For membranes irradiated up to 1000 kGy, solute rejection was found to be 82, 86.2, 80, 90.7 and 80% for Psf-1000, 0.1-ND-1000, 0.5-ND-1000, 1-ND-1000 and 2-ND-1000 membranes, respectively. Considering permeability and solute rejection capability, 0.5-1% ND impregnated membranes were found be the promising one.

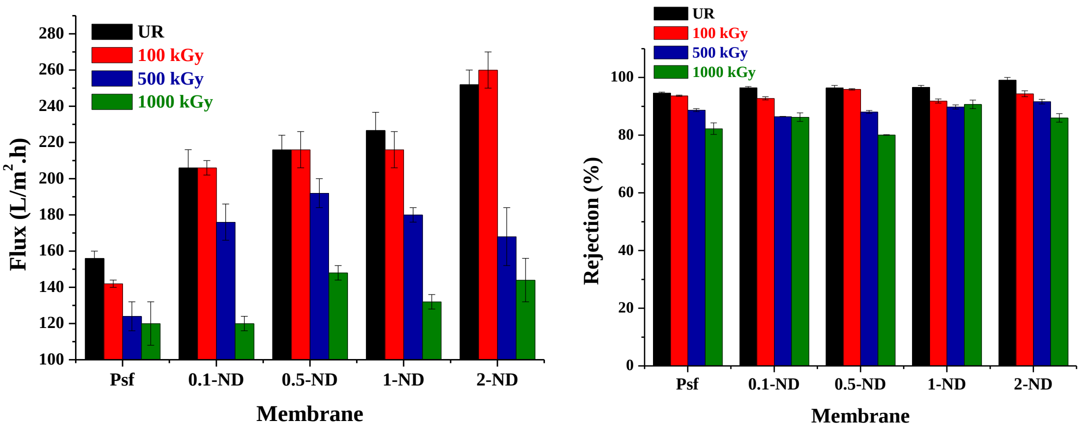

a

b

FIGURE 3.22: Performance of control Psf and Psf-ND MMMs with loading of ND and radiation dose: (a) Pure water permeability of membrane in terms of the flux of water through membranes , (b) Rejection of PEO solute by membranes.

3.2.12 Free radical scavenging capability of membrane

3.2.12.1 e^-_{aq} scavenging activity of membranes

Characteristic absorption spectrum of e^-_{aq} has a broad, structureless band with a maximum around 700 nm in aqueous system. In general, reactivity of e^-_{aq} is investigated by monitoring time absorption plot at 700 nm in presence of different concentration of solute. The ability of Psf-ND MMMs to scavenge e^-_{aq} was investigated and compared with control Psf membrane (Figure 3.23). Absorbance of e^-_{aq} at 700 nm decayed following first order kinetics with a rate of $2.0 \pm 0.5 \times 10^5\ s^{-1}$, which increased slightly in presence of control Psf membrane ($3.7 \pm 0.8 \times 10^5\ s^{-1}$). However, the rate of decay was found to increase with ND loading, with about 3 times enhancement for 2-ND MMMs ($1.2 \pm 0.4 \times 10^6 s^{-1}$), compared to that of control Psf. Scavenging of e_{aq}^- radical by ND (nanomaterial alone) was confirmed by monitoring their reaction with varying concentration of ND particles (Figure 3.7). Results showed that increasing ND concentration leads to rapid decay of hydrated electron, which confirms that ND is responsible for scavenging the radiolysed product (free radical) of water. Interestingly, this unique attribute of ND was translated to Psf-ND MMMs and therefore, the latter was found to exhibit enhanced radiation resistance properties, compared to control Psf membrane.

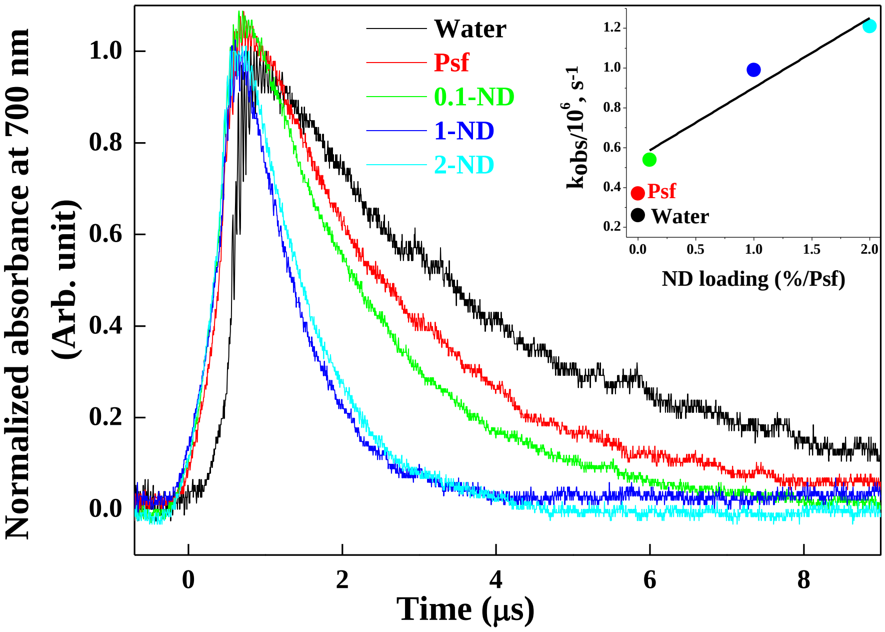

FIGURE 3.23: Absorption-time plot of hydrated electron of water at 700 nm in absence and presence of Psf-ND MMMs with different loading of ND in Psf matrix. Inset shows plot of observed rate as a function of Psf-ND MMMs with different loading of ND at pH 7.

3.2.12.2 Hydroxyl radical scavenging study

Maximum absorption peak of MG is at 615 nm. To understand the participation of Psf-ND MMMs in the reaction, oxidation of MG was performed by $OH^\bullet$ radical in presence of MMMs with different loading of ND particles. Figure 3.24 shows MG degradation in presence of Psf-ND MMMs. Control Psf membrane shows sudden reduction in degradation rate of MG. This is due to rapid reaction of $OH^\bullet$ radical with Psf chains, which causes the degradation of Psf membrane matrix by reduction in molecular weight of control Psf membrane under γ-radiation. Reaction of $OH^\bullet$ radical with organic substrate is non-specific as it reacts with three different processes, viz, hydrogen abstraction, $OH^{\bullet}$ radical addition, and one-electron oxidation. Hydrogen abstraction and radical addition process results in formation of carbon centered radicals which are known to react rapidly with oxygen and form peroxyl radical. Formation of peroxyl radical are deleterious as they initiate a chain reaction causing formation of more oxidants and thus results in rapid degradation of the polymer. On the other hand, functional group present in the surface of ND, interacts with $OH^{\bullet}$ and reduces them. Thus loading of ND in Psf membrane matrix gives extra radiation stability to the membrane. Hence reactivity of $OH^{\bullet}$ radical with Psf-ND MMMs is reduced.

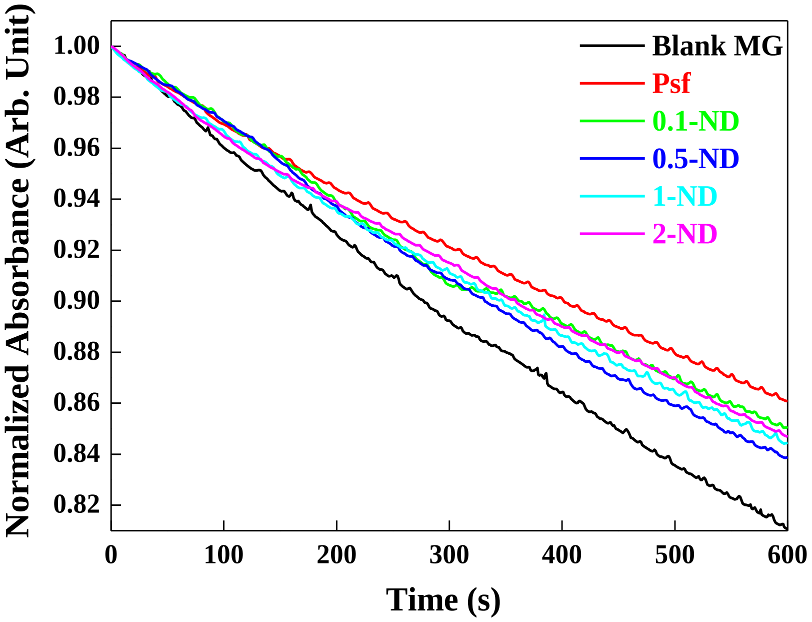

Figure 3.24: Hydroxyl radical reactivity with Psf-ND MMMs. Inhibition of absorbance of MG due to $OH^{\bullet}$ radical induced degradation in presence of different Psf membranes loaded with ND particles (0.1 - 2 wt%).

3.2.12.3 Peroxidase activity analysis

Peroxidase-like activity of ND particles was analyzed by using MG and hydrogen peroxide as substrate. Inset of Figure 3.9 shows time dependent peroxidase-like activity of ND particles. Peroxidase-like activity increases with increasing concentration of ND particles (Figure 3.9). As a result, for peroxidase activity of Psf-ND MMMs, initial velocity was found to increase with ND loading from 6.3×10^{-5} (blank MG) to 6.83×10^{-5} (control Psf membrane), and 7.8×10^{-5} $\mu M/s$ (0.5-ND membrane).

3.2.13 Life-span analysis of membrane using Monte Carlo simulation studies

An intermediate-level liquid radioactive waste (ILLRW) stream has a maximum activity of 1 Ci/L [248]. Radiation dose rate offered by this stream, as determined by Monte Carlo simulation, was found to be 115.4 Gy/h. From our studies, Psf membranes were found to be stable up to 100 kGy. Whereas, all Psf-ND MMMs were established to be stable up to 500 kGy, with 0.5-ND membrane being the most stable one. Dose rate obtained from Monte Carlo simulation studies was used to calculate the life-span of membranes in actual ILLRW environment. It was found that, to absorb a radiation dose of 500 kGy, Psf-ND MMMs would take 3 years and 8 months. Thus, 0.5-ND membrane can be operated for about 3 years and 8 months. On the other hand, Psf membrane, which is claimed to be stable up to 100 kGy, shall deteriorate in about 9 months. Thus, the Psf-ND MMMs with optimum loading of 0.5% ND is a radiation resistant membrane material, which can extend the application of polymeric membranes in radioactive domain.

3.3 Mathematical modeling of solute transport in Psf-ND MMMs

Mathematical modeling was applied to the Psf-ND MMMs for getting an insight into the transport mechanism of the membrane. Mathematical modelling of solute transport across Psf-ND MMMs was established based on the basic solute and solvent flux, by incorporation the pore theory using pore size distribution of membrane and size distribution of solute.

3.3.1 Experimental used for mathematical modeling

All the experimental values of flux and rejection were taken as mentioned in Figure 3.22.

Size distribution of solute (PEO, 100 kDa) was determined using DLS analysis, shown in Figure 3.25.

Membrane pore size distribution, for all the membranes, was determined with the help of BET analysis. Pore size distribution of unirradiated, 100 kGy irradiated,

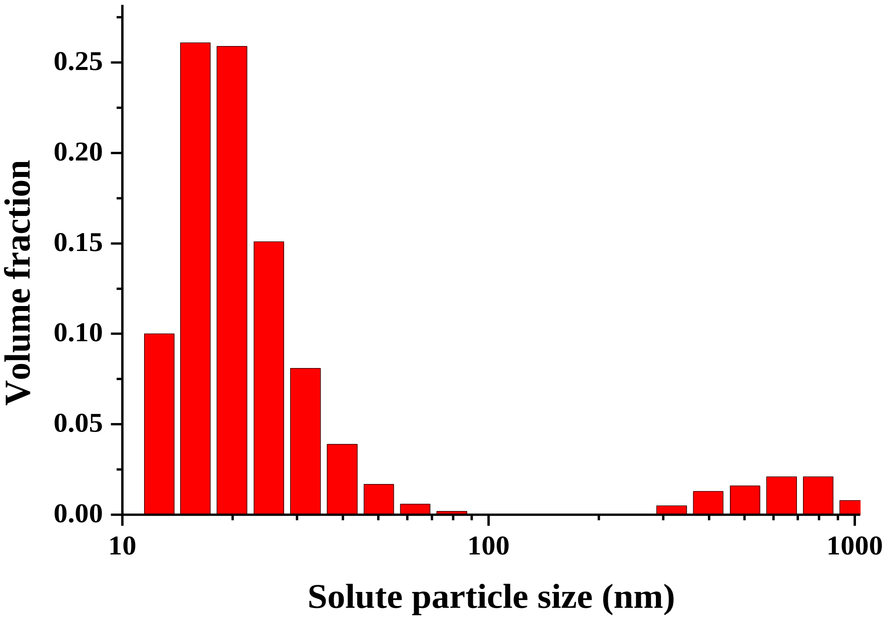

FIGURE 3.25: Particle size distribution of PEO solute (100 kDa).

500 kGy irradiated, and 1000 kGy irradiated Psf-ND membranes are shown in Appendix A (Figure A.1, A.2, A.3, and A.4, respectively).

3.3.2 Validation of mathematical model

Pore theory was incorporated into the model to obtain the value of reflection coefficient σ and solute permeability ω using Equation (2.19) and (2.20), respectively. To obtain the value of σ and ω, steric hindrance factors S_D and S_F were measured by Equation (2.22) and (2.23), respectively, are the function of q (ratio of solute radius to pore radius). The values of flux and rejection was then predicted by relation $J_s = C_p \times J_w$, using the Equation (2.27) and (2.28). The value of permeability (L_p) for all membranes were taken from the experimental value in Figure 3.22, transmembrane pressure (Δp) was maintained 1 bar during the experiments, and the feed concentration of PEO solute (C_m) was 200 ppm, solvent viscosity(μ) was taken 8.9×10^{-4} $Pa.s.$, and diffusivity constant (D) was taken 7×10^{-11} m^2/s. To measure the osmotic pressure, gas constant (R) was taken 8314 $J/kgmol.K$ and room temperature (T) was 298 K.

Table 3.2 shows that experimental flux and rejection offered by membranes, which are well in agreement with the predicted values of the modified mathematical model. Final modification of the mathematical model has been done by incorporating pore size distribution of membranes and size distribution of PEO solute.

The slight variation in the rejection rate is due to the factor of nanomaterial loading and γ-radiation dose, which causes the variation in membrane morphology. This variation is due to the alteration in free volume in the matrix caused by the interfacial defects between polymer and nanomaterial, as well as chain scissioning and cross-linking of Psf matrix as a result of γ-radiation. These small variations are not captured in BET analysis.

TABLE 3.2: Psf-ND MMM performance based on experiments and mathematical modeling. Flux (E/M) is the ratio of flux obtained from experiments to that obtained from mathematical modeling. Rejection (E/M) is the ratio of rejection obtained from experiments to that obtained from mathematical modeling.

Radiation dose	**Membranes**	**Flux (E/M)**	**Rejection (E/M)**
UR	**Psf**	1	1.12
	0.1-ND	1.05	1.02
	0.5-ND	1.05	1.21
	1-ND	1.05	1.07
	2-ND	1.05	1.19
100 kGy	**Psf-100**	1	1.08
	0.1-ND-100	1	1
	0.5-ND-100	1	1.04
	1-ND-100	1	1.04
	2-ND-100	1	1.03
500 kGy	**Psf-500**	1	0.98
	0.1-ND-500	1	0.97
	0.5-ND-500	1	0.94
	1-ND-500	1	0.95
	2-ND-500	1	1
1000 kGy	**Psf-1000**	1	0.91
	0.1-ND-1000	1	0.97
	0.5-ND-1000	1	0.84
	1-ND-1000	1	0.95
	2-ND-1000	1	1.05

To understand the effect of nanomaterial loading and γ-radiation dose, a correction factor is included to define the transport mechanism in Psf-ND MMM. Correction factor (K) proposed is shown in Equation (3.2).

$$K = \frac{R_E}{R_M} = a\ (L_{ND})^n\ +\ b\ (D_R)^m\ +\ c \tag{3.2}$$

Here, a, b, c, and n are the constants and the values of constants are found out to be: $a = 0.045$, $b = -0.165$, $c = 1.071$, $n = 0.1$, and $m = 0.005$. Final expression of K can be written as shown in Equation (3.3).

$$K = \frac{R_E}{R_M} = 0.045\ (L_{ND})^{0.1}\ -\ 0.165\ (D_R)^{0.005}\ +\ 1.071 \tag{3.3}$$

Correction factor (K) is defined as the ratio of solute rejection value obtained experimentally (R_E) to the rejection value obtained from mathematical modeling (R_M). Correction factor K is the function of ND loading in the membrane matrix (L_{ND}, in %) and the radiation dose to which membranes were exposed (D_R, in kGy).

Mathematical modelling of solute transport across Psf-ND MMMs was established based on the basic solute and solvent flux, by incorporation the pore theory using pore size distribution of membrane and size distribution of solute. For accuratelly predicting the transport mechanism of MMMs, correction factor was (K) incorporated.

3.4 Summary

The γ-radiation resistant Psf-ND MMMs were developed, with 0.5% loading of ND as the optimum. These membranes were found to be stable up to 500 kGy of radiation dose, without compromise in the performance, mechanical, and structural properties of the membrane. Radiation resistance property of MMMs was attributed to unique surface chemistry of ND, which protects the polymer chain from disintegration by scavenging secondary free radicals generated in γ-radiation induced radiolysis, as confirmed by free radical scavenging study. This is in addition to the most important feature of ND, that is hardness, which brings further stability to MMMs to act as a potential barrier against γ-radiation. Monte Carlo simulation studies coupled with experimental findings confirm that these MMMs with optimum loading of ND will have $\sim$ 5 times enhanced life span in an intermediate liquid radioactive effluent, compared to control Psf membranes. This improved stability of Psf-ND MMMs is a result of free radical scavenging ability of ND due to presence of functional groups. Scavenging ability of ND particles protects membrane matrix under γ-radiation from degradation, and enhances the lifetime. Underlying mechanism and kinetics of ND particle in scavenging highly reactive free radicals was understood, which is responsible for the stability of Psf-ND MMMs. Functional groups present with unsaturated carbon atoms further help the ND particles to scavenge hydroxyl radicals, and in turn protects the Psf-ND MMMs from damage by attack of highly reactive hydroxyl radicals. Peroxidase-like activity of ND particles helps in eliminating H_2O_2 and inhibits interaction with Psf membrane matrix. As a result, maximum initial velocity increased gradually with loading of ND from 6.3×10^{-5} μM/s (blank MG) to 7.8×10^{-5} μM/s (for 0.5-ND membranes). Thus, it is exciting to claim that these Psf-ND MMMs can have potential applications in nuclear fuel cycle, circumventing the practical limitations encountered in deployment of polymeric membranes in this domain.

Chapter 4

Polysulfone-carboxylated nanodiamond mixed-matrix membranes (Psf-CND MMMs): Effect of nanodiamond functionalization

4.1 Overview

Studies in Chapter 3 confirms the potential role of ND particles in protecting Psf membrane matrix from the deleterious effect of γ-radiation. The strong attraction forces between the particles result in agglomeration and thus non-homogeneous dispersion in the polymer host matrix. To address this issue, reinforcement of ND with additional functionalization is planned in the membrane matrix. Additional functionalization of ND particles is expected to result in homogeneous dispersion in Psf membrane matrix, as well as stronger interation with Psf matrix.

Carboxylated functionalized nanodiamond (CND) was chosen for the present study discussed in this chapter. CND was characterized by ATR-FTIR, XPS, and TEM to observe and analyse the functioanl groups over ND and in-turn dispersibility of particles. Effect of CND incorporation into Psf membrane matrix and stability in γ-radiation environment was measured by observing morphology (SEM); investigating surface properties (AFM, water contact angle analysis); examining membrane matrix internal structute by molecular weight studies (GPC); analysing oxidative degradation (DSC); evaluating mechanical properties (UTM); determining performance of MMMs (permeability and solute rejection capability); and hydroxyl radical scavenging activity. Interestingly, CNDs, owing to its inherent hardness along with uniform dispersion as well as the ability to capture more efficiently the secondary radiolysed products of water ($OH^{\bullet}$, $H^{\bullet}$, OH^{-}, $HO_2^{\bullet}$, e_{aq}^{-}, H_3O^{+}, H_2O_2, and H_2) [249, 250], has offered ∼ 10 times enhanced radiation resistant attributes to control Psf membranes, which is twice that of Psf-ND membranes at the same loading. Thus, a new class of radiation resistant membranes have emerged from this study.

4.2 Results and discussion

4.2.1 Characterization of nanodiamond particles

4.2.1.1 ATR-FTIR spectra of the nanodiamond and carboxylated nanodiamond particles

The surface functionalization of ND and CND nanoparticles was analyzed by FTIR, as shown in Figure 4.1. FTIR spectra shows a stronger peak of CND around 1653 cm^{-1} for C=O streching of carboxyl group, compared to that of ND. Also, new prominent peaks of CND around 1281 and 1398 cm^{-1} are related to H-O vibration of carboxyl group [251, 252]. Findings confirmed that additional carboxyl groups are present on the surface of CND.

4.2.1.2 XPS analysis of nanodiamond and carboxylated nanodiamond particles

Figure 4.2(a) shows XPS spectra for C-1s peak of ND particles. XPS spectra exhibits binding energy peaks for C-H bond at 283.8 eV, C-C bond at 285 eV, and C-O bond at 286.5 eV, while additional peak was observed in CND at 287.3 eV for C=O (Figure 4.2(b)) [253]. Figure 4.2(c) shows XPS spectra for O-1s peak of ND particles. XPS spectra exhibits binding energy peaks for C-O bond at 532.3 eV, -COO- bond at 531.2 eV, and oxide bond 530 eV, while for CND, additional oxide peak was observed at 530.5 eV (Figure 4.2(d)) [254]. XPS spectra for C-1s and O-1s peaks confirm signature of additional carboxyl groups on CND particles.

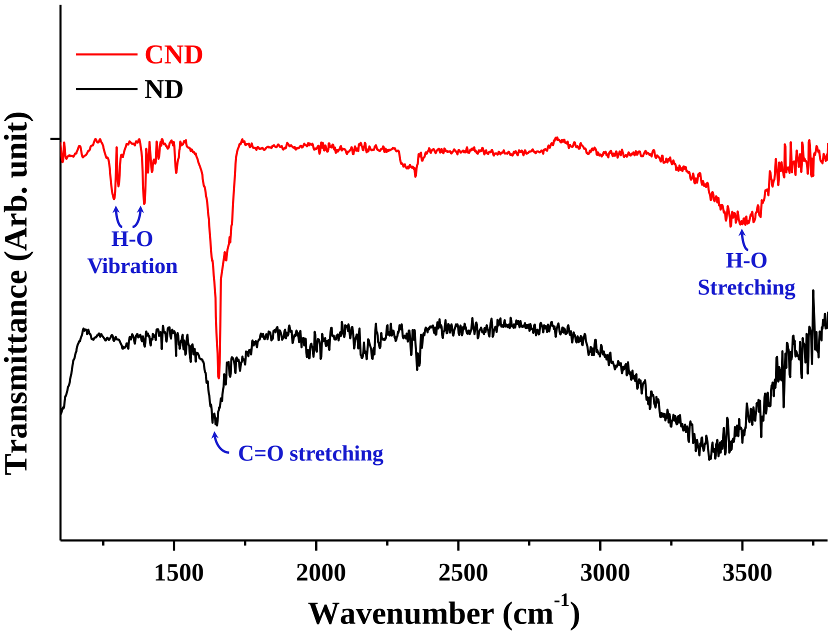

FIGURE 4.1: ATR-FTIR spectra of ND and CND particles.

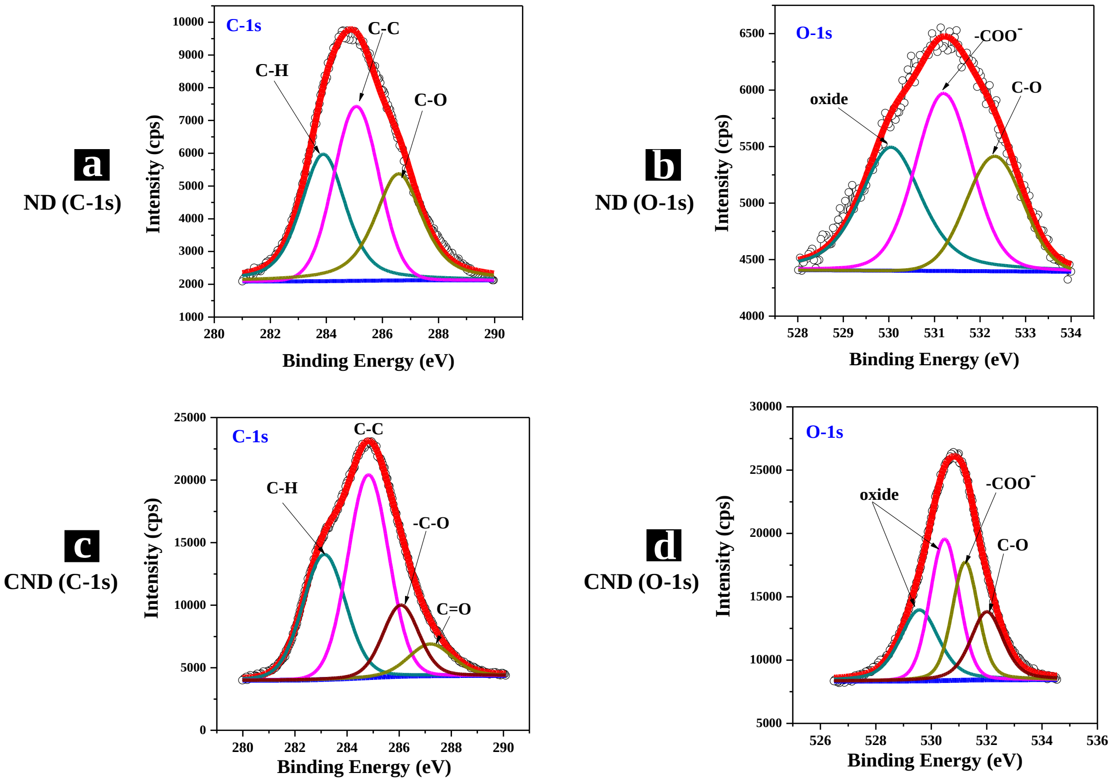

FIGURE 4.2: XPS spectra of ND; (a) C-1s peak & (b) O-1s peak, and CND; (c) C-1s peak & (d) O-1s peak.

4.2.1.3 TEM images of nanodiamond and carboxylated nanodiamond particles

Dispersion of ND and CND nanoparticles was observed in TEM images (Figure 4.3), which show that ND without functionalization has a tendency of agglomeration (Figure 4.3(a) & (b)) [255, 256]. On the other hand, CND particles are found homogeneously distributed without agglomeration (Figure 4.3(c) & (d)) [257]. Dispersion of CND is enhanced due to repulsive forces between CND particles owing to negative charge present over the surface carboxyl groups [242].

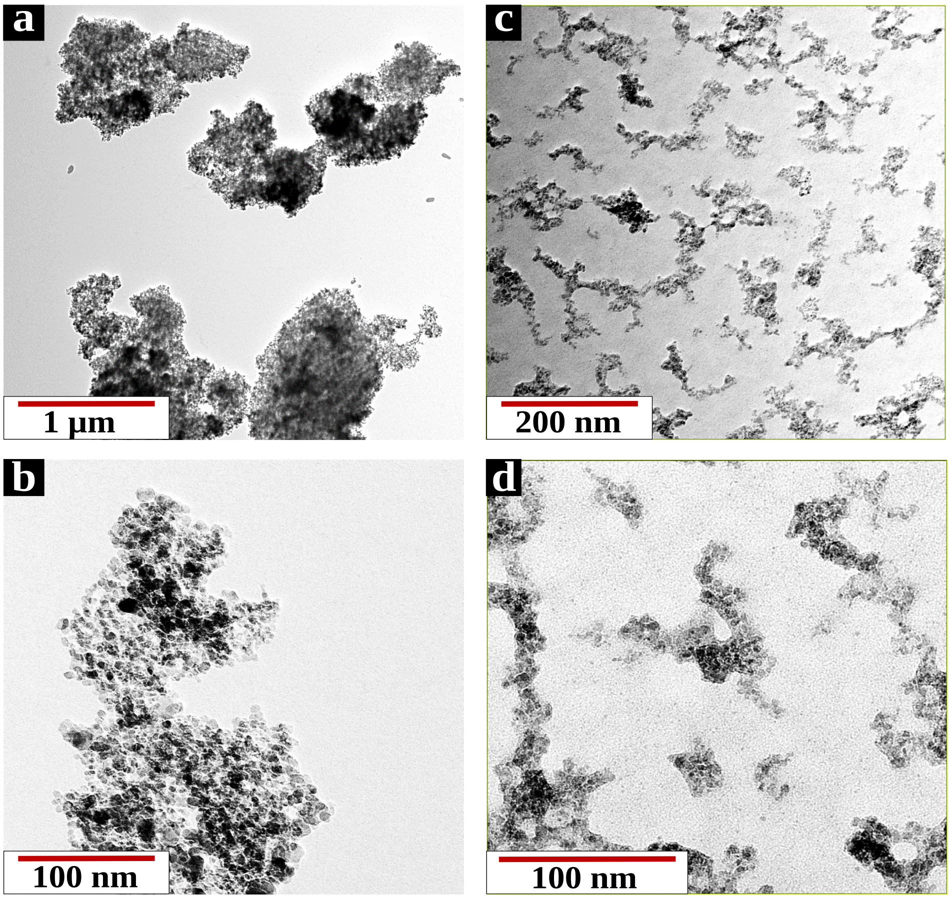

FIGURE 4.3: TEM images of ND, (a) & (b); and CND, (c) & (d).

4.2.2 Membrane morphology study using SEM

Morphology (surface and cross-section) of membranes can be observed in FE-SEM images shown in Figure 4.4. All membranes show dense top layer supported by porous finger-like structure, which is a characterstic property of ultrafiltration membranes synthesized by phase inversion technique. Top surface images of respective membranes can be observed in Figure 4.4(a) to (d), which reveals homogeneous dispersion of nanoparticles in Psf matrix for up to 0.5% loading of CND. A little agglomeration has been observed for 1% loading of CND. The fingering density of composite membranes has increased up to an addition of 0.5% CND, as clearly seen in FESEM images (Figure 4.4(e) to (h)), but no observable change in pore distribution (Figure 4.4(i) to (l)) of membrane is seen. This is because, kinetically favoured solvent-nonsolvent exchange occurred during phase inversion process, which is attributable to polar carboxyl groups present over CND. On the other hand, high concentration of CND (1%) leads to agglomeration of nanoparticles, accelerating the solvent-nonsolvent exchange, and thus leading to increased pore size of composite membranes (Figure 4.4(l)) [258, 259]. At 1000 kGy of radiation dose, pore size of membrane tends to increase due to simultaneous chain scissioning and cross-linking, which results in pore merger, pore splitting, and pore closure phenomena (Figure 4.4(q) to (t)) [69, 260]. It is important to note that membrane loaded with 0.5% of CND does not show much difference in morphology even after 1000 kGy of radiation dose, as homogeneous dispersion of ND particles ensures even distribution of carboxylic functional groups throughout Psf matrix. These carboxyl groups interact with and scavenge highly reactive secondary free radicals generated from γ-induced radiolysis of water and protect Psf matrix from deterioration. In terms of homogeneous dispersion in the Psf membrane matrix and its ability to protect the polymer in radiation environment, 0.5% loading of CND is found to be the optimum.

4.2.3 Molecular weight determination of membrane matrix using GPC

Polymers undergo simultaneous chain scissioning and cross-linking phenonmena under γ-radiation [261]. To observe changes in membrane network, weighted average molecular weight (M_w) of Psf-CND composite membranes were analysed using GPC, as shown in Figure 4.5. At a γ-radiation dose of 100 kGy, there is no significant change observed in control Psf matrix, while the M_w of Psf-CND composite membrane have slightly increasesd, as compared to their unirradiated counter parts. This increase in M_w illustrates predominant effect of cross-linking phenomena in Psf matrix [262].

At 500 kGy irradiation dose, chain scissioning of Psf starts dominating over cross-linking. Hence, M_w decreases by 25.6, 22.8, 22.1 and 14.3% for Psf-500, 0.1-CND-500, 0.5-CND-500 and 1-CND-500 membranes, respectively. At 1000 kGy

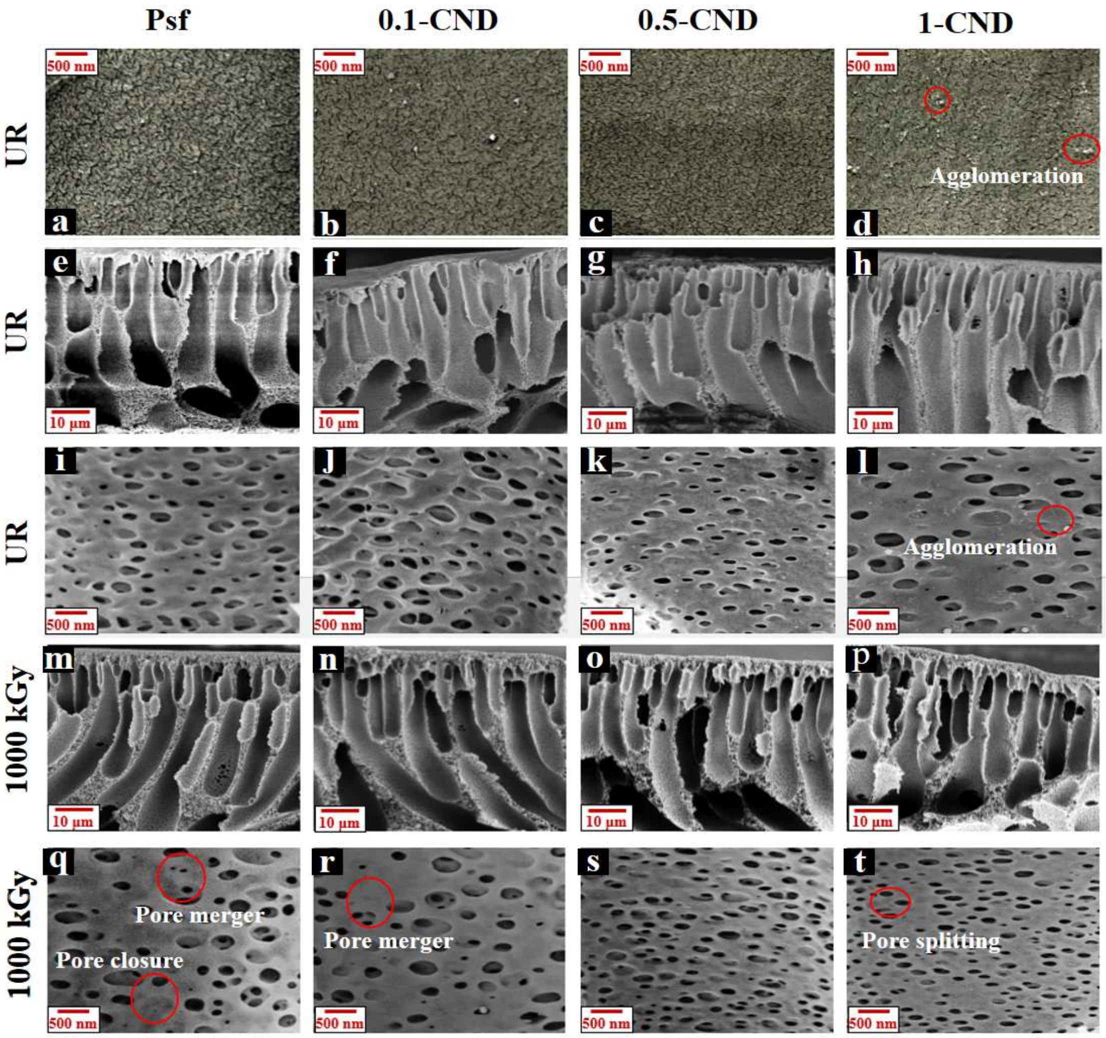

FIGURE 4.4: FESEM images of control Psf, 0.1-CND, 0.5-CND and 1-CND membranes; (a) to (d): top surface of unirradiated membranes, (e) to (h): cross-section of unirradiated membranes, (i) to (l): pore distribution of unirradiated membranes, (m) to (p) cross-section of 1000 kGy irradiated membranes, and (q) to (t): pore distribution of 1000 kGy irradiated membranes.

radiation dose, M_w reduced up to 44.7, 35, 24.5, and 9.2% for Psf-1000, 0.1-CND-1000, 0.5-CND-1000 and 1-CND-1000 membranes, respectively. The extent of change in M_w for Psf-CND composite membranes is very less even at 1000 kGy of radiation dose, compared to control Psf membrane. The 1-CND membrane shows least change in M_w and thus found least susceptible to chain scissioning.

4.2.4 Membrane surface topography measurement using AFM

Surface topography of membrane in terms of root mean square (RMS) roughness (Rq) was observed in AFM, as shown in Figure 4.6. Surface roughness value is ∼

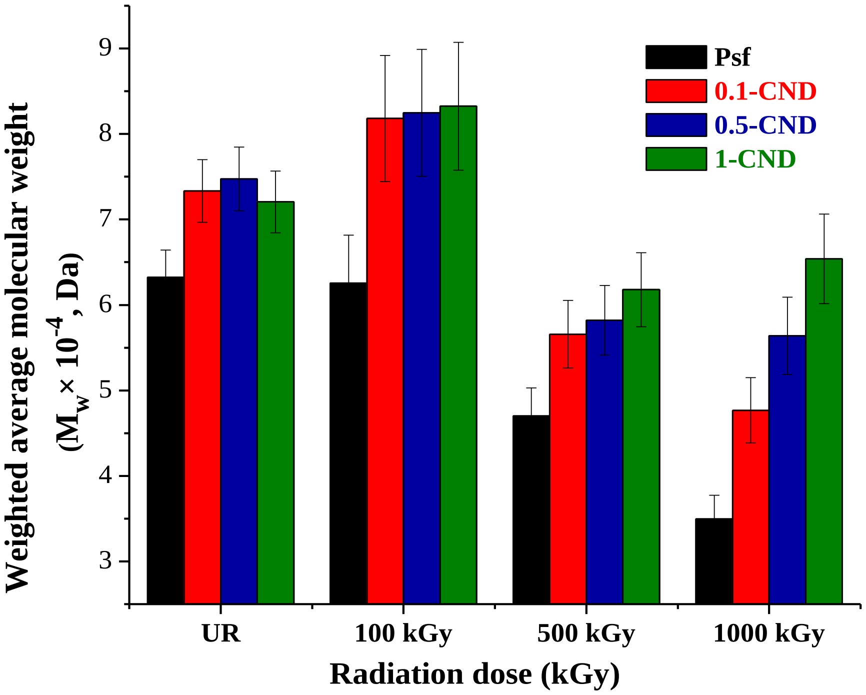

FIGURE 4.5: Variation in weighted average molecular weight (M_w) of the membranes with radiation dose.

2.02 nm for control Psf membrane. It increases with CND loading and roughness value is found to be ~ 3.14 nm for 1% loading of CND [263, 264]. This is due to interfacial defects created at the interface of CND and Psf host matrix. Also, surface roughness of membranes increases with radiation dose due to deterioration of membrane structure, which results in a rough topography. Control Psf membrane undergoes chain scissioning and cross-linking phenomena and surface roughness increases even at 100 kGy radiation dose. For Psf-CND composite membranes, change in roughness is not significant up to 100 kGy of radiation dose, while appreciable change was observed for radiation doses of 500 and 1000 kGy (as confirmed by GPC analysis, shown in Figure 4.5), which leads to increase in surface roughness values to 3.86 nm (1-CND-500) and 4.02 nm (1-CND-1000) [265]. Findings indicate that least deterioration of membrane structure has occurred at 1% loading, with only 28% increase in roughness value (1-CND-1000), as compared to control Psf membrane which shows 63.4% (Psf-1000) increase in roughness. AFM results demostrate that control Psf membrane surface starts deteriorating even at 100 kGy of radiation dose, while Psf-CND composite membranes show comparively stable surface even at 1000 kGy of radiation dose. This stability of membrane surface confirms that CND is effectively protecting the membrane matrix from γ-radiation.

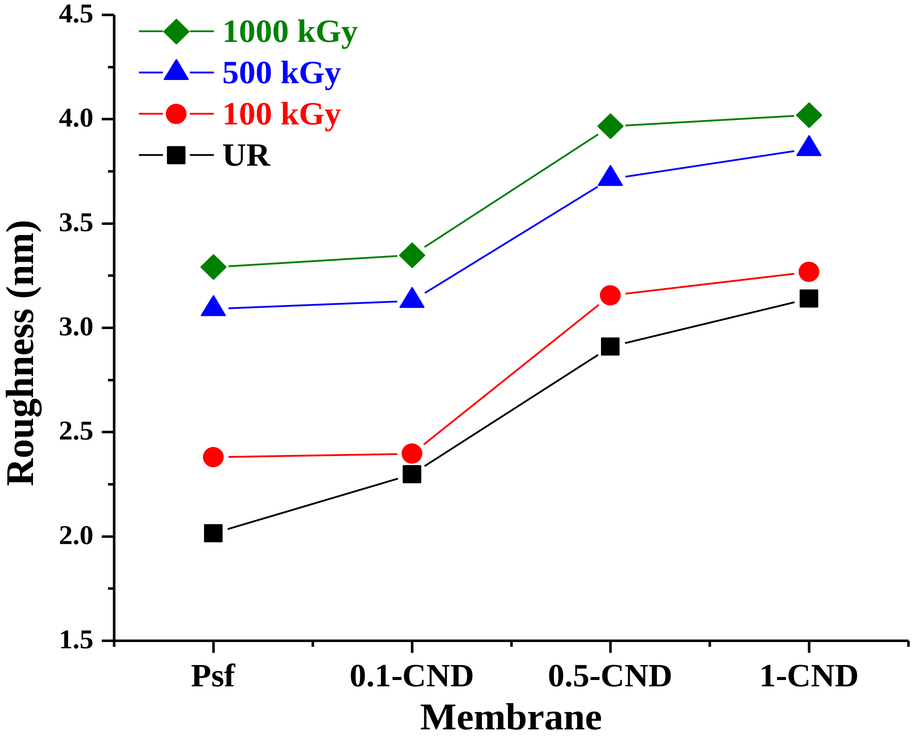

FIGURE 4.6: RMS surface roughness of membranes at different radiation dose.

4.2.5 Membrane surface water contact angle studies using DSA

Surface hydrophilicity/hydrophobicity was determined by studies of water contact angle on membrane surface, as shown in Figure 4.7. Water contact angle was found to be 80° for control Psf membrane, which decreases with loading of CND (up to 76.42° for 1-CND) because of enhanced surface hydrophilicity. Presence of carboxyl groups on the surface of CND (observed in FTIR and XPS spectra in Figure 4.1 and 4.2, respectively) increases hydrophilicity due to temporary hydrogen bonding between carboxyl group and water molecule [266]. At 100 kGy radiation dose, significant change of contact angle has been observed only in case of control Psf membrane due to enhancement of hydrophilicity, owing to increase in surface roughness (as reflected in surface roughness values, shown in Figure 4.6). At 500 kGy radiation dose, the value of contact angle decreases due to pore splitting, which increases the pore density and hence hydrophilicity. At 1000 kGy radiation dose, contact angle of membrane surface reaches up to 73.6°, 65.94°, 66.83°, and 68.92° for Psf-1000, 0.1-CND-1000, 0.5-CND-1000, and 1-CND-1000 membranes, respectively. Increased hydrophilicity of Psf-CND composite membranes with radiation dose results in increased permeability without much compromise in selectivity (discussed in section later). At the same time, pore size of control Psf membrane increases with radiation while pore density decreases due to pore closure (as observed in FESEM images, Figure 4.4). Hence, even with enhancement of hydrophilicity, both permeability and selectivity have decreased for control Psf membrane. These changes are in agreement with roughness measurements (Figure 4.6) of membrane surface, confirming contribution of the same in tuning the membrane surface hydrophilicity.

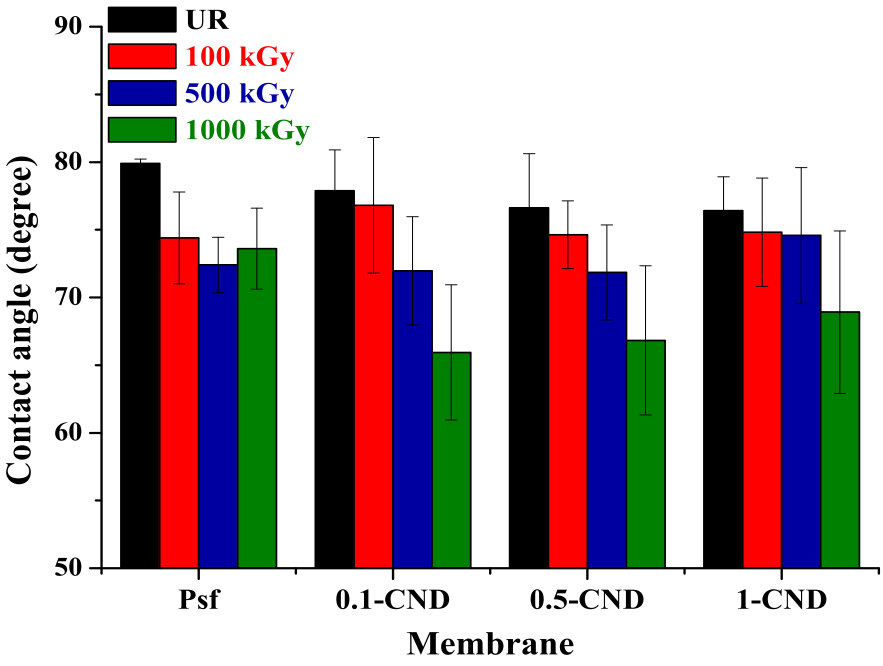

FIGURE 4.7: Membrane surface water contact angle at different radiation dose.

4.2.6 Membrane oxidative degradation analysis using DSC

Thermal oxidation decomposition of membranes was investigated by DSC studies. Figure 4.8(a) shows DSC thermograms of unirradiated membranes, where effect of CND loading can be observed on oxidation of membrane matrix. Thermogram clearly depicts three stages of oxidation degradation of Psf matrix, marked as stage 1, stage 2, and stage 3. These different stages of oxidation reveal short-to-long range ordered chain size of Psf present in the matrix. In stage 1, short-order chains (amorphous phase) of Psf are degrading by oxidation, while longest ordered chains (crystalline phase) of Psf are degrading in stage 3. Peak temperatures of different oxidation stages of membranes are shown in Table 4.1. Stage 1 oxidation of membrane occurs in temperature range from 430 to 435 $°C$ for unirradiated membranes. This reveals that amorphous phase of Psf matrix starts degrading at around 430 to 435 $°C$. Negligible intensity of heat flow for 0.1-CND-UR and 0.5-CND-UR indicates protection from degradation at low temperature due to loading of CND. Stage 2 oxidation of membranes is in the temperature range of 524 to 531 °C. Again lower intensity of heat flow for Psf-CND composite membrane at stage 2, as compared to stage 3, confirms lower extent of decomposition of membrane at low temperature. High peak intensity of Psf-CND composite membrane at stage 3 shows stability of membrane up to high temperature. On the other hand, higher intensity of heat flow for control Psf membrane at stage 2 reveals that a greater amount of Psf starts degrading at stage 2 only.

After radiation dose of 1000 kGy, stage 1 temperature is slightly reduced to the range of 423 to 425 °C. Further, due to the radiation induced damage of membrane matrix by chain scissioning and cross-linking, Psf chain ordering gets altered. This change in ordering of Psf chains can be clearly observed in Figure 4.8(b). Psf-1000 kGy is showing a broad peak from 534 °C to 556 °C, which indicates diverse sizes of Psf chains, due to chain scissioning and cross-linking phenomena (as observed in GPC analysis, shown in Figure 4.5). Moreover, reduced temperature of 0.1-CND-1000 and 1-CND-1000 membranes at stage 3 shows degradation of long chains of Psf. Stable peak at stage 3 and enhanced peak temperature at stage 2 of 0.5-CND-1000 membrane shows enhanced thermal oxidation stability of the membrane even up to 1000 kGy of radiation dose.

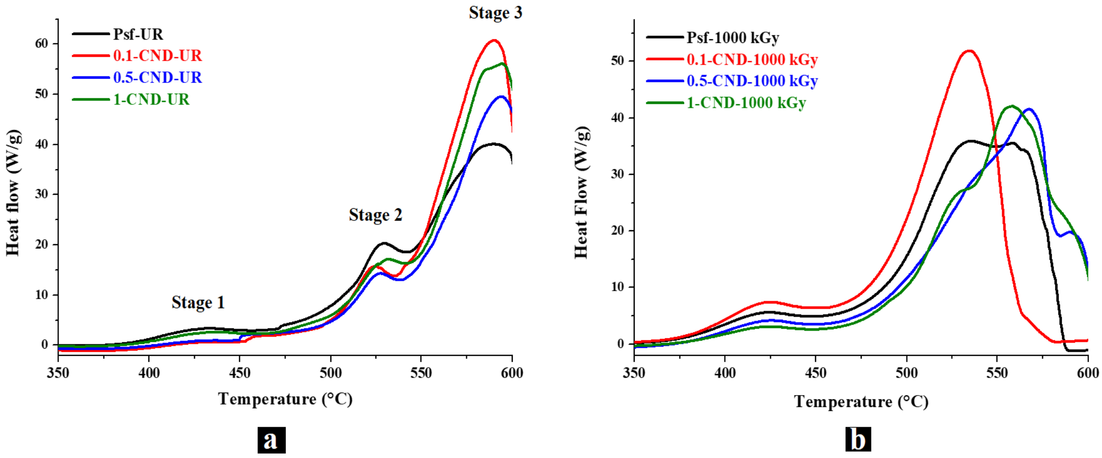

FIGURE 4.8: DSC thermograms of three-stage oxidative degradation of membranes: (a) unirradiated and (b) 1000 kGy irradiated membranes.

4.2.7 Membrane mechanical properties evaluation using UTM

UTM analysis (Figure 4.9(a)) shows that tensile strength (TS) of Psf membrane is 3.08 MPa, which decreases with loading of CND up to 2.37 MPa for 1-CND. Hard CND is expected to introduce rigidity between polymer chains as well as

TABLE 4.1: Three-stage oxidative degradation peak temperatures of unirradiated and 1000 kGy irradiated membranes.

Membrane	**Peak temperature ($^{\circ}C$)**					
	Unirradiated			**1000 kGy radiated**		
	Stage 1	**Stage 2**	**Stage 3**	**Stage 1**	**Stage 2**	**Stage 3**
Psf	430	529	589	424	534	556
0.1-CND	433	524	590	425	533	534
0.5-CND	433	527	593	425	567	590
1-CND	435	531	594	423	529	558

create interfacial defects at the interface of Psf and CND surface [267]. Percentage elongation at maximum force (%E) of unirradiated membranes does not get affected significantly on addition of CND (Figure 4.9(b)). No significant changes were observed in TS and %E up to 100 kGy radiation dose. Further irradiation of membranes leads to degradation in terms of chain scissioning of polymer chains and hence reduction in TS and %E [268]. At 1000 kGy irradiation, membranes shows 16.8, 17.6, 15.2, and 18.9% reduction in TS for Psf-1000, 0.1-CND-1000, 0.5-CND-1000, and 1-CND-1000 membranes, compared to their unirradiated counter parts. %E decreases with higher radiation dose, as chain scissioning of polymer reduces ductility of membranes. At 1000 kGy irradiation, membranes show reduction in %E up to 2.42, 5.14, 7.87, and 5.8 for Psf-1000, 0.1-CND-1000, 0.5-CND-1000, and 1-CND-1000 membranes, respectively. This confirms that Psf-CND composite membranes show better stability in terms of restored plasticity up to 1000 kGy radiation dose. The 0.5-CND composite membrane shows highest stability in mechanical properties amongst the compositions studied.

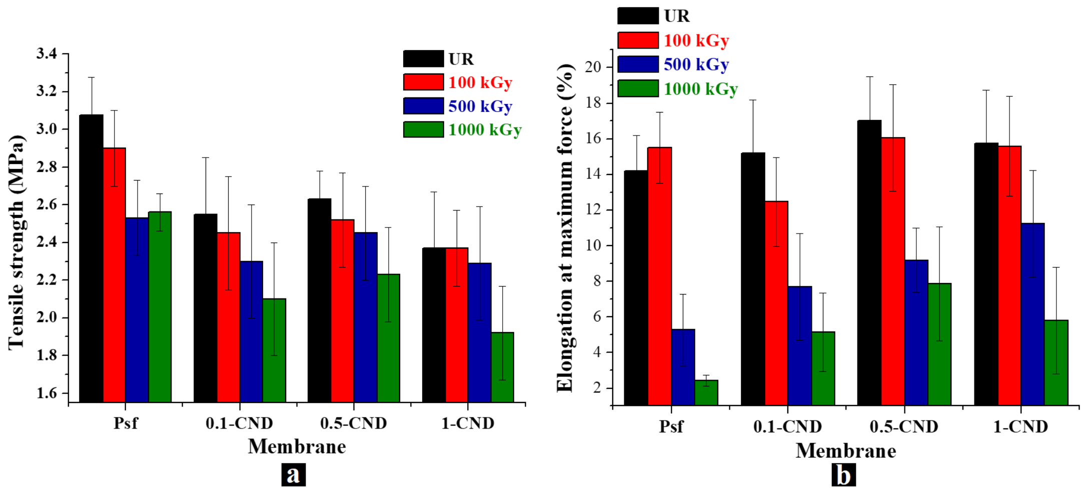

FIGURE 4.9: Mechanical properties of membranes at different radiation dose: (a) tensile strength and (b) percentage elongation at maximum force.

4.2.8 Membrane performance evaluation

Pure water permeability and solute rejection behaviour of membranes are not affected by addition of CND (Figure 4.10(a) and (b)). This confirms the observation made in FESEM images (Figure 4.4), that CND is not affecting the morphology of composite membrane. As membranes were exposed to γ-radiation, simultaneous chain scissioning and cross-linking events take place in polymer chains. As a result, internal structure of membrane gets altered leading to pore closure, pore merger, pore splitting, defect creation, etc. After 100 kGy of γ-radiation exposure, Psf-CND composite membranes did not show any observable changes in permeability, while slight reduction (9%) in permeability has been observed for control Psf membrane. This may be attributed to reduction of free volume (pore closure, reduction in pore density) within the polymer matrix. Further irradiation reduces permeability of control Psf membrane due to pore closure which reduces porosity, as observed in FESEM images in Figure 4.4. At the same time, permeability of Psf-CND composite membranes is unaffected by γ-radiation and also rejection is not much compromised. However, 1-CND membrane offers increased permeability with γ-radiation dose. Rise in permeability is attributed to increase in surface hyrophilicity (as observed in contact angle study, shown in Figure 4.7), as well as increased interfacial defects between agglomerated CND and Psf matrix. Considering permeability and solute rejection behavior, 0.1-0.5% CND impregnated membranes were found to be promising.

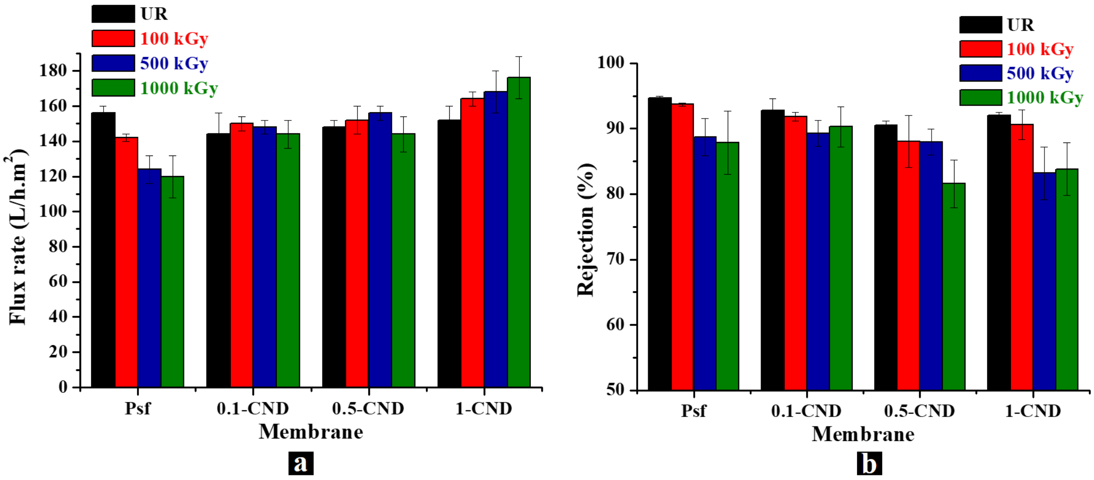

FIGURE 4.10: Membrane performance study at different radiation dose: (a) Pure water permeability and (b) Rejection of PEO solute.

4.2.9 Free radical scavenging capability of membrane

Maximum absorption peak of MG is at 615 nm. To understand the participation of Psf-CND MMMs in the reaction, oxidation of MG was performed by $OH^{\bullet}$ radical in presence of MMMs of varies loading of ND particles. Figure 4.11 shows MG degradation in presence of Psf-CND MMMs. Control Psf membrane shows sudden reduction in the degradation rate of MG. This is due to rapid reaction of $OH^{\bullet}$ radical with Psf chains, which causes degradation of Psf membrane matrix by reduction in molecular weight of control Psf membrane under γ-radiation. Reaction of $OH^{\bullet}$ radical with organic substrate is non-specific as it reacts with three different processes, viz, hydrogen abstraction, $OH^{\bullet}$ radical addition, and one-electron oxidation. Hydrogen abstraction and radical addition process results in formation of carbon centered radicals which are known to react rapidly with oxygen and form peroxyl radical. Formation of peroxyl radical are deleterious as they initiate a chain reaction causing formation of more oxidants and thus results in rapid degradation of the polymer. On the other hand, functional groups present on the surface of ND, interact with $OH^{\bullet}$ and reduce them. Thus loading of ND in Psf membrane matrix gives extra radiation stability to the membrane. Hence reactivity of $OH^{\bullet}$ radical with Psf-ND MMMs is reduced. However, additional functionalization of CND reduces the reactivity of $OH^{\bullet}$ radical with Psf even more to protect the Psf-CND MMMs.

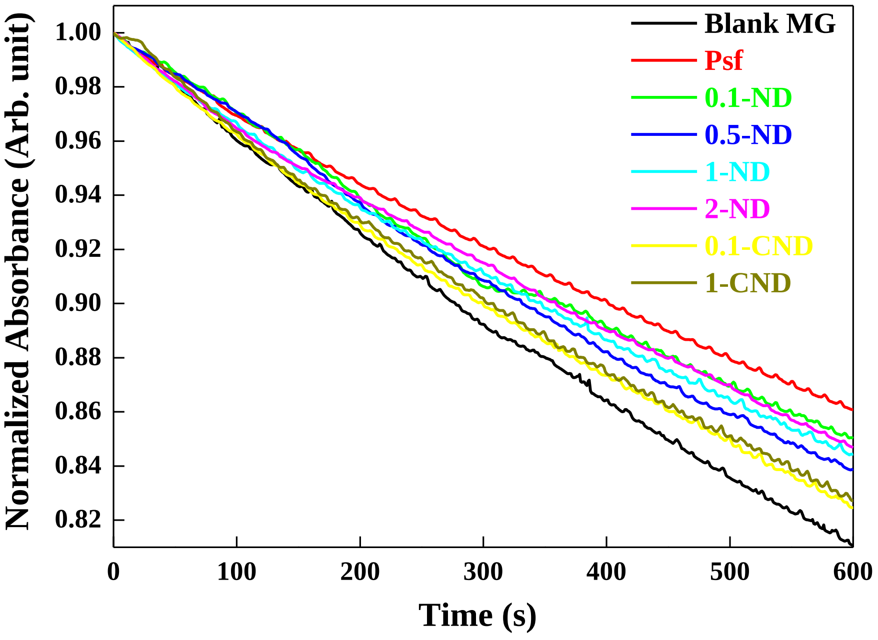

FIGURE 4.11: Hydroxyl radical reactivity with Psf-CND MMMs. The inhibition of absorbance of MG due to $OH^{\bullet}$ radical induced degradation in presence of different Psf membranes loaded with ND particles (0.1 2 wt%).

Table 4.2: Comparison of Psf-ND and Psf-CND MMMs.

Properties		**Psf-ND MMMs**	**Psf-CND MMMs**
Dispersion of ND		less	high
Functionalization of ND		less	high
$OH^{\bullet}$ scavenging		less	high
Optimum loading		0.5%	0.5%
Molecular weight stability		up to 500 kGy	up to 1000 kGy
Contact angle	with ND loading	Decreasing	∼ Constant
	with radiation dose	∼ Constant	Decreasing
Tensile strength	with ND loading	Decreasing	Decreasing
	with radiation dose	∼ Constant	Decreasing
%Elongation	with ND loading	Decreasing	Increasing
	with radiation dose	∼ Constant	Decreasing
Permeability	with ND loading	Increasing	Constant
	with radiation dose	Decreasing	Constant
Rejection	with ND loading	Constant	Constant
	with radiation dose	Decreasing	∼ Constant
Life-time compare to control Psf		∼ 5 times	∼ 10 times
Cost compare to Psf module		∼ 2 times	∼ 3 times

4.3 Summary

Radiation resistant Psf-CND MMMs were developed, with optimum loading of 0.5% of CND, which are found stable up to 1000 kGy of γ-radiation dose. Additional functionalization of carboxyl groups over the surface of ND impacts favorably in terms of its homogeneous dispersion in Psf membrane matrix, as well as restoring the morphology of base Psf membrane matrix. Moreover, CND was observed to protect the morphology of membrane matrix even up to 1000 kGy of radiation dose. Chain scissioning and cross-linking phenomena were prevented to a reasonable extent by CND, and hence less change in M_w was observed in Psf-CND composite membranes after irradiation, as compared to control Psf membrane. This protection of membrane matrix by CND restores the mechanical and thermal properties of membranes in γ-radiation environment. Roughness and hydrophilicity of the membrane surface were also enhanced due to addition of carboxyl functionalized ND. CND offers ∼ 2 times enhanced radiation resistance properties compared to that of ND (without additional functionalization), and ∼ 10 times to that of control Psf membranes. An emerging class of MMMs has been obtained with structural and thermal properties, as well as performance.

Chapter 5

Polysulfone-nanodiamond mixed-matrix membranes (Psf-ND MMMs): Effect of nanodiamond particle size

5.1 Overview

Studies show that the behaviour of small material is quite different from its bulk due to large number of surface atoms and less number of atoms inside the bulk [75]. Size of nanomaterial is one of the important parameters, as nature and extent of interaction of nanomatrial with polymer host matrix depends on fraction of atoms at the surface of nanoparticle. Also, the number of particles dispersed in membrane matrix at a particular loading will vary with size of nanomaterial. Atoms inside particles are highly coordinated with other atoms through strong bonding between them and have higher coordination number. On the other hand, atoms at the surface of particles are least saturated, that provides affinity to form bonds and interact with host matrix [77]. Attribute to variation in fraction of saturated and unsaturated atoms, due of varying size of nanoparticles, helps in exploiting different properties of nanomaterial, like mechanical, physio-chemical, and thermal properties. However, dispersion of nanomaterial in composite system, which is the most important factor in realizing desired objectives, is influenced by size [76, 78]. As the size of nanomaterial decreases, attraction forces between particles increase, which leads to aggregation of particles and loss of unique properties [79].

An extensive investigation on role of ND [269] as well as functionalised ND [243] was carried out in Chapter 3 and 4, respectively, and potential of ND was established in enhancing radiation resistance property of Psf membrane matrix. However, study involving effect of size of ND in the said application domain has been lacking. Thus, in this Chapter, a study has been undertaken, wherein different sizes (10, 250, and 500 nm) of ND have been used to synthesize Psf-ND MMMs and evaluate their γ-radiation resistant behavior by exploiting unique radiation-resistant property of ND, which can have prospective applications in treatment of radioactive effluent. Effect of size of nanomaterial has been clearly observed when MMMs are put into γ-radiation environment, which in turn plays a significant role in deciding the radiation resistance behaviour of MMMs. Psf-ND MMMs were synthesized using phase inversion technique by incorporating different loading of ND_{10} (10 nm), ND_{250} (250 nm), and ND_{500} (500 nm) into Psf membrane matrix. MMMs were characterized by surface and cross-section SEM images (morphology), AFM (topography), membrane surface water contact angle (hydrophilicity/hydrophobicity), GPC (molecular weight), UTM (mechanical properties), and performance (pure water permeability and solute (PEO, 100 kDa) rejection mesurements). The study provides an insight into the effect of ND particle size in altering the radiation resistance behaviour of MMMs.

5.2 Results and discussion

5.2.1 Characterization of nanodiamond particles

5.2.1.1 TEM images of ND particles

TEM images of different size ND particles are shown in Figure 5.1. TEM images of ND_{10} in Figure 5.1(a) & (b) show aggregated particles of ND_{10}. This aggregation of particles is due to small size (10 nm) of ND involving high attraction forces between particles [161]. Inset of Figure 5.1(b) shows SAED pattern of ND_{10} particles, wherein the ring pattern depicts polycrystalline behaviour of ND particles. Figure 5.1(c) & (d) show TEM images of ND_{250} particles and Figure 5.1(e) & (f) show TEM images of ND_{500} particles. ND_{250} and ND_{500} particles are well dispersed, because attraction forces reduce as size of nanoparticle increases. Inset of Figure 5.1(d) & (f) shows SAED pattern of ND_{250} and ND_{500} particles, which clearly depicts crystalline behavior of ND_{250} and ND_{500} particles due to higher priodicity of atoms in larger size of particles.

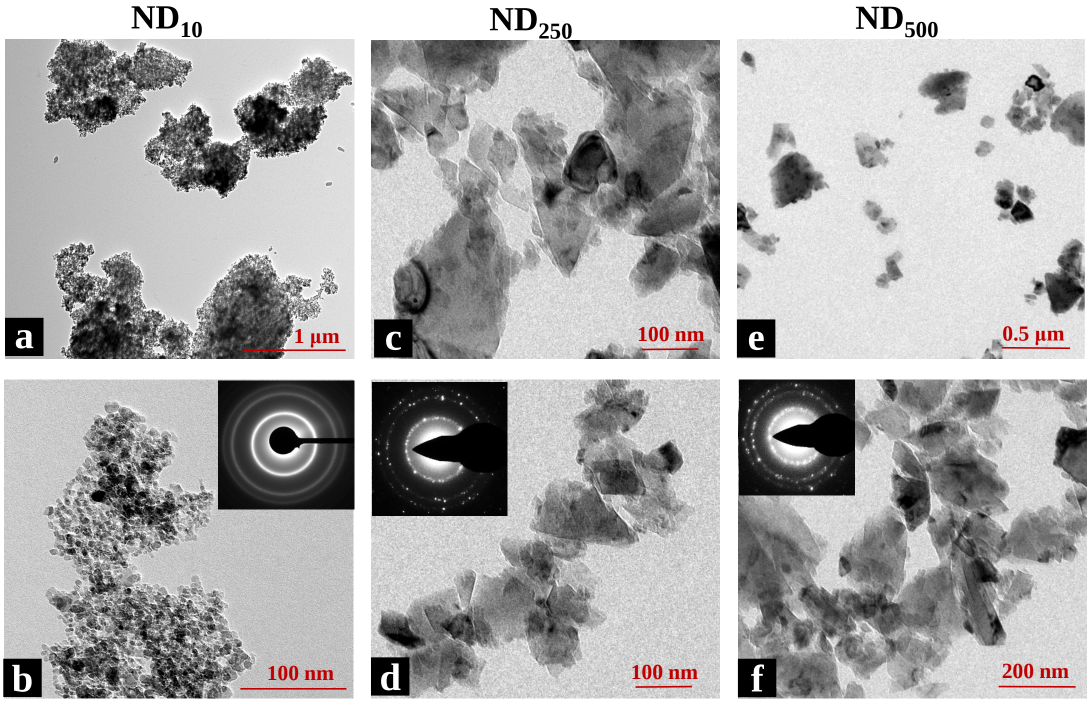

FIGURE 5.1: TEM images of ND particles: (a) & (b) ND_{10}, (c) & (d) ND_{250}, and (e) & (f) ND_{500}. Inset in image (b), (d), and (f) shows SAED pattern of ND_{10}, ND_{250}, and ND_{500} particle, respectively.

5.2.1.2 XPS spectra of ND particles

The XPS spectra for C-1s peak of ND particles is shown in Fig. 5.2. XPS spectra show presence of saturated (in bulk, C-C bond peak at $\sim$ 285 eV) and unsaturated (at surface, C=O and C-H bonds peak at $\sim$ 286.6 and 283.8 eV, respectively) carbon atoms. The ratio of unsaturated to saturated carbon atoms is 1.69, 0.45, and 0.38 for ND_{10}, ND_{250}, and ND_{500} particles, respectively. This confirms the postulate that, as size of particle decreases, number of atoms at the surface increases and so is the extent of functional groups. This variation of surface fuctionalization of ND due to the size variation ultimately affects the extent and nature of interaction between ND particles and Psf matrix (as discussed in section later).

5.2.1.3 ATR-FTIR spectra of ND particles

The FTIR spectra of ND particles in Fig. 5.3 show major absorption bands for OH stretching vibration at about 3410 cm^{-1} , C=O stretching of carboxyl groups at around 1647 cm^{-1}, and C-O stretching vibration of -COOH groups at around 1100 cm^{-1}. This confirms presence of carboxyl and hydroxyl functional groups on the surface of ND particles. These peaks are more prominent for ND_{10} particles due to the higher degree of functionalization.

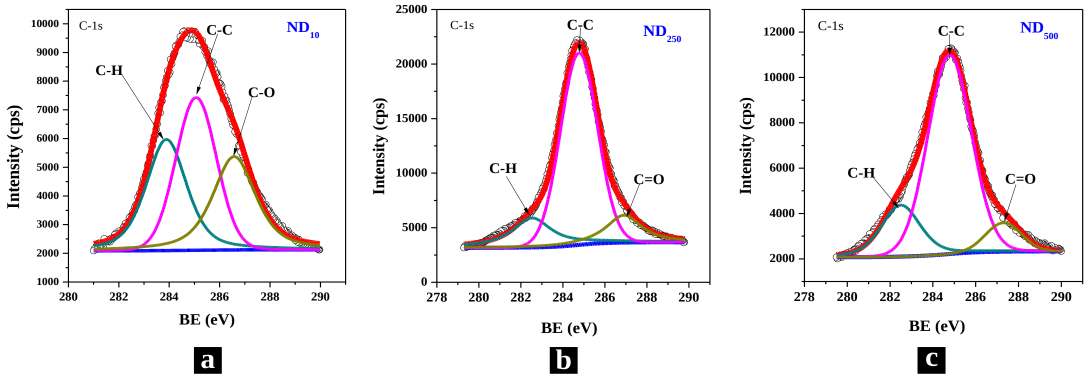

FIGURE 5.2: XPS spectra of ND particles: (a) ND_{10}, (b) ND_{250}, and (c) ND_{500}.

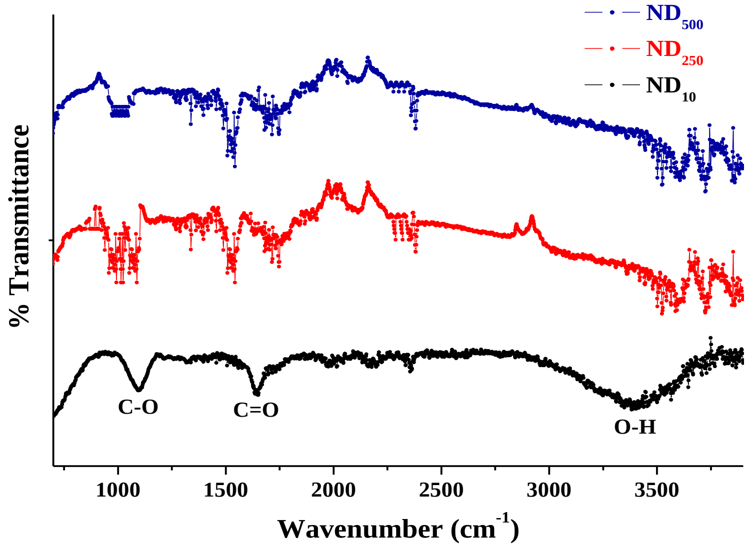

FIGURE 5.3: ATR-FTIR spectra of ND particles.

5.2.1.4 Size distribution of ND particles

Fig. 5.4(a) shows the particle size distribution of ND_{10} obtained from SAXS, wherein the average diameter of ND particles was determined to be ∼ 5 nm. On the other hand, the aggregate size of ND_{10} was found to be ∼ 62 nm from DLS studies, as shown in Fig. 5.4(b). ND_{250} and ND_{500} particles were not studied by SAXS technique, due to its limitation on study of large sized particles [270]. Fig. 5.4(c) and (d) shows the size distribution of ND_{250} and ND_{500} particles, respectively, determined by DLS technique. The average hydrodynamic diameter for ND_{250} and ND_{500} particles was found to be ∼ 345 and ∼ 632 nm, respectively.

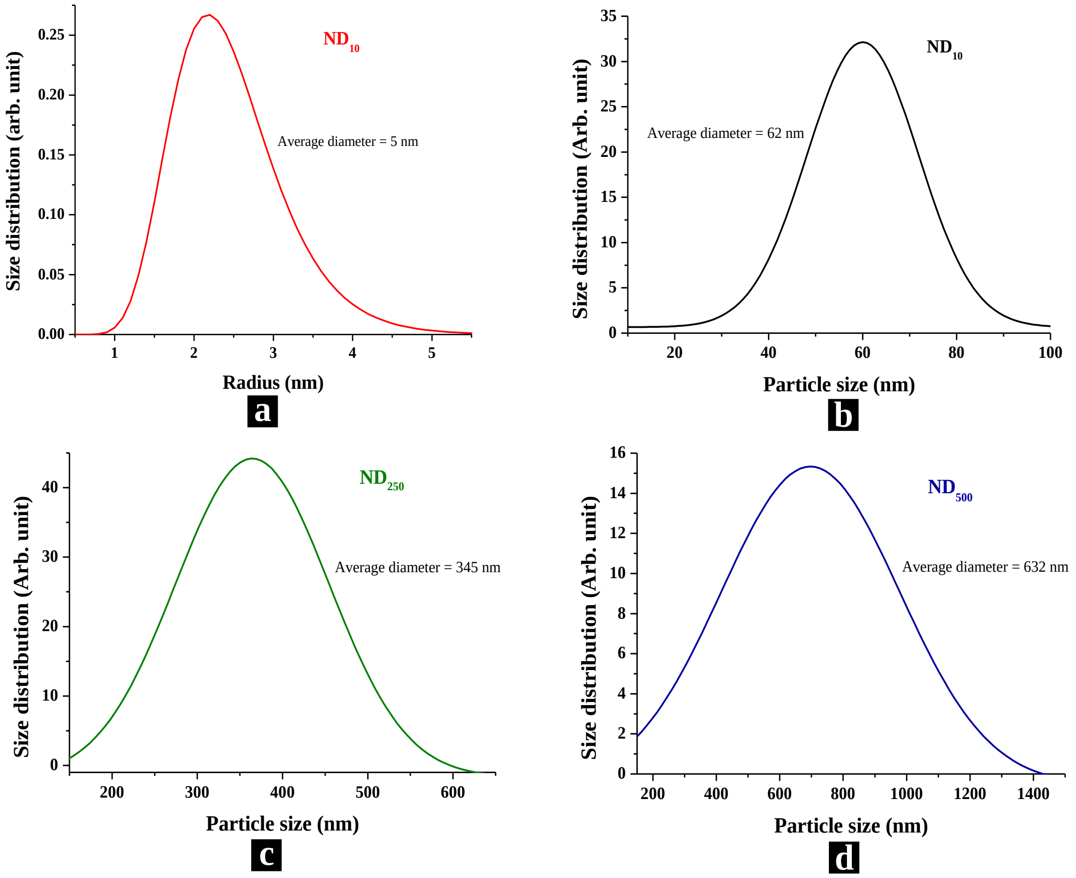

Figure 5.4: Size distribution of ND particles: (a) Size distribution of ND_{10} particles using SAXS technique, (b) Size distribution of ND_{10} agglomerated particles in solvent obtained by DLS analysis, (c) Size distribution of ND_{250} particles using DLS, and (d) Size distribution of ND_{500} particles by DLS.

5.2.2 Membrane mophology studies using SEM

Morphology of membranes was observed in FESEM, as shown in Figure 5.5, for different size and loading of ND in Psf membrane matrix. The top surface morphology of control Psf and Psf-ND MMMs are clearly distinguishable by presence of different size of ND particles, as shown in Figure 5.5(a) to (e). The 0.5-ND_{10} MMMs (Figure 5.5(b)) shows homogeneous dispersion of ND, while 1-ND_{10} MMM (Figure 5.5(c)) shows agglomeration. The 1-ND_{250} (Figure 5.5(d)) and 1-ND_{500} (Figure 5.5(e)) MMMs shows homogeneous distribution of NDs with a relatively rough texture of surface, due to larger sized particles. Results suggest that ND_{10}, due to its smaller size (10 nm), leads to higher attraction forces between ND particles (as observed in TEM images of ND_{10} particles, Figure 5.1) and thus tends to agglomarate at higher loading (1% ND). On the other hand, the distribution is homogeneous for ND_{250} and ND_{500} in MMMs, owing to relatively reduced surface energy and lesser extent of aggregation.

Pore distribution (Figure 5.5(f) to (j)) of membranes is affected due to presence of NDs during synthesis of MMMs. As observed in FESEM images (Figure 5.5(f) to (h)), structure and morphology of MMMs are not affected by presence of ND_{10} because of its smaller size, showing almost similar pore size distribution and pore density to that of control Psf membranes. The ND_{250} (Figure 5.5(i)) MMM shows increased pore size, due to larger size of ND_{250} (250 nm), causing non-homogeneous demixing of solvent and non-solvent during phase inversion process [271]. The ND_{500} (Figure 5.5(j)) MMM shows increased pore size compared to control Psf membrane, but smaller than the pore sizes observed in ND_{250} impregnated MMMs, due to relatively lower dispersion in terms of number of ND_{500} in the matrix as compared to ND_{250}.

After 1000 kGy of irradiation, pore size and pore density of membranes were altered because of pore closure, pore splitting, and pore merger events as an outcome of chain scissioning and cross-linking phenomena induced by γ-irradiation. Pore density decreases for Psf-1000 membrane (Figure 5.5(k)) due to pore closure. Pore size is increasing, while pore density is decreasing, for ND_{10} MMMs (Figure 5.5(l) and (m)) due to pore merger and pore closure phenomena. On the other hand, pore size and pore density both are decreasing for ND_{250} MMMs (Figure 5.5(n)) due to predominant pore splitting phenomena. Different from the above findings, pore size is increasing, while pore density is decreasing for ND_{500} MMMs (Figure 5.5(o)) due to predominant pore merger phenomena. Interestingly, ND_{10} MMMs show relatively less changes in pore size and pore density with radiation. SEM imges suggest that presence of ND_{10} has not affected the structure and morphology of Psf matrix due to its smaller size, and protects it in radiation environment.

5.2.3 Molecular weight determination of membrane matrix using GPC

Weighted average molecular weight (M_w) of MMMs are shown in Figure 5.6. Change in M_w of ND_{10} MMMs with radiation is shown in Figure 5.6(a). With exposure to γ-radiation, no significant change in M_w was observed till a dose of 100 kGy. At 500 kGy, M_w decreased for Psf-500 (25.6%), 0.1-ND_{10}-500 (2.6%) and 2-ND_{10}-500 (16.7%) membranes, due to chain-scissioning phenomenon of Psf [70, 244]. On the other hand, negligible rise was observed for 0.5-ND_{10}-500 (1.4%) and 1-ND_{10}-500 (8.1%), due to the predominant cross-linking of Psf chains. Psf-ND_{10} MMMs shows very less variation in M_w for a ND_{10} loading up to 1% and radiation dose up to 500 kGy. Results reveal the least effect of Psf chain scissioning

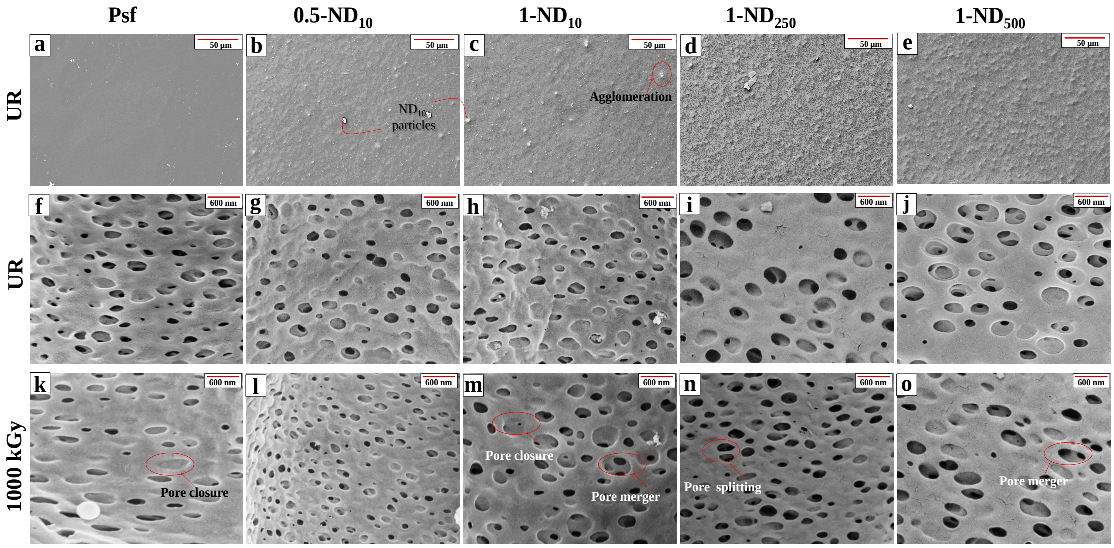

FIGURE 5.5: FESEM images of membranes: (a) to (e): Top surface of unirradiated membranes, (a) Psf, (b) 0.5-ND_{10}, (c) 1-ND_{10}, (d) 1-ND_{250}, and (e) 1-ND_{500}; (f) to (j): Pore distribution of unirradiated membranes, (f) Psf, (g) 0.5-ND_{10}, (h) 1-ND_{10}, (i) 1-ND_{250}, and (j) 1-ND_{500}; (k) to (o): Pore distribution of the membranes exposed to 1000 kGy radiation dose, (f) Psf, (g) 0.5-ND_{10}, (h) 1-ND_{10}, (i) 1-ND_{250}, and (j) 1-ND_{500}.

in presence of ND_{10}. The ND_{250} MMMs (Figure 5.6(b)) did not show change in M_w till 100 kGy radiation, while chain scissioning starts dominating after 500 kGy of radiation dose. The ND_{500} MMMs (Figure 5.6(c)) have shown enhancement in M_w at 100 kGy radiation dose, indicating dominant cross-linking at 100 kGy. As a result, membrane flux is decreasing, while rejection has not been affected (discussed in section later). The ND_{500} MMMs have not shown any significant changes in M_w up to 500 kGy radiation dose, while, 1 and 2% loading of ND_{500} have shown stability up to 1000 kGy radiation dose. This clearly confirms that higher loading of ND_{500} protects membranes from γ-radiation. Findings indicate that larger size and higher loading of ND_{500} protects the molecular weight of Psf membrane matrix up to γ-radiation dose of 1000 kGy, while deterioration was observed for control Psf membrane even beyond 100 kGy of radiation dose.

5.2.4 Membrane surface topography studies using AFM

Figure 5.7 shows RMS roughness values of membrane surface. Increase in loading of ND_{10} leads to increase in RMS roughness value and leads to 3.20 nm for 2% loading. The higher the size of ND, roughness of membrane surface is more, as observed in roughness values of ND_{250} (4.01 nm for 2% loading) and ND_{500} (5.03 nm for 2% loading impregnated) membranes. This is because the larger sized

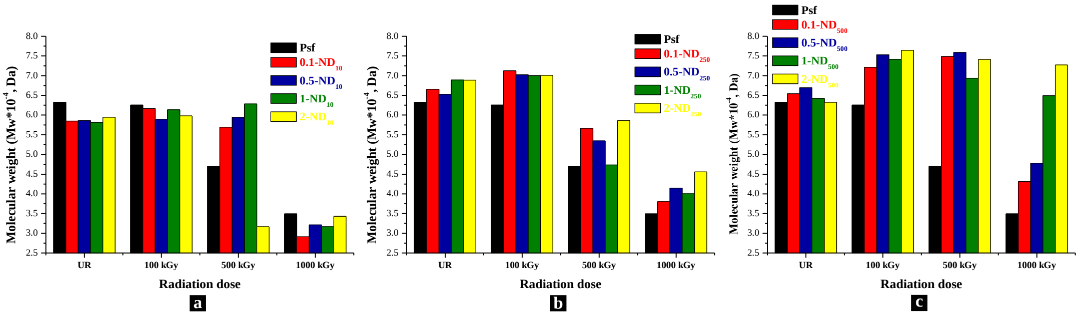

FIGURE 5.6: Weighted average molecular weight (M_w) of membranes with variation of ND size, loading, and radiation dose, obtained from gel permeation chromatography analysis: (a) MMM with ND_{10} particles, (b) MMM with ND_{250} particles, (c) MMM with ND_{500} particles.

nanoparticles tends to create more interfacial defects and results in a rough topography [272]. This interfacial free volume (between ND and Psf matrix) and surface roughness are responsible in enhancement of permeability of membrane (discussed in section later). In radiation environment, the surfaces of ND_{10} and ND_{250} MMMs are deteriorating due to chain scissioning and cross-linking of Psf chain (as observed in Figure 5.6), while pore size is increasing (as shown in Figure 5.5). This leads to increase in the surface roughness of MMMs at high radiation dose. The ND_{500} MMMs have not shown much difference with radiation dose, which is because of the large size of ND that compensates for the surface deterioration.

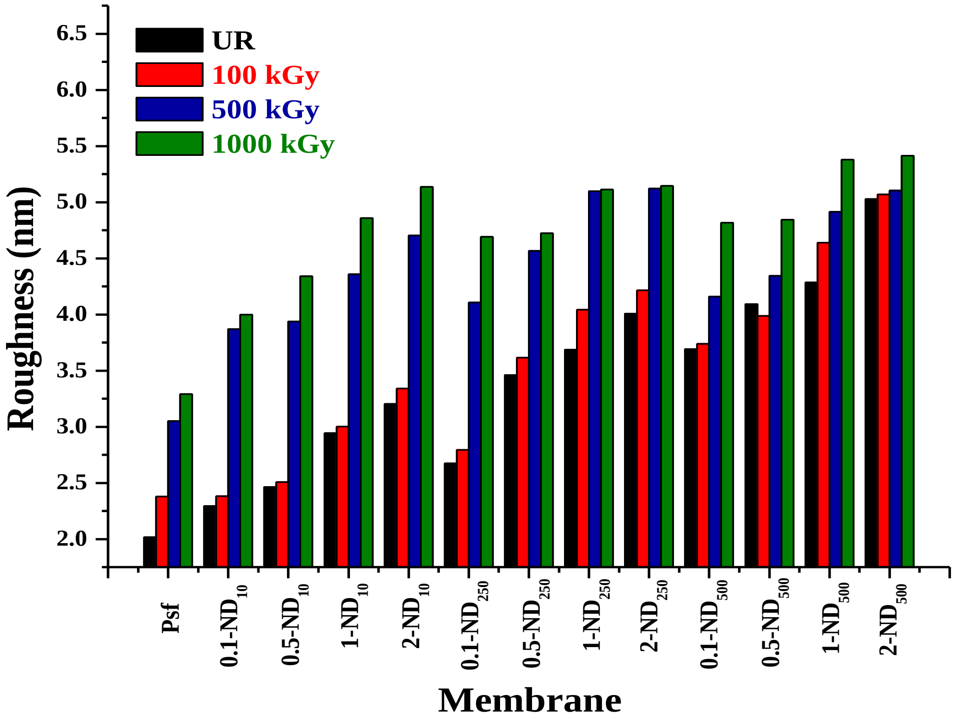

FIGURE 5.7: Variation of RMS roughness value of membranes embedded with different size of ND at different loadings and radiation dose.

5.2.5 Membrane surface water contact angle studies using DSA

Water contact angle of membrane surface was determined to analyse hydrophilicity/hydrophobocity of membranes embedded with different size and loading of ND in Psf host matrix, as shown in Figure 5.8. Water contact angle is 80° for control Psf membrane. On addition of ND_{10}, contact angle is decreasing due to presence functional groups (hydroxyl and carboxyl) over the surface of ND particles that leads to enhancement in hydrophilicity [155]. This enhancement in hydrophilicity results in enhanced permeability (discussed in section later). Contact angle decreases up to 70.2° for 0.5-ND_{10}, and then it starts increasing at higher loading due to aggregation of particles, reducing extent and availability of surface functional groups of ND on membrane surface. Addition of ND_{250} results in decrease of contact angle as compared to control Psf membrane. However, the decrease is less as compared to membranes embedded with ND_{10}. This can be explained by size of ND, wherein the size of ND_{250} is higher that provided lesser surface carbons and in turn lesser functional groups, and thus less enhancement in hydrophilicity [273]. Interestingly, contact angle of membranes embedded with ND_{250} shows a gradual decline with ND_{250} loading up to 2%, which corroborates with the proposition of homogeneous dispersion of particles. The extent of surface hydroxyl groups of ND_{500} is even less as compared to ND_{10} particles, but the interfacial defects created between ND_{500} particles and Psf matrix are more pronounced owing to larger size of ND_{500} particles. These interfacial defects result in high wettability of membrane surface and hydrophilicity. Hence decline in the contact angle is higher for membranes embedded with ND_{500} particles. Contact angle is decreasing for all membranes with increasing radiation dose. This is because the surface roughness is increasing with radiation dose (as observed in AFM results shown in Figure 5.7), as a result of disintegration in polymer network that leads to enhanced wettability of membrane surface.

5.2.6 Mechanical properties evaluation of the membrane using UTM

Mechanical properties of membranes embedded with different size and loading of ND were investigated through UTM analysis at various radiation doses. Figure 5.9(a) and (b) shows variation in tensile strength (TS) and percentage elongation at maximum force (%E) of membranes, respectively. Control Psf membrane exhibits

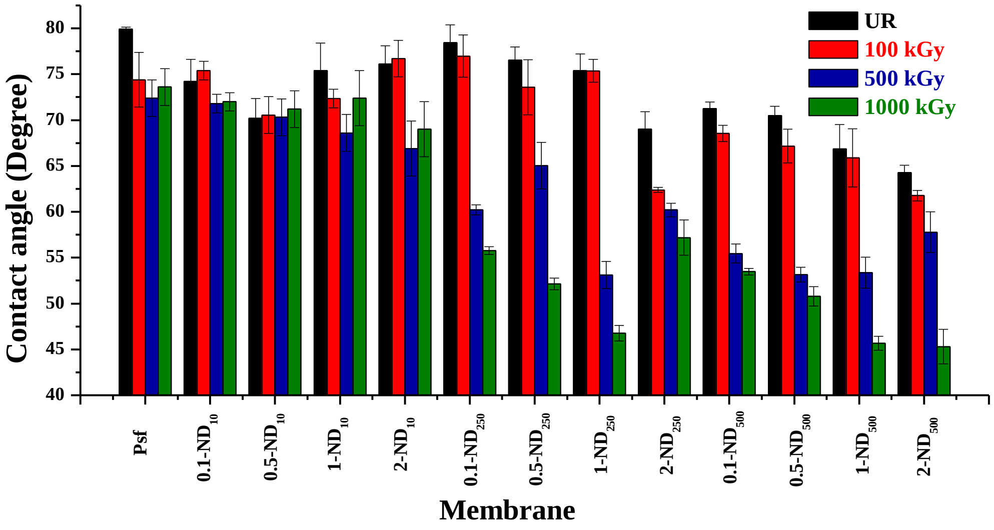

FIGURE 5.8: Membrane surface water contact angle: variation due to impregnation of different size and loading of ND in membrane matrix and radiation dose.

a TS ∼ 3.07 MPa and %E ∼ 14.2. On impregnation of ND_{10}, TS and %E are slightly decreasing up to 0.5% loading. This is because hardness of ND introduced rigidity in Psf matrix and reduced ductility. At higher loading, TS and %E again increased due to aggregation of particles that reduces interaction between ND and Psf matrix [246]. Impregnation of ND_{250} and ND_{500} creates interfacial defects in Psf matrix due to their larger sizes, which reduces the strength of membrane matrix and in turn TS and %E [13]. At radiation dose of 100 kGy, TS and %E are not much affected for ND_{10} and ND_{250} membranes, while ND_{500} membranes are showing drastic reduction in %E due to cross-linking as observed in GPC analysis (Figure 5.6(c)). Further irradiation of membranes leads to predominant chain scissioning of Psf network [42] (as observed in GPC studies, Figure 5.6), that results in decreased plasticity of membrane matrix, and thus deterioration in mechanical properties (TS and %E). Membranes embedded with ND_{10} at a loading of 0.5% shows negligible variation in TS up to 1000 kGy and least change in %E up to 500 kGy of radiation dose. Mechanical stability of membranes is realized with ND_{10} particles at an optimum loading of 0.5%.

5.2.7 Membrane performance evaluation

Performance of membranes was analyzed based on pure water permeability and PEO (100 kDa) solute rejection studies, as shown in Figure 5.10(a) and (b), respectively. Pure water permeability of membrane is increasing up to 61.5% at 2%

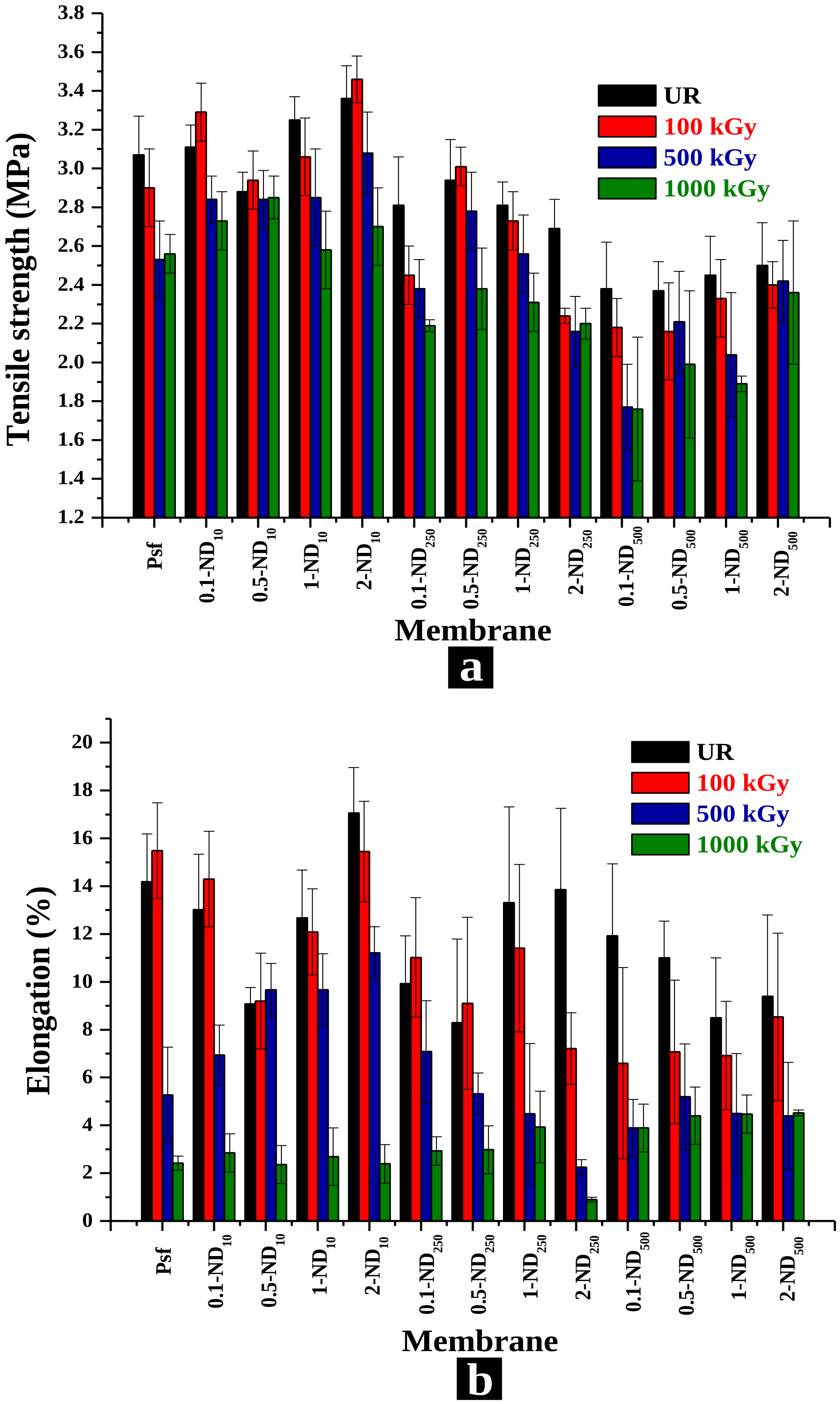

FIGURE 5.9: Mechanical properties of membranes embedded with different size and loading of ND in the membrane matrix and radiation dose: (a) Tensile strength and (b) Percentage elongation at maximum force.

loading of ND_{10} particles, as compared to control Psf membrane. This enhancement in permeability results from enhanced hydrophilicity (as observed in water contact angle analysis, Figure 5.8) due to the presence of substantial amount of hydroxyl and carboxyl groups at the surface of ND_{10} [7, 243]. Consequentially, solute rejection increases with impregnation of ND_{10} (from 94.63% for control Psf membrane to 99.11% for 2% loading of ND_{10}). Impregnation of ND_{250} leads to blockage of pores due to its larger size, which results in reduced permeability as compared to that of ND_{10} embedded membranes, but increased permeability compared to control Psf membrane (up to 35.9% for 1% loading of ND_{250}) due to the presence of hydroxyl and carboxyl groups. On the other hand, large size of ND_{250} creates defects in the matrix and reduces solute rejection (up to 85.9% for 1% loading) [274]. Impregnation of ND_{500} leads to enhanced permeability as compared to control Psf membrane and membranes embedded with ND_{250}. This is because the particle density is less for ND_{500} (as compared to ND_{250}), leading to reduction in extent of pore blockage. At the same time, large sized particles create significant interfacial defects in membrane matrix while reducing solute rejection ability of the membranes (reduced rejection in the range of 89-92%). Up to 100 kGy of radiation dose, there is not much change observed except the permeability of 0.1-ND_{250} and 1-ND_{500} membranes.

In radiation environment, porosity of membranes decreases due to pore closure and splitting phenomena (as observed in FESEM images, shown in Figure 5.5(k) and (l)), leading to decrease in permeability in radiation environment [275]. For membranes embedded with ND_{10} and ND_{500} particles, pore merger phenomena is dominant, which leads to increase in pore size but reduction in pore density, resulting in decreased solute rejection. The ND_{250} embedded membranes contribute to predominant pore splitting phenomenon, which leads to decreased permeability, while solute rejection is not affected significantly.

At 500 kGy, both permeability and solute rejection ability (88.7%) of control Psf membranes get reduced, while ND_{10} embedded membranes still offers rejection up to 91.6% (at 1% loading) without much compromise in permeability. On the other hand, in case of ND_{250} and ND_{500} embedded membranes, rejection is reduced within the range of 84.8 - 88.6% and 83.4 - 87%, respectively. Also, permeability of ND_{250} and ND_{500} embedded membranes drastically decreased on exposure to 500 kGy of radiation dose. Considering the results of permeability and solute rejection behaviour, performance of the membrane is found to be optimum for 1% loading of ND_{10} particles.

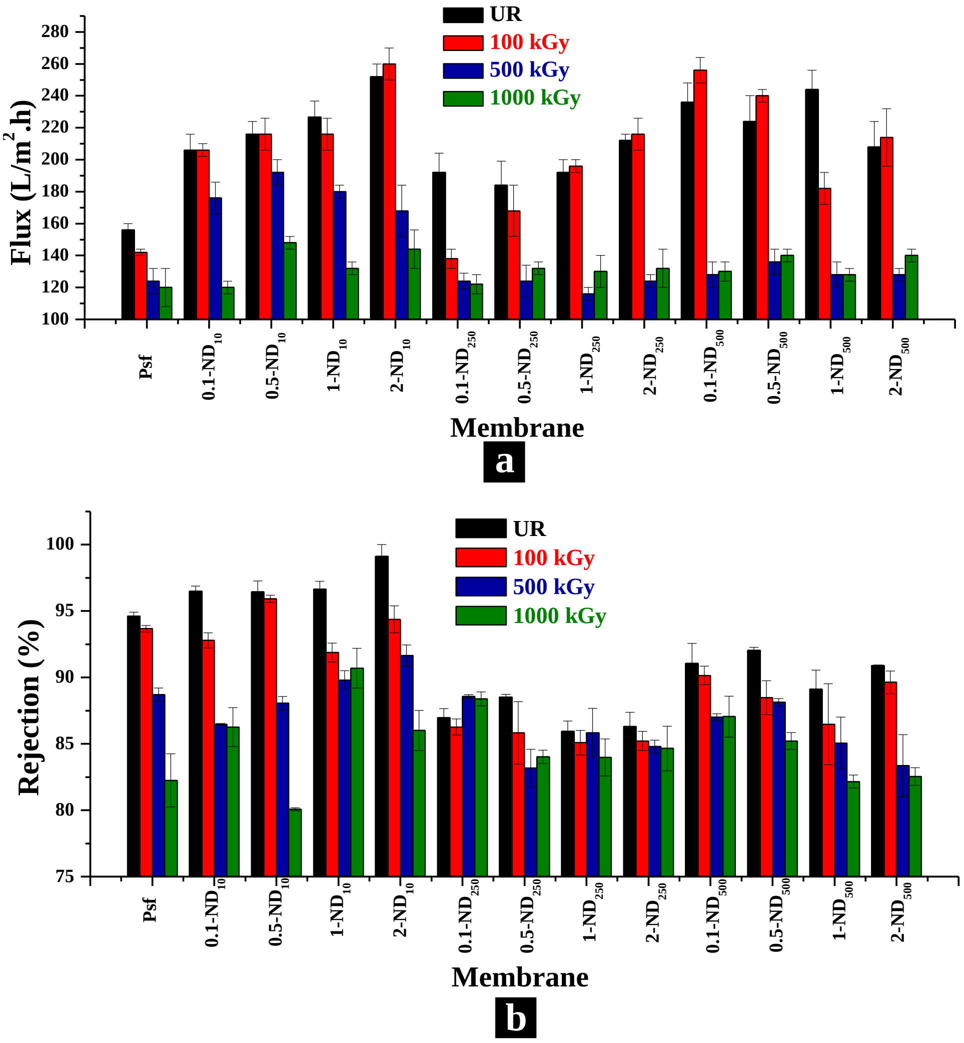

FIGURE 5.10: Membrane performance study for different size of ND loading in membrane matrix and radiation dose: (a) Pure water permeability and (b) Rejection of PEO solute.

5.3 Summary

Psf membranes embedded with ND particles were synthesized using three different size of nanodiamonds, i.e., ND_{10} (10 nm), ND_{250} (250 nm), and ND_{500} (500 nm), each up to a loading 2%. The prepared membranes were irradiated for different dose of γ-radiation and characterized to observe the effect of ND size and loading on the membrane morphology, structure, performance, mechanical stability, and radiation resistant properties. Significant findings are as follows:

1. High concentration of ND_{10} tends to agglomerate, while ND_{250} and ND_{500} offer homogeneous dispersion even at high concentration, owing to significant attraction forces between small-sized ND_{10} particles.

2. Small size of ND_{10} contributes to higher amount of surface carbon atoms, which offers large number of functional groups and stronger interaction with Psf matrix. On the other hand, ND_{250} and ND_{500} contains relatively less surface carbon atoms and hydroxyl and carboxyl groups that offer relatively lesser interaction with Psf matrix.

3. The ND_{10} particles are neither affecting the Psf membrane morphology, nor creating any observable defects in the host matrix. The larger size of the ND_{250} and ND_{500} particles are creating interfacial defects in Psf matrix.

4. Hydrophilicity of membranes embedded with ND_{10} particles increases due to presence of hydroxyl groups up to an optimum loading of 0.5-1%. This enhances performance of membrane and offers stability in radiation environment up to 500 kGy of radiation dose.

5. Mechanical properties of membranes are restored up to 500 kGy of radiation dose at an optimum 0.5% loading of ND_{10} particles, without creating defects in matrix.

6. MMM with 10 nm sized ND particles at a loading of 0.5% is found to be the optimum composition, which offers $\sim$ 5 times enhanced radiation stability compared to that of control Psf membrane.

Chapter 6

Polysulfone-ceria mixed-matrix membranes (Psf-ceria MMMs)

6.1 Overview

In this Chapter, properties of cerium oxide (ceria) nanoparticles are explored to develop radiation resistant membrane. Since ceria is a distinguished nanomaterial with an unique ability of interconversion of oxidation states between Ce^{4+} and Ce^{3+}, it was used as a scavenger of free radicals induced by radiolysis of water under γ-radiation. This feature of ceria offers extraordinary stability to the Psf membrane matrix against the γ-radiation.

In this Chapter, ceria nanoparticles were fabricated by gel combustion route using citric acid ($C_6H_8O_7.H_2O$) as a fuel and cerium nitrate ($Ce(NO_3)_3.6H_2O$) as an oxidizer. Febricated ceria nanoparticles were characterized by TEM, XRD, XPS, UV-Vis, ATR-FTIR, SEM, Raman spectroscopy, SAXS, EDS spectra, hydroxyl radical scavenging activity, and peroxidase-like activity. Psf-ceria MMMs were prepared by phase inversion technique with different loadings of ceria, viz., 0, 0.1, 0.5, 1 and 2%. Membranes were then irradiated with 100, 500 and 1000 kGy of γ-radiation dose, and characterized. Psf-ceria MMMs were characterized using SEM, to observe the effect of ceria loading and γ-radiation dose on membrane morphology; AFM, to analyse surface topography of membranes at different loading of ceria at different γ-radiation dose; membrane surface water contact angle, to determine surface hydrophilicity/hydrophobicity; ATR-FTIR, to obtain variation in functional groups in presence of ceria; GPC, to see the effect of γ-radiation on molecular weight of the membrane; XRD, to confirm the presence of ceria nanoparticles in Psf-ceria MMMs; PALS, to determine alteration in free volume of Psf membrane matrix due to ceria loading and γ-radiation dose; SAXS, to evaluate structural parameter in presence of ceria at different radiation dose; UTM, to analyse the effect of radiation on mechanical properties of membrane by incorporating ceria at different γ-radiation dose; flux and solute rejection attributes, to observe the performance of Psf-ceria membranes in radiation environment; free radical scavenging and peroxidase activity, to analyse the mechanism of protection of MMMs in γ-radiation environment through scavenging of highly reactive species by ceria present in the membrane matrix.

6.2 Results and discussions

6.2.1 Characterization of ceria nanoparticles

6.2.1.1 TEM image of ceria nanoparticles

TEM image in Figure 6.1 reveals nano-crystalline form of ceria nanoparticles. TEM image shows the crystal size of ceria nanoparticles in the range of $\sim 7 - 25$ nm.

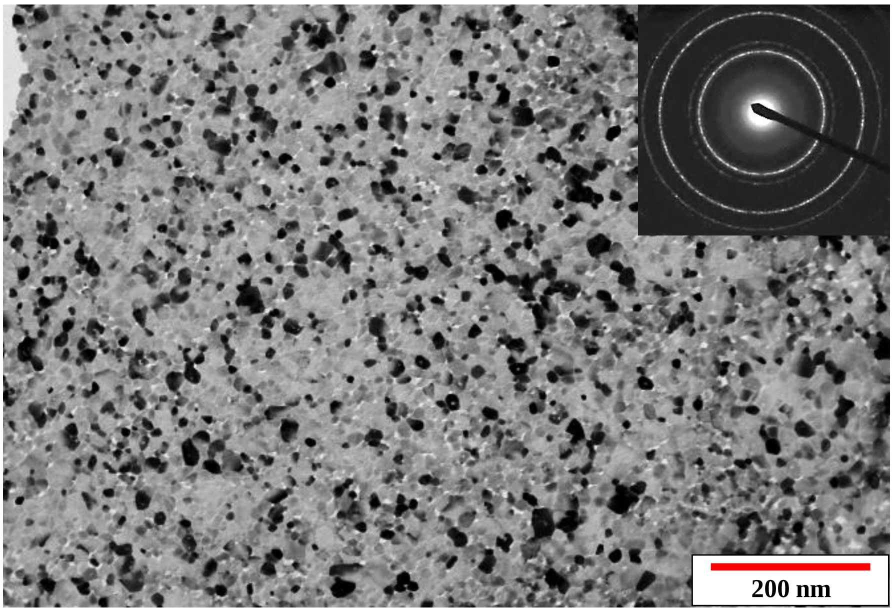

FIGURE 6.1: TEM image of ceria nanoparticles. Inset shows the SAED pattern of ceria nanoparticles.

6.2.1.2 XRD pattern of ceria nanoparticles

Figure 6.2 shows XRD spectrum of ceria nanoparticles. Sharp diffraction peaks at 2θ values of 28°, 32.6°, 47°, 55.8°, 58.5°, 68.9°, 76°, and 78.4° represent planes (111), (200), (220), (311), (222), (400), (331), and (420), respectively. The diffraction patterns indicate presence of face-centered cubic phase of ceria nanoparticles having the average crystal size $\sim$ 12.3 nm with superior crystallization and high purity.

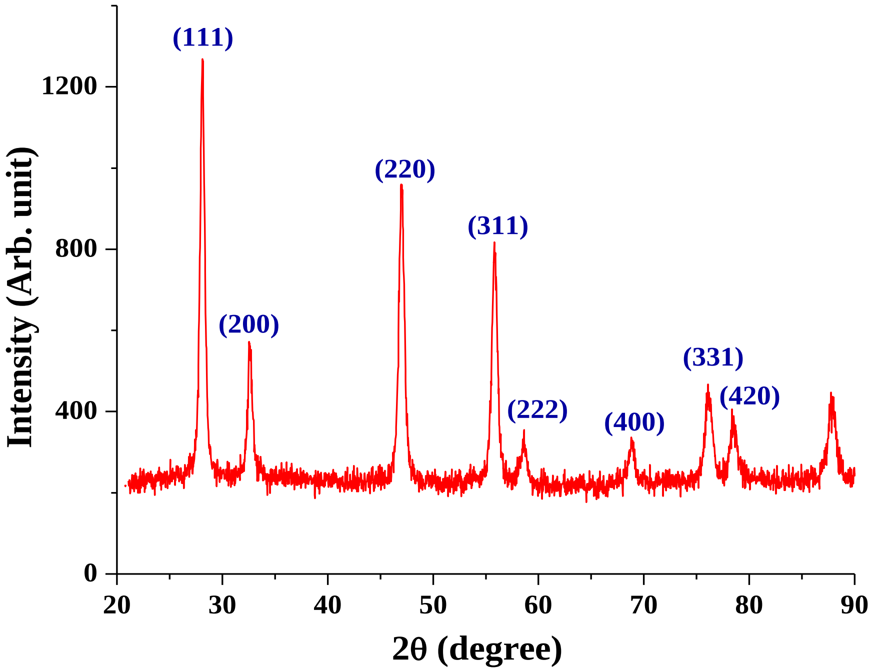

FIGURE 6.2: XRD pattern of ceria nanoparticles.

6.2.1.3 XPS spectra of ceria nanoparticles

XPS spectra (Figure 6.3) exhibit binding energy peaks around 881.8, 897.6, and 905 eV, which shows presence of Ce^{4+}. Peaks around 887.9, and 900.9 eV shows presence of Ce^{3+}. Therefore, XPS analysis illustrates presence of two oxidation states of cerium, Ce^{4+} and Ce^{3+} with composition $\sim$ 82.47 and 17.53 %, respectively.

6.2.1.4 UV-Vis spectra of ceria nanoparticles

UV-Vis absorption spectra of ceria nanoparticles are shown in Figure 6.4. The characteristic absorption peak of Ce^{3+} ion is seen at $\sim$ 230 nm wavelength, while a broad peak is observed in 300 - 400 nm, which is attributed to the overlapping

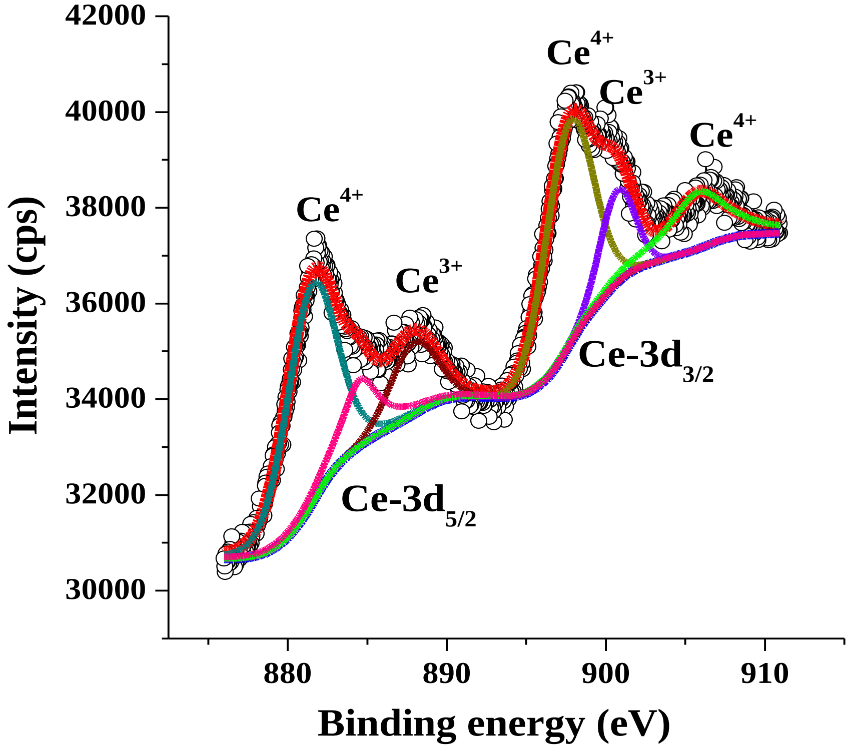

FIGURE 6.3: XPS spectra of ceria nanoparticles.

of two peaks, absorption of Ce^{4+} ($\sim$ 300 nm) and inter-band charge-transfer transition ($\sim$ 350 nm). Absorption study of ceria nanoparticles confirms the presence of Ce^{3+} and Ce^{4+} ions, as well as the transition phase.

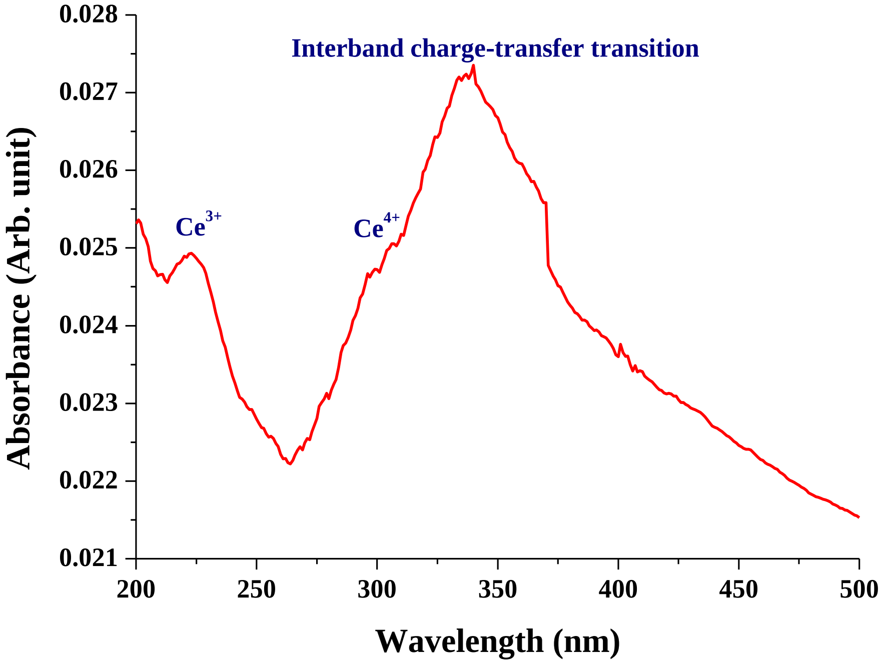

FIGURE 6.4: UV-Vis spectra of ceria nanoparticles.

6.2.1.5 ATR-FTIR spectra of the ceria nanoparticles

FTIR spectra of ceria nanoparticle (Figure 6.5) shows major absorption bands around 3370 cm^{-1} for O-H stretching vibration, 2365 cm^{-1} for absorption vibration of CO_2, 1538 cm^{-1} for H_2O bending vibration, 1322 cm^{-1} for Ce-O-Ce stretching vibration, and 722 cm^{-1} for Ce-O stretching vibration. Absorption bands at 3370 and 1538 cm^{-1} are due to adsorbed water molecules and hydroxyl groups on the surface of ceria.

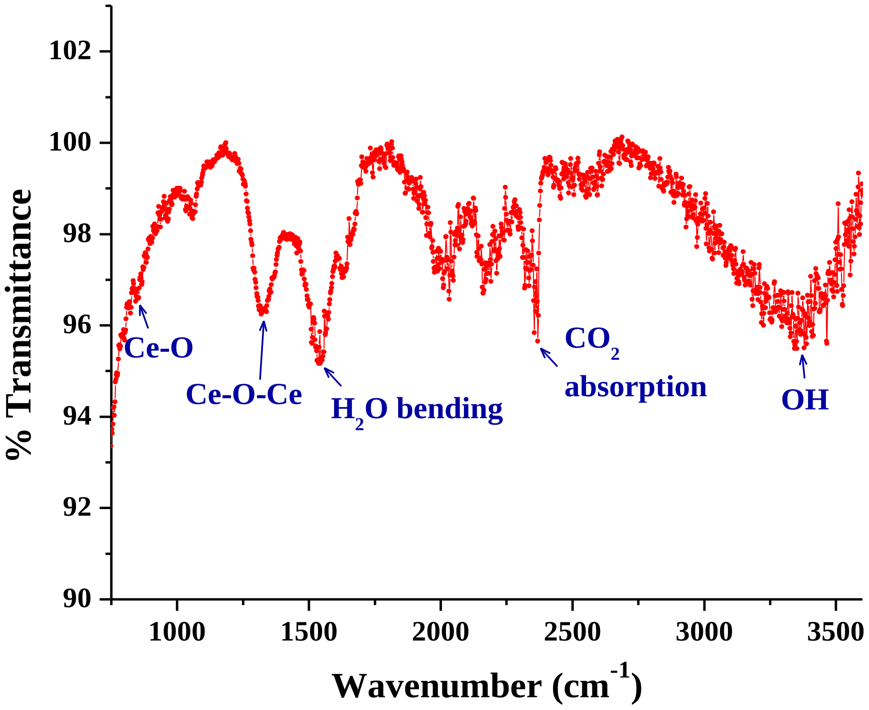

FIGURE 6.5: ATR-FTIR spectra of ceria nanoparticles.

6.2.1.6 Raman spectra of ceria nanoparticles

Figure 6.6 depicts Raman spectra of ceria nanoparticles. Face centred cubic fluorite CeO_2 belongs to Fm3m space group. CeO_2 exhibits one infrared active phonon of $T_{1\mu}$ symmetry and one Raman active phonon of T_{2g} symmetry. This Raman active triply degenerate stretching vibration mode appears in the form of a single sharp peak at $\sim$ 463 cm^{-1}, F_{2g} band, and can be attributed to symmetric breathing of oxygen atoms [276].

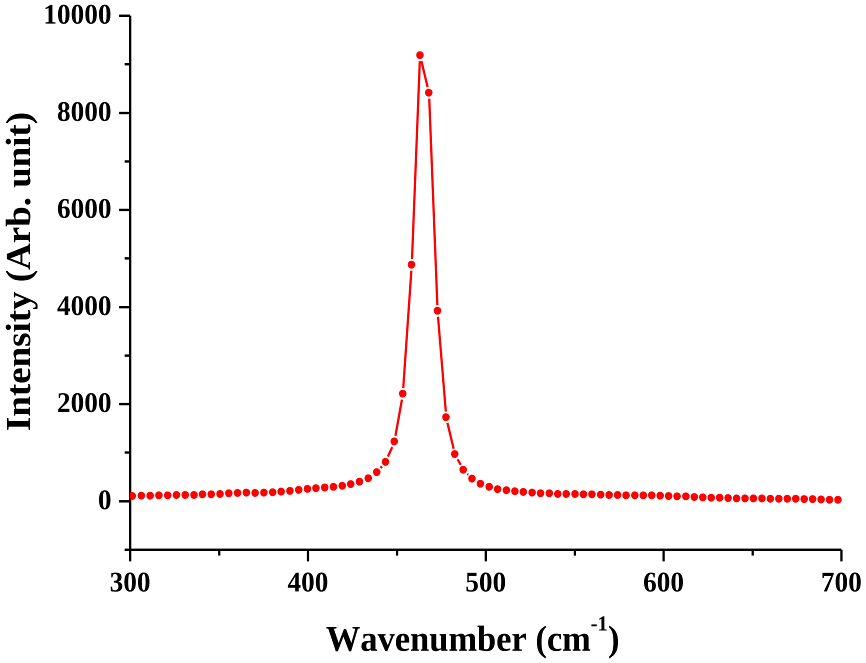

FIGURE 6.6: Raman spectra of ceria nanoparticles.

6.2.1.7 SAXS analysis for size distribution of ceria nanoparticles

SAXS analysis in Figure 6.7 shows size distribution of ceria nanoparticles, indicating ∼ 12 nm as the average particle diameter.

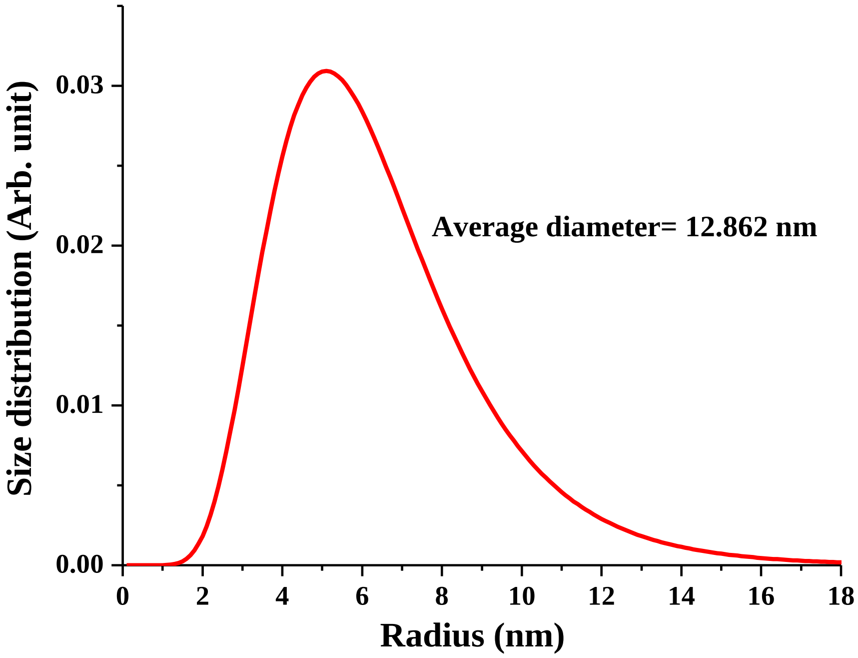

FIGURE 6.7: Size distribution of ceria nanoparticles obtained by SAXS analysis.

6.2.1.8 EDS spectra of ceria nanoparticles

EDS spectrum (Figure 6.8) shows elemental composition of cerium and oxygen confirming successful synthesis of ceria nanoparticle.

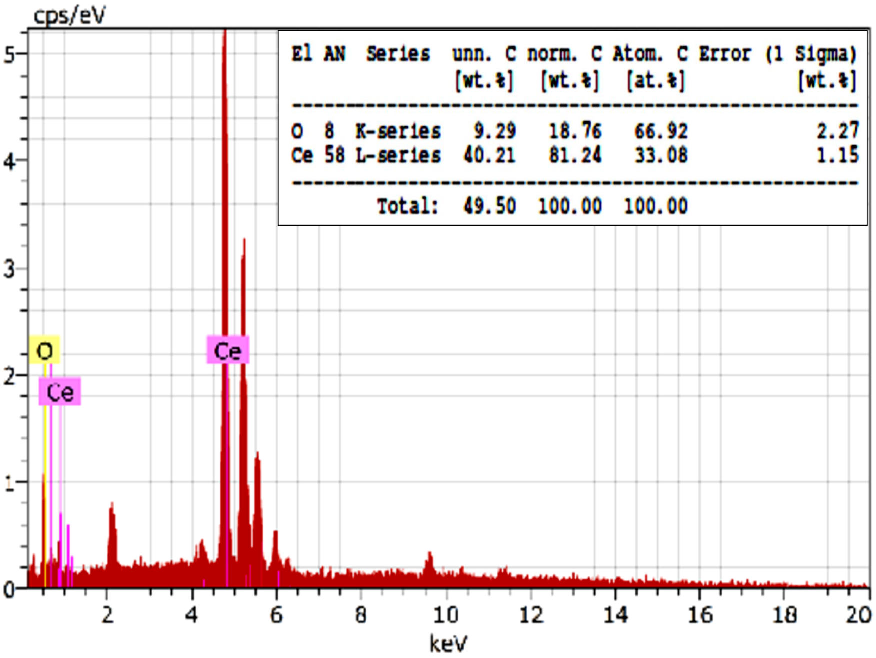

```
El AN  Series   unn. C norm. C Atom. C Error (1 Sigma)
                [wt.%]  [wt.%]  [at.%]          [wt.%]
-------------------------------------------------------
O  8  K-series   9.29   18.76   66.92             2.27
Ce 58 L-series  40.21   81.24   33.08             1.15
-------------------------------------------------------
         Total: 49.50  100.00  100.00
```

FIGURE 6.8: EDS spectrum of ceria nanoparticles.

6.2.1.9 Hydroxyl radical scavenging capability of ceria nanoparticles

Maximum absorption peak of MG is at 615 nm. To understand participation of ceria nanoparticles in reaction, oxidation of MG by $OH^{\bullet}$ radical in presence of different concentration of ceria nanoparticles. Figure 6.9 shows degradation of MG in presence of different concentration of ceria. As shown in inset of Figure 6.9, with increase in the concentration of ceria, degradation rate of MG decreases. This indicates scavenging of $OH^{\bullet}$ radical by ceria nanoparticles. The $OH^{\bullet}$ radical scavenging phenomenon of ceria nanoparticles can be expressed as in Equation (6.1).

$$Ce^{3+} + OH^{\bullet} + H^{+} \longrightarrow Ce^{4+} + H_2O \tag{6.1}$$

Decrease in degradation rate of MG (k_{obs}) with concentration of ceria depicts increase in ${}^{\bullet}OH$ radical scavenging activity of ceria.

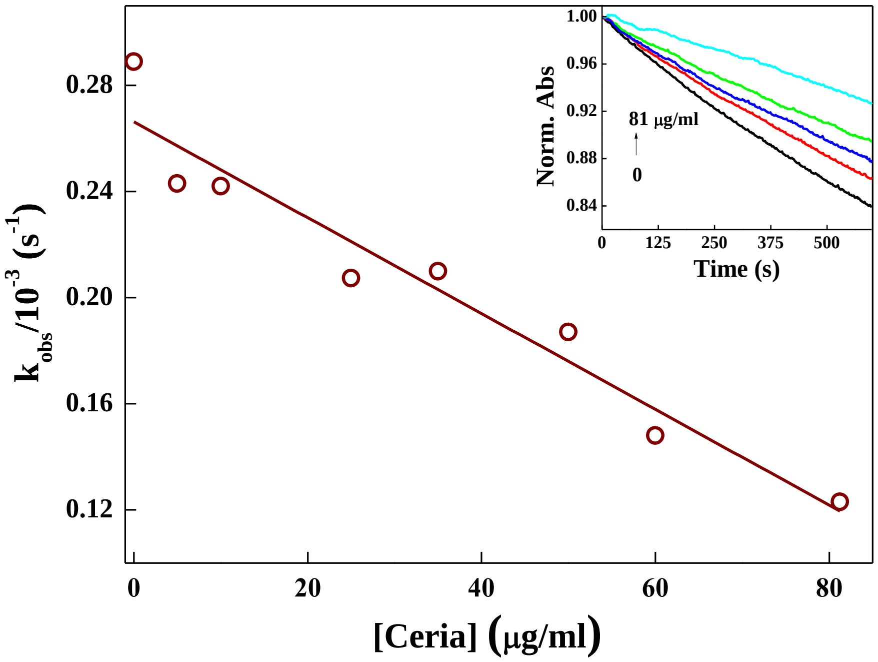

FIGURE 6.9: Hydroxyl radical scavenging by ceria nanoparticles. Inset shows inhibition of absorbance of MG due to $OH^\bullet$ radical induced degradation in presence of different concentration of ceria nanoparticles (5 - 81 $\mu g/ml$).

6.2.1.10 Peroxidase activity of ceria nanoparticles

Peroxidase-like activity of ceria nanoparticles was analyzed by using MG and hydrogen peroxide as substrate. Inset of Figure 6.10 shows time dependent peroxidase-like activity of ceria nanoparticles. Peroxidase-like activity increases with increasing concentration of ceria nanoparticles (Figure 6.10).

To understand affinity of MG with ceria nanoparticles, steady state kinetics was studied by varying the concentration of MG with fixed concentration of ceria and hydrogen peroxide, as shown in Figure 6.11. Steady state kinetic parameters were found using Linewear-Burk method. Value of K_m was estimated $\sim$ 0.2195 mM and V_{max} $\sim$ 5.1 nM/s. Similarly, to realize the affinity of H_2O_2 with ceria nanoparticles, steady state kinetics was determined by varying concentration of H_2O_2 with fixed concentration of ceria and MG, as shown in Figure 6.12. Kinetic parameters K_m and V_{max} were found to be $\sim$ 0.119 M and $\sim$ 82.1 μM/s, respectively. Higher value of K_m indicates low affinity of ceria nanoparticles with H_2O_2, while higher affinity with MG.

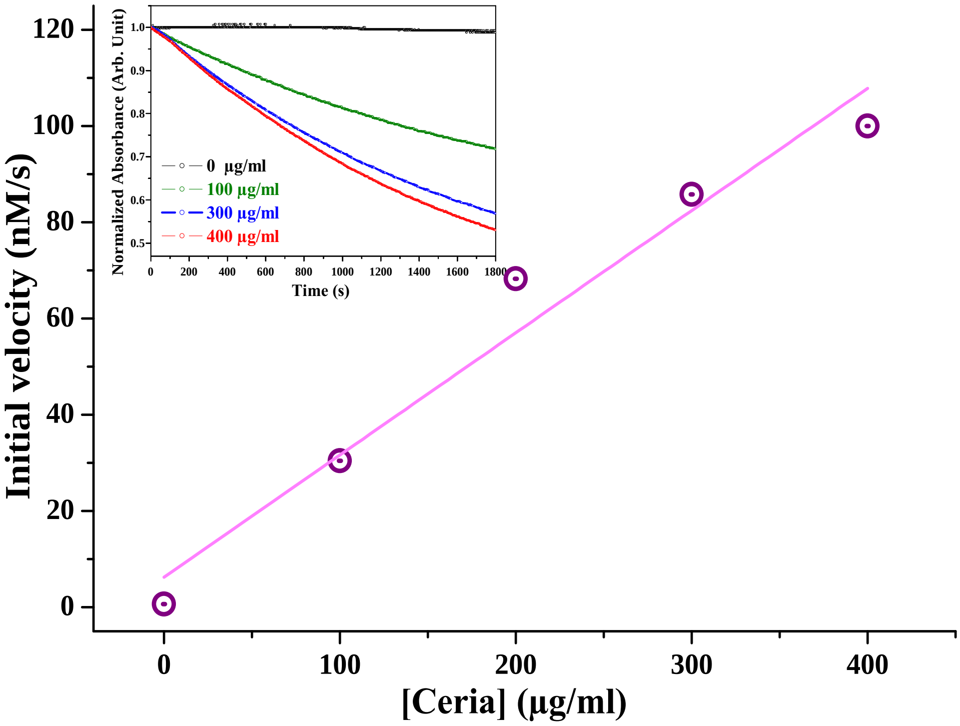

Figure 6.10: Peroxidase activity exhibited by different concentration of ceria nanoparticles. Inset shows the time dependent peroxidase-like activity for different concentration of ceria nanoparticles.

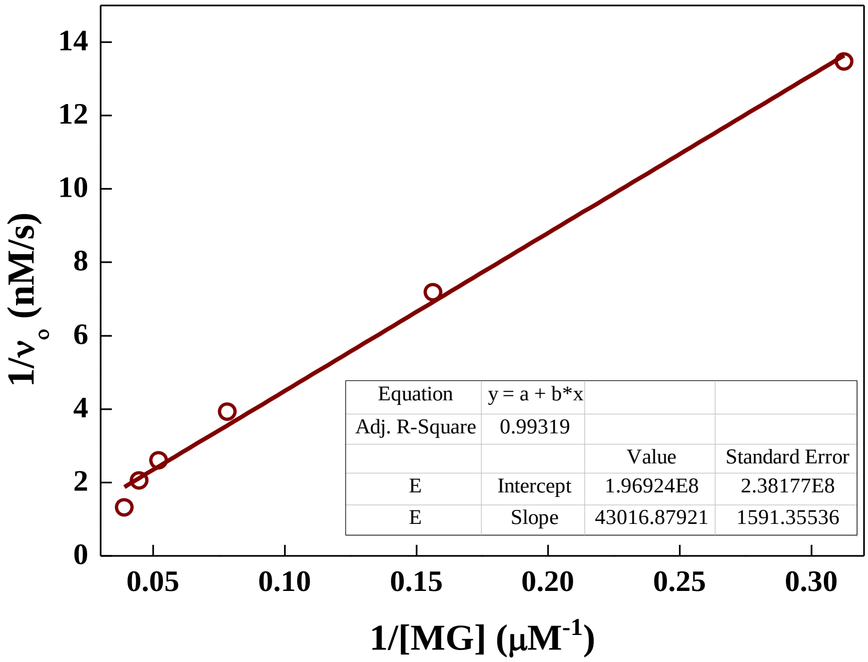

Equation	y = a + b*x		
Adj. R-Square	0.99319		
		Value	Standard Error
E	Intercept	1.96924E8	2.38177E8
E	Slope	43016.87921	1591.35536

Figure 6.11: Double reciprocal plot of initial velocity for the decay of MG by H_2O_2 catalyzed by ceria nanoparticles as a function of MG concentration.

6.2.2 Membrane morphology studies using SEM

Surface and cross-section morphologies of Psf-ceria MMMs, as observed in FESEM, are shown in Figure 6.13 and 6.14, respectively, for different ceria concentration

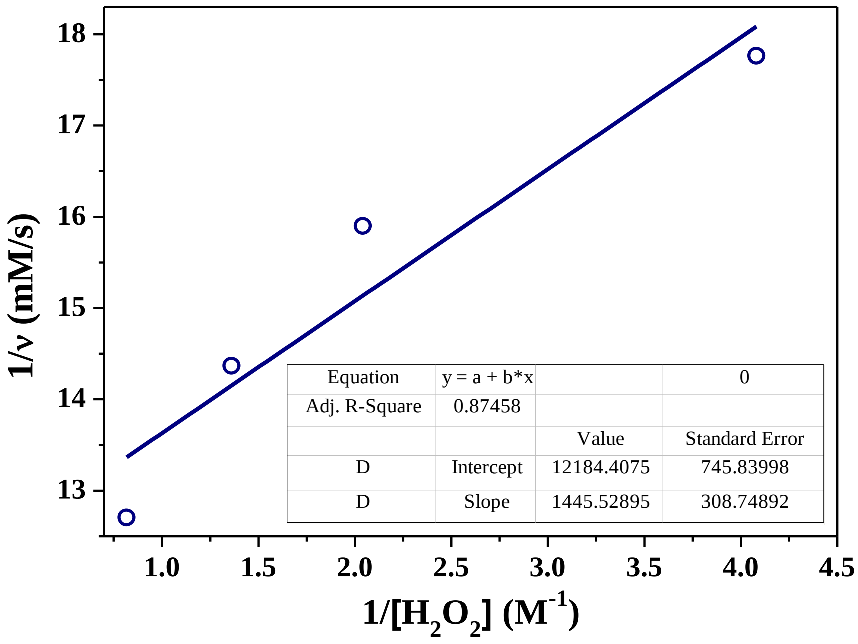

Equation	y = a + b*x		0
Adj. R-Square	0.87458		
		Value	Standard Error
D	Intercept	12184.4075	745.83998
D	Slope	1445.52895	308.74892

FIGURE 6.12: Double reciprocal plot of initial velocity for the decay of MG by H_2O_2 catalyzed by ceria nanoparticles as a function of hydrogen peroxide concentration.

in membrane matrix as well as γ-radiation doses. Top surface morphologies of Psf and the Psf-ceria MMMs are indistinguishable, except for the presence of ceria on MMMs [277], as shown in Figure 6.13. Ceria nanoparticles are homogeneously distributed on MMM surface, as observed by EDS mapping (insets of Figure 6.13). However, with increase in loading of ceria, the proportion of ceria nanoparticles increases on the top surface of membrane, leading to agglomeration at 1% ceria loading (Figure 6.13 (c), (f) and (i)). Fingering phenomenon is observed in all membranes, as clearly seen in Figure 6.14, which is a distinctive feature of membranes synthesized through non-solvent induced phase inversion technique [239]. FESEM images (insets of Figure 6.14(a), (b) & (c)) reveal that an increase in ceria loading results in decrease in pore density and increase in pore size. This clearly indicates that the kinetics of solvent-nonsolvent exchange plays an important role in case of a MMM, which is influenced by the nature of nano-filler. Presence of ceria delays exchange between solvent and non-solvent and thus increases the pore size of membrane, while decreasing the pore density. With radiation exposure, different phenomena like pore closure, pore merger and pore splitting [240] are observed because of cross-linking and chain scissioning [241], as seen in Figure 6.14. Pore closure phenomena results in decrease in the number of pores and thus the pore density, which is primarily observed in irradiated control Psf membranes shown in Figure 6.14 (d) and (g). Consequently, decreased porosity resulted in reduced permeability, as discussed in section later, dealing with performance of membrane.

However, pore splitting phenomena increases pore density but reduces pore size (Figure 6.14 (f)). On the other hand, pore merger phenomena increases pore size and reduces pore density (Figure 6.14 (i)). These two phenomena of pore splitting and pore merger are primarily observed in irradiated 1-Ce membranes. These phenomena resulted in alteration of membrane throughput and solute rejection attributes. Interestingly, 0.5-Ce MMM does not show any significant observable changes in morphology with radiation. This might be because of homogeneous distribution of ceria nanoparticles in membrane matrix, preserving the morphology of membrane. FESEM studies clearly confirmed that presence of ceria has got a profound positive implication on the structure and morphology of MMMs in general, which is restored to a reasonable extent in presence of γ-radiation.

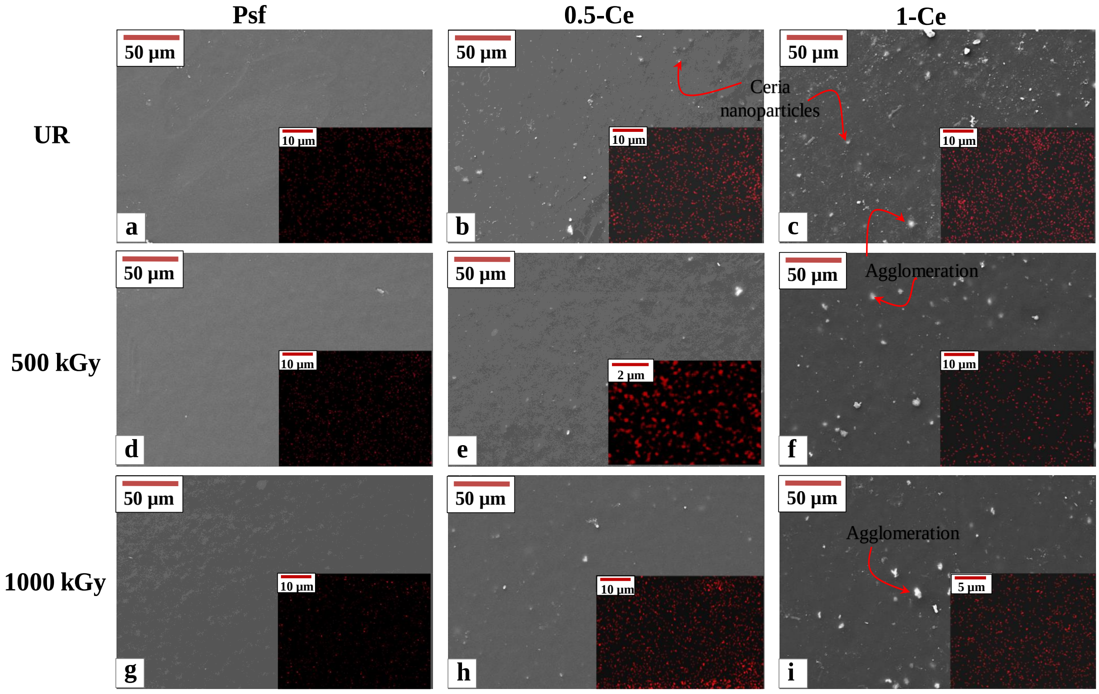

FIGURE 6.13: FESEM images of Psf and Psf-ceria MMMs surfaces with EDS mapping (inset) of cerium: Unirradiated MMMs (a) Psf, (b) 0.5-Ce, and (c) 1-Ce. Exposed to 500 kGy radiation dose (d) Psf-500, (e) 0.5-Ce-500, and (f) 1-Ce-500. Exposed to 1000 kGy radiation dose (g) Psf-1000, (h) 0.5-Ce-1000, and (i) 1-Ce-1000. Inset of every image shows EDS mapping of cerium on the surface of respective membranes.

6.2.3 Membrane surface topography studies using AFM

Variation in root mean square (RMS) roughness of membranes for different loadings of ceria and radiation doses is shown in Figure 6.15. RMS surface roughness of Psf membrane was found to be 2.02 nm. Surface roughness increases with increase in concentration of ceria, reaching up to 2.88 nm for 2-Ce MMM. Surface

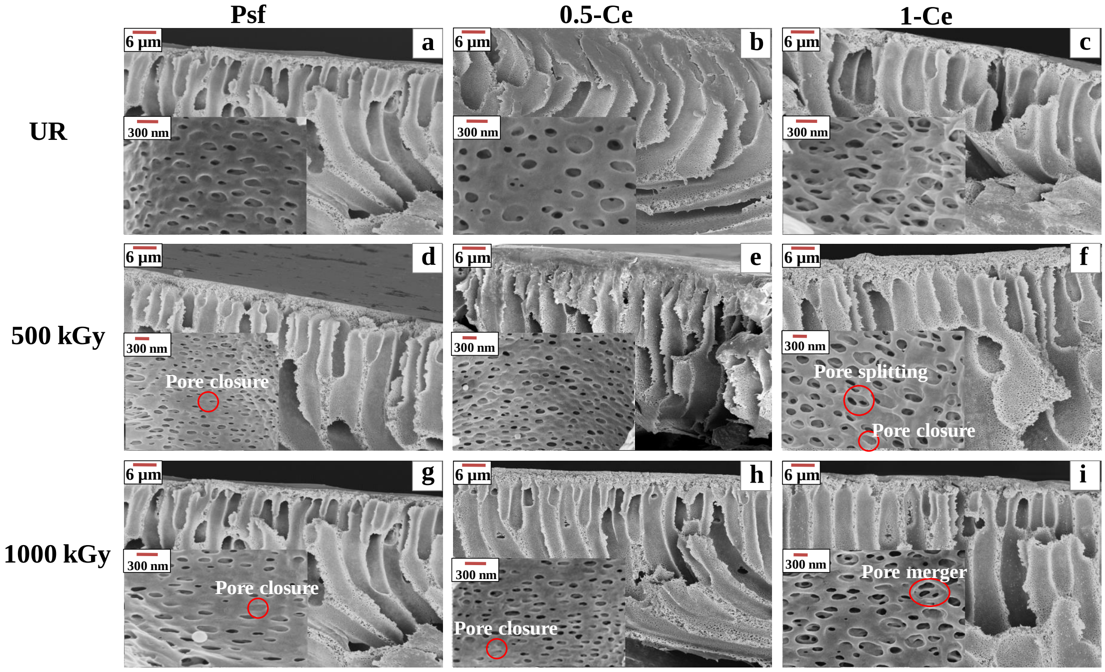

Figure 6.14: FESEM images of the cross-section of Psf and Psf-ceria MMMs: Unirradiated MMMs (a) Psf, (b) 0.5-Ce, and (c) 1-Ce.Exposed to 500 kGy radiation dose (d) Psf-500, (e) 0.5-Ce-500, and (f) 1-Ce-500. Exposed to 1000 kGy radiation dose (g) Psf-1000, (h) 0.5-Ce-1000, and (i) 1-Ce-1000. Inset of every image shows pore distribution of respective MMMs obtained by enlarging the cross-sectional area of membrane.

roughness of a given membrane was also found to increase with increase in radiation dose, due to deterioration of membrane surface as a result of simultaneous chain scissioning and cross-linking phenomena. Change in surface roughness of membranes due to radiation is relatively less for Psf-ceria MMMs, as compared to Psf membrane. Only 25.4, 19, 20.1, and 18.6% change in roughness has been observed for 0.1-Ce-1000, 0.5-Ce-1000, 1-Ce-1000 and 2-Ce-1000, respectively, with radiation while 63.4% change in RMS roughness has been observed for Psf-1000. This implies that the surface roughness of MMMs is less affected by radiation as compared to Psf membrane.

6.2.4 Membrane suface-water contact angle evaluation using DSA

Membrane surface water contact angle of Psf and Psf-ceria MMMs are shown in Figure 6.16. Contact angle for Psf membrane was found to be ~ 79.9°, which slightly increased on addition of ceria in Psf matrix, and reached up to 84.8° for 0.5-Ce MMMs. Due to hydrophobic characteristic of ceria nanoparticles [278], the contact angle increased up to 0.5% loading of ceria. However, contact angle

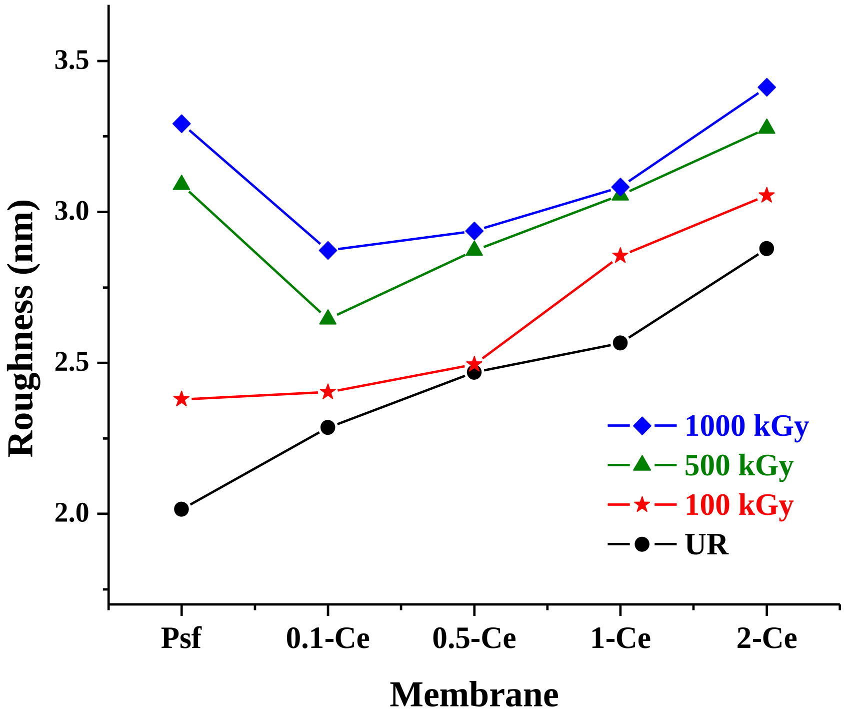

FIGURE 6.15: Variation of RMS roughness of membranes at different loading of ceria and radiation dose.

decreased with further increase in loading of ceria (1-2%). This might be due to uneven interaction of Psf matrix with ceria nanoparticles because of agglomeration tendency of nanoparticles at higher concentration. Also, during phase inversion, large pores were formed at higher concentrations of ceria (as shown in SEM images at higher loading of ceria, Figure 6.14(c)), leading to slight dip in contact angle value. However, contact angle decreased with radiation dose, which is due to increase in the surface roughness (as observed by AFM analysis, Figure 6.15). At a dose of 1000 kGy, contact angle decreased to 73.6°, 74.9°, 77.1°, 69.1°, and 60.23° for Psf-1000, 0.1-Ce-1000, 0.5-Ce-1000, 1-Ce-1000 and 2-Ce-1000 MMMs, respectively. Contact angle study is essential to determine the enhancement of hydrophobicity of Psf membrane by incorporating ceria nanoparticles. Higher concentration of ceria (1 & 2%) resulted in higher reduction in contact angle with radiation due to larger pore size as observed in SEM images shown in Figure 6.14(i).

6.2.5 Membrane suface functionalization studies using ATR-FTIR

ATR-FTIR spectral analysis of membranes was carried out in the region from 700 to 4000 cm^{-1}, as shown in Figure 6.17. Spectra exhibits significant absorption

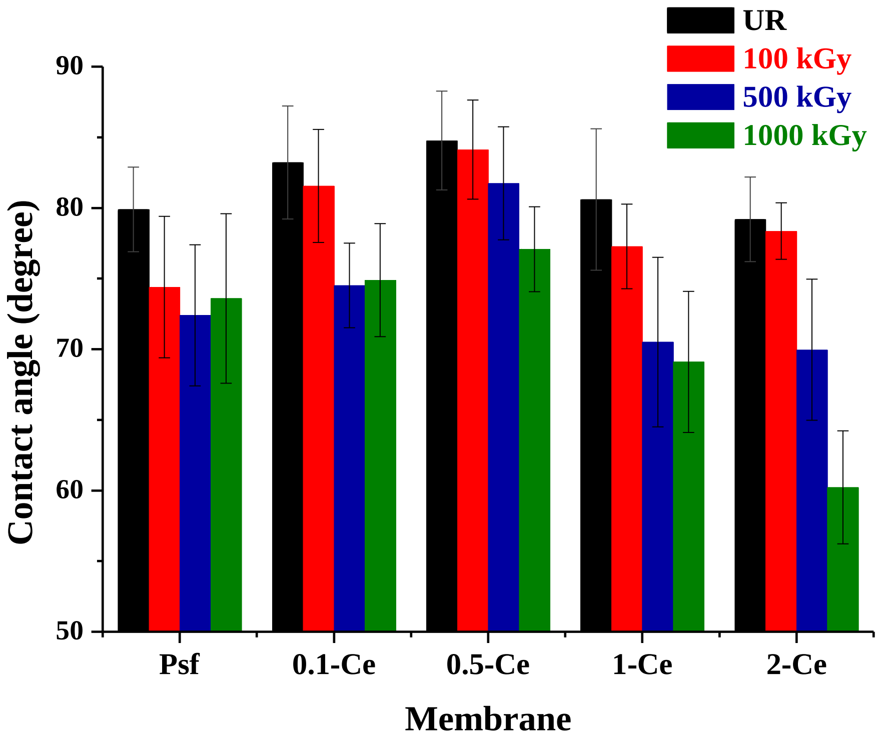

FIGURE 6.16: Variation in membrane surface water contact angle with the loading of ceria and radiation dose.

band around 834 cm^{-1} (C-H stretching of aromatic ring of Psf), 1014 cm^{-1} (symmetric O=S=O stretching of sulfone group), 1080 & 1105 cm^{-1} (Aromatic ring vibration), 1149 cm^{-1} (symmetric O=S=O stretching of sulfone group), 1168 cm^{-1} (asymmetric O=S=O stretching of sulfone group), 1238 cm^{-1} (asymmetric C-O-C stretching of Aryl ether group), 1293 & 1322 cm^{-1} (asymmetric O=S=O stretching of sulfone group), 1364 cm^{-1} (symmetric C-H bending deformation of methyl group), 1411 cm^{-1} (asymmetric C-H bending deformation of methyl group), 1487 & 1586 cm^{-1} (aromatic C=C stretching), 2873 & 2968 cm^{-1} (asymmetric and symmetric C-H stretching vibration of complete methyl group), and 3440 cm^{-1} (O-H stretching vibration). FTIR spectra of ceria nanoparticle shows major absorption bands around 3370 cm^{-1} (O-H stretching vibration), 2365 cm^{-1} (absorption vibration of the CO_2), 1538 cm^{-1} (H_2O bending vibration), 1322 cm^{-1} (Ce-O-Ce stretching vibration), and 722 cm^{-1} (Ce-O stretching vibration). Absorption bands at 3370 and 1538 cm^{-1} are due to adsorbed water molecules and hydroxyl groups on the surface of ceria. Absence of shifting in characteristic absorption bands of Psf-ceria MMMs confirms that incorporation of ceria in Psf matrix does not affect the internal structure of the membrane. Characteristic band of ceria at 2365 cm^{-1} shows physical presence of ceria, wherein intensity of adsorption band is increasing with loading of ceria.

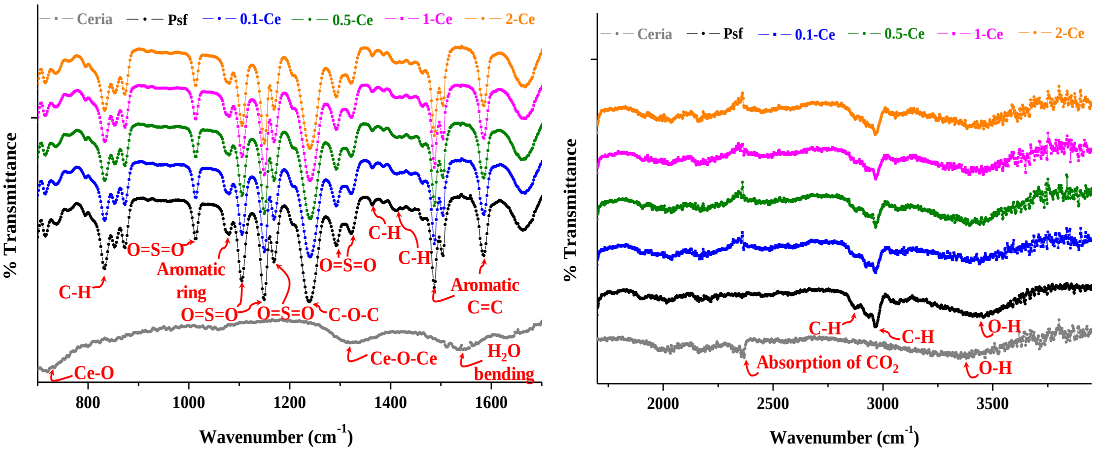

FIGURE 6.17: ATR-FTIR analysis of control Psf and Psf-ceria MMMs.

6.2.6 Weighted average molecular weight determination of the membrane using GPC

Weighted average molecular weight (M_w) of membranes with different loadings of ceria at different radiation doses is shown in Figure 6.18. For radiation dose up to 100 kGy, there is no significant change in the weighted average molecular weight (M_w) of all membranes. At a higher radiation dose beyond 100 kGy, M_w starts decreasing. This could be due to chain scissioning of Psf chains and elimination of sulfonic and carbonaceous groups in the form of CO_2, CO, and SO_2 gases. For radiation dose up to 1000 kGy, value of average M_w gets reduced by 44.8% for Psf membrane, while comparatively less reduction is seen as 41.9, 32.2, 38.5, and 37.7% for 0.1-Ce-1000, 0.5-Ce-1000, 1-Ce-1000, and 2-Ce-1000 membranes, respectively. This indicates that the presence of ceria nanoparticles protects MMMs from the effect of gamma radiation and as a result, extent of loss of molecular weight of MMMs is reduced. Ability of ceria to scavenge free radicals by swapping between two oxidation states ($Ce^{+4} \longleftrightarrow Ce^{+3}$) is responsible in protecting MMMs from negative effects of radiation and a loading of 0.5 to 1% of ceria seems to be optimum for obtaining enhanced radiation resistance behaviour.

6.2.7 XRD pattern of membrane

XRD pattern of ceria nanoparticles and membranes is shown in Figure 6.19. The pattern shows a predominant peak at 2θ of 22° and is attributed to amorphous nature of Psf membrane [279]. Significant characteristic peaks of ceria are at 2θ values of 28°, 32.6°, 47°, 55.8°, and 76° for the respective (111), (200), (220), (311), and (331) plane of ceria. These characteristic peaks of ceria nanoparticles

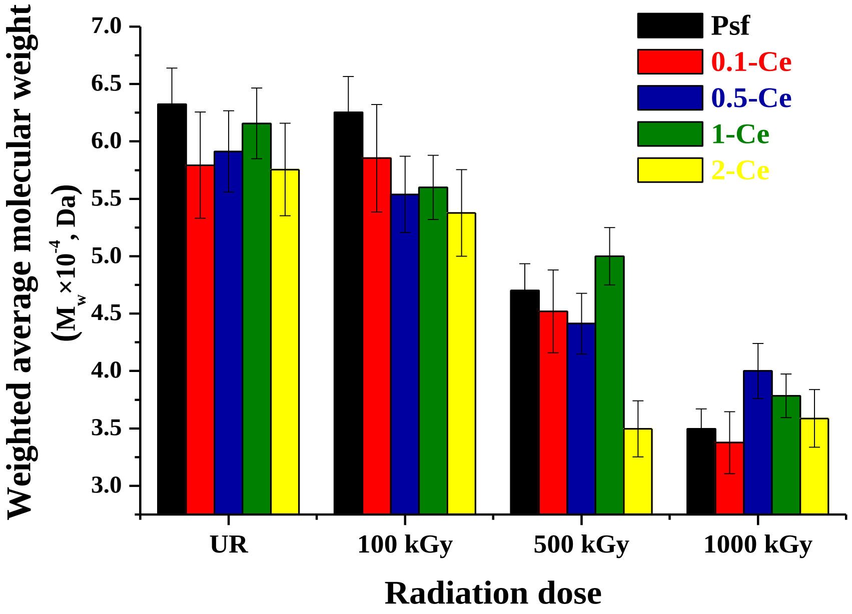

FIGURE 6.18: Effect of ceria loading and radiation dose on weighted average molecular weight (M_w) of MMMs.

can be clearly observed in the XRD pattern of Psf-ceria MMMs. The intensity of these peaks are enhanced with increase in loading of ceria, confirming successful incorporation of ceria nanoparticles into Psf membrane matrix.

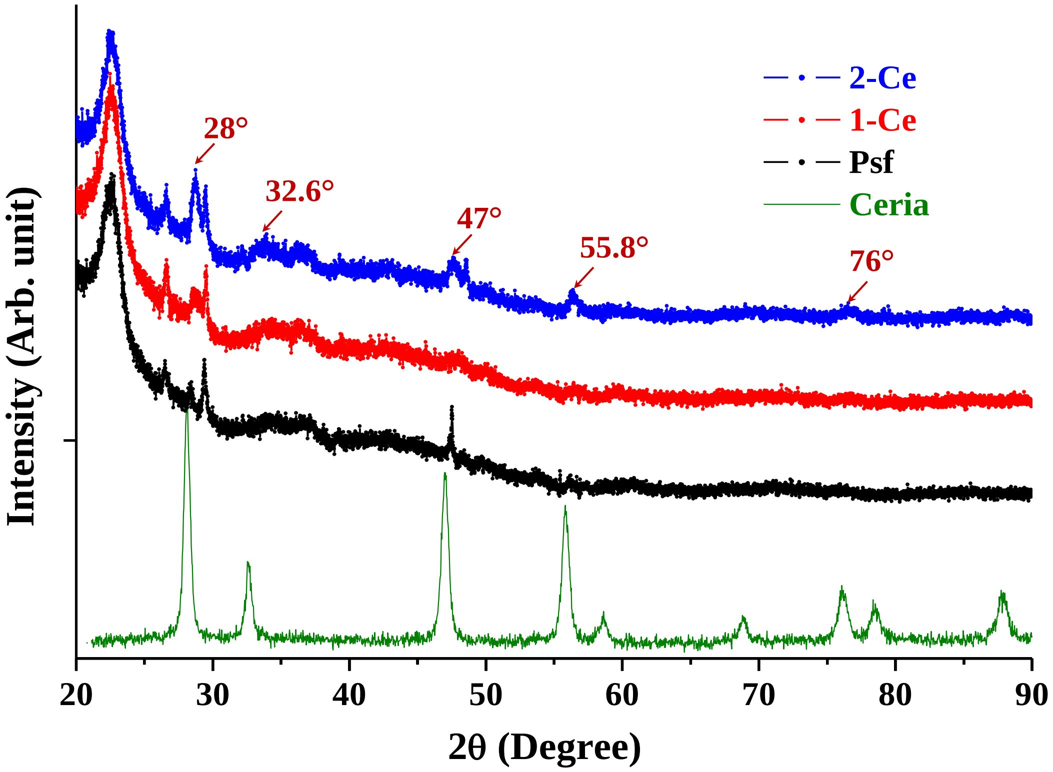

FIGURE 6.19: XRD pattern of ceria nanoparticles, Psf, and Psf-ceria MMMs.

6.2.8 Free volume determination in membrane matrix using PALS

Free volume in membrane matrix was investigated using PALS, and results are as shown in Figure 6.20. There was a rise in relative fractional free volume after incorporation of ceria in membrane matrix. This is due to formation of interfacial defects at the interface of ceria nanoparticles and polymer matrix [13]. These interfacial defects initially increase with concentration of ceria (up to 1% loading) and increase in the number of nanoparticles. Further increase in ceria loading up to 2% leads to agglomeration of particles, leading to reduction in overall density of interfacial defects, and hence a small reduction in relative fractional free volume. On exposure to radiation, there is an increase in relative fractional free volume for Psf membrane, owing to defects created in membrane matrix as a result of structural rearrangement of polymer chains. However, relative fractional free volume decreases for Psf-ceria MMMs after irradiation, indicating the role of ceria in bringing about pore closure and merger phenomena and not forming any defects (as observed in SEM images, inset of Figure 6.14). Extent of change in relative fractional free volume increases with loading of ceria nanoparticles. This is because the pore density decreases with increase in loading of ceria nanoparticles.

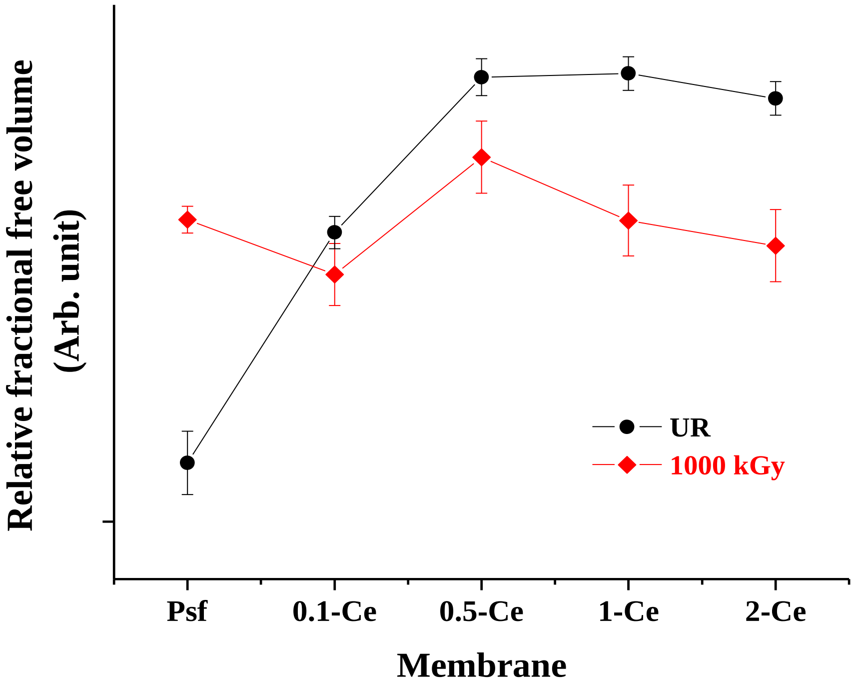

Figure 6.20: Variation of relative fractional free volume with loading of ceria in membrane matrix and at 1000 kGy radiation dose, obtained from PALS.

6.2.9 Structure evaluation of membrane matrix using SAXS

Structural evalution of Psf-ceria MMMs, as probed by SAXS analysis, is shown in Figure 6.21. An even distribution of ceria nanoparticles in membrane matrix is observed. As seen in Figure 6.21, relative number density increases with increasing ceria concentration with respect to control Psf membrane. Besides, relative scattering contrast decreases with radiation dose, which indicates that the pore density decreases with radiation dose due to pore closure, as has already been observed in FESEM images (inset of Figure 6.14) and also confirmed by PALS result (Figure 6.20). On further increasing the loading of ceria, change in scattering contrast increases with radiation dose.

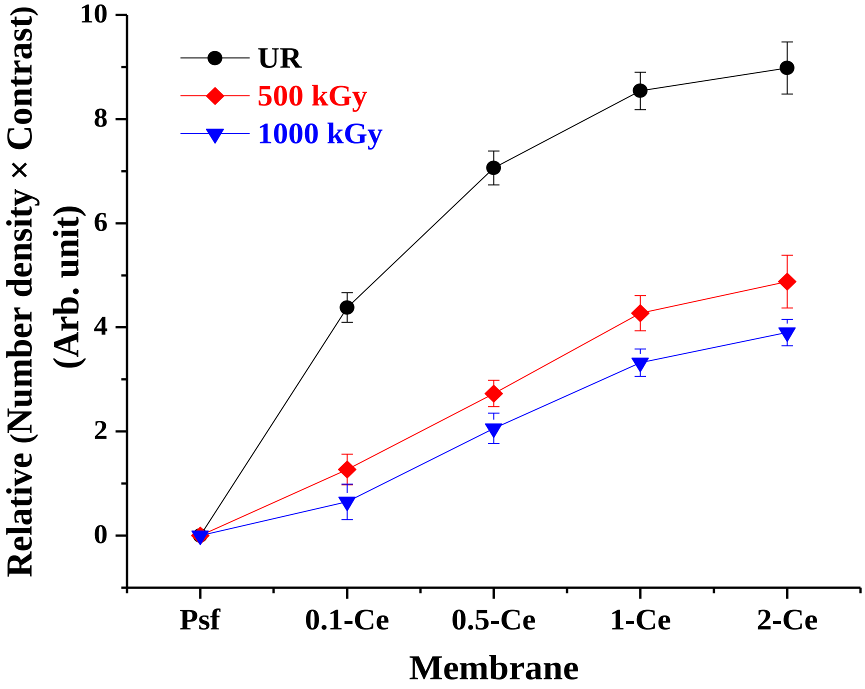

FIGURE 6.21: Variation of relative number density of ceria nanoparticles in the Psf matrix with the loading of ceria and contrast pore density at different radiation dose with respect to control Psf membrane, obtained from SAXS.

6.2.10 Mechanical properties evaluation of the membrane using UTM

Tensile strength (TS) and percentage elongation at maximum force (%E) of membranes are shown in Figure 6.22. TS of Psf membrane was found to be 3.07 MPa, which increases with loading of ceria to 3.77 MPa for 1-Ce membrane matrix. This indicates that the strength of Psf matrix gets enhanced by incorporation of ceria nanoparticles due to excessive toughness of nano-fillers present in membrane matrix. However, as the concentration of ceria increases further, TS of membrane is reduced to 3.31 MPa for 2-Ce membrane. Reduction in TS is due to agglomeration of ceria which leads to lesser interaction with Psf matrix (similar trend has been observed in drop shape analysis, Figure 6.16). On the other hand, introduction of ceria nanoparticles introduces rigidity between Psf polymer chains, reducing %E force from 14.2 (Psf) to 12.5, 13.6, and 14.1 for 0.1-Ce, 0.5-Ce, and 1-Ce membranes, respectively. This shows reduction in ductility of membrane matrix due to incorporation of ceria. At higher concentration (2-Ce), %E again increases up to 17.1. This increase in %E shows that there is less interaction of ceria nanoparticles (due to agglomeration) with Psf matrix and hence 2-Ce MMM behaves like a Psf membrane. Mechanical stability of membranes starts deteriorating after exposure to γ-radiation due to simultaneous chain scissioning and cross-linking phenomena. Hence, there is rearrangement of polymer chain which reduces average molecular weight and decreases the strength as well as flexibility of membrane. While chain scissioning is predominantly responsible for reduction in TS of membranes, cross-linking increases TS and reduces ductility in membranes, leading to decrease in %E values [277]. At 500 kGy radiation dose, TS decreases by 17.5, 12.5, 12.3, 21.2, and 6.1% for Psf-500, 0.1-Ce-500, 0.5-Ce-500, 1-Ce-500, and 2-Ce-500 membranes, respectively. The %E also decreases by 62.8, 57.8, 38.2, 32.6, and 45.5% for Psf-500, 0.1-Ce-500, 0.5-Ce-500, 1-Ce-500, and 2-Ce-500 membranes, respectively. This reduction in TS and %E implies reduced plasticity of Psf chain due to irradiation. At 500 kGy radiation dose, membrane with 2% loading of ceria shows more brittle behavior. This may be due to chain scissioning of Psf, which increases the density of ceria nanoparticles in Psf matrix. Change in mechanical properties of Psf-ceria MMMs is less as compared to that in Psf membrane, owing radiation stability of ceria nanoparticles due to switching of cerium from one oxidation state to other ($Ce^{+3} \longleftrightarrow Ce^{+4}$). The 0.5 - 1% loading of ceria nanoparticles of Psf matrix is found to be the optimum in terms of mechanical stability, owing to strong interaction between ceria and Psf matrix without undergoing agglomeration. Psf-ceria MMMs exhibit greater mechanical stability up to 500 kGy of γ-radiation dose. However, plasticity of membranes has been lost at irradiation dose of 1000 kGy due to loss of polymer chains by chain scissioning and membranes become brittle. Monte Carlo simulation (Chapter 3) has shown that, to absorb a radiation dose of 500 kGy, membrane would take 3 years and 8 months. Thus, Psf-ceria MMMs can be operated for about 3 years and 8 months. On the other hand, Psf membrane, which is claimed to be stable for 100 kGy, shall deteriorate in about 9 months.

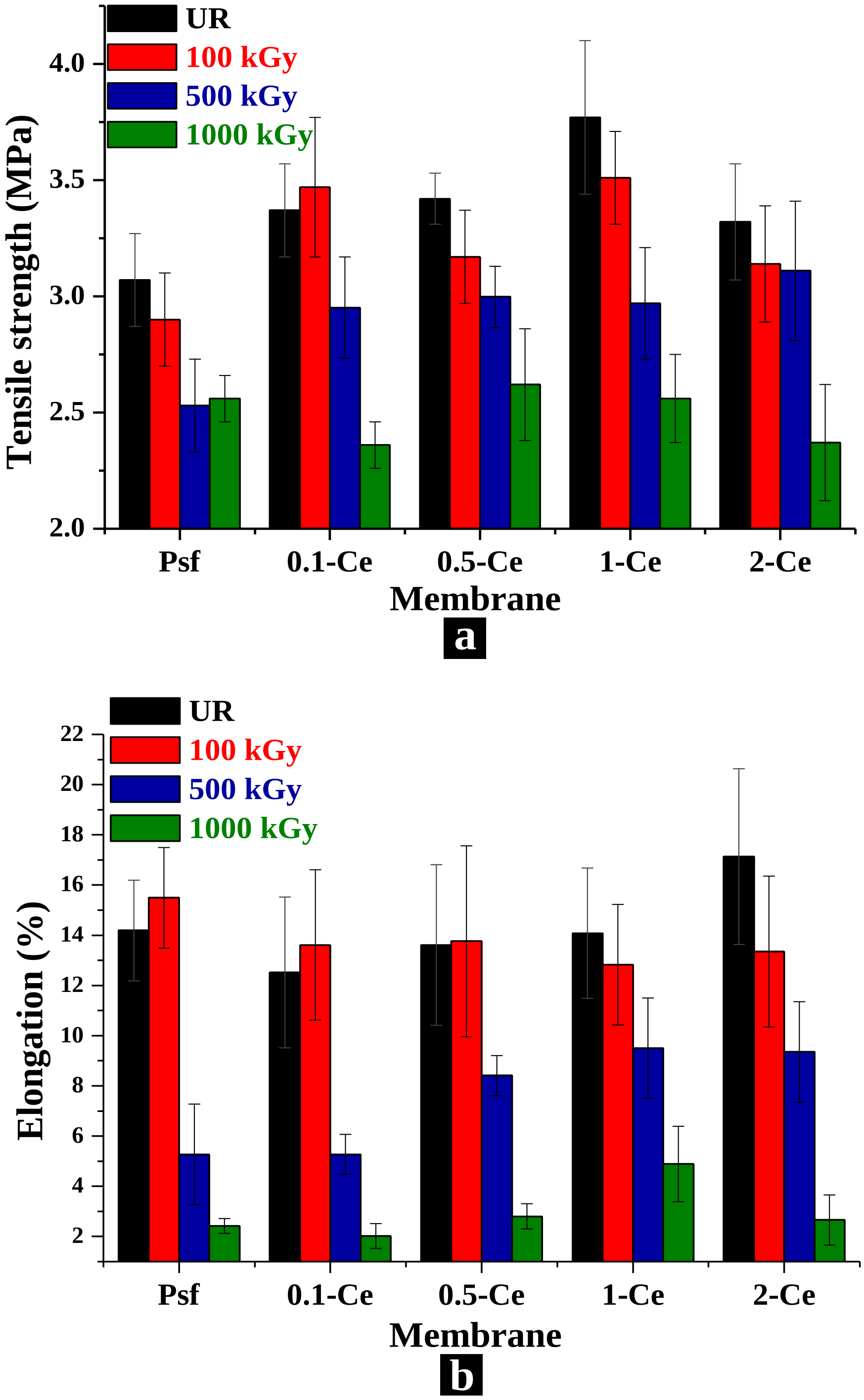

FIGURE 6.22: Effect of ceria loading and radiation dose on mechanical properties of membranes: (a) Variation in tensile strength of the membranes (b) Change in the percentage elongation at maximum force of the membranes

6.2.11 Membrane performance evaluation

Pure water permeability offered by Psf membrane was around 156 $LM^{-2}h^{-1}$ (Figure 6.23(a)), which decreases by 28% for 0.5-Ce membrane. Further loading (1-2%) of ceria increases permeability up to 194 $LM^{-2}h^{-1}$ for 2-Ce MMMs. Initial decline in permeability may be attributed to enhanced surface hydrophobicity on incorporation of ceria nanoparticles. However, agglomeration at higher loading offsets the effect of nanoparticle induced hydrophobicity and leads to increase in permeability, as confirmed by contact angle studies of membranes (Figure 6.16). Also, increased surface roughness (Figure 6.15) of the membrane at higher loading (2-Ce) of ceria improves hydrophilicity of membrane surface and in turn permeability.

Solute (PEO: 100 kDa) rejection offered by Psf membrane was found to be 94.6%, which remains almost same at around 96% for 0.5-Ce membrane, as mentioned in Figure 6.23(b). Rejection decreased on further increasing the concentration of ceria (1-Ce and 2-Ce membranes). This is because of agglomeration of ceria nanoparticles, leading to interfacial defects and hence loss in selectivity. When membranes are exposed to 100 kGy of gamma radiation, their permeability decreased by 9 and 13% for Psf and 2-Ce MMMs, respectively. This is due to reduction in pore density and pore shrinkage by gamma radiation [280]. However, the rejection has not been affected. Permeability variation of Psf-ceria MMMs (0.1-Ce-100, 0.5-Ce-100, and 1-Ce-100) is not significant compared to their unirradiated counter parts, indicating stability of membranes against radiation up till 100 kGy of dose. At 500 kGy of radiation dose, molecular weight decreases (as shown in Figure 6) due to chain scissioning of polymer chains leading to increase in intra-polymeric and polymer-nanoparticle interfacial defects. Due to this, permeability increases for 0.5-Ce-500 and 1-Ce-500 MMMs. Simultaneous cross-linking and chain scissioning of Psf chains increases the pore size but reduces pore density, leading to decrease in permeability for Psf-500 and 2-Ce-500 MMMs. Solute rejection decreases for all membranes at 500 kGy radiation dose. Internal structure of the membrane deteriorates drastically upon exposure to 1000 kGy radiation dose. At 1000 kGy, density of ceria nanoparticles in the Psf host matrix increases due to loss of polymeric chains by chain scissioning. Hence, reduced free volume in polymer matrix (confirmed from PALS analysis given in Figure 6.20 and SAXS analysis given in Figure 6.21) leads to decrease in permeability. Moreover, membranes became fragile (Figure 6.22) and rejection for all membranes is reduced. Extent of variation in permeability of Psf-ceria MMMs is less as compared to that of Psf membrane.

6.2.12 Hydroxyl radical scavenging studies of membrane

To understand reactivity of MMMs with $OH^\bullet$, oxidation of MG by $OH^\bullet$ radical was determined in presence of MMMs with different loading of ceria nanoparticles. Figure 6.24 shows MG degradation in presence of MMMs. Control Psf membrane

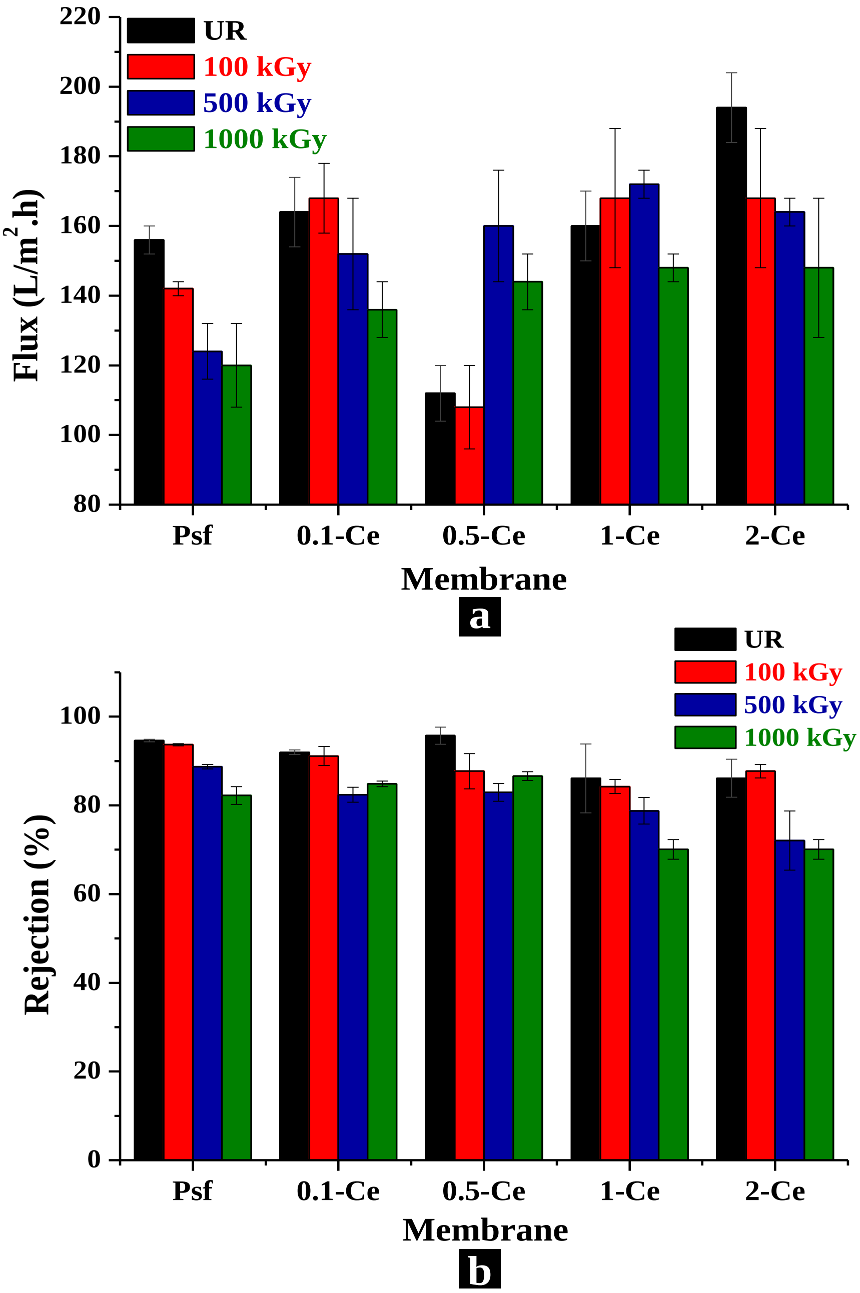

FIGURE 6.23: Performance of the Psf membrane and Psf-ceria MMMs with variation of radiation dose: (a) Pure water permeability of membrane in terms of the flux of water through membranes and (b) PEO rejection percentage by the membranes.

shows sudden reduction in degradation rate of MG. This is due to rapid reaction of $OH^\bullet$ radical with Psf chains, which causes degradation of Psf membrane matrix by reduction in molecular weight under γ-radiation. Reaction of $OH^\bullet$ radical with organic substrate is non-specific, as it reacts with three different processes, viz, hydrogen abstraction, $OH^\bullet$ radical addition, and one-electron oxidation. The hydrogen abstraction and radical addition process results in formation of carbon centered radicals which are known to react rapidly with oxygen and form peroxyl radical. Formation of peroxyl radical are deleterious as they initiate a chain reaction causing formation of more oxidants and thus results in rapid degradation of polymer. On the other hand, inorganic component like Ce^{3+} is known to reduce $OH^{\bullet}$ radical to form Ce^{+4}, which is a relatively stable entity and less deleterious as compared to peroxyl radicals. Thus loading of ceria in Psf membrane matrix gives extra radiation stability to the membrane. Hence reactivity of $OH^{\bullet}$ radical with Psf-ceria MMMs is reduced.

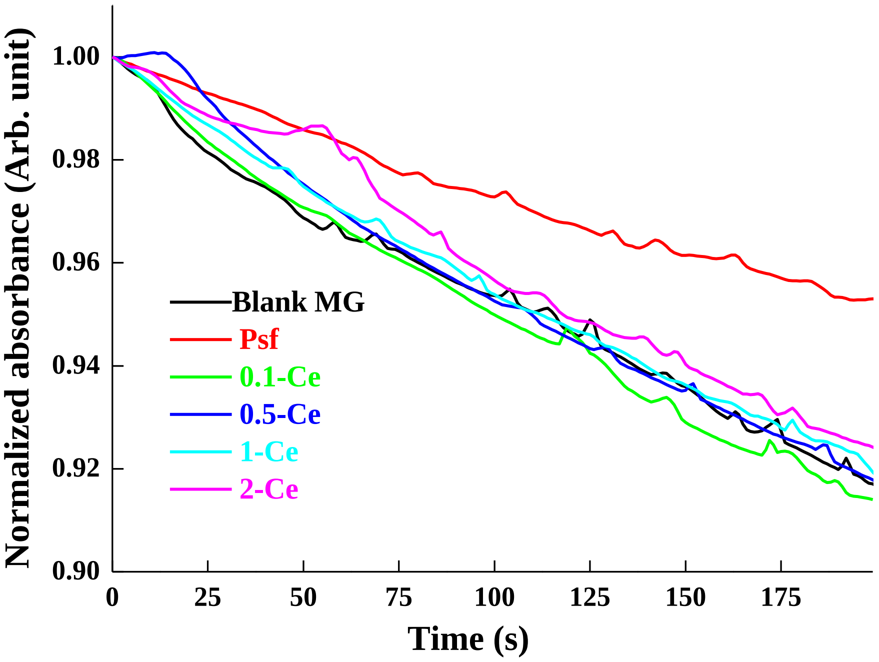

FIGURE 6.24: Hydroxyl radical reactivity with Psf-ceria MMMs. Inhibition of absorbance of MG due to $OH^{\bullet}$ radical induced degradation in presence of different Psf membranes loaded with ceria nanoparticles (0.1 - 2 wt%).

6.2.13 Peroxidase activity analysis of membrane

Peroxidase-like activity of ceria nanoparticles was analyzed by using MG and hydrogen peroxide as substrate. Peroxidase-like activity increases with increasing concentration of ceria nanoparticles (Figure 6.10). As a result, for peroxidase activity of Psf-ceria MMMs, initial velocity was found to increase with ceria loading from 6.3×10^{-5} (blank MG) to 6.83×10^{-5}, 6.86×10^{-5}, and 10×10^{-5} M/s for control Psf, 0.1-Ce, and 1-Ce MMMs, respectively. Results depict participation of ceria nanoparticles in MMMs, performing peroxidase-like activity.

6.3 Summary

γ-radiation resistant polymeric composite membranes were developed by impregnation of ceria into Psf host matrix. Membranes were prepared with different loadings of ceria (0.1, 0.5, 1.0 and 2.0% of polymer weight) and irradiated with 100, 500 and 1000 kGy of gamma radiation dose. Properties of irradiated membranes were analyzed using instrumental techniques and membrane performance studies. All Psf-ceria MMMs exhibited enhanced radiation resistance up to 500 kGy, as compared to control Psf membranes. The 0.5-1% loaded MMMs were found to be the most radiation resistant, as physico-chemical and mechanical properties (tensile strength and percentage elongation), as well as its performance, were found to be stable even up to 500 kGy of radiation dose.

This improved stability of Psf-ceria MMMs is a result of unique swapping ability of cerium ions ($Ce^{3+} \longleftrightarrow Ce^{4+}$), while scavenging the highly reactive free radicals generated by radiolysis of water induced by γ-radiation. Scavenging ability of ceria nanoparticles protects membrane matrix in γ-radiation from degradation, and enhances its life. Peroxidase-like activity of ceria nanoparticles helps to eliminate H_2O_2 and inhibits interaction with Psf membrane matrix. The distinctive scavenging capability of highly reactive oxygen species by ceria membrane provides significant opportunities to Psf-ceria MMMs for application in γ-radiation environment. Findings confirmed that these radiation resistant Psf-ceria MMMs can have potential applications in treatment of radioactive effluents with $\sim$ 5 times increased life-span as compared to control Psf membranes.

Chapter 7

Polysulfone-(nanodiamond + ceria) hybrid mixed-matrix membranes (Psf-(ND+Ce) MMMs)

7.1 Overview

This Chapter investigated the combined effect of ND and ceria nanoparticles on radiation resistant property of membrane. Role of ND and ceria nanoparticles was evaluated in Chapter 3 and Chapter 6, respectively, with individual nanomaterials. Promising properties of ND were explored to provide stability to Psf membrane matrix in γ-radiation environment, while ceria nanoparticles were explored for their free radical scavenging ability to protect the Psf membrane matrix from highly reactive free radicals generated by the radiolysis of water induced from γ-radiation. Integrated effect of both the nanomaterials (ND and ceria) is investigated in this Chapter.

Hybrid nanocomposite membranes [Psf-(ND+Ce)] were developed and their stability in γ-radiation environment was evaluated.

Psf-(ND+Ce) hybrid MMMs were characterized using; SEM, to observe the effect of ND and ceria loading, and γ-radiation dose on membrane morphology; AFM, to analyse surface topography of membrane at different loading of ND and ceria at different γ-radiation dose; water contact angle study of membrane surface, to determine surface hydrophilicity/hydrophobicity with ND and ceria loading, and γ-radiation dose; GPC, to see the effect of γ-radiation on molecular weight of membrane; DSC, to determine oxidative degradation of membranes at high temperature; UTM, to analyse the effect on mechanical properties of membrane; flux and solute rejection behaviour, to observe the performance of Psf-(ND+Ce) hybrid MMMs in radiation environment.

7.2 Results and discussion

7.2.1 Membrane morphology studies using SEM

Surface and cross-section morphologies of membranes are shown in Figure 7.1. All membranes demonstrate typical morphology usually observed in films produced by phase inversion technique, a dense top layer supported by finger-like structure. Top surface of control Psf membrane is comparatively dense, while the membranes impregnated with ceria and ND nanoparticles have more free volume (shown in Figure 7.1(a) to (e)). Free volume of the membrane represents pore channels that assist in enhancing permeability of the membrane [281]. During phase inversion, addition of nanoparticles (ND and ceria) delays the exchange of solvent and non-solvent due to increased viscosity of casting solution, resulting in a wide finger-like structure [258, 259]. Hydrophilic hydroxyl and carboxyl functional groups attached to ND (Chapter 3) attract water molecules which increases the pore density of membranes, as shown in Figure 7.2 [282]. Surface and cross-section morphology (Figure 7.1) shows that by impregnating ND and ceria nanoparticles into Psf host matrix, free volume of membrane increases due to increased pore density (shown in Figure 7.2), while pore size does not get affected by impregnation of nanoparticle (confirmed by the average pore size using porometer, discussed in concerned section later). γ-radiation alters morphology of membranes due to simultaneous chain scissioning and cross-linking of Psf chain [69, 260]. As a result, control Psf membrane showed lower pore density, but increased pore size. However, presence of ceria and ND protects Psf matrix and prevents, to a reasonable extent, the onset of any deteriorating effects in porous morphology. Therefore, pore density and average pore size of hybrid membranes increases after irradiation, leading to enhancement in permeability and decline in solute rejection abilities. However, 0.5ND-0.5Ce hybrid membrane does not shown much variation in average pore size of the membrane matrix even after 1000 kGy of radiation dose, while pore density increases. Optimum concentration with 0.5% each of ND and ceria depicts strong interfacial interation of nanomaterials with polymer matrix, which prevents MMM from γ-radiation-induced degradation. Permeability is thus enhanced without significant variation in solute rejection attributes.

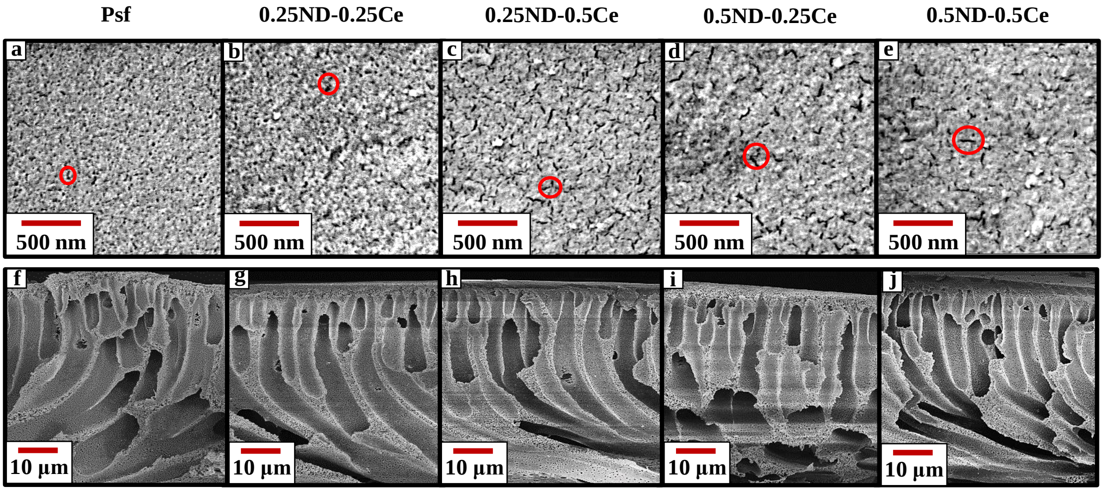

FIGURE 7.1: FESEM images of top surface (a, b, c, d, and e) and cross-section (f, g, h, i, and j) of unirradiated Psf, 0.25ND-0.25Ce, 0.25ND-0.5Ce, 0.5ND-0.25Ce, and 0.5ND-0.5Ce membranes, respectively.

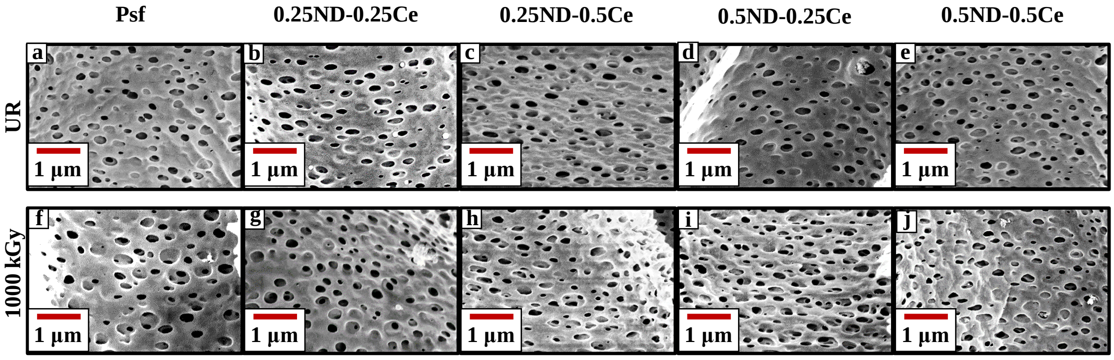

FIGURE 7.2: FESEM images of membrane surface of unirradiated (a, b, c, d, and e) and 1000 kGy irradiated (f, g, h, i, and j) Psf, 0.25ND-0.25Ce, 0.25ND-0.5Ce, 0.5ND-0.25Ce, and 0.5ND-0.5Ce membranes, respectively.

7.2.2 Membrane pore size analysis using porometer

The average pore size of membranes obtained from porometer is found to be in the range of 0.08 - 0.1 μm for all membranes (control Psf and hybrid), which confirms that nanoparticles does not affect the pore size of membrane matrix. At 1000 kGy of radiation dose, average pore size increases up to 0.13, 0.26, 0.31, 0.23, and 0.16 μm for control Psf, 0.25ND-0.25Ce, 0.25ND-0.5Ce, 0.5ND-0.25Ce, and 0.5ND-0.5Ce membranes, respectively. Increase in pore size leads to decline in solute rejection attribute (discussed in concerned section later). It is important to note that 0.5ND-0.5Ce hybrid membrane shows the least variation in pore size, hence solute rejection attribute has not been significantly affected.

7.2.3 Membrane surface topography studies using AFM

Figure 7.3 shows membrane surface roughness obtained from AFM studies. Impregnation of nanomaterials (ND and ceria) slightly increased the surface roughness of membranes [263] from 3.26 (control Psf membrane) to 3.62 nm (0.5ND-0.5Ce hybrid membrane). This is due to enhanced porosity of the membrane, as observed in FESEM images (Figure 7.2). Pore size of control Psf membrane increases after irradiation (Figure 7.2(f)), leading to increase in surface roughness with radiation dose. Surface roughness of hybrid membranes also increases with increase in radiation dose due to increase in pore density (shown in Figure 7.2(g) to (j)). However, up to 1000 kGy radiation dose, increase in roughness for 0.5ND-0.5Ce hybrid membrane is only 8.6%, compared to 18.8% increase for control Psf membrane. Rise in surface roughness resulted in increased transportation of solvent through membrane, as observed in pure water permeability values discussed in the section later.

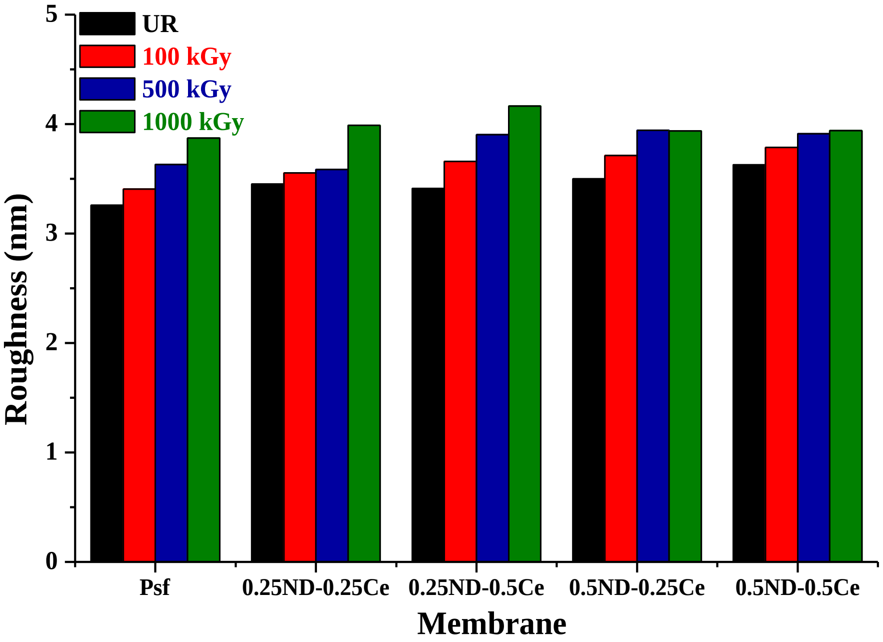

Figure 7.3: Variation in RMS surface roughness of membrane with ND and ceria loadings, at different radiation dose.

7.2.4 Membrane suface-water contact angle evaluation using DSA

Hydrophilicity/ hydrophobicity of membrane surface was determined by water contact angle studies. As shown in Figure 7.4, water contact angle of control Psf membrane is ∼ 80°, which slightly increases up to 85° on addition of ceria and ND nanoparticles. Small rise in contact angle is due to hydrophobic characteristic of ceria nanoparticles [278]. Contact angle of each membrane decreases with radiation dose due to increased surface roughness, as discussed in previous section (Figure 7.3). Decline of contact angle is more pronounced in hybrid membranes (at 1000 kGy radiation dose, 64.5, 71.6, 57, and 60.9° for 0.25ND-0.25Ce, 0.25ND-0.5Ce, 0.5ND-0.25Ce, and 0.5ND-0.5Ce membranes, respectively), compared to control Psf membrane (73.6° at 1000 kGy radiation dose). This is due to increased pore density (shown in Figure 2(g) to (j)) with radiation resulting in higher water uptake and enhancement of hydrophilicity [283]. Radiation enhances water permeability by enhancing hydrophilicity through disturbing the pore structure and porosity, while nanoparticles stabilize membrane matrix in radiation environment.

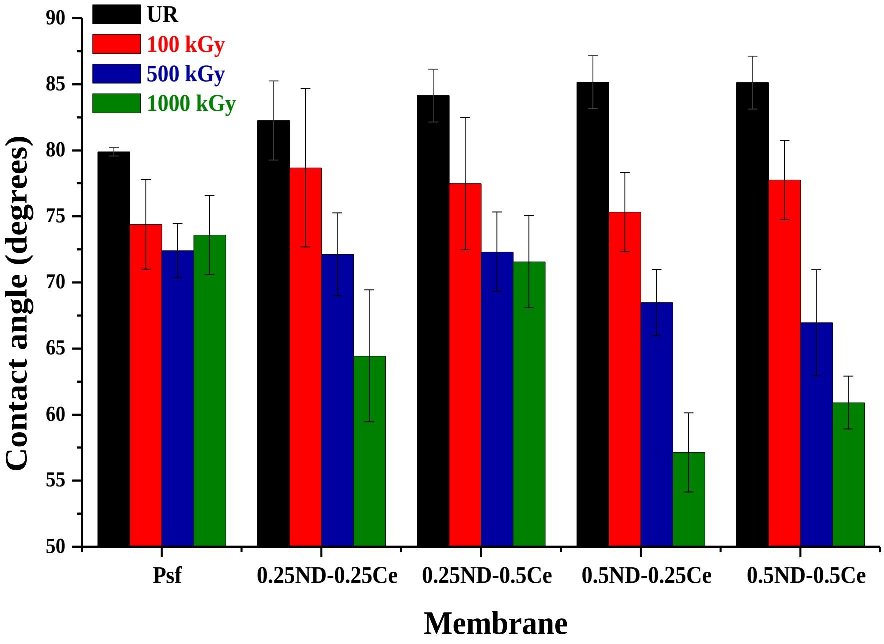

Figure 7.4: Variation in membrane surface water contact angle with different loadings of ND and ceria nanoparticles, at different radiation dose.

7.2.5 Weighted average molecular weight determination of membrane using GPC

Weighted average molecular weight (M_w) of membranes was determined by GPC to observe cross-linking and chain-scissioning phenomena during irradiation [261]. As shown in Figure 7.5, M_w of control Psf membrane slightly decreased after 100 kGy irradiation, while that of hybrid membranes increased. Variation in M_w indicates chain-scissioning in control Psf, and cross-linking in hybrid membranes, as predominant phenomena. For control Psf membrane, influence of chain-scissioning phenomena increases with radiation dose, therefore M_w decreases from 63241 Da for unirradiated Psf (Psf-UR) to 34954 Da for Psf irradiated up to 1000 kGy (Psf-1000 kGy). On the other hand, hybrid membranes exhibit cross-linking phenomena up to 500 kGy radiation dose. Above 500 kGy radiation dose, chain-scissioning predominates and consequently M_w starts to decrease. The 0.5ND-0.5Ce hybrid membrane does not show significant difference in M_w even up to 1000 kGy of radiation dose. Results confirm enhanced stability of Psf membrane matrix up to 1000 kGy due to the presence of 0.5% ND and 0.5% ceria. This stability against γ-radiation can be attributed to free radical scavenging property of ceria (scavenging ability of ceria nanoparticles shown in Chapter 6) [275] and radiation resistant property of ND (hardness and free radical scavenging ability of ND shown in Chapter 3) [269]. Owing to two stable states of cerium (Ce^{+3} and Ce^{+4}), ceria can scavenge free radicals generated from γ-induced radiolysis of water, by swapping from one state to another $Ce^{+3} \longleftrightarrow Ce^{+4}$. Also, ND, owing to its hardness as well as free radical scavenging ability, protects hybrid membrane matrix by acting as a barrier to γ-rays and radiolysed products of water.

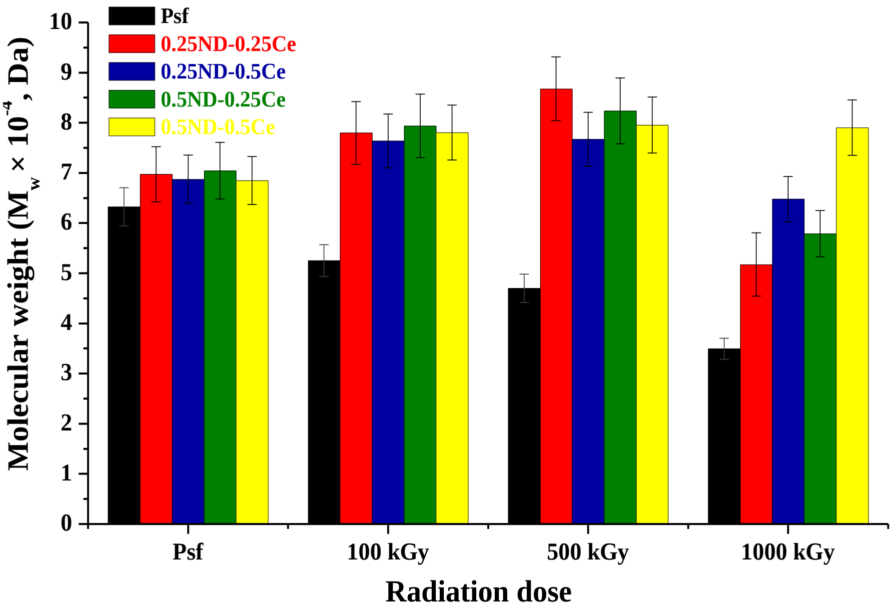

FIGURE 7.5: Change in weighted average molecular weight (M_w) of membranes with different radiation dose.

7.2.6 Studies on oxidative degradation of membrane using DSC

Thermal oxidation of membranes was investigated by DSC studies. Figure 7.6(a) shows DSC thermograms of unirradiated membranes, where the effect of ND and ceria loading can be observed on thermal oxidation degradation of membrane matrix. DSC thermogram of the control Psf membrane shows three exotherms with increasing temperatures having peaks at ~ 430, ~ 530, and $\sim 590\ °C$. Since Psf is a polymeric network, it undergoes crystallization/partial crystallization with heating (which also gives exothermic DSC trace). Reinforcement of Psf with ND and ceria nanoparticles (0.25-0.50 wt%) does not show any observable effects on peak temperature of the first exotherm ($\sim 430\ °C$). While all four membrane samples show single peak, membrane 0.5ND-0.5Ce shows two peaks before the onset of second exotherm, indicating that higher loading of ND and ceria has affected the thermal response of Psf towards this exothermic phenomenon. Stage 2 exotherm also remains almost invariant in terms of peak temperature (~ 525 to $529\ °C$). Stage 3 exotherm shows distinct behavior with ND and ceria loading, wherein the peak at $\sim 589\ °C$ for control Psf went down sharply by $\sim 15\ °C$ for 0.25ND-0.25Ce membrane sample, indicating that MMM has reduced thermo-oxidative stability as compared to control Psf membrane. Also, onset of exotherm is shifted to lower temperatures, further corroborating the inference of composite's lowered thermal stability. Decomposition is apparently completed before 600 $°C$ for both 0.25ND-0.25Ce and 0.25ND-0.50Ce membrane samples, which was incomplete for control Psf membrane sample till 600 $°C$. Further reinforcement of nanoparticles shows further reduction in peak temperature to $\sim 565\ °C$ (reduced by $\sim 10\ °C$) for 0.5ND-0.25Ce membrane, which is in line with the observed trend. However, at the same time, exotherm clearly broadens with additional high temperature exotherm overlapped with 565 $°C$ peak, which can be seen from shoulder type peak. This suggests that ND doping has distinct effect on thermo-oxidative stability than that of ceria reinforcement. Very interestingly, 0.5ND-0.5Ce membrane sample shows anomalous increase in peak decomposition temperature (stage 3), which indicates increased thermal stability. Also, decomposition is not completed till 600 $°C$ (similar to that of control Psf). The findings show distinctly higher thermal stability of this MMM, while the ones with lower loadings (0.25ND-0.25Ce, 0.25ND-0.5Ce and 0.5ND-0.25Ce) show opposite behavior. Regarding irradiated samples, lowering of peak temperature of stage 1 by 5 - 6 $°C$ for control Psf membrane indicates radiation induced degradation in Psf matrix, which led to reduced stability of polymer membrane around 430 $°C$. Increase in stage 1 peak temperature (430 $°C$) of irradiated MMMs with higher ND loading (0.5ND-0.25Ce & 0.5ND-0.5Ce) again indicates that ND does have a stabilizing effect towards thermal response. Stage 2 and stage 3 of irradiated Psf is highly overlapped. Interestingly, stage 2 peak has shown upwards shift while that of stage 3 has shown significant downward shift in temperature. Since it is control Psf, these effects are manifestation of irradiation on weakening of polymer network. In all the irradiated samples, stage 2 is much more intense than stage 3 while the reverse is observed in all the unirradiated samples. Due to radiation induced damage of membrane matrix by chain scissioning and cross-linking, the range of ordering in Psf chain has been altered, which is clearly observed in Figure 7.6(b). Psf-1000 kGy is showing a broad peak in the range 534 to 556 $°C$, which indicates diverse sizes of Psf chains are formed due to chain scissioning and cross-linking phenomena (as observed in GPC analysis shown in Figure 7.5). Table 7.1 shows only small effect for higher order chains in stage 3 for hybrid membranes, owing to chain scissioning at 1000 kGy (as observed in GPC analysis, Figure 7.5). This is clear from the comparison of thermograms of unirradiated membrane samples with that of irradiated ones that the Psf network is affected significantly by irradiation, compared to that of the MMMs, with 0.5ND-0.5Ce membranes offering optimum stability against thermo-oxidative degradation.

TABLE 7.1: Three-stage oxidation degredation peak temperatures of unirradiated and 1000 kGy irradiated membranes.

	Peak temperature ($°C$)					
Membrane	**Unirradiated**			**1000 kGy irradiated**		
	Stage 1	**Stage 2**	**Stage 3**	**Stage 1**	**Stage 2**	**Stage 3**
Psf	430	529	589	424	534	556
0.25ND-0.25Ce	430	526	575	425	532	534
0.25ND-0.5Ce	430	528	576	424	533	557
0.5ND-0.25Ce	430	526	564	430	530	566
0.5ND-0.5Ce	430	525	594	430	538	550

7.2.7 Mechanical properties evaluation of membrane using UTM

Mechanical properties of membranes were investigated in terms of tensile strength (TS) and percentage elongation at maximum force (%E), as shown in Figure 7.7. TS and %E of control Psf membrane are 3.07 MPa and 14.2, respectively. By impregnation of ND and ceria, mechanical strength of all hybrid membrane has increased, with TS and %E of 4.17 MPa and 19.2, respectively, for membrane impregnated with 0.5% each of ND and ceria [284]. Mechanical properties of membranes mainly depend on two factors. One is the size of nanoparticles, which is crucial for interfacial interaction between nanoparticles and Psf. Average size of ND nanoparticles is about 5 nm (Chapter 3) and that of ceria is about 12 nm (Chapter 6), which leads to high surface to volume ratio of nanoparticles and

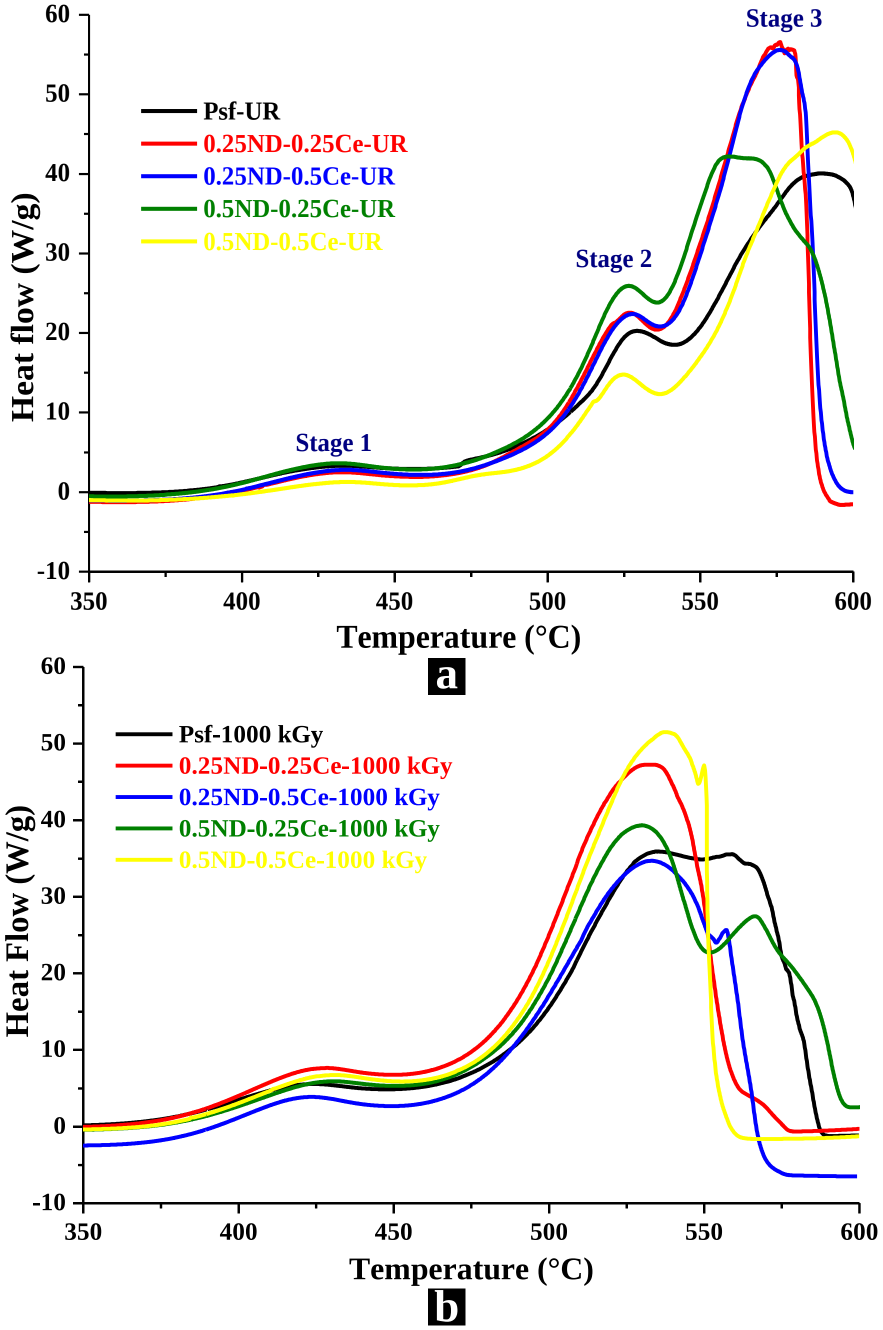

FIGURE 7.6: DSC thermograms of membrane at different loading of ND and ceria: (a) unirradiated and (b) 1000 kGy irradiated membranes.

hence, an excellent interfacial area for enhanced interaction between the polymer and nanomaterials. Another factor is distribution of nanoparticles in membrane matrix. The uniform distribution of nanoparticles provides strong interaction with the polymer matrix, while agglomeration reduces number density of particles resulting in reduced interaction. The 0.5% loading each of ND and ceria in Psf host matrix was found to be optimum in terms of uniform distribution and strong interaction, thus offering enhanced mechanical properties [82]. After 100 kGy of irradiation, control Psf membrane starts losing its mechanical strength due to chain scissioning, as observed in GPC analysis shown in Figure 7.5 [268]. On the other hand, value of %E slightly increased, because the chain scissioning leads to the increased flexibility of Psf chain. Similar observation has been made for 0.25ND-0.25Ce membrane, as small amount of loading of nanomaterials has not affected the rigidity of the Psf matrix by much. On the other hand, higher loading of nanomaterials introduced rigidity in Psf matrix. Futher increment in radiation dose leads to chain scissioning of Psf chains, as a result of which mechanical properties deteriorate. Increase in pore density of hybrid membranes (as observed in pore distribution images, Figure 7.2) due to radiation also results in reduced TS and %E [285]. Reduction in %E of hybrid membranes is less than that of control Psf membrane up to 1000 kGy radiation dose, as shown in Figure 7.7 (b). Results indicate that mechanical properties of hybrid membranes are restored even after 1000 kGy radiation dose. The 0.25ND-0.25Ce and 0.5ND-0.5Ce hybrid membranes were found to be most stable in radiation environment in terms of their mechanical properties.

7.2.8 Membrane performance evaluation

Figure 7.8 shows membrane performance based on pure water permeability and solute rejection attributes of membranes for PEO-100 kDa. Permeability offered by control Psf membrane was found to be about 156 $L\ m^{-2}\ h^{-1}$ with 94.6% rejection, while all hybrid membranes exhibited improved permeability and rejection. Inherent trade-off found in any polymeric membrane systems is observed to have reduced to a reasonable extent in hybrid membranes. Permeability of 0.5ND-0.5Ce membrane increased up to 192 $L\ m^{-2}\ h^{-1}$ with solute rejection of 97.6%. Performance is enhanced due to increased pore density of the membrane, as shown in FESEM image in Figure 7.2(e) [286]. This indicates that presence of ND and ceria nanoparticles could create additional pathways for water flow, without increasing the pore size. Enhanced surface roughness (Figure 7.3) and hydrophilic groups present on the ND surface (Chapter 3) also contributes to increase in permeability. Hence, solute rejection as well as solvent flux increases. On exposure to radiation, permeability of control Psf membrane decreased to 120 $L\ m^{-2}\ h^{-1}$ and rejection rate to 87%, which could be due to increase in pore size and reduced pore density of the membrane, as can be seen in FESEM image in Figure 7.2(f). This is due to degradation of Psf matrix owing to chain scissioning by γ-radiation, as confirmed by GPC analysis as shown in Figure 7.5. On the other hand, due to increased pore density of hybrid membrane in radiation environment (FESEM

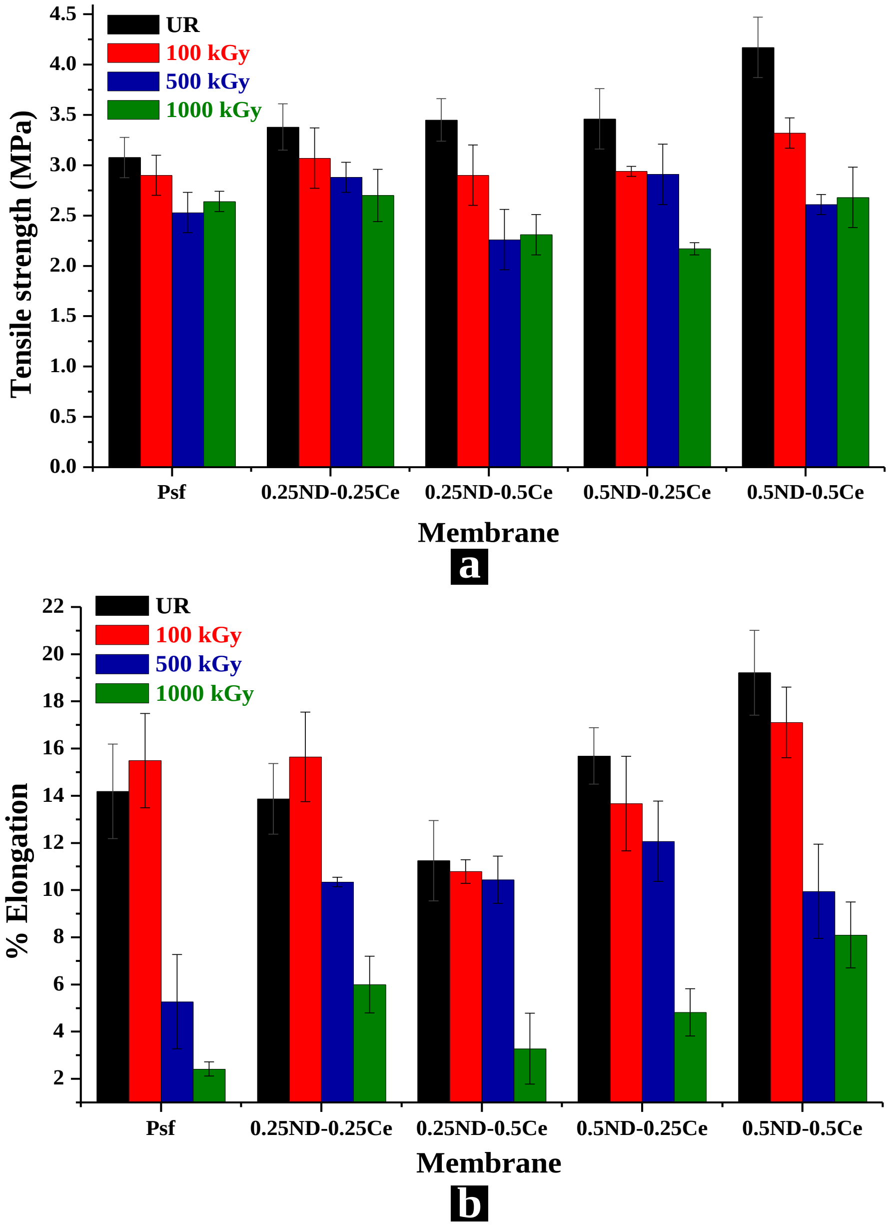

FIGURE 7.7: Mechanical properties of membranes: Variation in (a) tensile strength and (b) percentage elongation at maximum force, with loading of ND and ceria in membrane matrix at different radiation dose.

images in Figure 7.2), permeability is enhanced with slight reduction in rejection attributes. At 1000 kGy of radiation dose, 0.5ND-0.5Ce hybrid membrane shows permeability of 288 $L\ m^{-2}\ h^{-1}$ with 88.5% rejection. This ascertains the resistance of hybrid membranes against chain scissioning and cross-linking phenomena, as also confirmed by consistent molecular weight of hybrid membrane (GPC analysis in Figure 7.5). These results clearly confirm improved performance of membranes and stability in radiation environment with impregnation of ND and ceria nanoparticles.

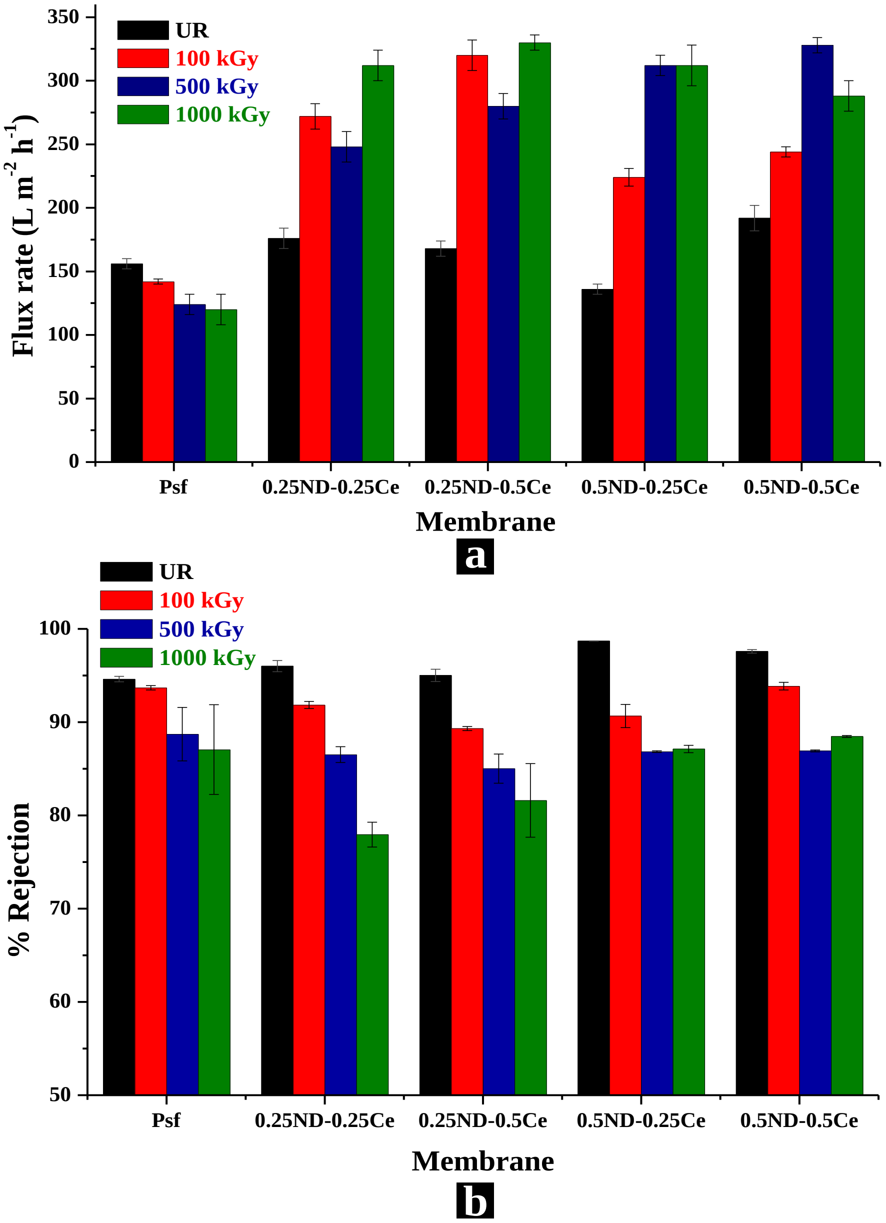

FIGURE 7.8: Variation in (a) pure water permeability and (b) percentage rejection of PEO solute, with loading of ND and ceria in membrane matrix at different radiation dose.

7.3 Summary

Psf-(ND+Ce) hybrid membranes were synthesized by impregnation of ND and ceria into Psf host matrix. Ceria protects Psf membrane matrix by scavenging secondary free radicals generated due to γ-radiolysis of water, while ND provides strength to enhance overall lifetime of membrane under γ-radiation environment. These Psf-(ND+Ce) hybrid membranes are found to offer increased free volume, compared to control Psf membranes, due to enhanced pore density. This results in increased surface roughness and permeability of hybrid membranes, without compromise in selectivity. Mechanical properties of hybrid membranes also get improved in terms of tensile strength and percentage elongation. In addition, loading of ND and ceria makes Psf matrix stable against oxidative degradation at high temperature in radiation environment. All Psf-(ND+Ce) hybrid membranes are found to be stable up to 500 kGy of radiation dose, while 0.5ND-0.5Ce membrane is found to be stable up to 1000 kGy. Hybrid membrane with optimum composition of 0.5 wt% each of ND and ceria is found to be $\sim$ 10 times radiation resistant, compared to control Psf membrane. The present study has made a classic beginning to the development of an important class of hybrid membranes with enhanced radiation stability.

Chapter 8

Conclusions and future work

8.1 Summary of contributions

The research results presented in this thesis have contributed significantly towards development of radiation resistant membranes for expanding the scope of application of polymeric membranes in radioactive effluent treatment. This is a novel research carried out by exploring unique properties of nanomaterials for a specific application domain. The research provids role of nanomaterials, their functionalization, size, as well as combined effect of two nanomaterials on mixed-matrix membranes. Important outcomes of the research are briefly summarized in this Chapter.

Polysulfone-nanodiamond (Psf-ND) mixed-matrix membranes

In Chapter 3, polsulfone-nanodiamond (Psf-ND) MMMs were successfully developed with enhanced radiation resistant attributes. ND loading in Psf membrane matrix was optimised based on the membrane properties and performance in radiation environment. Psf-ND MMM with optimum 0.5% loading of ND was found to be stable up to 500 kGy of radiation dose, without compromise in performance, mechanical and structural properties of the membrane. Radiation resistance property of MMMs was attributed to most important feature of ND, that is hardness, which acts as a potential barrier to γ-radiation. This is in addition to the unique surface chemistry of ND, which protects the polymer chain from disintegration by scavenging secondary free radicals generated in γ-induced radiolysis of water. Psf-ND MMMs will have ~ 5 times enhanced life-span in radiation environment, compared to that of control Psf membrane. Monte Carlo simulation studies confirmed that life-span of Psf-ND MMMs is about 3 years and 8 months for treatment of intermediate level liquid radioactive effluent. However, control Psf membrane will deteriorate in about 9 months.

Polysulfone-carboxylated nanodiamond (Psf-CND) mixed-matrix membranes: Effect of ND funtionalization

Radiation resistant Psf-CND MMMs were examined in Chapter 4 to explore the advantage of additional functionalization of ND. Psf-CND MMMs with 0.5% loading of CND, as optimum, was found to be stable up to 1000 kGy of radiation dose. Additional functionalization over ND surface provided an opportunity for better interaction of CND with polymer matrix, as well as efficient scavanging of free radicals as compared to ND. This offered enhanced protection to membrane matrix from radiation damage. As a result, Psf-CND MMM was found to be ~ 2 times more radiation resistant as compared to Psf-ND MMMs and ~ 10 times as compared to that of control Psf membrane.

Polysulfone-nanodiamond (Psf-ND) mixed-matrix membranes: Effect of ND size

In Chapter 5, effect of ND particle size on the properties of Psf-ND MMMs was observed. Psf membranes embedded with ND particles were synthesized using three different size of NDs, i.e. ND_{10} (10 nm), ND_{250} (250 nm), and ND_{500} (500 nm). ND particles size was optimized based on membrane performance, structural and mechanical properties, as well as stability in radiation environment. Important factor considered and analysed here was the size of nanomaterial and in-turn the surface area to volume ratio, which is responsible for enhanced interaction between nanomaterial and polymer matrix. MMM with loading of ND_{10} was found to enhance membrane properties without any structural change and defects in membrane matrix up to 0.5% loading of ND_{10}, while higher loading leads to agglomaration of ND particles. Though, ND_{250} and ND_{500} particles were homogeneously distributed in membrane matrix even at higher loading, it created defects in membrane matrix due to larger size and also less interaction with Psf matrix. Psf-ND MMM with 10 nm sized ND particles at a loading of 0.5% was found to be optimum composition, which offered ~ 5 times enhanced radiation stability compared to that of control Psf membrane.

Polysulfone-ceria (Psf-ceria) mixed-matrix membranes

Development of radiation resistant Psf-ceria MMMs is described in Chapter 6. Loading of ceria nanoparticles in membrane matrix was optimised based on the performance, structural and mechanical properties of membrane, as well as stability in radiation environment. Psf-ceria MMMs with loading of 1% ceria was found to be optimum, which provided the stability up to 500 kGy of radiation dose. Radiation resistant property of membrane is attributed to unique swapping ability of cerium ions ($Ce^{3+} \leftrightarrow Ce^{4+}$) by scavenging the highly reactive free radicals generated by γ-radiation. Studies determined the kinetics of scavenging of reactive oxygen species and peroxidase-like activity of ceria nanoparticles and their effect in Psf-ceria mixed-matrix membranes. Psf-ceria MMMs provided ~ 5 times enhanced life-span as compared to control Psf membrane.

Polysulfone-(nanodiamond+ceria) [Psf-(ND+Ce)] hybrid mixed-matrix membranes

Combined effect of ND and ceria nanoparticles was explored in Chapter 7, by developing Psf-(ND+Ce) hybrid MMMs. Performance of Psf-(ND+Ce) MMMs was found to be optimum for 0.5% loading of ND and ceria each, which offered stability up to 1000 kGy of radiation dose. This enhanced stability of MMMs ~ 10 times is mainly attributed to radiation hardness of ND and free radical scavenging capability of ceria. Combined effect of both the nanomaterials protects membrane matrix from disintegration in radiation environment, i.e., hardness of ND provides protection of membrane matrix against direct impingement of radiation, while ceria scavenges highly reactive free radicals generated by radiolysis of water and in-turn protects the membrane from free-radical attack.

8.2 Future work

This thesis presented ground research on development of radiation resistant polymeric nanocomposite membranes for treatment of radioactive effluent. Based on experience in this work, recommendations, as mentioned below, can be explored further in view of specific application in industries.

1. Spiral module of radiation resistant MMM can be fabricated and put in actual radioactive effluent treatment for evaluation on on-field performance.

2. MMMs can be synthesized in tubular and capillary configuration for supported liquid membrane applications in radioactive environment.
3. Thin film composite based nanofiltration and reverse osmosis membranes can be fabricated by impregnation of radiation resistant nanomaterials on top layer of polyamide membranes, which will extend the application of these membranes in removal of dissolved radionuclides.
4. Fouling behaviour of radiation resistant MMM in actual radioactive environment can be analysed to assess true life-span of these MMMs.
5. Theoretical studies can be taken up to understand intricate correlations between loading of nanomaterials, radiation dose, membrane morphology, and performance.
6. Role and compatibility of ND and ceria with different other polymeric matrices, like polyethersulfone and polyacrylonitrile, can be studied.

TABLE 8.1: Summary table for all MMMs.

Properties	**Psf-ND MMMs**	**Psf-CND MMMs**	**Psf-Ceria MMMs**	**Psf-(ND+Ce) hybrid MMMs**
Nanomaterial as additive	Nanodiamond (ND)	Carboxylated nanodiamond (CND)	Cerium oxide (ceria)	Nanodiamond and ceria
Properties of nanomaterial utilized	Hardness	Hardness and functionalization	Free radical scavenging	Hardness + free radical scavenging
Optimum loading of nanomaterial	0.5%	0.5%	1%	0.5% each
Contact angle	Decreasing	∼ Constant	Increasing	Increasing
Structural stability up to	500 kGy	1000 kGy	500 kGy	1000 kGy
Mechanical stability up to	500 kGy	1000 kGy	500 kGy	1000 kGy
Permeability	Decreasing	∼ Constant	∼ Constant	Increasing
Rejection	∼ Constant	∼ Constant	∼ Constant	Decreasing
Enhanced life-time	∼ 5 times	∼ 10 times	∼ 5 times	∼ 10 times
Cost compare to Psf module	∼ 2 times	∼ 3 times	∼ 1.2 times	∼ 2 times

Abstract

A broad spectrum of radioactive waste (low, intermediate, and high level) is generated at various stages of nuclear fuel processing (uranium ore mining and milling, fuel fabrication, reactor operation, and spent fuel reprocessing). Hence, safe and effective management of radioactive waste is of utmost importance. Various methods have been established to treat and manage radioactive wastes. These processes typically include chemical treatment, adsorption, filtration, evaporation, ion exchange, extraction, etc. However, these processes have limitations in terms of their efficiency in eliminating all contaminants, high operating cost and/or production of secondary solid wastes.

Membrane technology has been demonstrated for successful removal of radioactive substances with significant advantages over the above-mentioned conventional processes. Inorganic (ceramic) membranes have been found to have excellent stability against the radioactive environment, but their application is limited owing to the difficulty in their fabrication, inherent brittleness, and more importantly, limitation in fine-tuning pore sizes.

Polymeric membranes have gained attention due to their higher flexibility, processability, simple pore formation mechanism, tailorable properties, low cost and negligible secondary waste generation. Also, properties of polymeric membranes can be altered for specific application by functionalization and/or modification in its internal structure (pores/porosity, internal network, etc.), with enhanced thermal, chemical, and mechanical stability. However, application of polymeric membranes is limited in radioactive domain, owing to their low radiation stability.

Since nanomaterials have unique properties such as high surface area, tunability, low density, high porosity, etc., they offer unprecedented opportunities to tailor-make membranes with desirable attributes keeping into account the targeted applications. In polymer nanocomposites, larger surface-to-volume ratio of nanofillers results in a significant increase in the volume of interphase between nanomaterial and polymer, which makes the properties of the composite different from that of bulk polymer.

Two unique materials, namely nanodiamond (ND) and cerium oxide (ceria) nanoparticles were found in literature that have radiation resistant properties. ND and ceria nanoparticles were incorporated into the polysulfone matrix to enhance radiation resistance of polysulfone-nanomaterial mixed matrix membrane.

Major advantages of ND particles over their essential properties for nanocomposite materials are: (i) Superior Young's modulus, hardness, high thermal conductivity and electrical resistivity, low coefficient of friction, chemical stability, and biocompatibility indulged by diamond structure. (ii) Quantum confinement and uniformity in size, provides compatibility for utilization, while eliminating the necessity of costly fractionation procedures. (iii) Stable and approximately spherical shape of ND particles. (iv) High external surface area, offer excessive interaction with polymer matrix. (v) Superabundant and adjustable surface chemistry contributes in wise application of nanocomposite. (vi) Radiation resistant attributes.

Ceria possesses a fluorite crystalline structure, which has emerged as an outstanding material having promising applications in several domains. The Ce atom acquires 4f shell for electron sharing and bonding, and hence, it can undergo conversion between Ce^{4+} and Ce^{3+}. In sync with Ce atom, an oxygen vacancy also gets created, transferred and eliminated. This property can be exploited for absorption of reactive oxygen radicals as well as electron transfer. Moreover, ceria can also act as radiation absorber. The valence switching ability between Ce^{3+} and Ce^{4+} provides reactive oxygen species (ROS) scavenging capability as well as catalytic activity of ceria nanoparticles. These distinctive properties of ceria nanoparticles are utilized to enhance radiation stability of polymeric membranes in the present study for application in treatment of radioactive effluent. Impregnation of ceria in Psf membrane matrix helps to protect the matrix by scavenging ROS ($OH^{\bullet}$, e^{-}_{aq}, H_2O_2, $^{\bullet}H$, H_2, H_3O^{+}) produced by water radiolysis under γ-radiation.

The research work presented in this thesis attempts to enhance the radiation resistant property of polymeric membranes for their sustainable application in radioactive effluent treatment. To achieve the desired objectives, unique properties of ND and ceria nanoparticles were explored and utilized for protection of Psf membrane matrix from consequences of radiation damage and attack of free radicals. Mixed-matrix membranes with enhanced radiation resistance attributes were fabricated and characterized. Following investigations were carried out in this thesis.

1. Effect of reinforcement of ND particles on radiation resistant behaviour of Psf membrane and life-span analysis in radioactive environment.
2. Effect of carboxylated ND and comparison as to how it is superior than ND particles in offering enhanced radiation resistant feature to Psf membrane.
3. Effect of ND size on radiation resistant property of membrane, and finding an optimum size.
4. Effect of ceria nanoparticles on radiation resistant property of Psf membrane and assessment of life-span in radiation environment.
5. Combined effect of reinforcement of both ND and ceria nanoparticles on the radiation resistant property of membrane.

These objectives helped in understanding the role and influence of nanomaterials (ND and ceria) towards enhancing the life of polymeric membrane matrix in radiation environment.

Nomenclature

List of Acronyms

AFM	Atomic force microscope
ATR-FTIR	Attenuated total reflectance Fourier-transform infrared spectroscopy
BET	Brunauer-Emmett-Teller
CND	Carboxylated nanodiamond
CNT	Carbon nanotube
DLS	Dynamic light scattering
DSA	Drop shape analyser
DSC	Differential scanning calorimetry
E	Elongation
ED	Electrodialysis
EDS	Energy dispersive X-ray spectrometer
FESEM	Field emission scanning electron microscope
GO	Graphene oxide
GPC	Gel permeation chromatography
HLW	High-level waste
ILW	Intermediate-level waste
LLW	Low-level waste
LRW	Liquid radioactive waste

MF	Microfiltration
MG	Triphenyl methane dye
MMM	Mixed-matrix membrane
MWNT	Multiple-walled carbon nanotube
ND	Nanodiamond
ND_{10}	10 nm sized nanodiamond
ND_{250}	250 nm sized nanodiamond
ND_{500}	500 nm sized nanodiamond
NF	Nanofiltration
NMP	N-methyl-2-pyrrolidone
PALS	Positron annihilation lifetime spectroscopy
PEO	Polyethylene oxide
Psf	Polysulfone
PVP	Polyvinyl pyrrolidone
PWP	Pure water permeability
rGO	Reduced graphene oxide
RMS	Root mean square
RO	Reverse osmosis
ROS	Reactive oxygen species
SAED	Selected area electron diffraction
SAXS	Small angle X-ray scattering
SWNT	Single-walled carbon nanotube
TEM	Transmission electron microscope
TFC	Thin film composite
THF	Tetrahydrofuran
TS	Tensile strength
UF	Ultrafiltration

UTM	Universal testing machine
UV	Ultraviolet
VLLW	Very low-level waste
WAO	Wet air oxidation
XPS	X-ray photoelectron spectroscopy
XRD	X-ray diffraction

List of Symbols

$(C_s)_{ln}$	Logarithmic concentration
$\%R_{PEO}$	Percentage rejection of PEO solute
A	Membrane area
A_k	Ratio of total cross-sectional pore area to the effective membrane area
C_1	q independent constant parameter
C_2	q independent constant parameter
C_3	q independent constant parameter
C_4	q independent constant parameter
C_f	Concentration in feed stream
C_m	Concentration of solute on membrane surface
C_p	Concentration in permeate stream
Ce_{Ce}^{X}	Neutral cerium
Ce'_{Ce}	Ce^{3+} atom in a Ce^{4+} site
D_R	Radiation dose (kGy) in which membrane were exposed
e_{aq}^{-}	Hydrated electron
$f(q)$	Correction factor
$F(t)$	Number of counts at time t
$g(q)$	Correction factor

H_2O_2	Hydrogen peroxide
I_3	Relative intensity of third lifetime component
I_i	Intensity of i^{th} component
J_s	Solute flux
J_v	Solvent flux
k	Number of exponential decays
K_m	Menten constants
L_p	Filtration coefficient
L_{ND}	ND loading (%) in the membrane matrix
M_w	Weighted average molecular weight
O_O^X	Neutral oxygen
$OH^\bullet$	Hydroxyl radical
R_E	Solute rejection value obtained experimentally
R_M	Solute rejection value obtained from mathematical modelling
r_p	Pore radius
r_s	Solute radius
S_D	Steric hindrance factor for diffusion
S_F	Steric hindrance factor for filtration flow
T	Time period
t	Time
V	Initial velocity
$V_{\ddot{O}}$	+2 oxygen vacancy
V_{max}	Maximum initial velocity
Ce	Cerium
D	Diffusivity of solute
D(r)	Particle size distribution
f	Relative fractional free volume

G	Radiation chemical yield
I(q)	Radial average scattering intensity
K	Correction factor
P(q,r)	Form factor of a spherical particle of radius r
q	Wave vector transfer
R	Average radius of spherical free volume
S(q,r)	Structure factor
V	Volume

List of Greek Symbols

2θ	Scattering angle
$\delta\pi$	Osmotic pressure difference between the fluid on membrane surface and product stream
δp	Pressure drop across the membrane
δX	Pore length
ϵ	Extinction coefficient
λ	Wavelength
ω	Solute permeability
σ	Reflection coefficient
τ_3	Third lifetime component
τ_i	Lifetime of i^{th} component

Appendix A

Membrane pore size distribution

Pore size distribution for all the membranes was determined with the help of BET analysis. Figure A.1, A.2, A.3, and A.4 shows the pore size distribution of unirradiated, 100 kGy irradiated, 500 kGy irradiated, and 1000 kGy irradiated membranes, respectively.

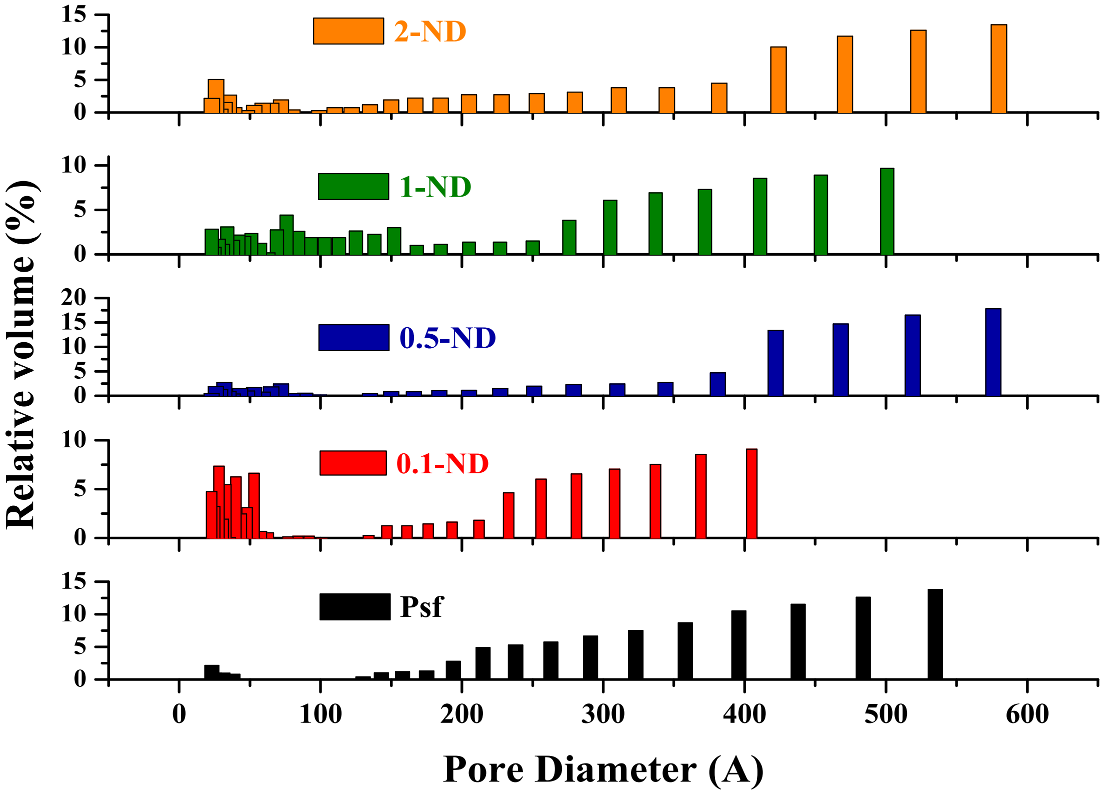

Figure A.1: Pore size distribution of the unirradiated Psf-ND membranes.

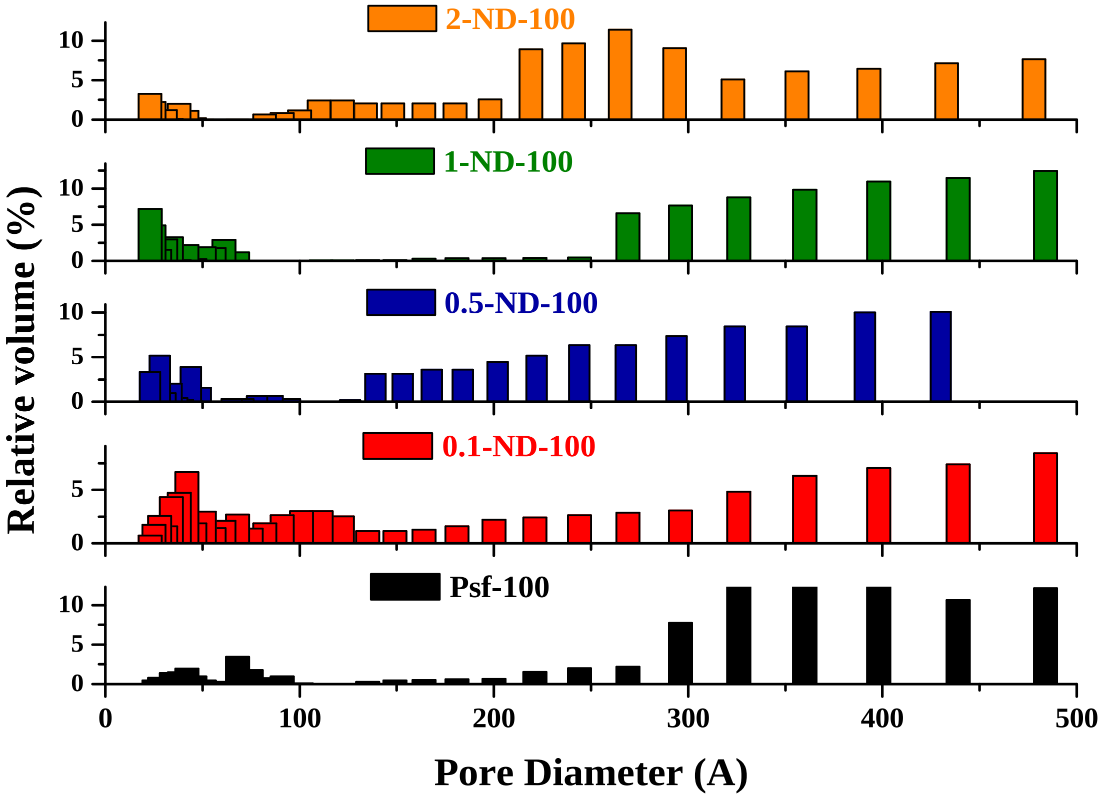

Figure A.2: Pore size distribution of 100 kGy irradiated Psf-ND membranes.

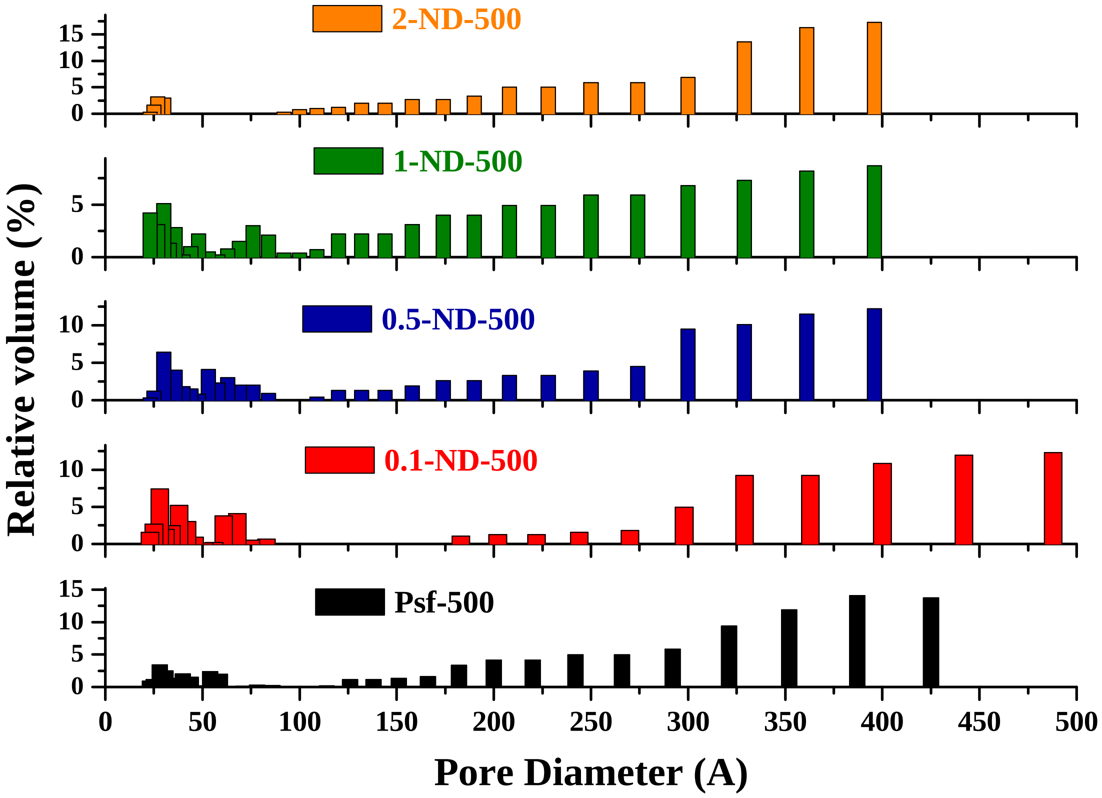

Figure A.3: Pore size distribution of 500 kGy irradiated Psf-ND membranes.

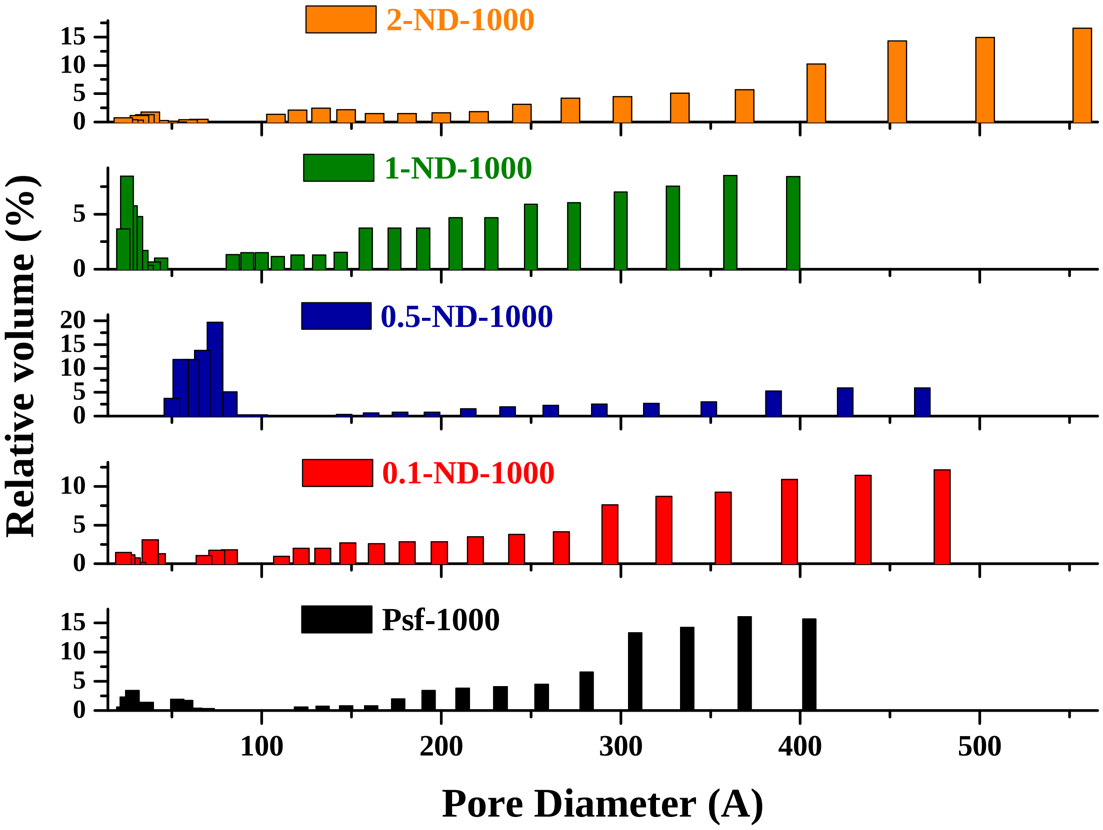

Figure A.4: Pore size distribution of 1000 kGy irradiated Psf-ND membranes.

Appendix B

Hansen solubility parameters

Before introducing concepts and the theory developed by Charles Hansen, it is beneficial to give a short physical argument about the solvation process [287]. For any solution to occur spontaneously, thermodynamics requires that the Gibbs free energy change in the mixing process be zero or negative. In a simplified description, the Gibbs free energy ΔG^M can be divided in two parts, as shown in Equation (B.1).

$$\Delta G^M = \Delta G^M_{comb} + \Delta G^M_{noncomb} \tag{B.1}$$

where the combinatorial part ΔG^M_{comb} is related to the combinatorial entropy change ΔS^M_{comb} (that results by simply mixing components) by Equation (B.2).

$$\Delta G^M_{comb} = -T\Delta S^M_{comb} \tag{B.2}$$

and the noncombinatorial part $\Delta G^M_{noncomb}$ refers to all other free energy effects, including the heat of mixing, and can be calculated by Equation (B.3).

$$\Delta G^M_{noncomb} = \varphi_1 \varphi_2 V_M (\delta_1 - \delta_2)^2 \tag{B.3}$$

In the above equations, T is the absolute temperature, φ_1 and φ_2 are volume fractions of solvent and polymer/nanomaterial, V_M is the volume of the mixture and δ_1 and δ_2 are called solubility parameters of solvent and polymer/nanomaterial. By analysing Equation (B.1), (B.2) and (B.3), one can see that the difference in solubility parameters for the solvent-solute pair is important in determining the system energy equilibrium. It is clear that a match in solubility parameters leads to a zero change in noncombinatorial free energy and the positive entropy change (the combinatorial entropy change), found in simple mixing to result in a disordered mixture compared to the pure components, will ensure that a solution is possible from a thermodynamic point of view. The maximum difference in solubility parameters that can be tolerated for a solution that still occurs corresponds to the case $\Delta G^{M}_{comb} = 0$. From Equation (B.1), (B.2) and (B.3), this condition can be expressed as in Equation (B.4).

$$(\delta_1 - \delta_2)^2 = (T\Delta S^{M}_{comb})/(\varphi_1\varphi_2 V_M) \tag{B.4}$$

Equation (B.4) clearly shows that an alternate view of the solubility situation at its limit is that it is the entropy change that dictates how closely the solubility parameters must match each other for the mixture to stabilize.

Solubility parameters are sometimes called cohesion energy parameters as they derive from the energy required to convert a liquid to a gas state. All types of bonds holding molecules together are broken in the vaporization process. Thus the energy of vaporization is a direct measure of the total cohesive energy holding the liquid molecules together and both can be considered as being identical to each other. The term solubility parameter was first used by Hildebrand in 1949 [288]. The Hildebrand solubility parameter is defined as the square root of the total cohesive energy density, as in Equation (B.5).

$$\delta = (E/V)^{1/2} \tag{B.5}$$

where V is the molar volume of the pure solvent and E is its (measurable) energy of vaporization.

The Hildebrand solubility parameters are applicable to the regular solutions, which implies strictly nonpolar systems. As this is not the case for most real systems, other researchers have tried to extend Hildebrands original idea, splitting the Hildebrand solubility parameter into two or more components. The approach proposed by Charles Hansen in 1967 is one of the most proeminent in this regard [289].

The basis of Hansen solubility parameters (HSPs) is that the total cohesive energy (E) of a liquid consists of three major intermolecular interactions: (nonpolar) dispersion forces, (polar) permanent dipole-permanent dipole forces, and (polar) hydrogen bonding. The most general is the nonpolar cohesive energy (E_D), derived from induced dipole forces and also called atomic or dispersion interactions in scientific literature. All molecules contain these types of attractive forces. The second type is the polar cohesion energy (E_P), which results from inherently molecular interactions and is essential found in polar (non-centrosymmetric) molecules. The molecular dipole moment is the primary parameter used to calculate it. The third major cohesive energy source (E_H) comes from hydrogen bonds which, according to a modern definition [290], are “attractive interactions between a hydrogen atom from a molecule or a molecular fragment X-H in which X is more electronegative than H and an atom or a group of atoms in the same or a different molecule in which there is evidence of bond formation”.

Therefore, the basic equation governing the assignment of Hansen parameters is that E must be the sum of the individual energies that make it up, as in Equation (B.6).

$$E = E_D + E_P + E_H \tag{B.6}$$

Dividing this by the molar volume gives the square of the total (or Hildebrand) solubility parameter as the sum of the squares of Hansen components, shown in Equation (B.7).

$$E/V = (E_D/V) + (E_P/V) + (E_H/V) \tag{B.7}$$

$$(\delta)^2 = (\delta_D)^2 + (\delta_P)^2 + (\delta_H)^2 \tag{B.8}$$

Within Hansen space, a solute is represented not only by their HSPs, as with solvents, but also by an interaction radius (R_0), thus defining a solubility sphere whose centre coordinates are the HSPs ($\delta_D, \delta_P, \delta_H$). All substances qualified as good solvents for the solute should stay within this sphere and all considered bad (nonsolvents) should lie outside. A useful parameter for comparing two substances is the solubility parameter distance (R_a), based on their respective HSP components, expressed in Equation (B.9).

$$(R_a)^2 = 4(\delta_{D2} - \delta_{D1})^2 + (\delta_{P2} - \delta_{P1})^2 + (\delta_{H2} - \delta_{H1})^2 \tag{B.9}$$

The solubility, or high affinity, requires $R_a < R_0$, so a RED (Relative Energy Difference) number is often used to quantify distances R_a relative to the interaction radius R_0, as shown in Equation (B.10).

$$RED = R_a/R_0 \tag{B.10}$$

By this definition, $RED = 0$ is equivalent to no energy difference, $RED < 1$ indicates high solute-solvent affinity, $RED > 1$ indicates low affinity and $RED = 1$ (or around 1) reflects a boundary condition.

Table B.1: Hansen solubility parameters.

Material	δ_D	δ_P	δ_H	R_0	**RED**	**Remarks**
NMP	18.0	12.3	7.2	-	-	-
Psf	19.6	10.8	9.2	6.2	0.655	Soluble in NMP
ND	15.9	10.0	8.0	8.4	0.588	Well dispersed in NMP
					0.473	Strong affinity with Psf

Hansen solubility parameters [291, 292] in Table B.1 shows that the polysulfone (Psf) is soluble in the N-methyl 2-pyrrolidone (NMP). Furthermore, Nanodiamond (ND) particles are highly dispersible in NMP and shows strong affinity with Psf matrix.

Appendix C

Long term performance of MMMs and nanomaterial leaching study

C.1 Long term performance study of Psf-ND MMMs

Long term stability of ND particles in Psf-ND MMMs has been determined by measuring pure water permeability of 0.5-ND (optimum loading of ND) membrane over a duration 200 h, as shown in Figure C.1. A consistent permeability values gives an indication for stability of ND particles in MMM.

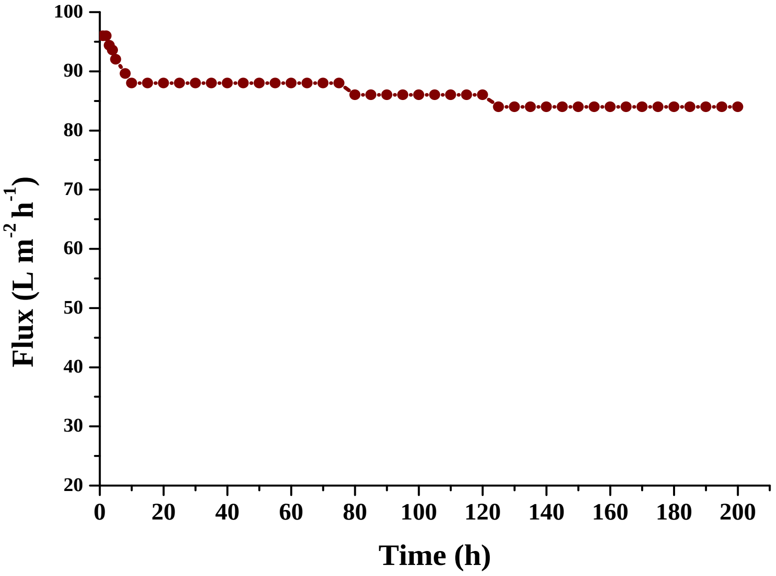

FIGURE C.1: Variation in pure water permeability of 0.5-ND membrane with the time up to 200 h.

Leaching of ND through membrane has been determined by keeping the membranes in solutions at different pH values (pH: 5, 6, 7, 8, and 9) for 100 h followed by analysis using total organic carbon (TOC) analyser. There is no detectable leaching of ND observed.

C.2 Long term performance study of Psf-CND MMMs

Long term stability of CND particles in Psf-CND MMMs has been determined by measuring pure water permeability of 0.5-CND (optimum loading of CND) membrane over 200 h duration, as shown in Figure C.2. A consistent permeability values gives an indication for stability of CND particles in MMM.

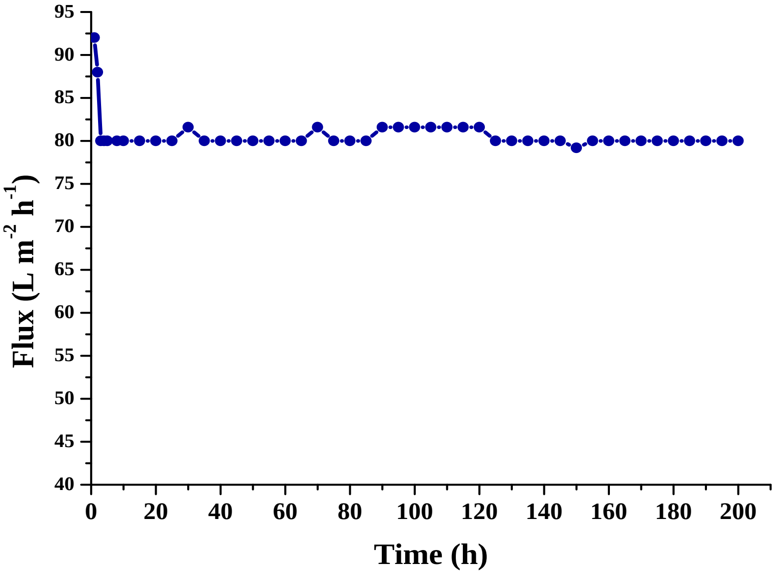

FIGURE C.2: Variation in pure water permeability of 0.5-CND membrane with the time up to 200 h.

Leaching of CND through membrane has been determined by keeping the membranes in solutions at different pH values (pH: 5, 6, 7, 8, and 9) for 100 h followed by analysis using total organic carbon (TOC) analyser. There is no detectable leaching of CND observed.

C.3 Long term performance study of Psf-ceria MMMs

Long term stability of ceria nanoparticles in Psf-ceria MMMs has been determined by measuring pure water permeability of 0.5-Ce (optimum loading of ceria) membrane over 200 h duration, as shown in Figure C.3. The consistent permeability indicates the stability of ceria in MMM.

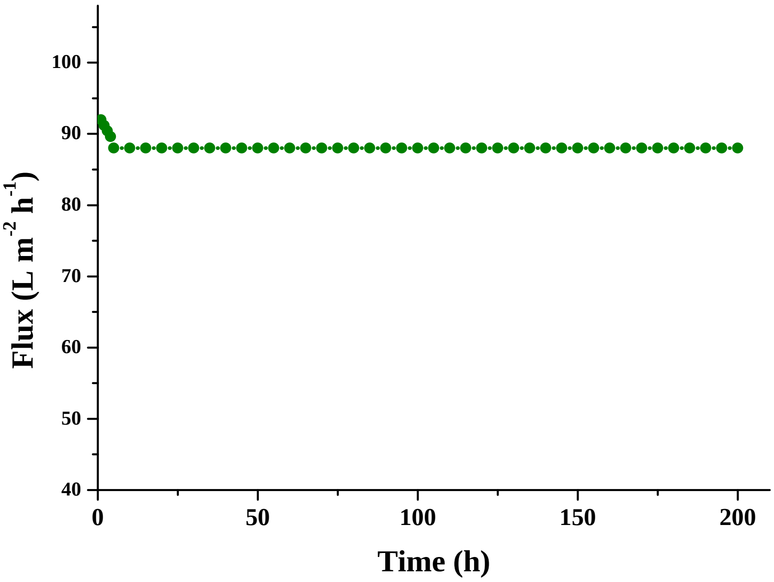

Figure C.3: Variation in pure water permeability of 0.5-Ce membrane with the time up to 200 h.

Leaching of ceria through membrane has been determined using ICP-OES analysis of cerium by collecting the permeate samples in every 10 h and no detectable leaching of ceria was observed up to 200 h. Similar findings are obtained upon exposure of membranes to different pH (5, 6, 7, 8, and 9) solutions, which confirm the stability of ceria in the MMM.

C.4 Long term performance study of Psf-(ND+Ce) MMMs

Long term stability of ND and ceria nanoparticles in Psf-(ND+Ce) hybrid MMMs has been determined by measuring pure water permeability of 0.5ND-0.5Ce (optimum loading of ND and ceria) membrane over 200 h duration, as shown in Figure C.4. A consistent permeability over this duration depicts the stability of ND and ceria in MMM.

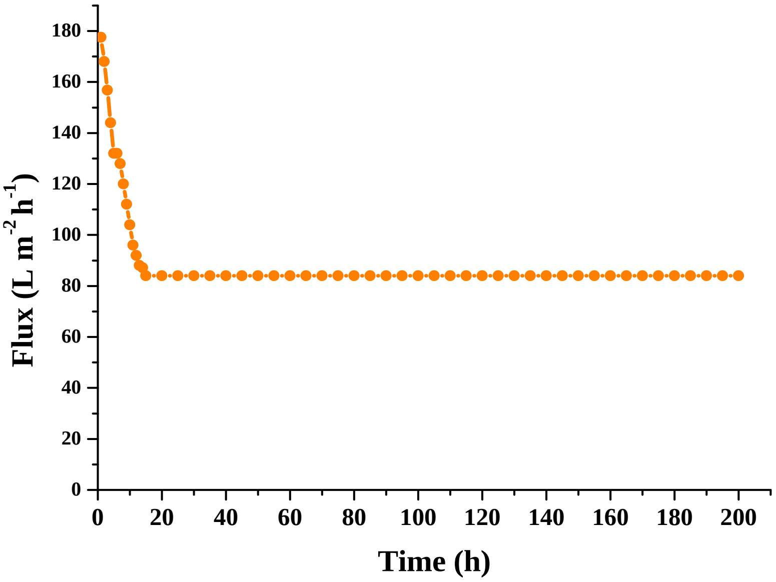

Figure C.4: Variation in pure water permeability of 0.5ND-0.5Ce hybrid membrane with the time up to 200 h.

Leaching of ND through membrane in acidic medium has been determined by keeping the membranes in solutions at different pH values (pH: 5, 6, 7, 8, and 9) for 100 h followed by analysis using total organic carbon (TOC) analyser. There is no detectable leaching of ND observed. However, leaching of ceria through membrane has been determined using ICP-OES analysis of cerium by collecting the permeate samples in every 10 h and no detectable leaching of ceria was observed up to 200 h. Similar findings are obtained upon exposure of membranes to different pH (5, 6, 7, 8, and 9) solutions, which confirm the stability of ceria in the MMM.

Appendix D

Cost estimation

UF module (spiral 2512) consists of $1m^2$ area of polysulfone membrane on the support of polyester woven fabric, feed spacer, and product collection tube. To sythesize $1m^2$ polysulfone UF layer, it required 25 gm polysulfone, 7.5 gm PVP, and 100 ml NMP.

Cost of Psf UF module = Rs. 500

D.1 Cost estimation of Psf-ND MMM module

Optimum loading of nanodiamond (ND) in Psf-ND MMM is 0.5%. Quantity of ND particles required for $1m^2$ membrane module is 0.125 gm.

Price of ND = Rs. 5099/ gm

Cost of 0.125 gm ND = Rs. 637

Cost of Psf-ND MMM UF module = Rs. 1137

The cost of Psf-ND MMM module increased by ~ 2 times, as compare to the Psf module. However, it will provide the enhanced life span more than 5 times, as compare to Psf module.

D.2 Cost estimation of Psf-CND MMM module

Optimum loading of carboxylated nanodiamond (CND) in Psf-CND MMM is 0.5%. Quantity of CND particles required for $1m^2$ membrane module is 0.125 gm.

Price of CND = Rs. 9024/ gm

Cost of 0.125 gm CND = Rs. 1128

Cost of Psf-CND MMM UF module = Rs. 1628

The cost of Psf-CND MMM module increased by $\sim$ 3 times, as compare to the Psf module. However, it will provide the enhanced life span more than 10 times, as compare to Psf module.

D.3 Cost estimation of Psf-ceria MMM module

Optimum loading of cerium oxide (ceria) nanoparticles in Psf-ceria membrane is 1%. Quantity of ceria nanoparticles required for $1m^2$ membrane module is 0.25 gm.

Price of ceria nanoparticles = Rs. 11688/ 25 gm

Cost of 0.25 gm ceria = Rs. 117

Cost of Psf-ceria MMM UF module = Rs. 617

The cost of Psf-ceria MMM module increased by only $\sim$ 1.2 times, as compare to the Psf module. Nevertheless, it will provide the enhanced life span more than 5 times, as compare to Psf module.

D.4 Cost estimation of Psf-(ND+ceria) hybrid MMM module

Optimum loading of ND and ceria nanoparticles in Psf-(ND+ceria) hybrid membrane is 0.5% each. Quantity of ND and ceria nanoparticles required for $1m^2$ membrane module is 0.125 gm each.

Cost of 0.125 gm ND = Rs. 637

Cost of 0.125 gm ceria = Rs. 58.5

Cost of Psf-(ND+ceria) hybrid MMM UF module = Rs. 1195.5

The cost of Psf-(ND+ceria) hybrid MMM module increased by ~ 2 times, as compare to the Psf module. However, it will provide the enhanced life span more than 10 times, as compare to Psf module.

Bibliography

[1] P. D. Wilson, “The nuclear fuel cycle from ore to wastes,” 1996.

[2] L. E. Roberts, “Radioactive waste management,” *Annual Review of Nuclear and Particle Science*, vol. 40, no. 1, pp. 79–112, 1990.

[3] R. E. Berlin and C. C. Stanton, “Radioactive waste management,” 1988.

[4] M. I. Ojovan and W. E. Lee, *An introduction to nuclear waste immobilisation.* Newnes, 2013.

[5] C. Hill, J.-F. Dozol, V. Lamare, H. Rouquette, S. Eymard, B. Tournois, J. Vicens, Z. Asfari, C. Bressot, R. Ungaro *et al.*, “Nuclear waste treatment by means of supported liquid membranes containing calixcrown compounds,” in *Calixarenes 50th Anniversary: Commemorative Issue.* Springer, 1994, pp. 399–408.

[6] International atomic energy agency, *Application of Membrane Technologies for Liquid Radioactive Waste Processing*, ser. Technical Reports Series. International atomic energy agency, 2004, no. 431.

[7] Y. Lu, T. Chen, X. Chen, M. Qiu, and Y. Fan, “Fabrication of TiO_2-doped ZrO_2 nanofiltration membranes by using a modified colloidal sol-gel process and its application in simulative radioactive effluent,” *Journal of Membrane Science*, vol. 514, pp. 476–486, 2016.

[8] W. Koros, G. Fleming, S. Jordan, T. Kim, and H. Hoehn, “Polymeric membrane materials for solution-diffusion based permeation separations,” *Progress in Polymer Science*, vol. 13, no. 4, pp. 339–401, 1988.

[9] S. A. Piletsky, H. Matuschewski, U. Schedler, A. Wilpert, E. V. Piletska, T. A. Thiele, and M. Ulbricht, “Surface functionalization of porous polypropylene membranes with molecularly imprinted polymers by photograft copolymerization in water,” *Macromolecules*, vol. 33, no. 8, pp. 3092–3098, 2000.

[10] N. Combernoux, L. Schrive, V. Labed, Y. Wyart, E. Carretier, A. Benony-Rhodier, and P. Moulin, “Study of polyamide composite reverse osmosis

membrane degradation in water under gamma rays," *Journal of Membrane Science*, vol. 480, pp. 64 – 73, 2015.

[11] A. S. Edelstein and R. Cammaratra, *Nanomaterials: synthesis, properties and applications*. CRC press, 1998.

[12] R. A. Damodar, S.-J. You, and H.-H. Chou, "Study the self cleaning, antibacterial and photocatalytic properties of TiO_2 entrapped pvdf membranes," *Journal of hazardous materials*, vol. 172, no. 2-3, pp. 1321–1328, 2009.

[13] P. Tewari, *Nanocomposite Membrane Technology: Fundamentals and Applications*. CRC Press, 2015.

[14] K. Rao, "Radioactive waste: The problem and its management," *current science*, vol. 81, no. 12, pp. 1534–1546, 2001.

[15] M. I. Ojovan, W. E. Lee, and S. N. Kalmykov, *An introduction to nuclear waste immobilisation*. Elsevier, 2019.

[16] D. McGinnes, "Waste sources and classification," *Radioactivity in the Environment*, vol. 9, pp. 8–40, 2007.

[17] N. Khelurkar, S. Shah, and H. Jeswani, "A review of radioactive waste management," in *2015 International Conference on Technologies for Sustainable Development (ICTSD)*. IEEE, 2015, pp. 1–6.

[18] R. P. Rechard, M. S. Tierney, L. C. Sanchez, and M.-A. Martell, "Bounding estimates for critical events when directly disposing highly enriched spent nuclear fuel in unsaturated tuff," *risk analysis*, vol. 17, no. 1, pp. 19–35, 1997.

[19] W. Lee, M. Ojovan, M. Stennett, and N. Hyatt, "Immobilisation of radioactive waste in glasses, glass composite materials and ceramics," *Advances in Applied Ceramics*, vol. 105, no. 1, pp. 3–12, 2006.

[20] J. Lento and R. Harjula, "Separation of cesium from nuclear waste solutions with hexacyanoferrate (ii) s and ammonium phosphomolybdate," *Solvent Extraction and Ion Exchange*, vol. 5, no. 2, pp. 343–352, 1987.

[21] S. A. Khan, M. A. Khan *et al.*, "Adsorption of chromium (iii), chromium (vi) and silver (i) on bentonite," *Waste Management*, vol. 15, no. 4, pp. 271–282, 1995.

[22] K. Raj, K. Prasad, and N. Bansal, "Radioactive waste management practices in india," *Nuclear Engineering and Design*, vol. 236, no. 7-8, pp. 914–930, 2006.

[23] E. P. Horwitz, M. L. Dietz, R. Chiarizia, H. Diamond, S. L. Maxwell III, and M. R. Nelson, "Separation and preconcentration of actinides by extraction chromatography using a supported liquid anion exchanger: application to the characterization of high-level nuclear waste solutions," *Analytica Chimica Acta*, vol. 310, no. 1, pp. 63–78, 1995.

[24] X. Sun, H. Luo, and S. Dai, "Ionic liquids-based extraction: a promising strategy for the advanced nuclear fuel cycle," *Chemical reviews*, vol. 112, no. 4, pp. 2100–2128, 2011.

[25] R. Rahman, H. A. Ibrahium, and Y. T. Hung, "Liquid radioactive wastes treatment: a review," *Water*, vol. 3, no. 2, pp. 551–565, 2011.

[26] "3 processing liquid and solid radioactive wastes," in *Disposal of Radioactive Wastes*, ser. Studies in Environmental Science, Z. Dlouh, Ed. Elsevier, 1982, vol. 15, pp. 65 – 97.

[27] J. Mulder, *Basic principles of membrane technology.* Springer Science & Business Media, 2012.

[28] N. N. Li, A. G. Fane, W. W. Ho, and T. Matsuura, *Advanced membrane technology and applications.* John Wiley & Sons, 2011.

[29] N. L. Le and S. P. Nunes, "Materials and membrane technologies for water and energy sustainability," *Sustainable Materials and Technologies*, vol. 7, pp. 1–28, 2016.

[30] D. Humpert, M. Ebrahimi, and P. Czermak, "Membrane technology for the recovery of lignin: A review," *Membranes*, vol. 6, no. 3, p. 42, 2016.

[31] S. Nunes and K. Peinemann, "Membrane technology wiley online library," 2001.

[32] G. Zakrzewska-Trznadel, M. Harasimowicz, and A. G. Chmielewski, "Membrane processes in nuclear technology-application for liquid radioactive waste treatment," *Separation and purification technology*, vol. 22, pp. 617–625, 2001.

[33] A. G. Chmielewski, M. Harasimowicz, B. Tyminski, and G. Zakrzewska-Trznadel, "Concentration of low-and medium-level radioactive wastes with three-stage reverse osmosis pilot plant," *Separation Science and Technology*, vol. 36, no. 5-6, pp. 1117–1127, 2001.

[34] L. Buckley, S. Bushart, V. Efremenkov, Y. Karlin, R. Kohout, A. Pabby, and G. Tapsell, "Application of membrane technologies for liquid radioactive waste processing," *IAEA-TRS No. 431. 2004. 145 p*, 2004.

[35] A. Giwa, N. Akther, V. Dufour, and S. W. Hasan, "A critical review on recent polymeric and nano-enhanced membranes for reverse osmosis," *Rsc Advances*, vol. 6, no. 10, pp. 8134–8163, 2016.

[36] G. M. Geise, D. R. Paul, and B. D. Freeman, "Fundamental water and salt transport properties of polymeric materials," *Progress in Polymer Science*, vol. 39, no. 1, pp. 1–42, 2014.

[37] B. D. Freeman, "Basis of permeability/selectivity tradeoff relations in polymeric gas separation membranes," *Macromolecules*, vol. 32, no. 2, pp. 375–380, 1999.

[38] J. Nicolas, S. Mura, D. Brambilla, N. Mackiewicz, and P. Couvreur, "Design, functionalization strategies and biomedical applications of targeted biodegradable/biocompatible polymer-based nanocarriers for drug delivery," *Chemical Society Reviews*, vol. 42, no. 3, pp. 1147–1235, 2013.

[39] F. Wang, T. Chen, and J. Xu, "Sodium sulfonate-functionalized poly (ether ether ketone) s," *Macromolecular Chemistry and Physics*, vol. 199, no. 7, pp. 1421–1426, 1998.

[40] M. Ulbricht, "Advanced functional polymer membranes," *Polymer*, vol. 47, no. 7, pp. 2217–2262, 2006.

[41] N. Nady, M. C. Franssen, H. Zuilhof, M. S. M. Eldin, R. Boom, and K. Schroën, "Modification methods for poly (arylsulfone) membranes: A mini-review focusing on surface modification," *Desalination*, vol. 275, no. 1-3, pp. 1–9, 2011.

[42] K. Murakami and H. Kudo, "Gamma-rays irradiation effects on polysulfone at high temperature," *Nuclear Instruments and Methods in Physics Research Section B: Beam Interactions with Materials and Atoms*, vol. 265, no. 1, pp. 125–129, 2007.

[43] N. Fortin, B. Albela, L. Bonneviot, S. Rouif, J. Y. Sanchez, D. Portinha, and E. Fleury, "How does γ-irradiation affect the properties of a microfiltration membrane constituted of two polymers with different radiolytic behavior?" *Radiation Physics and Chemistry*, vol. 81, no. 3, pp. 331–338, 2012.

[44] V. Ramachandhran and B. Misra, "Studies on effect of irradiation on semipermeable membranes," *Journal of Applied Polymer Science*, vol. 27, no. 9, pp. 3427–3435, 1982.

[45] G. Zakrzewska-Trznadel, "Advances in membrane technologies for the treatment of liquid radioactive waste," *Desalination*, vol. 321, pp. 119–130, 2013.

[46] A. K. Pabby, "Membrane techniques for treatment in nuclear waste processing: global experience," *Membrane technology*, vol. 2008, no. 11, pp. 9–13, 2008.

[47] A. K. Pabby, J. V. Sonawane, and A. M. Sastre, "Membrane-based techniques for nuclear waste processing," *Encyclopedia of Membrane Science and Technology*, pp. 1–21, 2013.

[48] W. Miles Jr, M. Poirier, and D. Brown, "F/h effluent treatment facility filtration upgrade alternative evaluations overview," Westinghouse Savannah River Co., Aiken, SC (United States), Tech. Rep., 1992.

[49] B. Chaufer and A. Deratani, "Removal of metal ions by complexation-ultrafiltration using water-soluble macromolecules: perspective of application to wastewater treatment," *Nuclear and chemical waste management*, vol. 8, no. 3, pp. 175–187, 1988.

[50] I. Cumming and A. Turner, "Recent developments in testing new membrane systems at aere harwell for nuclear applications," in *Future industrial prospects of membrane processes*, 1989.

[51] V. Ramachandhran, S. Samanta, and B. Misra, "Radiocerium separation behavior of ultrafiltration membranes," *Journal of radioanalytical and nuclear chemistry*, vol. 237, no. 1-2, pp. 121–124, 1998.

[52] A. P. Kryvoruchko, L. Y. Yurlova, I. D. Atamanenko, and B. Y. Kornilovich, "Ultrafiltration removal of u (vi) from contaminated water," *Desalination*, vol. 162, pp. 229–236, 2004.

[53] Y. Karlin, D. Gorbachev, A. Volkov, and A. Barinov, "Advantageous technology for treatment of laundry waters," Tech. Rep., 2001.

[54] K. Suzuki, M. Hirano, T. Nakashima, R. Baker, and P. Baldwin, "A study of removal of hazardous metals and radionuclides in groundwater," in *Proc. Waste Management Conf. Tucson, AZ*, 1997, p. 29.

[55] L. Buckley, S. Vijayan, and P. Wong, "Remediation process technology for ground water," in *Proceedings of the 1993 international conference on nuclear waste management and environmental remediation. Volume 2: High level radioactive waste and spent fuel management*, 1993.

[56] B. Van der Bruggen, C. Vandecasteele, T. Van Gestel, W. Doyen, and R. Leysen, "A review of pressure-driven membrane processes in wastewater treatment and drinking water production," *Environmental progress*, vol. 22, no. 1, pp. 46–56, 2003.

[57] J. Yin and B. Deng, “Polymer-matrix nanocomposite membranes for water treatment,” *Journal of membrane science*, vol. 479, pp. 256–275, 2015.

[58] Y. Wang, K. S. Chen, J. Mishler, S. C. Cho, and X. C. Adroher, “A review of polymer electrolyte membrane fuel cells: Technology, applications, and needs on fundamental research,” *Applied energy*, vol. 88, no. 4, pp. 981–1007, 2011.

[59] W. J. Koros and G. Fleming, “Membrane-based gas separation,” *Journal of membrane science*, vol. 83, no. 1, pp. 1–80, 1993.

[60] M. M. Amiji, “Permeability and blood compatibility properties of chitosan-poly (ethylene oxide) blend membranes for haemodialysis,” *Biomaterials*, vol. 16, no. 8, pp. 593–599, 1995.

[61] R. Boock, M. A. Rixman, H. Zhang, M. J. Estes, and K. Lawrence, “Polymer membranes for continuous analyte sensors,” Oct. 1 2009, uS Patent App. 12/413,166.

[62] A. Salahi, A. Gheshlaghi, T. Mohammadi, and S. S. Madaeni, “Experimental performance evaluation of polymeric membranes for treatment of an industrial oily wastewater,” *Desalination*, vol. 262, no. 1-3, pp. 235–242, 2010.

[63] K. L. Nash and G. J. Lumetta, *Advanced separation techniques for nuclear fuel reprocessing and radioactive waste treatment.* Elsevier, 2011.

[64] A. Davis, “Comparison of the thermal and thermo oxidative stability of polycarbonate, polyphenylene oxide, polysulphone and two polyarylates,” *Die Makromolekulare Chemie: Macromolecular Chemistry and Physics*, vol. 132, no. 1, pp. 23–33, 1970.

[65] H. Vogel, “Polyarylsulfones, synthesis and properties,” *Journal of Polymer Science Part A-1: Polymer Chemistry*, vol. 8, no. 8, pp. 2035–2047, 1970.

[66] J. Brown and J. O’Donnell, “The radiation stability of an aromatic polysulfone,” *Journal of Polymer Science Part B: Polymer Letters*, vol. 8, no. 2, pp. 121–126, 1970.

[67] M. Khayet, “Treatment of radioactive wastewater solutions by direct contact membrane distillation using surface modified membranes,” *Desalination*, vol. 321, pp. 60–66, 2013.

[68] L. Y. Ng, A. W. Mohammad, C. P. Leo, and N. Hilal, “Polymeric membranes incorporated with metal/metal oxide nanoparticles: a comprehensive review,” *Desalination*, vol. 308, pp. 15–33, 2013.

[69] J. Brown and J. O'Donnell, "Effects of gamma radiation on two aromatic polysulfones," *Journal of Applied Polymer Science*, vol. 19, no. 2, pp. 405–417, 1975.

[70] N. N. Rupiasih and P. Vidyasagar, "Comparative study of effect of low and medium dose rate of γ irradiation on microporous polysulfone membrane using spectroscopic and imaging techniques," *Polymer Degradation and Stability*, vol. 93, no. 7, pp. 1300–1307, 2008.

[71] S. Le Caër, "Water radiolysis: influence of oxide surfaces on h2 production under ionizing radiation," *Water*, vol. 3, no. 1, pp. 235–253, 2011.

[72] P. B. Ayscough, K. Ivin, and J. O'Donnell, "Electron spin resonance spectra of γ-irradiated sulphones and polysulphones," *Transactions of the Faraday Society*, vol. 61, pp. 1110–1117, 1965.

[73] M. Geoffroy and E. Lucken, "Electron spin resonance spectra of RSO_2 radicals formed by the x radiolysis of sulfones," *The Journal of Chemical Physics*, vol. 55, no. 6, pp. 2719–2723, 1971.

[74] D. Boyle, W. Simpson, and J. Waldron, "A study of short chain branching in hydrocarbon polymers by the irradiation method. ithe detection of side chains," *Polymer*, vol. 2, pp. 323–334, 1961.

[75] E. Roduner, "Size matters: why nanomaterials are different," *Chemical Society Reviews*, vol. 35, no. 7, pp. 583–592, 2006.

[76] K. Koga, T. Ikeshoji, and K.-i. Sugawara, "Size-and temperature-dependent structural transitions in gold nanoparticles," *Physical review letters*, vol. 92, no. 11, p. 115507, 2004.

[77] E. Roduner, *Nanoscopic materials: Size-dependent phenomena and growth principles.* Royal Society of Chemistry, 2015.

[78] A. Köhn, F. Weigend, and R. Ahlrichs, "Theoretical study on clusters of magnesium," *Physical Chemistry Chemical Physics*, vol. 3, no. 5, pp. 711–719, 2001.

[79] C. Guozhong, *Nanostructures and nanomaterials: synthesis, properties and applications.* World scientific, 2004.

[80] D. Ciprari, K. Jacob, and R. Tannenbaum, "Characterization of polymer nanocomposite interphase and its impact on mechanical properties," *Macromolecules*, vol. 39, no. 19, pp. 6565–6573, 2006.

[81] P. Kanagaraj, S. Neelakandan, A. Nagendran, D. Rana, T. Matsuura, and A. Muthumeenal, "Performance studies of pei/spei blend ultra-filtration membranes via surface modification using csmm additives," *RSC Advances*, vol. 5, no. 35, pp. 27 594–27 602, 2015.

[82] U. Maitra, K. E. Prasad, U. Ramamurty, and C. Rao, "Mechanical properties of nanodiamond-reinforced polymer-matrix composites," *Solid State Communications*, vol. 149, no. 39-40, pp. 1693–1697, 2009.

[83] Y. C. Wang, S. C. Fan, K. R. Lee, C. L. Li, S. H. Huang, H. A. Tsai, and J. Y. Lai, "Polyamide/sds–clay hybrid nanocomposite membrane application to water–ethanol mixture pervaporation separation," *Journal of membrane science*, vol. 239, no. 2, pp. 219–226, 2004.

[84] Y. Kim, D. Rana, T. Matsuura, and W.-J. Chung, "Towards antibiofouling ultrafiltration membranes by blending silver containing surface modifying macromolecules," *Chemical Communications*, vol. 48, no. 5, pp. 693–695, 2012.

[85] S. R. Lakhotia, M. Mukhopadhyay, and P. Kumari, "Cerium oxide nanoparticles embedded thin-film nanocomposite nanofiltration membrane for water treatment," *Scientific reports*, vol. 8, no. 1, p. 4976, 2018.

[86] J. Liu, Y. Gao, D. Cao, L. Zhang, and Z. Guo, "Nanoparticle dispersion and aggregation in polymer nanocomposites: insights from molecular dynamics simulation," *Langmuir*, vol. 27, no. 12, pp. 7926–7933, 2011.

[87] J. Oberdisse, "Aggregation of colloidal nanoparticles in polymer matrices," *Soft matter*, vol. 2, no. 1, pp. 29–36, 2006.

[88] P. Goh, B. Ng, W. Lau, and A. Ismail, "Inorganic nanomaterials in polymeric ultrafiltration membranes for water treatment," *Separation & Purification Reviews*, vol. 44, no. 3, pp. 216–249, 2015.

[89] I. Armentano, M. Dottori, E. Fortunati, S. Mattioli, and J. Kenny, "Biodegradable polymer matrix nanocomposites for tissue engineering: a review," *Polymer degradation and stability*, vol. 95, no. 11, pp. 2126–2146, 2010.

[90] P. B. Palani, R. Kannan, S. Rajashabala, S. Rajendran, and G. Velraj, "Effect of nano-composite on polyvinyl alcohol-based proton conducting membrane for direct methanol fuel cell applications," *Ionics*, vol. 21, no. 2, pp. 507–513, 2015.

[91] Y. N. Pandey, G. J. Papakonstantopoulos, and M. Doxastakis, "Polymer/-nanoparticle interactions: bridging the gap," *Macromolecules*, vol. 46, no. 13, pp. 5097–5106, 2013.

[92] G. Polizos, E. Tuncer, A. L. Agapov, D. Stevens, A. P. Sokolov, M. Kidder, J. Jacobs, H. Koerner, R. Vaia, K. More *et al.*, "Effect of polymer–nanoparticle interactions on the glass transition dynamics and the conductivity mechanism in polyurethane titanium dioxide nanocomposites," *Polymer*, vol. 53, no. 2, pp. 595–603, 2012.

[93] G. Schmidt and M. M. Malwitz, "Properties of polymer–nanoparticle composites," *Current opinion in colloid & interface science*, vol. 8, no. 1, pp. 103–108, 2003.

[94] N. Hilal, M. Khayet, and C. J. Wright, *Membrane modification: Technology and applications.* CRC press, 2016.

[95] H. Zhao, L. Wu, Z. Zhou, L. Zhang, and H. Chen, "Improving the antifouling property of polysulfone ultrafiltration membrane by incorporation of isocyanate-treated graphene oxide," *Physical Chemistry Chemical Physics*, vol. 15, no. 23, pp. 9084–9092, 2013.

[96] M. Miyauchi, A. Nakajima, T. Watanabe, and K. Hashimoto, "Photocatalysis and photoinduced hydrophilicity of various metal oxide thin films," *Chemistry of Materials*, vol. 14, no. 6, pp. 2812–2816, 2002.

[97] S. Madaeni and N. Ghaemi, "Characterization of self-cleaning ro membranes coated with TiO_2 particles under uv irradiation," *Journal of Membrane Science*, vol. 303, no. 1-2, pp. 221–233, 2007.

[98] Y. Yang and P. Wang, "Preparation and characterizations of a new ps/TiO_2 hybrid membranes by sol–gel process," *Polymer*, vol. 47, no. 8, pp. 2683–2688, 2006.

[99] H. Rabiee, M. H. D. A. Farahani, and V. Vatanpour, "Preparation and characterization of emulsion poly (vinyl chloride)(epvc)/TiO_2 nanocomposite ultrafiltration membrane," *Journal of membrane science*, vol. 472, pp. 185–193, 2014.

[100] Z. Yu, X. Liu, F. Zhao, X. Liang, and Y. Tian, "Fabrication of a low-cost nano-SiO_2/pvc composite ultrafiltration membrane and its antifouling performance," *Journal of Applied Polymer Science*, vol. 132, no. 2, 2015.

[101] S. Liang, K. Xiao, Y. Mo, and X. Huang, "A novel zno nanoparticle blended polyvinylidene fluoride membrane for anti-irreversible fouling," *Journal of membrane science*, vol. 394, pp. 184–192, 2012.

[102] P. Daraei, S. S. Madaeni, N. Ghaemi, E. Salehi, M. A. Khadivi, R. Moradian, and B. Astinchap, "Novel polyethersulfone nanocomposite membrane prepared by pani/fe3o4 nanoparticles with enhanced performance for cu(ii) removal from water," *Journal of Membrane Science*, vol. 415-416, pp. 250 – 259, 2012.

[103] M. Homayoonfal, M. R. Mehrnia, M. Shariaty-Niassar, A. Akbari, A. F. Ismail, and T. Matsuura, "A comparison between blending and surface deposition methods for the preparation of iron oxide/polysulfone nanocomposite membranes," *Desalination*, vol. 354, pp. 125–142, 2014.

[104] J. H. Jhaveri and Z. Murthy, "A comprehensive review on anti-fouling nanocomposite membranes for pressure driven membrane separation processes," *Desalination*, vol. 379, pp. 137–154, 2016.

[105] J. H. Li, X. S. Shao, Q. Zhou, M. Z. Li, and Q. Q. Zhang, "The double effects of silver nanoparticles on the pvdf membrane: Surface hydrophilicity and antifouling performance," *Applied Surface Science*, vol. 265, pp. 663–670, 2013.

[106] H. Basri, A. F. Ismail, and M. Aziz, "Polyethersulfone (pes)–silver composite uf membrane: effect of silver loading and pvp molecular weight on membrane morphology and antibacterial activity," *Desalination*, vol. 273, no. 1, pp. 72–80, 2011.

[107] W. L. Chou, D. G. Yu, and M. C. Yang, "The preparation and characterization of silver-loading cellulose acetate hollow fiber membrane for water treatment," *Polymers for advanced technologies*, vol. 16, no. 8, pp. 600–607, 2005.

[108] A. Dasari, J. Quirós, B. Herrero, K. Boltes, E. García-Calvo, and R. Rosal, "Antifouling membranes prepared by electrospinning polylactic acid containing biocidal nanoparticles," *Journal of Membrane Science*, vol. 405, pp. 134–140, 2012.

[109] S. Kar, M. Subramanian, A. Ghosh, R. Bindal, S. Prabhakar, J. Nuwad, C. Pillai, S. Chattopadhyay, and P. Tewari, "Potential of nanoparticles for water purification: a case-study on anti-biofouling behaviour of metal based polymeric nanocomposite membrane," *Desalination and Water Treatment*, vol. 27, no. 1-3, pp. 224–230, 2011.

[110] N. Akar, B. Asar, N. Dizge, and I. Koyuncu, "Investigation of characterization and biofouling properties of pes membrane containing selenium and copper nanoparticles," *Journal of Membrane Science*, vol. 437, pp. 216–226, 2013.

[111] P. Goh and A. Ismail, "Graphene-based nanomaterial: The state-of-the-art material for cutting edge desalination technology," *Desalination*, vol. 356, pp. 115–128, 2015.

[112] K. A. Mahmoud, B. Mansoor, A. Mansour, and M. Khraisheh, "Functional graphene nanosheets: The next generation membranes for water desalination," *Desalination*, vol. 356, pp. 208–225, 2015.

[113] C. Lee, X. Wei, J. W. Kysar, and J. Hone, "Measurement of the elastic properties and intrinsic strength of monolayer graphene," *science*, vol. 321, no. 5887, pp. 385–388, 2008.

[114] A. Hashimoto, K. Suenaga, A. Gloter, K. Urita, and S. Iijima, "Direct evidence for atomic defects in graphene layers," *Nature*, vol. 430, no. 7002, pp. 870–873, 2004.

[115] M. E. Suk and N. R. Aluru, "Water transport through ultrathin graphene," *The Journal of Physical Chemistry Letters*, vol. 1, no. 10, pp. 1590–1594, 2010.

[116] D. Cohen-Tanugi and J. C. Grossman, "Water permeability of nanoporous graphene at realistic pressures for reverse osmosis desalination," *The Journal of chemical physics*, vol. 141, no. 7, p. 074704, 2014.

[117] H. Du, J. Li, J. Zhang, G. Su, X. Li, and Y. Zhao, "Separation of hydrogen and nitrogen gases with porous graphene membrane," *The Journal of Physical Chemistry C*, vol. 115, no. 47, pp. 23 261–23 266, 2011.

[118] K. Sint, B. Wang, and P. Král, "Selective ion passage through functionalized graphene nanopores," *Journal of the American Chemical Society*, vol. 130, no. 49, pp. 16 448–16 449, 2008.

[119] M. Hu and B. Mi, "Enabling graphene oxide nanosheets as water separation membranes," *Environmental science & technology*, vol. 47, no. 8, pp. 3715–3723, 2013.

[120] P. Sun, M. Zhu, K. Wang, M. Zhong, J. Wei, D. Wu, Z. Xu, and H. Zhu, "Selective ion penetration of graphene oxide membranes," *ACS nano*, vol. 7, no. 1, pp. 428–437, 2013.

[121] R. Joshi, P. Carbone, F.-C. Wang, V. G. Kravets, Y. Su, I. V. Grigorieva, H. Wu, A. K. Geim, and R. R. Nair, "Precise and ultrafast molecular sieving through graphene oxide membranes," *science*, vol. 343, no. 6172, pp. 752–754, 2014.

[122] F. Perreault, M. E. Tousley, and M. Elimelech, “Thin-film composite polyamide membranes functionalized with biocidal graphene oxide nanosheets,” *Environmental Science & Technology Letters*, vol. 1, no. 1, pp. 71–76, 2014.

[123] Z. Wang, H. Yu, J. Xia, F. Zhang, F. Li, Y. Xia, and Y. Li, “Novel go-blended pvdf ultrafiltration membranes,” *Desalination*, vol. 299, pp. 50–54, 2012.

[124] L. Yu, Y. Zhang, B. Zhang, J. Liu, H. Zhang, and C. Song, “Preparation and characterization of hpei-go/pes ultrafiltration membrane with antifouling and antibacterial properties,” *Journal of membrane science*, vol. 447, pp. 452–462, 2013.

[125] J. Zhang, Z. Xu, W. Mai, C. Min, B. Zhou, M. Shan, Y. Li, C. Yang, Z. Wang, and X. Qian, “Improved hydrophilicity, permeability, antifouling and mechanical performance of pvdf composite ultrafiltration membranes tailored by oxidized low-dimensional carbon nanomaterials,” *Journal of Materials Chemistry A*, vol. 1, no. 9, pp. 3101–3111, 2013.

[126] J. Lee, H. R. Chae, Y. J. Won, K. Lee, C. H. Lee, H. H. Lee, I. C. Kim, and J. m. Lee, “Graphene oxide nanoplatelets composite membrane with hydrophilic and antifouling properties for wastewater treatment,” *Journal of membrane science*, vol. 448, pp. 223–230, 2013.

[127] K. P. Loh, Q. Bao, G. Eda, and M. Chhowalla, “Graphene oxide as a chemically tunable platform for optical applications,” *Nature chemistry*, vol. 2, no. 12, p. 1015, 2010.

[128] V. Singh, D. Joung, L. Zhai, S. Das, S. I. Khondaker, and S. Seal, “Graphene based materials: past, present and future,” *Progress in materials science*, vol. 56, no. 8, pp. 1178–1271, 2011.

[129] H. Wang, X. Yuan, Y. Wu, H. Huang, X. Peng, G. Zeng, H. Zhong, J. Liang, and M. Ren, “Graphene-based materials: fabrication, characterization and application for the decontamination of wastewater and wastegas and hydrogen storage/generation,” *Advances in Colloid and Interface Science*, vol. 195, pp. 19–40, 2013.

[130] T. Kuilla, S. Bhadra, D. Yao, N. H. Kim, S. Bose, and J. H. Lee, “Recent advances in graphene based polymer composites,” *Progress in polymer science*, vol. 35, no. 11, pp. 1350–1375, 2010.

[131] S. Gahlot, P. P. Sharma, H. Gupta, V. Kulshrestha, and P. K. Jha, "Preparation of graphene oxide nano-composite ion-exchange membranes for desalination application," *RSC Advances*, vol. 4, no. 47, pp. 24 662–24 670, 2014.

[132] S. Chatterjee, F. Nafezarefi, N. Tai, L. Schlagenhauf, F. Nüesch, and B. Chu, "Size and synergy effects of nanofiller hybrids including graphene nanoplatelets and carbon nanotubes in mechanical properties of epoxy composites," *Carbon*, vol. 50, no. 15, pp. 5380–5386, 2012.

[133] S. Y. Yang, W. N. Lin, Y. L. Huang, H. W. Tien, J. Y. Wang, C. C. M. Ma, S. M. Li, and Y. S. Wang, "Synergetic effects of graphene platelets and carbon nanotubes on the mechanical and thermal properties of epoxy composites," *Carbon*, vol. 49, no. 3, pp. 793–803, 2011.

[134] H. Yang, F. Li, C. Shan, D. Han, Q. Zhang, L. Niu, and A. Ivaska, "Covalent functionalization of chemically converted graphene sheets via silane and its reinforcement," *Journal of Materials Chemistry*, vol. 19, no. 26, pp. 4632–4638, 2009.

[135] A. Y. Park, H. Kwon, A. J. Woo, and S. J. Kim, "Layered double hydroxide surface modified with (3-aminopropyl) triethoxysilane by covalent bonding," *Advanced Materials*, vol. 17, no. 1, pp. 106–109, 2005.

[136] Y. Zhao, Z. Xu, M. Shan, C. Min, B. Zhou, Y. Li, B. Li, L. Liu, and X. Qian, "Effect of graphite oxide and multi-walled carbon nanotubes on the microstructure and performance of pvdf membranes," *Separation and Purification Technology*, vol. 103, pp. 78–83, 2013.

[137] S. Zinadini, A. A. Zinatizadeh, M. Rahimi, V. Vatanpour, and H. Zangeneh, "Preparation of a novel antifouling mixed matrix pes membrane by embedding graphene oxide nanoplates," *Journal of Membrane Science*, vol. 453, pp. 292–301, 2014.

[138] Z. Xu, J. Zhang, M. Shan, Y. Li, B. Li, J. Niu, B. Zhou, and X. Qian, "Organosilane-functionalized graphene oxide for enhanced antifouling and mechanical properties of polyvinylidene fluoride ultrafiltration membranes," *Journal of Membrane Science*, vol. 458, pp. 1–13, 2014.

[139] L. Liu, F. Zhao, J. Liu, and F. Yang, "Preparation of highly conductive cathodic membrane with graphene (oxide)/ppy and the membrane antifouling property in filtrating yeast suspensions in embr," *Journal of membrane science*, vol. 437, pp. 99–107, 2013.

[140] J. H. Choi, J. Jegal, and W. N. Kim, “Fabrication and characterization of multi-walled carbon nanotubes/polymer blend membranes,” *Journal of Membrane Science*, vol. 284, no. 1-2, pp. 406–415, 2006.

[141] Y. H. Liu, B. Yi, Z. G. Shao, D. Xing, and H. Zhang, “Carbon nanotubes reinforced nafion composite membrane for fuel cell applications,” *Electrochemical and Solid-State Letters*, vol. 9, no. 7, p. A356, 2006.

[142] C. Zhijiang, Z. Cong, X. Ping, G. Jie, and Z. Kongyin, “Calcium alginate-coated electrospun polyhydroxybutyrate/carbon nanotubes composite nanofibers as nanofiltration membrane for dye removal,” *Journal of Materials Science*, vol. 53, no. 20, pp. 14 801–14 820, 2018.

[143] S. K. Verma, A. Modi, and J. Bellare, “Polyethersulfone-carbon nanotubes composite hollow fiber membranes with improved biocompatibility for bioartificial liver,” *Colloids and Surfaces B: Biointerfaces*, vol. 181, pp. 890–895, 2019.

[144] V. N. Mochalin, O. Shenderova, D. Ho, and Y. Gogotsi, “The properties and applications of nanodiamonds,” *Nature nanotechnology*, vol. 7, no. 1, p. 11, 2012.

[145] V. Y. Dolmatov, “Detonation-synthesis nanodiamonds: synthesis, structure, properties and applications,” *Russian Chemical Reviews*, vol. 76, no. 4, p. 339, 2007.

[146] D. Amans, A. C. Chenus, G. Ledoux, C. Dujardin, C. Reynaud, O. Sublemontier, K. Masenelli Varlot, and O. Guillois, “Nanodiamond synthesis by pulsed laser ablation in liquids,” *Diamond and Related Materials*, vol. 18, no. 2-3, pp. 177–180, 2009.

[147] J.-P. Boudou, P. A. Curmi, F. Jelezko, J. Wrachtrup, P. Aubert, M. Sennour, G. Balasubramanian, R. Reuter, A. Thorel, and E. Gaffet, “High yield fabrication of fluorescent nanodiamonds,” *Nanotechnology*, vol. 20, no. 23, p. 235602, 2009.

[148] E. Dekempeneer, L. Eersels, J. Smeets, J. Meneve, R. Jacobs, B. Blanpain, and J. Roos, “Rf plasma-assisted chemical vapour deposition of diamond-like carbon films on complex geometries,” *Diamond and Related Materials*, vol. 2, no. 2-4, pp. 272–277, 1993.

[149] S. Kazi, “A review article on nanodiamonds discussing their properties and applications,” *Int J Pharm Sci Inv*, vol. 3, pp. 40–45, 2014.

[150] S. Welz, Y. Gogotsi, and M. J. McNallan, "Nucleation, growth, and graphitization of diamond nanocrystals during chlorination of carbides," *Journal of applied physics*, vol. 93, no. 7, pp. 4207–4214, 2003.

[151] T. Daulton, M. Kirk, R. Lewis, and L. Rehn, "Production of nanodiamonds by high-energy ion irradiation of graphite at room temperature," *Nuclear Instruments and Methods in Physics Research Section B: Beam Interactions with Materials and Atoms*, vol. 175, pp. 12–20, 2001.

[152] F. Banhart, T. Füller, P. Redlich, and P. Ajayan, "The formation, annealing and self-compression of carbon onions under electron irradiation," *Chemical Physics Letters*, vol. 269, no. 3-4, pp. 349–355, 1997.

[153] A. K. Khachatryan, S. Aloyan, P. May, R. Sargsyan, V. Khachatryan, and V. Baghdasaryan, "Graphite-to-diamond transformation induced by ultrasound cavitation," *Diamond and Related Materials*, vol. 17, no. 6, pp. 931–936, 2008.

[154] T. Petit, J. C. Arnault, H. A. Girard, M. Sennour, T. Y. Kang, C. L. Cheng, and P. Bergonzo, "Oxygen hole doping of nanodiamond," *Nanoscale*, vol. 4, no. 21, pp. 6792–6799, 2012.

[155] Y. Liu, S. Chen, X. Quan, and H. Yu, "Efficient electrochemical reduction of carbon dioxide to acetate on nitrogen-doped nanodiamond," *Journal of the American Chemical Society*, vol. 137, no. 36, pp. 11 631–11 636, 2015.

[156] A. Krueger and D. Lang, "Functionality is key: recent progress in the surface modification of nanodiamond," *Advanced Functional Materials*, vol. 22, no. 5, pp. 890–906, 2012.

[157] R. Ahmad, "Diamond nanostructured devices for chemical sensing applications," Ph.D. dissertation, UCL (University College London), 2011.

[158] A. Shakun, J. Vuorinen, M. Hoikkanen, M. Poikelispää, and A. Das, "Hard nanodiamonds in soft rubbers: Past, present and future–a review," *Composites Part A: Applied Science and Manufacturing*, vol. 64, pp. 49–69, 2014.

[159] A. S. Barnard and M. Sternberg, "Crystallinity and surface electrostatics of diamond nanocrystals," *Journal of Materials Chemistry*, vol. 17, no. 45, pp. 4811–4819, 2007.

[160] V. N. Mochalin and Y. Gogotsi, "Nanodiamond–polymer composites," *Diamond and Related Materials*, vol. 58, pp. 161–171, 2015.

[161] I. Kulakova, "Surface chemistry of nanodiamonds," *Physics of the solid state*, vol. 46, no. 4, pp. 636–643, 2004.

[162] E. Alishahi, S. Shadlou, S. Doagou-R, and M. R. Ayatollahi, "Effects of carbon nanoreinforcements of different shapes on the mechanical properties of epoxy-based nanocomposites," *Macromolecular Materials and Engineering*, vol. 298, no. 6, pp. 670–678, 2013.

[163] P. Karami, S. S. Khasraghi, M. Hashemi, S. Rabiei, and A. Shojaei, "Polymer/nanodiamond composites-a comprehensive review from synthesis and fabrication to properties and applications," *Advances in colloid and interface science*, 2019.

[164] S. Kumar, M. Nehra, D. Kedia, N. Dilbaghi, K. Tankeshwar, and K. H. Kim, "Nanodiamonds: Emerging face of future nanotechnology," *Carbon*, vol. 143, pp. 678 – 699, 2019.

[165] A. Tizchang, Y. Jafarzadeh, R. Yegani, and E. Shokri, "Polysulfone nanocomposite membrane embedded by silanized nanodiamond for removal of humic acid from water," *Journal of Water and Environmental Nanotechnology*, vol. 4, no. 3, pp. 213–226, 2019.

[166] S. Osswald, G. Yushin, V. Mochalin, S. O. Kucheyev, and Y. Gogotsi, "Control of sp2/sp3 carbon ratio and surface chemistry of nanodiamond powders by selective oxidation in air," *Journal of the American Chemical Society*, vol. 128, no. 35, pp. 11 635–11 642, 2006.

[167] V. Mochalin, S. Osswald, and Y. Gogotsi, "Contribution of functional groups to the raman spectrum of nanodiamond powders," *Chemistry of Materials*, vol. 21, no. 2, pp. 273–279, 2009.

[168] A. Tizchang, Y. Jafarzadeh, R. Yegani, and S. Khakpour, "The effects of pristine and silanized nanodiamond on the performance of polysulfone membranes for wastewater treatment by mbr system," *Journal of Environmental Chemical Engineering*, vol. 7, no. 6, p. 103447, 2019.

[169] M. Ayatollahi, E. Alishahi, S. Doagou-R, and S. Shadlou, "Tribological and mechanical properties of low content nanodiamond/epoxy nanocomposites," *Composites Part B: Engineering*, vol. 43, no. 8, pp. 3425–3430, 2012.

[170] A. Gavrilov and A. Voznyakovskii, "Rheological characteristics and relaxation properties of polymer-nanodiamond composites," *Russian Journal of Applied Chemistry*, vol. 82, no. 6, pp. 1041–1045, 2009.

[171] E. Roumeli, E. Pavlidou, A. Avgeropoulos, G. Vourlias, D. N. Bikiaris, and K. Chrissafis, "Factors controlling the enhanced mechanical and thermal properties of nanodiamond-reinforced cross-linked high density polyethylene," *The Journal of Physical Chemistry B*, vol. 118, no. 38, pp. 11 341–11 352, 2014.

[172] J. Y. Lee and D. S. Lim, “Tribological behavior of ptfe film with nanodiamond,” *Surface and Coatings Technology*, vol. 188, pp. 534–538, 2004.

[173] L. L. Beecroft and C. K. Ober, “Nanocomposite materials for optical applications,” *Chemistry of materials*, vol. 9, no. 6, pp. 1302–1317, 1997.

[174] Q. Zhang, V. N. Mochalin, I. Neitzel, I. Y. Knoke, J. Han, C. A. Klug, J. G. Zhou, P. I. Lelkes, and Y. Gogotsi, “Fluorescent plla-nanodiamond composites for bone tissue engineering,” *Biomaterials*, vol. 32, no. 1, pp. 87–94, 2011.

[175] Z. Hu, S. Haneklaus, G. Sparovek, and E. Schnug, “Rare earth elements in soils,” *Communications in Soil Science and Plant Analysis*, vol. 37, no. 9-10, pp. 1381–1420, 2006.

[176] C. Bouzigues, T. Gacoin, and A. Alexandrou, “Biological applications of rare-earth based nanoparticles,” *ACS nano*, vol. 5, no. 11, pp. 8488–8505, 2011.

[177] J. Conesa, “Computer modeling of surfaces and defects on cerium dioxide,” *Surface Science*, vol. 339, no. 3, pp. 337–352, 1995.

[178] S. Patil, S. Kuiry, S. Seal, and R. Vanfleet, “Synthesis of nanocrystalline ceria particles for high temperature oxidation resistant coating,” *Journal of Nanoparticle Research*, vol. 4, no. 5, pp. 433–438, 2002.

[179] A. Trovarelli, “Catalytic properties of ceria and CeO_2-containing materials,” *Catalysis Reviews*, vol. 38, no. 4, pp. 439–520, 1996.

[180] A. B. Stambouli and E. Traversa, “Solid oxide fuel cells (sofcs): a review of an environmentally clean and efficient source of energy,” *Renewable and sustainable energy reviews*, vol. 6, no. 5, pp. 433–455, 2002.

[181] A. Corma, P. Atienzar, H. Garcia, and J.-Y. Chane-Ching, “Hierarchically mesostructured doped ceo 2 with potential for solar-cell use,” *Nature materials*, vol. 3, no. 6, p. 394, 2004.

[182] I. Celardo, J. Z. Pedersen, E. Traversa, and L. Ghibelli, “Pharmacological potential of cerium oxide nanoparticles,” *Nanoscale*, vol. 3, no. 4, pp. 1411–1420, 2011.

[183] T. S. Stefanik and H. L. Tuller, “Ceria-based gas sensors,” *Journal of the European ceramic society*, vol. 21, no. 10-11, pp. 1967–1970, 2001.

[184] L. Wang, K. Zhang, Z. Song, and S. Feng, “Ceria concentration effect on chemical mechanical polishing of optical glass,” *Applied surface science*, vol. 253, no. 11, pp. 4951–4954, 2007.

[185] Y. J. Wang, H. Dong, G. M. Lyu, H. Y. Zhang, J. Ke, L. Q. Kang, J. L. Teng, L. D. Sun, R. Si, J. Zhang *et al.*, "Engineering the defect state and reducibility of ceria based nanoparticles for improved anti-oxidation performance," *Nanoscale*, vol. 7, no. 33, pp. 13 981–13 990, 2015.

[186] F. Zhang, Q. Jin, and S.-W. Chan, "Ceria nanoparticles: size, size distribution, and shape," *Journal of applied physics*, vol. 95, no. 8, pp. 4319–4326, 2004.

[187] F. Esch, S. Fabris, L. Zhou, T. Montini, C. Africh, P. Fornasiero, G. Comelli, and R. Rosei, "Electron localization determines defect formation on ceria substrates," *Science*, vol. 309, no. 5735, pp. 752–755, 2005.

[188] S. Fernandez-Garcia, L. Jiang, M. Tinoco, A. B. Hungria, J. Han, G. Blanco, J. J. Calvino, and X. Chen, "Enhanced hydroxyl radical scavenging activity by doping lanthanum in ceria nanocubes," *The Journal of Physical Chemistry C*, vol. 120, no. 3, pp. 1891–1901, 2016.

[189] A. Bosnjakovic and S. Schlick, "Nafion perfluorinated membranes treated in fenton media: radical species detected by esr spectroscopy," *The Journal of Physical Chemistry B*, vol. 108, no. 14, pp. 4332–4337, 2004.

[190] C. T. Campbell and C. H. Peden, "Oxygen vacancies and catalysis on ceria surfaces," *Science*, vol. 309, no. 5735, pp. 713–714, 2005.

[191] M. Medhat and M. Fayez-Hassan, "Elemental analysis of cement used for radiation shielding by instrumental neutron activation analysis," *Nuclear Engineering and Design*, vol. 241, no. 6, pp. 2138–2142, 2011.

[192] W. Xia, J. Zhao, T. Wang, L. Song, H. Gong, H. Guo, B. Gao, X. Fan, and J. He, "Anchoring ceria nanoparticles on graphene oxide and their radical scavenge properties under gamma irradiation environment," *Physical Chemistry Chemical Physics*, vol. 19, no. 25, pp. 16 785–16 794, 2017.

[193] H. Y. Li, H. F. Wang, X. Q. Gong, Y. L. Guo, Y. Guo, G. Lu, and P. Hu, "Multiple configurations of the two excess 4 f electrons on defective ceo 2 (111): origin and implications," *Physical Review B*, vol. 79, no. 19, p. 193401, 2009.

[194] J. D. Cafun, K. O. Kvashnina, E. Casals, V. F. Puntes, and P. Glatzel, "Absence of ce3+ sites in chemically active colloidal ceria nanoparticles," *Acs Nano*, vol. 7, no. 12, pp. 10 726–10 732, 2013.

[195] B. Goris, S. Turner, S. Bals, and G. Van Tendeloo, "Three-dimensional valency mapping in ceria nanocrystals," *ACS nano*, vol. 8, no. 10, pp. 10 878–10 884, 2014.

[196] S. Schlick, M. Danilczuk, A. R. Drews, and R. S. Kukreja, “Scavenging of hydroxyl radicals by ceria nanoparticles: effect of particle size and concentration,” *The Journal of Physical Chemistry C*, vol. 120, no. 12, pp. 6885–6890, 2016.

[197] M. Anandkumar, C. Ramamurthy, C. Thirunavukkarasu, and K. S. Babu, “Influence of age on the free-radical scavenging ability ofCeO_2 and Au/CeO_2 nanoparticles,” *Journal of materials science*, vol. 50, no. 6, pp. 2522–2531, 2015.

[198] L. Wu, H. Wiesmann, A. Moodenbaugh, R. Klie, Y. Zhu, D. Welch, and M. Suenaga, “Oxidation state and lattice expansion of CeO_2- x nanoparticles as a function of particle size,” *Physical Review B*, vol. 69, no. 12, p. 125415, 2004.

[199] M. S. Lord, M. Jung, W. Y. Teoh, C. Gunawan, J. A. Vassie, R. Amal, and J. M. Whitelock, “Cellular uptake and reactive oxygen species modulation of cerium oxide nanoparticles in human monocyte cell line u937,” *Biomaterials*, vol. 33, no. 31, pp. 7915–7924, 2012.

[200] P. Arunkumar, M. Meena, and K. S. Babu, “A review on cerium oxide-based electrolytes for itsofc,” *Nanomaterials and Energy*, vol. 1, no. 5, pp. 288–305, 2012.

[201] T. Osawa, Y. Nakai, A. Mouri, and I. Y. S. Lee, “Studies of the preparation method of ceria-promoted nickel catalyst for carbon dioxide reforming of methane,” *Applied Catalysis A: General*, vol. 474, pp. 100–106, 2014.

[202] Y. Xue, Q. Luan, D. Yang, X. Yao, and K. Zhou, “Direct evidence for hydroxyl radical scavenging activity of cerium oxide nanoparticles,” *The Journal of Physical Chemistry C*, vol. 115, no. 11, pp. 4433–4438, 2011.

[203] G. Vinothkumar, S. Rengaraj, P. Arunkumar, S. W. Cha, and K. Suresh Babu, “Ionic radii and concentration dependency of RE^{3+} (Eu^{3+}, Nd^{3+}, Pr^{3+}, *and* La^{3+})-doped cerium oxide nanoparticles for enhanced multienzyme-mimetic and hydroxyl radical scavenging activity,” *The Journal of Physical Chemistry C*, vol. 123, no. 1, pp. 541–553, 2018.

[204] Y. Hakuta, S. Onai, H. Terayama, T. Adschiri, and K. Arai, “Production of ultra-fine ceria particles by hydrothermal synthesis under supercritical conditions,” *Journal of materials science letters*, vol. 17, no. 14, pp. 1211–1213, 1998.

[205] P.-L. Chen and I.-W. Chen, “Reactive cerium (iv) oxide powders by the homogeneous precipitation method,” *Journal of the American Ceramic Society*, vol. 76, no. 6, pp. 1577–1583, 1993.

[206] R. Purohit, B. Sharma, K. Pillai, and A. Tyagi, “Ultrafine ceria powders via glycine-nitrate combustion,” *Materials Research Bulletin*, vol. 36, no. 15, pp. 2711–2721, 2001.

[207] H. Gu and M. D. Soucek, “Preparation and characterization of monodisperse cerium oxide nanoparticles in hydrocarbon solvents,” *Chemistry of Materials*, vol. 19, no. 5, pp. 1103–1110, 2007.

[208] T. S. Sreeremya, K. M. Thulasi, A. Krishnan, and S. Ghosh, “A novel aqueous route to fabricate ultrasmall monodisperse lipophilic cerium oxide nanoparticles,” *Industrial & Engineering Chemistry Research*, vol. 51, no. 1, pp. 318–326, 2011.

[209] S. Sathyamurthy, K. J. Leonard, R. T. Dabestani, and M. P. Paranthaman, “Reverse micellar synthesis of cerium oxide nanoparticles,” *Nanotechnology*, vol. 16, no. 9, p. 1960, 2005.

[210] H.-L. Lin, C.-Y. Wu, and R.-K. Chiang, “Facile synthesis of CeO_2 nanoplates and nanorods by [1 0 0] oriented growth,” *Journal of colloid and interface science*, vol. 341, no. 1, pp. 12–17, 2010.

[211] L. Mädler, W. J. Stark, and S. E. Pratsinis, “Flame-made ceria nanoparticles,” *Journal of Materials Research*, vol. 17, no. 6, pp. 1356–1362, 2002.

[212] R. Purohit, A. Tyagi, M. Mathews, and S. Saha, “Combustion synthesis and bulk thermal expansion studies of ba and sr thorates,” *Journal of nuclear materials*, vol. 280, no. 1, pp. 51–55, 2000.

[213] Y. Zhou and M. N. Rahaman, “Effect of redox reaction on the sintering behavior of cerium oxide,” *Acta materialia*, vol. 45, no. 9, pp. 3635–3639, 1997.

[214] J. Kingsley, K. Suresh, and K. Patil, “Combustion synthesis of fine-particle metal aluminates,” *Journal of Materials Science*, vol. 25, no. 2, pp. 1305–1312, 1990.

[215] J. W. Lee, C. Lee, J. H. Lee, S.-K. Kim, H.-S. Cho, M. Kim, W. C. Cho, J. H. Joo, and C.-H. Kim, “Cerium oxide–polysulfone composite separator for an advanced alkaline electrolyzer,” *Polymers*, vol. 12, no. 12, p. 2821, 2020.

[216] J. Wei, H. Yao, Y. Wang, and G. Luo, "Controllable preparation and catalytic performance of magnetic fe3o4@ ceo2-polysulfone nanocomposites with core–shell structure," *Industrial & Engineering Chemistry Research*, vol. 57, no. 44, pp. 15 039–15 045, 2018.

[217] N. M. Ushakov, G. Y. Yurkov, L. V. Gorobinskii, O. V. Popkov, and I. D. Kosobudskii, "Nanocomposites based on the cerium oxide nanoparticles and polyethylene matrix: Syntheses and properties," *Acta Materialia*, vol. 56, no. 10, pp. 2336–2343, 2008.

[218] M. Breitwieser, C. Klose, A. Hartmann, A. Büchler, M. Klingele, S. Vierrath, R. Zengerle, and S. Thiele, "Cerium oxide decorated polymer nanofibers as effective membrane reinforcement for durable, high-performance fuel cells," *Advanced Energy Materials*, vol. 7, no. 6, p. 1602100, 2017.

[219] L. S. Schadler, "6.3 the elusive interphase/interface in polymer nanocomposites," 2018.

[220] J. Castle, "Practical surface analysis by auger and x-ray photoelectron spectroscopy. d. briggs and mp seah (editors). john wiley and sons ltd, chichester, 1983, 533 pp.,£ 44.50," *Surface and Interface Analysis*, vol. 6, no. 6, pp. 302–302, 1984.

[221] J. F. Moulder, "Handbook of x-ray photoelectron spectroscopy," *Physical electronics*, pp. 230–232, 1995.

[222] P. Kirkegaard, J. V. Olsen, M. M. Eldrup, and N. J. Pedersen, "Palsfit: A computer program for analysing positron lifetime spectra," 2009.

[223] S. Tao, "Positronium annihilation in molecular substances," *The Journal of Chemical Physics*, vol. 56, no. 11, pp. 5499–5510, 1972.

[224] M. Eldrup, D. Lightbody, and J. N. Sherwood, "The temperature dependence of positron lifetimes in solid pivalic acid," *Chemical Physics*, vol. 63, no. 1-2, pp. 51–58, 1981.

[225] T. Freltoft, J. Kjems, and S. Sinha, "Power-law correlations and finite-size effects in silica particle aggregates studied by small-angle neutron scattering," *Physical Review B*, vol. 33, no. 1, p. 269, 1986.

[226] S. Babu, A. Velez, K. Wozniak, J. Szydlowska, and S. Seal, "Electron paramagnetic study on radical scavenging properties of ceria nanoparticles," *Chemical Physics Letters*, vol. 442, no. 4-6, pp. 405–408, 2007.

[227] A. Ferrari, P. R. Sala, A. Fasso, and J. Ranft, "Fluka: A multi-particle transport code (program version 2005)," Tech. Rep., 2005.

[228] T. Böhlen, F. Cerutti, M. Chin, A. Fassò, A. Ferrari, P. Ortega, A. Mairani, P. R. Sala, G. Smirnov, and V. Vlachoudis, "The fluka code: developments and challenges for high energy and medical applications," *Nuclear data sheets*, vol. 120, pp. 211–214, 2014.

[229] K. H. Youm and W. S. Kim, "Prediction of intrinsic pore properties of ultrafiltration membrane by solute rejection curves: effects of operating conditions on pore properties," *Journal of chemical engineering of Japan*, vol. 24, no. 1, pp. 1–7, 1991.

[230] T. Noordman and J. Wesselingh, "Transport of large molecules through membranes with narrow pores: the maxwell–stefan description combined with hydrodynamic theory," *Journal of Membrane Science*, vol. 210, no. 2, pp. 227–243, 2002.

[231] M. Soltanieh and W. N. Gill', "Review of reverse osmosis membranes and transport models," *Chemical Engineering Communications*, vol. 12, no. 4-6, pp. 279–363, 1981.

[232] J. R. Pappenheimer, "Passage of molecules through capillary walls," *Physiological Reviews*, vol. 33, no. 3, pp. 387–423, 1953.

[233] A. Verniory, R. Du Bois, P. Decoodt, J. Gassee, and P. Lambert, "Measurement of the permeability of biological membranes application to the glomerular wall," *The Journal of general physiology*, vol. 62, no. 4, pp. 489–507, 1973.

[234] S. I. Nakao and S. Kimura, "Analysis of solutes rejection in ultrafiltration," *Journal of Chemical Engineering of Japan*, vol. 14, no. 1, pp. 32–37, 1981.

[235] Q. Zou, Y. Li, L. Zou, and M. Wang, "Characterization of structures and surface states of the nanodiamond synthesized by detonation," *Materials Characterization*, vol. 60, no. 11, pp. 1257–1262, 2009.

[236] C. Deng and P. Molian, "Laser shock wave treatment of polycrystalline diamond tool and nanodiamond powder compact," *The International Journal of Advanced Manufacturing Technology*, vol. 63, no. 1-4, pp. 259–267, 2012.

[237] F. Xie, W. Xie, L. Gong, W. Zhang, S. Chen, Q. Zhang, and J. Chen, "Surface characterization on graphitization of nanodiamond powder annealed in nitrogen ambient," *Surface and interface analysis*, vol. 42, no. 9, pp. 1514–1518, 2010.

[238] O. Shenderova, A. Panich, S. Moseenkov, S. Hens, V. Kuznetsov, and H.-M. Vieth, "Hydroxylated detonation nanodiamond: Ftir, xps, and nmr studies,"

The Journal of Physical Chemistry C, vol. 115, no. 39, pp. 19 005–19 011, 2011.

[239] C. Barth, M. Goncalves, A. Pires, J. Roeder, and B. Wolf, “Asymmetric polysulfone and polyethersulfone membranes: effects of thermodynamic conditions during formation on their performance,” *Journal of Membrane Science*, vol. 169, no. 2, pp. 287–299, 2000.

[240] L. Varshney, “Role of natural polysaccharides in radiation formation of pva–hydrogel wound dressing,” *Nuclear Instruments and Methods in Physics Research Section B: Beam Interactions with Materials and Atoms*, vol. 255, no. 2, pp. 343–349, 2007.

[241] D. R. Sekuli, B. M. Babi, L. M. Kljajevi, J. M. Sta, and B. V. Kaluerovi, “The effect of gamma radiation on the properties of activated carbon cloth,” *Journal of the Serbian Chemical Society*, vol. 74, no. 10, pp. 1125–1132, 2009.

[242] Y. Li, S. Huang, S. Zhou, A. G. Fane, Y. Zhang, and S. Zhao, “Enhancing water permeability and fouling resistance of polyvinylidene fluoride membranes with carboxylated nanodiamonds,” *Journal of Membrane Science*, vol. 556, pp. 154–163, 2018.

[243] A. Bedar, P. K. Tewari, R. C. Bindal, and S. Kar, “Enhancing γ-radiation resistant property of polysulfone membranes with carboxylated nanodiamond: Impact and effect of surface tunability,” *Applied Surface Science*, vol. 507, p. 144897, 2020.

[244] A. Zegaoui, A. r. Wang, A. Q. Dayo, B. Tian, W. b. Liu, J. Wang, and Y. g. Liu, “Effects of gamma irradiation on the mechanical and thermal properties of cyanate ester/benzoxazine resin,” *Radiation Physics and Chemistry*, vol. 141, pp. 110–117, 2017.

[245] G. Choudalakis and A. Gotsis, “Free volume and mass transport in polymer nanocomposites,” *Current opinion in colloid & interface science*, vol. 17, no. 3, pp. 132–140, 2012.

[246] Y. Zhang, K. Y. Rhee, D. Hui, and S.-J. Park, “A critical review of nanodiamond based nanocomposites: Synthesis, properties and applications,” *Composites Part B: Engineering*, 2018.

[247] H. Shintani, “Study on radiation sterilization-resistant polysulfones fabricated free from bisphenol a,” *Trends Biomater. Artif. Organs*, vol. 18, no. 1, pp. 36–40, 2004.

[248] M. Carter, H. Li, Y. Zhang, E. Vance, and D. Mitchell, “Titanate ceramics for immobilisation of uranium-rich radioactive wastes arising from 99mo production,” *Journal of Nuclear Materials*, vol. 384, no. 3, pp. 322–326, 2009.

[249] M. Francisco-Marquez, A. Galano, and A. Martínez, “On the free radical scavenging capability of carboxylated single-walled carbon nanotubes,” *The Journal of Physical Chemistry C*, vol. 114, no. 14, pp. 6363–6370, 2010.

[250] W. Xia, H. Xue, J. Wang, T. Wang, L. Song, H. Guo, X. Fan, H. Gong, and J. He, “Functionlized graphene serving as free radical scavenger and corrosion protection in gamma-irradiated epoxy composites,” *Carbon*, vol. 101, pp. 315–323, 2016.

[251] C. Moreno-Castilla, M. Lopez-Ramon, and F. Carrasco-Marın, “Changes in surface chemistry of activated carbons by wet oxidation,” *Carbon*, vol. 38, no. 14, pp. 1995–2001, 2000.

[252] S. A. Rakha, N. Ali, Y. A. Haleem, F. Alam, A. A. Khurram, and A. Munir, “Comparison of mechanical properties of acid and uv ozone treated nanodiamond epoxy nanocomposites,” *Journal of Materials Science & Technology*, vol. 30, no. 8, pp. 753–758, 2014.

[253] O. Shenderova, I. Petrov, J. Walsh, V. Grichko, V. Grishko, T. Tyler, and G. Cunningham, “Modification of detonation nanodiamonds by heat treatment in air,” *Diamond and related materials*, vol. 15, no. 11-12, pp. 1799–1803, 2006.

[254] D. G. Lim, K. H. Kim, E. Kang, S. H. Lim, J. Ricci, S. K. Sung, M. T. Kwon, and S. H. Jeong, “Comprehensive evaluation of carboxylated nanodiamond as a topical drug delivery system,” *International journal of nanomedicine*, vol. 11, p. 2381, 2016.

[255] I. Rehor and P. Cigler, “Precise estimation of hpht nanodiamond size distribution based on transmission electron microscopy image analysis,” *Diamond and Related Materials*, vol. 46, pp. 21–24, 2014.

[256] O. Kuznetsov, Y. Sun, R. Thaner, A. Bratt, V. Shenoy, M. S. Wong, J. Jones, and W. Billups, “Water-soluble nanodiamond,” *Langmuir*, vol. 28, no. 11, pp. 5243–5248, 2012.

[257] Y. Lei, M.-L. Zheng, Z.-S. Zhao, and X.-M. Duan, “Carboxylated nanodiamond: Aggregation properties in aqueous dispersion system and application in living cell fluorescence imaging,” *Journal of nanoscience and nanotechnology*, vol. 16, no. 3, pp. 2319–2324, 2016.

[258] J. H. Kim and K.-H. Lee, “Effect of peg additive on membrane formation by phase inversion,” *Journal of Membrane Science*, vol. 138, no. 2, pp. 153–163, 1998.

[259] V. Vatanpour, S. S. Madaeni, R. Moradian, S. Zinadini, and B. Astinchap, “Fabrication and characterization of novel antifouling nanofiltration membrane prepared from oxidized multiwalled carbon nanotube/polyethersulfone nanocomposite,” *Journal of Membrane Science*, vol. 375, no. 1-2, pp. 284–294, 2011.

[260] J. Brown and J. O’Donnell, “Effects of gamma radiation on two aromatic polysulfones. ii. a comparison of irradiation at various temperatures in air-vacuum environments,” *Journal of Applied Polymer Science*, vol. 23, no. 9, pp. 2763–2775, 1979.

[261] D. J. Hill, K. Milne, J. H. O’Donnell, and P. J. Pomery, “A recent advance in the determination of scission and cross-linking yields of gamma-ray irradiated polymers.” ACS Publications, 1996.

[262] L. E. Nielsen, “Cross-linking–effect on physical properties of polymers,” *Journal of Macromolecular Science, Part C*, vol. 3, no. 1, pp. 69–103, 1969.

[263] C. Ong, P. Goh, W. Lau, N. Misdan, and A. Ismail, “Nanomaterials for biofouling and scaling mitigation of thin film composite membrane: A review,” *Desalination*, vol. 393, pp. 2–15, 2016.

[264] M. Gaur, P. K. Singh, R. Chauhan *et al.*, “Structural and thermal properties of polysulfone-zno nanocomposites,” *Journal of thermal analysis and calorimetry*, vol. 111, no. 1, pp. 743–751, 2013.

[265] Y. H. Ting, C. C. Liu, S. M. Park, H. Jiang, P. F. Nealey, and A. E. Wendt, “Surface roughening of polystyrene and poly (methyl methacrylate) in Ar/O_2 plasma etching,” *Polymers*, vol. 2, no. 4, pp. 649–663, 2010.

[266] B. Ganesh, A. M. Isloor, and A. F. Ismail, “Enhanced hydrophilicity and salt rejection study of graphene oxide-polysulfone mixed matrix membrane,” *Desalination*, vol. 313, pp. 199–207, 2013.

[267] M. S. Islam, R. Masoodi, and H. Rostami, “The effect of nanoparticles percentage on mechanical behavior of silica-epoxy nanocomposites,” *Journal of Nanoscience*, vol. 2013, 2013.

[268] A. P. Pêgo, D. W. Grijpma, and J. Feijen, “Enhanced mechanical properties of 1, 3-trimethylene carbonate polymers and networks,” *Polymer*, vol. 44, no. 21, pp. 6495–6504, 2003.

[269] A. Bedar, N. Goswami, A. K. Singha, V. Kumar, A. K. Debnath, D. Sen, V. K. Aswal, S. Kumar, D. Dutta, B. Keshavkumar *et al.*, "Nanodiamonds as a state-of-the-art material for enhancing the gamma radiation resistance properties of polymeric membranes," *Nanoscale Advances*, vol. 2, no. 3, pp. 1214–1227, 2020.

[270] O. Glatter and O. Kratky, *Small angle X-ray scattering.* Academic press, 1982.

[271] M. J. Han and S. T. Nam, "Thermodynamic and rheological variation in polysulfone solution by pvp and its effect in the preparation of phase inversion membrane," *Journal of Membrane Science*, vol. 202, no. 1-2, pp. 55–61, 2002.

[272] P. K. Mallick, *Fiber-reinforced composites: materials, manufacturing, and design.* CRC press, 2007.

[273] V. Vatanpour, S. S. Madaeni, A. R. Khataee, E. Salehi, S. Zinadini, and H. A. Monfared, "TiO_2 embedded mixed matrix pes nanocomposite membranes: Influence of different sizes and types of nanoparticles on antifouling and performance," *Desalination*, vol. 292, pp. 19–29, 2012.

[274] M. Safarpour, A. Khataee, and V. Vatanpour, "Thin film nanocomposite reverse osmosis membrane modified by reduced graphene oxide/TiO_2 with improved desalination performance," *Journal of Membrane Science*, vol. 489, pp. 43–54, 2015.

[275] A. Bedar, R. Lenka, N. Goswami, V. Kumar, A. K. Debnath, D. Sen, S. Kumar, S. Ghodke, P. Tewari, R. Bindal *et al.*, "Polysulfone–ceria mixed-matrix membrane with enhanced radiation resistance behavior," *ACS Applied Polymer Materials*, vol. 1, no. 7, pp. 1854–1865, 2019.

[276] D. Mukherjee, B. G. Rao, and B. M. Reddy, "Characterization of ceria-based nano-oxide catalysts by raman spectroscopy," *Topics in Catalysis*, vol. 60, no. 19-20, pp. 1673–1681, 2017.

[277] D. Rana, H. L. Kim, H. Kwag, J. Rhee, K. Cho, T. Woo, B. H. Lee, and S. Choe, "Blends of ethylene 1-octene copolymer synthesized by ziegler–natta and metallocene catalysts. ii. rheology and morphological behaviors," *Journal of applied polymer science*, vol. 76, no. 13, pp. 1950–1964, 2000.

[278] G. Azimi, R. Dhiman, H. M. Kwon, A. T. Paxson, and K. K. Varanasi, "Hydrophobicity of rare-earth oxide ceramics," *Nature materials*, vol. 12, no. 4, p. 315, 2013.

[279] M. Khayet and M. García-Payo, "X-ray diffraction study of polyethersulfone polymer, flat-sheet and hollow fibers prepared from the same under different gas-gaps," *Desalination*, vol. 245, no. 1-3, pp. 494–500, 2009.

[280] A. Lepit, M. Yahya, N. Aini, N. Jaafar, A. Ali, and K. Dahlan, "Effects of γ-ray irradiation on electrical and physico-chemical properties of sulfonated pvdf-hfp/1h-1, 2, 4-triazole proton conducting membranes," *Int. J. Electrochem. Sci*, vol. 7, pp. 7712–7719, 2012.

[281] J. Ma, Y. Zhao, Z. Xu, C. Min, B. Zhou, Y. Li, B. Li, and J. Niu, "Role of oxygen-containing groups on mwcnts in enhanced separation and permeability performance for pvdf hybrid ultrafiltration membranes," *Desalination*, vol. 320, pp. 1–9, 2013.

[282] S. Bano, A. Mahmood, S. J. Kim, and K. H. Lee, "Graphene oxide modified polyamide nanofiltration membrane with improved flux and antifouling properties," *Journal of Materials Chemistry A*, vol. 3, no. 5, pp. 2065–2071, 2015.

[283] E. Eren, A. Sarihan, B. Eren, H. Gumus, and F. O. Kocak, "Preparation, characterization and performance enhancement of polysulfone ultrafiltration membrane using pbi as hydrophilic modifier," *Journal of Membrane Science*, vol. 475, pp. 1–8, 2015.

[284] O. Rozhin, A. Ferrari, and W. I. Milne, "Nanomaterial polymer compositions and uses thereof," Dec. 4 2012, uS Patent 8,323,789.

[285] S. Prasadh and R. C. W. Wong, "Unraveling the mechanical strength of biomaterials used as a bone scaffold in oral and maxillofacial defects," *Oral Science International*, vol. 15, no. 2, pp. 48–55, 2018.

[286] M. Siddiqui, A. Arif, and S. Bashmal, "Permeability-selectivity analysis of microfiltration and ultrafiltration membranes: Effect of pore size and shape distribution and membrane stretching," *Membranes*, vol. 6, no. 3, p. 40, 2016.

[287] C. M. Hansen, *Hansen solubility parameters: a user's handbook.* CRC press, 2007.

[288] J. H. Hildebrand, "A critique of the theory of solubility of non-electrolytes." *Chemical reviews*, vol. 44, no. 1, pp. 37–45, 1949.

[289] C. M. Hansen, "The universality of the solubility parameter," *Industrial & engineering chemistry product research and development*, vol. 8, no. 1, pp. 2–11, 1969.

[290] E. Arunan, G. R. Desiraju, R. A. Klein, J. Sadlej, S. Scheiner, I. Alkorta, D. C. Clary, R. H. Crabtree, J. J. Dannenberg, P. Hobza *et al.*, “Definition of the hydrogen bond (iupac recommendations 2011),” *Pure and applied chemistry*, vol. 83, no. 8, p. 1637, 2011.

[291] G. C. Vebber, P. Pranke, and C. N. Pereira, “Calculating hansen solubility parameters of polymers with genetic algorithms,” *Journal of Applied Polymer Science*, vol. 131, no. 1, 2014.

[292] J. C. Zuaznabar-Gardona and A. Fragoso, “Determination of the hansen solubility parameters of carbon nano-onions and prediction of their dispersibility in organic solvents,” *Journal of Molecular Liquids*, vol. 294, p. 111646, 2019.

Thesis Highlight

Name of the Student: Amita Bedar

Name of the CI/OCC: Bhabha Atomic Research Centre, Mumbai

Enrolment No.: ENGG01201504008

Thesis Title: Development and Characterization of radiation resistant nanocomposite polymeric membranes

Discipline: Engineering Sciences **Sub-Area of Discipline:** Chemical Engineering

Date of viva voce: 23rd March, 2021

The polymeric membranes have inherent limitations of low radiation stability, as the backbone is susceptible to radiation induced damages. In order to develop radiation resistant property of polymeric membranes, for the first time the research was oriented towards development of mixed-matrix membranes with enhanced radiation resistance attributes. These membranes can have sustainable application in radioactive effluent treatment. In the PhD work, attempts were made to exploit the unique properties of nanodiamond (ND) and cerium oxide (ceria) nanoparticles for protection of polysulfone (Psf) membrane matrix from consequences of radiation induced damage and attack of free radicals generated in water during membrane operation. The following investigations were carried out in the PhD thesis.

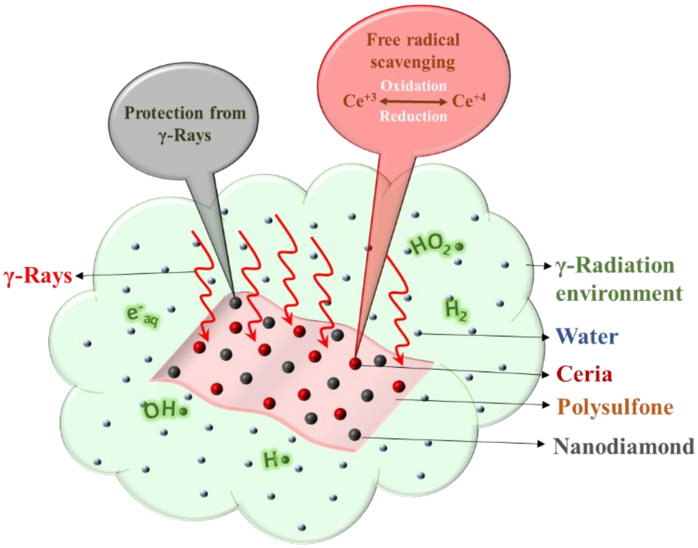

FIGURE 1: schematic representation of mixed matrix membrane and the role of nanomaterials (nanodiamond and ceria) for the protection of mixed matrix membrane in γ-radiation environment.

1. Effect of reinforcement of ND particles on radiation resistant behaviour of Psf membrane and life-span analysis in radioactive environment by Monte Carlo simulation studies.
2. Effect of carboxylated ND and its comparison with ND particles in terms of superiority in offering enhanced radiation resistant feature to Psf membrane.
3. Effect of ND size on radiation resistant property of membrane, and finding an optimum size.
4. Effect of ceria nanoparticles on radiation resistant property of Psf membrane and assessment of life-span in radiation environment.
5. Combined effect of reinforcement of both ND and ceria nanoparticles on radiation resistant property of membrane.

These objectives, for the first time, helped in understanding the role and influence of nanomaterials (ND and ceria) towards enhancing the life of polymeric membrane matrix in radiation environment.

Mixed-matrix membranes showed up to 10 times enhanced life-span in γ-radiation environment as compared to the control polymeric membrane, without compromise in its structural, mechanical, and chemical properties, as well as membrane performance (throughput and selectivity). This has been a unique study wherein the potential role of two nanomaterials was established in the gamma radiation environment.